

INFORMATION TO USERS

This manuscript has been reproduced from the microfilm master. UMI films the text directly from the original or copy submitted. Thus, some thesis and dissertation copies are in typewriter face, while others may be from any type of computer printer.

The quality of this reproduction is dependent upon the quality of the copy submitted. Broken or indistinct print, colored or poor quality illustrations and photographs, print bleedthrough, substandard margins, and improper alignment can adversely affect reproduction.

In the unlikely event that the author did not send UMI a complete manuscript and there are missing pages, these will be noted. Also, if unauthorized copyright material had to be removed, a note will indicate the deletion.

Oversize materials (e.g., maps, drawings, charts) are reproduced by sectioning the original, beginning at the upper left-hand corner and continuing from left to right in equal sections with small overlaps. Each original is also photographed in one exposure and is included in reduced form at the back of the book.

Photographs included in the original manuscript have been reproduced xerographically in this copy. Higher quality 6" x 9" black and white photographic prints are available for any photographs or illustrations appearing in this copy for an additional charge. Contact UMI directly to order.

U·M·I

University Microfilms International
A Bell & Howell Information Company
300 North Zeeb Road, Ann Arbor, MI 48106-1346 USA
313/761-4700 800/521-0600

Order Number 9307648

Near-infrared spectroscopy as an astrophysical tool

Kelly, Douglas Michael, Ph.D.

The University of Arizona, 1992

U·M·I
300 N. Zeeb Rd.
Ann Arbor, MI 48106

NEAR-INFRARED SPECTROSCOPY AS
AN ASTROPHYSICAL TOOL

by
Douglas Michael Kelly

A Dissertation Submitted to the Faculty of the
DEPARTMENT OF ASTRONOMY
In Partial Fulfillment of the Requirements
For the Degree of
DOCTOR OF PHILOSOPHY
In the Graduate College
THE UNIVERSITY OF ARIZONA

1 9 9 2

THE UNIVERSITY OF ARIZONA
GRADUATE COLLEGE

2

As members of the Final Examination Committee, we certify that we have
read the dissertation prepared by Douglas Michael Kelly
entitled Near-Infrared Spectroscopy as an Astrophysical Tool

and recommend that it be accepted as fulfilling the dissertation
requirement for the Degree of Doctor of Philosophy

George Rieke
George Rieke

11/13/92
Date

Jill Bechtold
Jill Bechtold

11/13/92
Date

John Biegging
John Biegging

11/13/92
Date

John Black
John Black

13 November, 1992
Date

Adam Burrows
Adam Burrows

11/13/92
Date

Final approval and acceptance of this dissertation is contingent upon
the candidate's submission of the final copy of the dissertation to the
Graduate College.

I hereby certify that I have read this dissertation prepared under my
direction and recommend that it be accepted as fulfilling the dissertation
requirement.

George Rieke
Dissertation Director

George Rieke

11/13/92
Date

STATEMENT BY AUTHOR

This dissertation has been submitted in partial fulfillment of requirements for an advanced degree at The University of Arizona and is deposited in the University Library to be made available to borrowers under rules of the Library.

Brief quotations from this dissertation are allowable without special permission, provided that accurate acknowledgment of source is made. Requests for permission for extended quotation from or reproduction of this manuscript in whole or in part may be granted by the head of the major department or the Dean of the Graduate College when in his or her judgment the proposed use of the material is in the interests of scholarship. In all other instances, however, permission must be obtained from the author.

SIGNED: Douglas Michael Kelly

ACKNOWLEDGEMENTS

I would like to thank my advisor, George Rieke, for all of his help, support, and patience while I worked on this thesis. George gave me a lot of room to make mistakes and learn on my own, yet he kept me on track towards completing my thesis, and he taught me how to approach writing and research. The lessons I learned from George will serve me well in the years to come. Thanks also to the other faculty at Steward Observatory, especially Marcia Rieke, John Black, Jill Bechtold, Adam Burrows, and Jim Liebert.

Thanks to the wonderful graduate students at Steward observatory, especially Kim McLeod, my good friend and sometimes juggling partner; Bill Latter, my favorite collaborator; and Mike Fulbright, with whom I have survived some of my most memorable hikes. Thanks also to Dennis Zaritsky, Hans-Walter Rix, Buell Jannuzi, Joe Haller, Liz Paley, Jim Bollinger, Brian McLeod, Davy Kirkpatrick, Dante Minniti, Doug Williams, Kim Dow, Jeff Regester, Pat Hall, Crystal Martin, Milagros Ruiz, and Chris Fryer.

Special thanks go to my family for all of their love and support. My Mom has been a constant source of good advice and common sense. My brother Steve is a bum, but he is also a great guy and a good friend. Lori has enriched my life this past year with stories about little Andy. Barb has inspired me to take the time to get out and enjoy nature. Finally, my Dad continues to influence me with his strong ethics and his dedication to the family.

Thanks also to my good friends - Matt Keating, Gordy & Patti Harvieux, Zeb & Mo Mordick, and my neighbor Bob Pardee. Thanks to the Steward telescope operators - Dennis Means, Gary Rosenbaum, & Vic Hansen. Thanks also to the people who got me started on infrared astronomy at the University of Minnesota -Bob Gehrz, Terry Jones, and Geoff Lawrence.

Thanks to the Wildcats basketball team for five exciting basketball seasons. Thanks also to the Twinkies for kicking Ted Turner and Jane Fonda's butts in the 1991 World Series.

Finally, thanks to Karen Visnovsky for her love and friendship over the past three and a half years. My life has been greatly enriched by our time together, and I look forward to many happy years to come.

DEDICATION

This thesis is dedicated in loving memory of my Dad,
who always encouraged me to study hard.

TABLE OF CONTENTS

LIST OF ILLUSTRATIONS	11
LIST OF TABLES	13
ABSTRACT	15
CHAPTER 1: INTRODUCTION	17
1.1 Motivation	17
1.2 The GeSpec	20
1.3 Observations and Data Reduction	24
1.4 Atomic Line Ratios	27
CHAPTER 2: THE SPECTRUM OF AFGL 618	33
2.1 Introduction	33
2.2 Background	34
2.3 Observations and Data Reduction	39
2.4 Atomic Spectrum	49
2.4.1 Background	49
2.4.2 Diagnostic Lines	50
2.4.3 Individual Sets of Lines	52
2.4.3.1 [S II]	52
2.4.3.2 [N I]	53
2.4.3.3 [N II]	53
2.4.3.4 [Fe II]	54
2.4.3.5 [O I]	55
2.4.3.6 [C I]	55

	7
2.4.3.7 [S III]	56
2.4.3.8 H I	56
2.4.3.9 He I	57
2.4.3.10 O I	58
2.4.4 Discussion	61
2.4.4.1 Extinction	61
2.4.4.2 Temperature Regimes	65
2.4.4.3 Shocks	65
2.4.4.4 Filling Factors	69
2.4.5 Summary of Atomic Data	71
2.5 Molecular Hydrogen Emission	73
2.5.1 Extinction to the H ₂ Emitting Region	74
2.5.2 Origin of the H ₂ Spectrum	76
2.5.3 Discussion	84
2.5.4 Summary of Molecular Data	90
CHAPTER 3: THE TEMPERATURE SCALE FOR M DWARFS DERIVED USING SPECTRA FROM 0.6 TO 1.5 MICRONS	101
3.1 Introduction	101
3.2 Observations and Data Reduction	103
3.3 Combining the Red and Infrared Spectra	105
3.4 Spectral Features	110
3.5 Fits to Theoretical Spectra of M Dwarfs	115
3.5.1 Fits in the Red Region	116
3.5.2 Fits in the Infrared Region	120
3.5.3 Synthetic Photometry	127
3.5.4 Comparison to Ruan's Models	129

3.6	Temperature Scale	130
3.7	Discussion	136
3.8	Summary	138
 CHAPTER 4: NEAR-INFRARED SPECTROSCOPY OF YOUNG STELLAR OBJECTS		
		148
4.1	Introduction	148
4.2	Observations and Data Reduction	150
4.3	Analysis	151
4.3.1	MWC 349	164
4.3.1.1	Extinction	167
4.3.1.2	Physical Structure	167
4.3.1.3	Fluorescence	169
4.3.2	LkH α 101	170
4.3.2.1	Extinction	171
4.3.2.2	Physical Structure	174
4.3.2.3	Fluorescence	175
4.3.2.4	Shocks	176
4.3.3	R Mon	176
4.3.3.1	Extinction	178
4.3.3.2	Physical Structure	179
4.3.3.3	Fluorescence	179
4.3.4	V645 Cyg	180
4.3.4.1	Extinction	182
4.3.4.2	Physical Structure	182
4.3.4.3	Shocks	185
4.3.5	GL 490	185

4.3.5.1	Extinction	187
4.3.5.2	Fluorescence	188
4.3.6	T Tau	188
4.3.6.1	Extinction	190
4.3.6.2	Physical Structure	191
4.3.6.3	Fluorescence	192
4.3.6.4	Shocks	192
4.3.7	HH 1	193
4.3.7.1	Extinction	193
4.3.7.2	Physical Structure	194
4.3.7.3	Fluorescence	195
4.3.7.4	Shocks	195
4.4	Conclusions	198
4.4.1	Extinction	198
4.4.2	Physical Structure	199
4.4.3	Fluorescence	200
4.4.4	Shocks	200
CHAPTER 5:	HIGH-EXCITATION OBJECTS	222
5.1	Introduction	222
5.2	Observations and Data Reduction	223
5.3	Analysis	230
5.3.1	High-Excitation Lines	230
5.3.2	Lines in Common to All Objects	234
5.3.3	Other Lines	239
5.3.4	Line Widths in the Spectrum of NGC 1068 ..	246

	10
5.4 Summary	248
CHAPTER 6: CONCLUSIONS	260
REFERENCES	264

LIST OF ILLUSTRATIONS

1.1	Schematic Diagram of the GeSpec	22
1.2	Grotrian Diagram for [C I]	28
1.3	Grotrian Diagram for [S II]	29
2.1	Schematic Diagram of AFGL 618	36
2.2	0.84 - 1.35 μm Spectrum of the Eastern Lobe of AFGL 618	42
2.3	Small Aperture 1.04 μm Spectra of AFGL 618	45
2.4	Small Aperture 1.32 μm Spectra of AFGL 618	46
2.5	0.40 - 0.69 μm Spectrum of the Eastern Lobe of AFGL 618	47
2.6	Grotrian Diagram for O I	58
2.7.1	Density-Temperature Plot for the Eastern Lobe of AFGL 618	67
2.7.2	Density-Temperature Plot for the Western Lobe of AFGL 618	68
2.8	Thermal and Fluorescent H ₂ Models for AFGL 618	82
3.1	0.63 - 1.50 μm Spectra of M Dwarfs	107
3.2.1	Identifications in the Spectrum of the M2 Dwarf GL 411	113
3.2.2	Identifications in the Spectrum of the M8 Dwarf GL 752B	114
3.3	Model Fits to the 0.63 - 0.90 μm Spectra of M Dwarfs	118
3.4	0.67 - 1.5 μm Spectrum of GL 752 B Plotted with the Model that Provides the Best Fit in the Red	122
3.5	Model Fits to the 1.08 - 1.35 μm Spectra of M Dwarfs	124
3.6.1	The H-R Diagram for M Dwarfs Compared to Models by D'Antona & Mazzitelli and Burrows, Hubbard, & Lunine	134

LIST OF ILLUSTRATIONS — *Continued*

3.6.2	The H-R Diagram for M Dwarfs Compared to Models by D'Antona & Mazzitelli and Dorman, Nelson, & Chau	135
4.1	0.40 - 0.69 μm Spectra of Young Stellar Objects ...	152
4.2.1	0.90 - 1.35 μm Spectrum of MWC 349	153
4.2.2	0.90 - 1.35 μm Spectrum of LkH α 101	154
4.2.3	0.90 - 1.35 μm Spectrum of R Mon	155
4.2.4	0.90 - 1.35 μm Spectrum of V645 Cyg	156
4.2.5	0.90 - 1.35 μm Spectrum of GL 490	157
4.2.6	0.90 - 1.35 μm Spectrum of T Tau	158
4.2.7	0.90 - 1.35 μm Spectrum of HH 1	159
4.3	Reddening Curves for Young Stellar Objects	163
4.4.1	Schematic Diagram of MWC 349	165
4.4.2	Schematic Diagram of R Mon	177
4.4.3	Schematic Diagram of V645 Cyg	180
4.4.4	Schematic Diagram of GL 490	186
4.4.5	Schematic Diagram of T Tau	189
4.5	Grotrian Diagram for Mg II	173
5.1	0.89 - 1.35 μm Spectrum of NGC 4151	224
5.2	0.89 - 1.35 μm Spectrum of NGC 1068	225
5.3	0.89 - 1.35 μm Spectrum of WR 110	226
5.4	0.89 - 1.35 μm Spectrum of NGC 7027	227
5.5	0.89 - 1.35 μm Spectrum of Hubble 12	228
5.6	0.89 - 1.35 μm Spectrum of the Orion Nebula	229

LIST OF TABLES

2.1	Line Identifications and Fluxes for AFGL 618	92
2.2	Densities in AFGL 618 as given by the [N I] (0.5198 + 0.5200)/(1.0398 + 1.0408) μm Ratio	97
2.3	Densities in AFGL 618 as given by the [N II] 0.5755/(0.6548 + 0.6583) μm Ratio	97
2.4	Densities in AFGL 618 as given by the [C I] 0.8727/(0.9824 + 0.9850) μm Ratio	98
2.5	H ₂ Line Flux Densities in AFGL 618	99
2.6	H ₂ v = 2 \rightarrow 0 and v = 2 \rightarrow 1 Lines Originating from the Same Upper State	100
3.1	Log of M Dwarf Observations	140
3.2	Comparison of I - J Values	141
3.3	Surface Gravities	142
3.4	Temperatures Derived from the Best Fit to Allard's Model Spectra with [M/H] = 0, log g = 5	143
3.5	Observed vs. Synthetic Colors	144
3.6	Comparison of Temperature Sequences	145
4.1	Log of Infrared Observations of Young Stellar Objects	202
4.2	Log of Visible Observations of Young Stellar Objects	203
4.3.1	Line Identifications and Fluxes in the 0.41 - 0.68 μm Spectra of MWC 349, LkH α 101, and R Mon .	204
4.3.2	Line Identifications and Fluxes in the 0.41 - 0.68 μm Spectra of V645 Cyg and T Tau	209
4.3.3	Line Identifications and Fluxes in the 0.89 - 1.35 μm Spectra of MWC 349, LkH α 101, and R Mon .	211
4.3.4	Line Identifications and Fluxes in the 0.89 - 1.35 μm Spectra of V645 Cyg, GL 490, T Tau, and HH 1	219

LIST OF TABLES — *Continued*

5.1	Log of Observations of High-Excitation Objects	249
5.2	Line Identifications and Fluxes in the Infrared Spectra of NGC 4151, NGC 1068, and WR 110	250
5.3	Line Identifications and Fluxes in the Infrared Spectra of NGC 7027, Hubble 12, and the Orion Nebula	253
5.4	Ionization Potentials for Ions of S, Ni, Fe, and Mn	259

ABSTRACT

Recent improvements in infrared detector arrays make it possible for the first time to conduct detailed spectroscopic studies of a complete range of objects in the 0.9 - 1.35 μm region. In this dissertation, I examine the 0.9 - 1.35 μm spectra of planetary and proto-planetary nebulae, M dwarfs, young stellar objects, Seyfert galaxies, an H II region, and a Wolf-Rayet star. Line identifications are made for each of these objects, and extensive line lists are presented. I also investigate what the lines can tell us about each object.

The 0.9 - 1.35 μm spectrum of the proto-planetary nebula AFGL 618 is dominated by recombination lines, low-ionization, shock-excited lines, and thermal and fluorescent H_2 lines. We use ratios of forbidden lines to show that there are two distinct physical regions in the lobes of AFGL 618, including one which must have been excited by shocks. We also show that the H_2 lines in the 0.9 - 1.35 μm region are ideal for detecting low levels of fluorescent H_2 emission, even when a strong thermal component is present.

We present 0.6 - 1.5 μm spectra for M dwarfs ranging from M2 through M9. These spectra are compared with recent theoretical models, and a temperature scale is determined. In late-M dwarfs, the shape of the infrared spectrum and the depth of the 1.35 μm H_2O feature are good temperature

indicators. The temperatures we derive for the M dwarfs are higher than the temperatures found in earlier studies and are in closer agreement with theoretical tracks of the lower main sequence.

We present 0.9 - 1.35 μm spectra for 7 young stellar objects. These objects exhibit a wide variety of behavior, including strong fluorescent emission. We show that the infrared spectra can be used to study all of the regions that are detected with visible and red spectra. As a result, 0.9 - 1.35 μm spectroscopy should be quite useful for studying heavily embedded sources.

The 0.9 - 1.35 μm spectra of high-excitation objects include a number of distinctive features, including He II lines, several high ionization lines, and very strong [S III] lines. We find that the excitation level of a source can be estimated based on these features alone.

Chapter 1

Introduction

1.1 Motivation

Visible-band spectroscopy has played an important role in astronomy for many years. With recent advances in infrared detector technology, it is now possible to build high resolution, very sensitive infrared spectrometers. If there is sufficient motivation and interest, infrared spectrometers could become as widely available as shorter wavelength spectrometers. In this thesis, I examine some of the unique aspects of the 0.9 - 1.35 μm wavelength region and show that the lines in this spectral interval contain much of the same information found in visible spectra.

One of the primary motivations for working in the infrared is the reduced effects of dust attenuation. One magnitude of extinction at 0.55 μm corresponds to only 0.404 mag at 1.0 μm , 0.282 mag at 1.25 μm , 0.210 mag at 1.5 μm , and 0.118 mag at 2.15 μm (Cardelli, Clayton, & Mathis 1989). Based on these numbers, it would appear that observations in the K atmospheric window (1.95 - 2.4 μm) would be preferable

to observations in the 1 μm region for studying obscured sources. However, the 1 μm region has several distinct advantages. First, the density of atomic lines is much higher at shorter wavelengths. The 2 μm region includes lines from the Brackett series of hydrogen, a bright He I line, and a number of permitted and forbidden iron lines. The 1 μm region contains the Paschen series of hydrogen, several bright He I lines, and a large number of permitted and forbidden metal lines. As will be discussed in Section 1.3, most metals have only five energy levels within 5 eV of the ground state (see Bashkin & Stoner 198?), and transitions between these levels provide the bulk of the cooling in gaseous nebulae. Most of the lines connecting these low-lying levels appear either in the visible, the red, or the 0.9 - 1.35 μm region of the spectrum. Ratios of these forbidden lines can be used as temperature and density indicators (see Chapter 5 of Osterbrock 1989), and as I show in this thesis, the infrared lines provide much of the same information as the visible and red lines. In addition, when combined with shorter wavelength spectra, the infrared lines provide several new indicators, including several line ratios that are nearly independent of density and temperature and can be used to measure the extinction to a source.

A second feature of infrared spectra is the strength of the molecular lines. The 2 μm region contains the bright, $\Delta v = 2$ bands of CO. The 1 μm region contains the much

fainter, $\Delta v = 4$ CO bands. The 2 μm region is also host to a large number of $\Delta v = 1$ rotational-vibrational lines of H_2 (see Black & van Dishoeck (1987) for a list of lines). These lines are usually excited either by shocks or by collisions in warm gas. The 1 μm region contains the $\Delta v = 2$ and $\Delta v = 3$ rotational-vibrational lines of H_2 . These lines are generally weak in collisionally excited gas but are expected to be quite strong in gas excited by UV fluorescence (Black & van Dishoeck 1987). The 1 μm region is thus the ideal place to look for fluorescence-excited H_2 emission. The 1 μm region is also the ideal place to look for fluorescence-excited O I emission. The 0.8446, 1.1287, and 1.3165 μm lines of O I can all be excited by UV fluorescence, and the 0.8446 and 1.1287 μm lines can be further enhanced by Ly β fluorescence (Grandi 1975).

There are several other important aspects to the 0.9 - 1.35 μm region. First, cool stars emit most of their flux in the infrared, and they peak in the near-infrared. The near-infrared is thus an ideal place to study brown dwarf candidates and stars on the lower end of the main sequence. Second, the 0.9 - 1.35 μm spectrum can be easily linked to shorter wavelength spectra. In extending to longer wavelengths, it is usually necessary to leave gaps in the spectral coverage because of the strong, infrared, water absorption bands. Third, the 0.9 - 1.35 μm region contains the He I 1.0830 μm line. As is demonstrated in this thesis,

this extraordinary line is one of the brightest lines in almost all emission line objects, and it has considerable potential for studying very faint objects, including heavily obscured objects in star formation regions. Finally, the Paschen series of hydrogen includes many lines that have the same upper level as easily observable Balmer and Brackett lines. Ratios of these lines can be used to determine the extinction to a source independent of assumptions about the density and temperature. Alternatively, if the reddening is already known, the line ratios might provide information on the optical depths of the hydrogen lines.

1.2 The GeSpec

The observations discussed in this thesis were made using an infrared, grating spectrometer known as the GeSpec. The GeSpec is designed for operation from 0.8 - 1.6 μm with modest resolution ($R \approx 10^3$) and high sensitivity. The principal investigators responsible for the design and construction of the GeSpec are George and Marcia Rieke. The instrument design is the work of Chris McAlary and Craig Thompson. The electronics work and mechanical construction were completed by Craig Thompson and Earl Montgomery. Additional instrument support was provided by Nat Carleton, Rich Boyle, and Frank Low. I am indebted to each of these people for producing such a fine instrument.

The optical design for the GeSpec is shown in Figure 1.1. The majority of the optics is operated at ambient temperature, and the dewar is cooled to 77 K. The F/9 or F/13.5 beam enters through the top of the instrument and passes through a dual-hole aperture plate. The apertures are 600 μm in diameter (6" on the 90" telescope) and are separated by 6 mm (60"). 800 μm diameter apertures are usually used on the Multiple Mirror Telescope, providing a beam size of 3" with a separation of 22". The aperture plate is tilted so that off-axis light is deflected to an acquisition camera for use in pointing and guiding.

The diverging beams from the twin apertures pass through several stages of baffling before reaching a collimating mirror. The collimated beams of light are directed towards the grating assembly, which consists of a pair of gold-coated gratings mounted back-to-back on a turntable. One grating has 600 1/mm, is blazed at 22 degrees, and provides a resolution of 1800 at 1.2 μm . The other grating has 150 1/mm, is blazed at 5.4 degrees, and provides a resolution of 400 at 1.2 μm . The grating drive encoder has an accuracy that corresponds to ~ 0.25 pixel at the detector array. The grating is tilted so that the desired wavelength is deflected by 14.5 degrees, towards the camera mirror. The camera mirror restores the beam to its input f/ratio. The tilt of the camera mirror is controlled by actuators and can be adjusted electronically. Continuum and xenon lamps can be

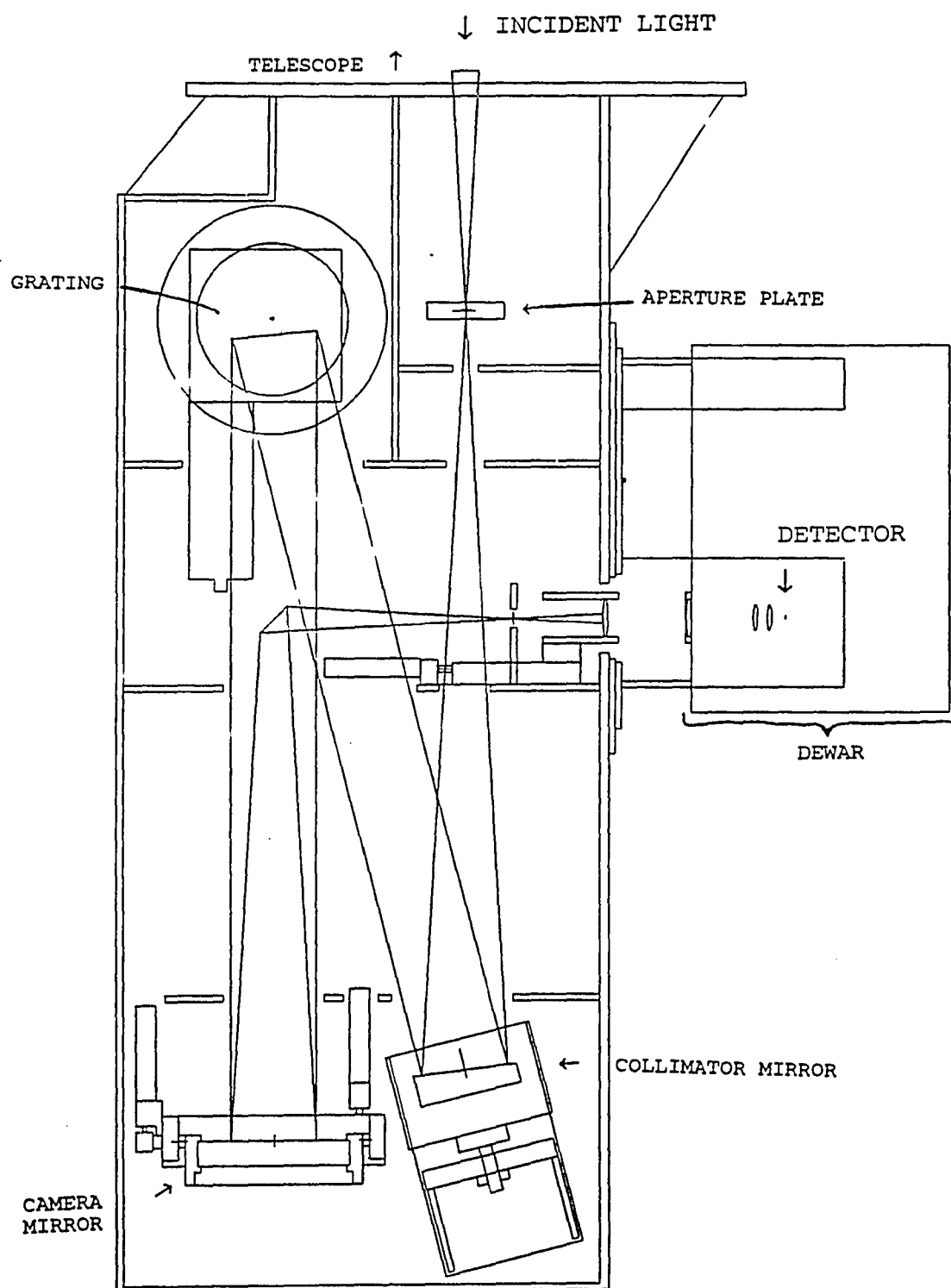


Figure 1.1 Schematic Diagram of the GeSpec

placed above the aperture plate to test whether light passing through the twin apertures is centered on the two sides of the array and is properly dispersed. Corrections are made to the alignment by adjusting the tilt of the camera mirror. Changing the grating tilt does not noticeably change the alignment. Instrument flexure produces small misalignments, primarily in the direction transverse to the array.

The collimated light from the camera mirror is deflected towards the dewar by a flat mirror. The flat mirror hides in the shadow of the hole in the primary mirror of the 90" telescope and between the 6 individual beams of the Multiple Mirror Telescope. When used on the 61" telescope, the flat mirror vignettes about 10% of the $f/13.5$ beam. From the flat mirror, the beams pass through a focal point, where there is additional baffling, and through a focussing lens that forms the first stage of a pupil-forming doublet. The second stage of the doublet is the aperture window of the dewar. An order-blocking filter and a cold stop are located at the pupil, 1" inside the dewar. A final doublet forms images at the detector.

The detector is a 2×32 front-illuminated array of germanium photodiodes developed at Ford Aerospace for potential use with the 2nd generation Hubble Space Telescope instrument, NICMOS. Each pixel is $125 \times 300 \mu\text{m}$ and is separated from neighboring pixels by $40 \mu\text{m}$. Rieke (1990) describes the tests that were performed on the germanium

photodiode arrays. The germanium diodes offer very low dark current, of order 1 electron per second, and high impedance. There is no significant read noise from the detector because it is run near zero bias. The quantum efficiency of the diodes is around 65% from 0.8 - 1.5 μm . The spectrometer can be operated out to 1.6 μm , but with rapidly decreasing efficiency.

The cold electronics used to read out the array consist of four 1 x 16 JFET integrators directed to four RCA CMOS multiplexers. The detector and cold electronics are operated at 77 K. The JFET integrators work by collecting photocharge on the combined capacitance of the detector and the JFET gate (Low 1984). The output of the JFETs can be read non-destructively, which allows a rapid sampling scheme that filters out the high frequency components of read noise. The read noise of the JFET integrators is ~ 80 electrons. The low read noise and dark current of the GeSpec permit background-limited operation over much of its spectral range, even when using the high resolution grating.

1.3 Observations and Data Reduction

Observations are made by centering an object in one of the two apertures. The other aperture provides a measurement of the nearby sky. During an integration, the JFET integrator outputs are sampled non-destructively at a rate

of typically 4 Hz. Lines are fit to these data by linear regression, and the slopes of the lines are proportional to the incident flux. Between integrations, the telescope is wobbled to place the object in the other aperture, and a new exposure is begun. This sequence is repeated, building up a series of alternating sky and object measurements on each side of the array. Similar measurements are made of a bright flatfield star in the same part of the sky. Late F and early G dwarfs are used for flatfielding since they have nearly featureless infrared spectra (Campins, Rieke, & Lebofsky 1985).

The data are reduced using a non-interactive Fortran program that was written by Hans-Walter Rix (see Rix et al. 1990) and which was later modified by me and by Kim McLeod. Because of pixel-to-pixel response variations, the two sides of the array are skysubtracted and flatfielded independently. The first step in the reduction is the removal of cosmic rays and bad readouts. Next, the sky is subtracted using the average of adjacent sky frames. The resulting skysubtracted spectra are scaled to the average of their median pixel values and combined. The uncertainty at each pixel is taken to be the dispersion in the typically 3 - 10 coadded flux values. A similar pair of skysubtracted spectra is produced for the flatfield star. The object spectra are divided by the flatfield star spectra, removing terrestrial absorption features and factoring out pixel-to-pixel sensitivity

variations. The spectra from the two sides of the array, now in units of the flatfield star flux, are normalized to the same median flux and are combined. The spectra are flux calibrated using photometric properties of the flatfield star (m_v , $J - V$, and T_{eff}) under the assumption that the flatfield star spectrum is a featureless blackbody. Finally, line fluxes are measured using the Image Reduction and Analysis Facility (IRAF), a data reduction package made available to the astronomical community through the National Optical Astronomy Observatories. The flux calibration of infrared spectra could be improved by establishing a set of carefully measured reference standards, similar to the ones used for visible spectroscopy (e.g. Massey et al. 1988). A greater number of standards is required for infrared spectroscopy since the object and reference star have to be close in the sky for proper removal of the strong atmospheric absorption features.

One of the primary sources of noise in the 0.9 - 1.35 μm region is OH airglow emission. A potentially greater source of noise in bright sources is variations in the strength of terrestrial absorption features. Both of these noise sources vary on relatively short time scales so it is important to monitor sky conditions carefully. The twin apertures of the GeSpec allow continuous monitoring of the sky without sacrificing on-source observing time. We track atmospheric transmission variations by interweaving

measurements of the object and reference star.

1.4 Atomic Line Ratios

Most of the spectroscopy in this thesis involves the detection of emission lines from photoionized gas. In all cases, the exciting source is much hotter than the surrounding gas. Energy is provided to the gas by photoionization and sometimes also by shock heating. Recombination and free-free emission provide little cooling. Metals, on the other hand, provide a large amount of cooling even though the metals constitute only a small fraction of the gas. The metals cool the gas by converting the kinetic energy of the electrons into photon energy. As shown in Figure 3.3 of Osterbrock (1989), the most efficient cooling lines are the forbidden line transitions connecting the ground and first excited terms of N^+ , O^+ , and O^{++} .

Most metals have low-lying energy levels that can be excited by collisions. When densities are high ($\geq 10^6 \text{ cm}^{-3}$), collisions de-excite the atoms before they can radiate. In lower density gas, the electrons de-excite radiatively by magnetic dipole and electric quadrupole transitions. Typical transition probabilities for these processes are of order tenths per second (Mendoza 1983). Since nebulae are almost always optically thin in the metal lines, the photons escape and carry energy away from the gas. The cooling efficiency

of the metals varies with temperature in such a way that most nebular gas has an electron temperature of about 10^4 K, regardless of the strength or hardness of the exciting radiation field.

Metals with a p^2 ground-state electron configuration (e.g. C^0 , N^+ , O^{++} , P^+ , and S^{++}) have 1D and 1S levels lying a few eV above a 3P ground term (see Figure 1.2). Higher

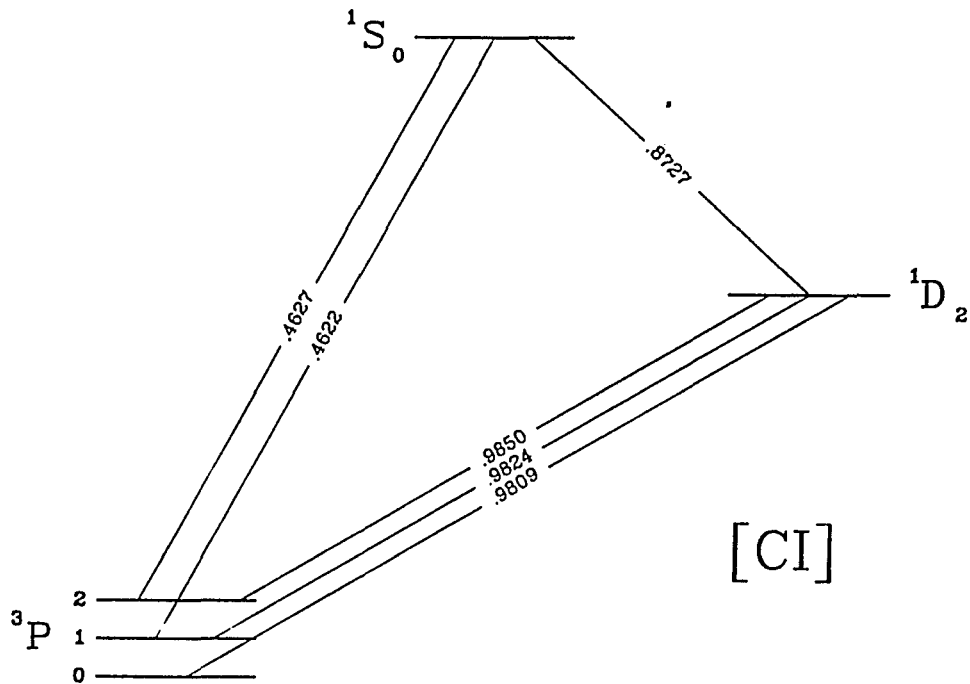


Figure 1.2: Grotrian Diagram for [C I]

levels are at much greater energies so collisions are usually only effective at populating the five lowest levels. A similar situation applies for metals with a p^3 configuration (e.g. N^0 , O^+ , and S^+), which have a 4S ground state and 2D and 2P excited states (see Figure 1.3), and for metals with a p^4

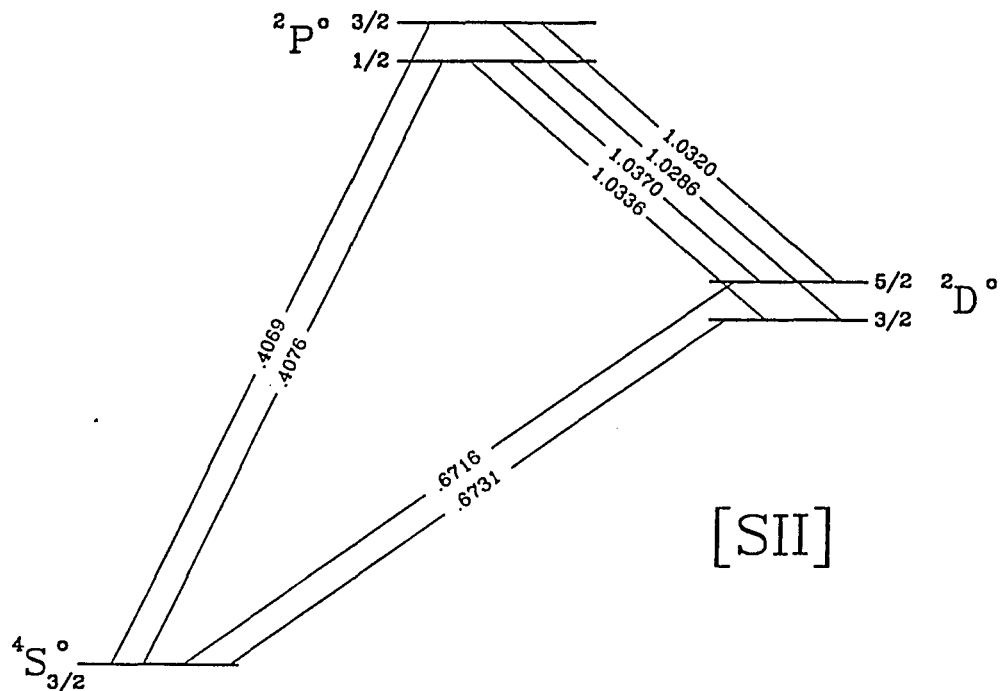


Figure 1.3: Grotrian Diagram for [S II]

configuration (e.g. O^0), which has a level structure similar to that of the p^2 metals except that the order of the fine-structure sublevels in the ground term is reversed.

The steady-state populations of the five lowest levels of these metals can be determined by balancing the rates at which collisions and radiative transitions populate and depopulate each level. For a sample two level atom with upper level i , lower level j , and populations N_i and N_j , the detailed balance equation is: $N_i(A_{ij} + n_e q_{ij}) = N_j n_e q_{ji}$, where A_{ij} is the rate coefficient for radiative transitions from level i to level j , n_e is the number density of electrons, q_{ij} is the electron de-excitation rate coefficient, and q_{ji} is

the electron excitation rate coefficient. In the case of a five level atom, the rate equation for excitation level i takes the form:

$$\sum_{j \neq i} n_{ij} n_e q_{ij} + \sum_{j > i} n_j A_{ji} = \sum_{j \neq i} n_i n_e q_{ij} + \sum_{j < i} n_i A_{ij}$$

The first term on the left describes the collisional population of level i from other levels. The second term describes radiative transitions from higher levels into level i . The third term describes collisions from level i into other levels. The last term describes radiative transitions from level i to lower levels. We omit terms describing excitation by absorption and by stimulated emission, which are more important at longer infrared wavelengths. The radiative transition probabilities, A_{ij} and A_{ji} , are independent of density and temperature. The collisional excitation and de-excitation rate coefficients both depend on the electron temperature. The de-excitation rate ($i > j$) is given by:

$$q_{ij} = \frac{8.629 \times 10^{-6}}{T_e^{1/2}} \frac{\Omega(j, i)}{\omega_i} \text{ cm}^{-3} \text{ s}^{-1}$$

where T_e is the electron temperature, ω_i is the statistical weight of level i , and $\Omega(j, i)$ is the mean collision strength.

The collision strength here is a temperature-averaged value that is generally insensitive to temperature. The collisional excitation rate is related to the de-excitation rate by:

$$q_{ji} = \frac{\omega_i}{\omega_j} q_{ij} \exp(-\chi_{ij}/kT)$$

where k is Boltzmann's constant and χ_{ij} is the excitation energy difference between levels i and j .

For a five level atom, there are four independent rate equations. The rate equations can be solved simultaneously by matrix methods to determine N_i/N_j for each of the four upper levels. Once the steady-state populations have been determined, they can be used to determine theoretical line ratios. The intensity of an emission line is proportional to the energy of a single photon, hc/λ_{ij} , times the rate at which photons are emitted, $N_i A_{ij}$. Line ratios are given by $(N_i A_{ij}/\lambda_{ij})_1 / (N_i A_{ij}/\lambda_{ij})_2$. Since level populations depend on the electron density and electron temperature, observational and theoretical line ratios can be compared to determine physical conditions in an emitting region. De Robertis, Dufour, & Hunt (1987) have written a Fortran program that solves the rate equations for most atoms of astrophysical interest. I wrote similar software to calculate line ratios for this thesis.

Much of the analysis in this thesis involves using line ratios to determine physical conditions in emitting regions. In Chapter 2, I examine the spectrum of the protoplanetary nebula AFGL 618. Both visible and infrared line ratios are used to determine physical conditions. In Chapter 3, I compare the 0.6 - 1.5 μm spectra of red dwarfs with model spectra to determine a temperature sequence for these objects. In Chapter 4, I examine the spectra of seven young stellar objects. This analysis again involves considerable use of metal line ratios and shows the usefulness of the infrared for studying heavily obscured objects. In Chapter 5, I examine the spectra of high-excitation objects, including Seyfert galaxies, planetary nebulae, a Wolf-Rayet star, and the Orion nebula. I identify the features that are produced in high-excitation spectra, and I examine what these features can tell us about excitation conditions in these objects. In Chapter 6, I review the highlights from the previous chapters, and I discuss future applications of 0.90 - 1.35 μm spectroscopy.

Chapter 2

The Spectrum of AFGL 618

2.1 Introduction

In this chapter, I discuss the spectrum of the proto-planetary nebula AFGL 618. The data are examined in minute detail, partly to see how much can be learned from a single, high quality, infrared spectrum. The work in this chapter was done in collaboration with Bill Latter and George Rieke. In particular, I did most of the observing, all of the data reduction, and most of the atomic line analysis. Bill did the modelling and analysis of the molecular hydrogen spectrum.

We have measured the 0.84 - 1.35 μm spectrum for the eastern lobe and the 0.40 - 0.68 μm spectra for both lobes of the bipolar nebula AFGL 618. These rich emission spectra are highlighted by strong forbidden lines. An extensive line list was compiled from these spectra, including many identifications in the poorly explored 1.0 - 1.35 μm region. Atomic line ratios provide evidence for two distinct physical regions in the lobes. The warmer region is apparently

excited by shocks and has an electron temperature of $T_e \approx 25000$ K. The electron density is $n_e \approx 8000 \text{ cm}^{-3}$. The cooler region has $T_e \approx 10000$ K and $n_e \approx 1600 \text{ cm}^{-3}$. By using line strengths to determine filling factors, we determined that the cooler component fills most of the visible lobes.

The near-infrared spectrum also includes emission from molecular hydrogen. By comparison of H_2 lines with a common upper level, we show that there is a visual extinction of $A_v = 3.4^{+4.0}_{-2.0}$ mag to the H_2 emitting region. Models of collisionally excited and fluorescent H_2 emission are compared with the data: the near-infrared H_2 spectrum is dominated by emission from collisionally excited molecules at $T_{\text{ex}} \approx 2000$ K, but a component of fluorescent emission is also present. The low level of fluorescent emission might indicate a clumpy structure, or one which partly shields the emitting region from the stellar continuum. It is shown that this type of near-infrared spectrum is an excellent tool for discriminating relatively low levels of fluorescent H_2 emission from a strong, collisionally excited component.

2.2 Background

AFGL 618 was first studied in detail by Westbrook et al. (1975), who observed it at visible, infrared, and radio wavelengths. They recognized AFGL 618 as a proto-planetary nebula, an object in rapid transition between the asymptotic

giant branch and planetary nebula phases of stellar evolution.

The general physical structure of AFGL 618 is shown in Figure 2.1. This picture is based on our data and on schematic diagrams presented by Kwok & Bignell (1984), Burton & Geballe (1986), and Neri et al. (1992). As suggested by Neri et al., it is likely that bow shocks form when high velocity outflowing material encounters dense clumps in the inner envelope. We discuss shocks further in Section 2.4.4.3.

As illustrated in Figure 2.1, AFGL 618 has a bipolar appearance. As stars evolve off the asymptotic giant branch (AGB) on the HR diagram to become planetary nebulae, they sometimes (perhaps always) take on the observed form of bipolar nebulae (e.g. Zuckerman & Gatley 1988). Such objects are characterized by symmetric lobes of gas and dust flowing outward from an obscured central star. This apparently brief period in a star's life (Morris 1981; Jura & Kroto 1990) is also one of the least understood. It has been suggested that bipolar nebulae result from stellar mass-loss in a close asynchronous binary system (Livio, Salzman & Shaviv 1979; Morris 1981, 1987; Bond & Livio 1990). While there is good reason to believe that duplicity shapes at least some bipolar nebulae, it might not be the only mechanism. Another hypothesis is that rapid stellar rotation causes a preferred

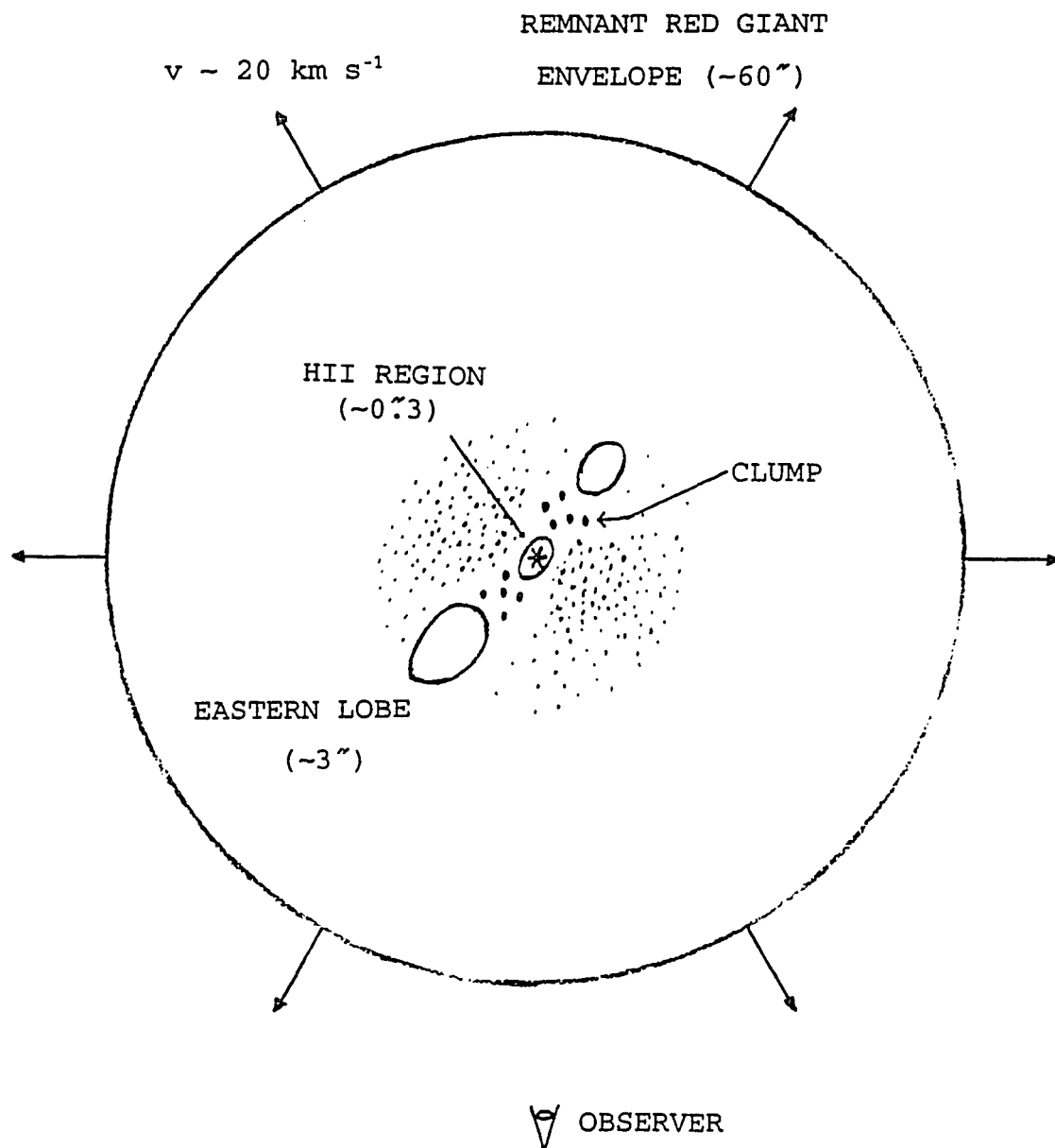


Figure 2.1: Schematic Diagram of AFGL 618

direction for mass ejection (Kwok & Bignell 1984; Calvet & Peimbert 1983; Morris 1981). This suggestion is, however, difficult to test.

Westbrook et al. (1975) observed AFGL 618 at $11.2\ \mu\text{m}$ and found a single, compact ($\sim 0''.4$ in diameter) infrared source midway between the two visible nebulosities. They measured an infrared ($3.5 - 34\ \mu\text{m}$) color temperature of $T_c \approx 275\ \text{K}$ for the compact source (see also Kleinmann et al. 1978 and Deutsch 1990). The bipolar structures are separated by $\sim 7''$ in the east-west direction (Calvet & Cohen 1978). Centimeter-wavelength radio observations reveal an elongated compact source ($0''.4 \times 0''.1$) aligned with the bipolar lobes (Kwok & Bignell 1984). Visible spectropolarimetry shows the two lobes to be reflection nebulae (Schmidt & Cohen 1981; hereafter SC81). SC81 derived an uncertain distance of $D \sim 1.8\ \text{kpc}$ (see discussion in Section II.b of SC81). The total luminosity derived from this distance, $L_{\text{tot}} \sim 2.6 \times 10^4 L_\odot$, is consistent with that expected for a post-AGB star. The infrared spectrum is dominated by dust continuum emission which arises primarily from the compact source (Kleinmann et al. 1978; Russell, Soifer, & Willner 1978). CO observations indicate an expansion velocity for the outer envelope of $V \approx 20\ \text{km s}^{-1}$ and a mass-loss rate on the order of $\dot{M} \sim 10^{-4} M_\odot \text{ yr}^{-1}$ (Lo & Bechis 1976; Thronson & Mozurkewich 1983; Knapp & Morris 1985; Bachiller et al. 1988).

Observations of the CO ($J = 2 \rightarrow 1$ and $J = 3 \rightarrow 2$) rotational transitions (Gammie et al. 1989; Cernicharo et al. 1989) indicate outflow velocities $V > 190 \text{ km s}^{-1}$. In addition, there exists an expanding central H II region (Kwok & Feldman 1981; Kwok & Bignell 1984; Martín-Pintado et al. 1988) and high velocity $\text{H}_2 \text{ v} = 1 \rightarrow 0 \text{ S}(1)$ emission (Burton & Geballe 1986). The ionization and forbidden line emission from the visible lobes might be explained by clumpiness within the visible lobes or by low velocity shocks (see SC81). The visible lines indicate an expansion velocity for the lobe material of $V \sim 80 \text{ km s}^{-1}$ (Carsenty & Solf 1982). The 20 km s^{-1} CO component appears to be the remnant AGB circumstellar envelope, while the 200 km s^{-1} component may be the onset of a "fast wind". Indeed, AFGL 618 has visibly brightened on a human timescale, increasing ~ 2 magnitudes since 1940 (Gottlieb & Liller 1976).

Of particular note for the atomic line analysis of this chapter is the work of SC81. They constructed a physical model for AFGL 618 based on their spectropolarimetric data. They found that the forbidden lines originate in the lobes, whereas the permitted line radiation comes in large part from the central nebula and is subsequently scattered into the line of sight by dust grains in the lobes. Forbidden lines dominate the spectrum, and the [NI] and [OI] lines are several orders of magnitude stronger relative to $\text{H}\alpha$ than in

typical, fully developed planetary nebulae. In addition, SC81 found evidence for two different temperature regions in the lobes.

In this chapter, we present the 0.84 - 1.34 μm spectrum of the eastern lobe of AFGL 618; we also present small-beam spectral data that were gathered at several places along the bipolar axis of the object. The infrared data are combined with a new, visible, long-slit spectrum, and we use the atomic line ratios to determine physical conditions in the emission regions. These results are compared with previous studies, in particular SC81, and we discuss how the new results change or support the physical picture of this object.

AFGL 618 has molecular material in close proximity to its central ultraviolet source. These conditions are expected to be favorable for fluorescent excitation of H_2 . We test this hypothesis by detailed modelling of the molecular spectrum. Earlier observations of molecular hydrogen emission (e.g. Thronson 1981; Beckwith, Beck, & Gatley 1984; Burton & Geballe 1986) have provided insight into the physical conditions in the nebula. We discuss how our observations strengthen or alter the earlier work.

2.3 Observations and Data Reduction

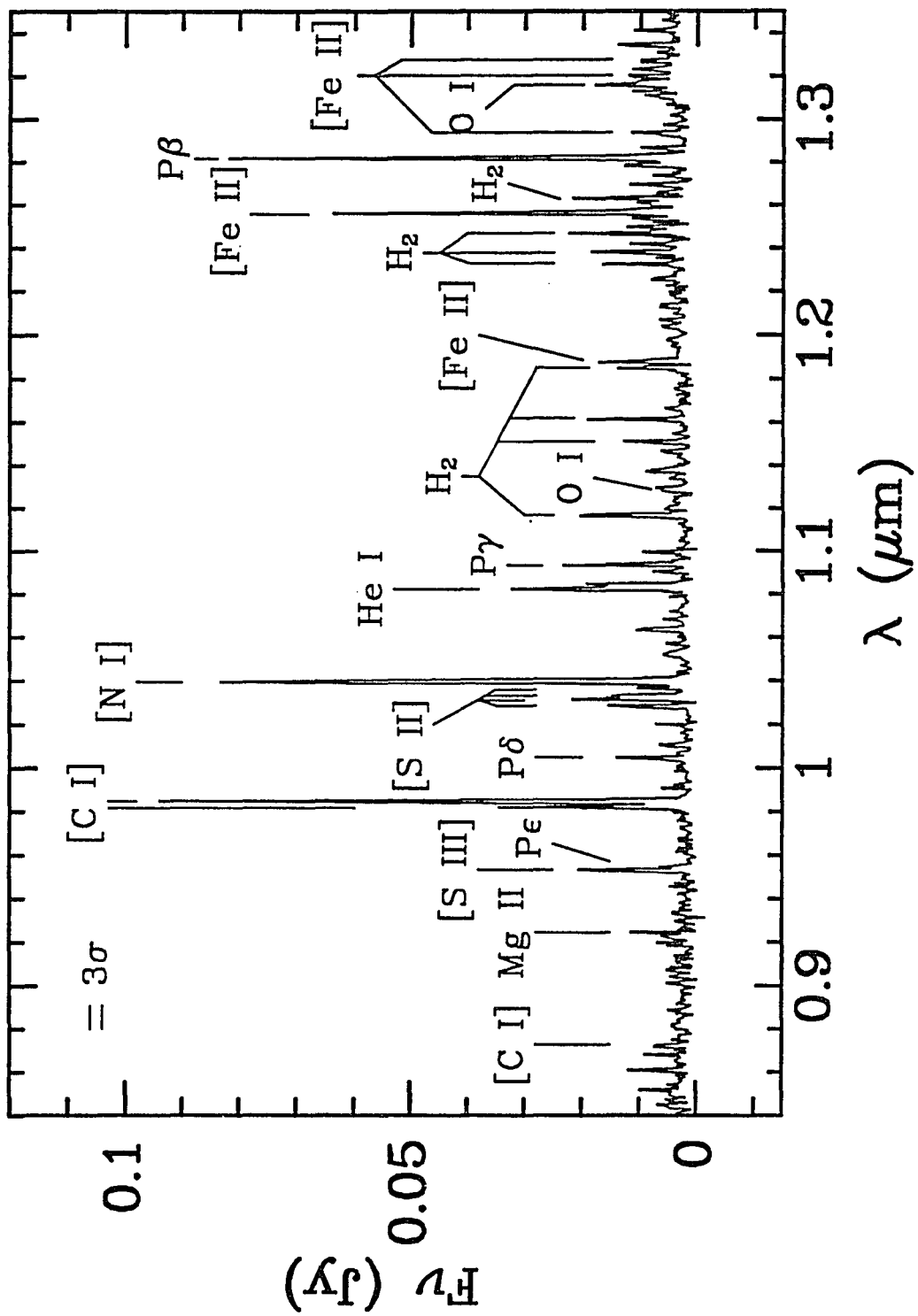
We measured the near-infrared spectrum of the eastern

lobe of AFGL 618 using the Steward Observatory 2.3 m telescope and the GeSpec during observing runs in 1989 February, September, and November, and in 1990 October. The spectrometer was used with a pair of round 6" apertures separated by 60" and with the 600 l/mm grating, providing a dispersion ranging from 7.0×10^{-4} $\mu\text{m}/\text{pixel}$ at 0.9 μm to 6.3×10^{-4} $\mu\text{m}/\text{pixel}$ at 1.5 μm .

The observing procedure and data reduction are as discussed in Section 1.3. HR 1489, a G0 V star (Hoffleit & Jaschek 1982), was used for flatfielding and flux calibration. The wavelength coverage at a given grating tilt is only 0.022 μm so many tilts were needed to obtain complete coverage from 0.84 - 1.35 μm . The individual pieces of spectrum do not match up perfectly, but the pieces have little overlap and the signal-to-noise ratios of the continuum points are low, so rescaling factors are highly uncertain and were not used. The combined spectrum is shown in Figure 2.2. The spectral pieces were rescaled in making the figure, so line fluxes should not be measured directly from the figure. The typical 1σ noise level of the continuum is $\approx 7 \times 10^{-4}$ Jy. The uncertainty in absolute flux calibration is estimated to be $\approx 15\%$.

We made additional observations in 1991 February with the Multiple Mirror Telescope using 3" apertures separated by 20". Starting from beyond the visible edge of the eastern

Figure 2.2: 0.84 - 1.35 μm spectrum of the eastern lobe of AFGL 618 acquired with the Steward Observatory 2.3 m telescope and Ge spectrometer through a 6" circular aperture. A number of the most prominent atomic and molecular features are identified. Further line identifications and fluxes are listed in Table 2.1. Error bars on individual points are determined by comparison of typically 8 - 10 sky-subtracted measurements. A representative 3σ error bar is shown.



lobe, we made observations at 2" intervals along the polar axis of the object, finishing beyond the visible edge of the western lobe. These data are shown in Figures 2.3 and 2.4.

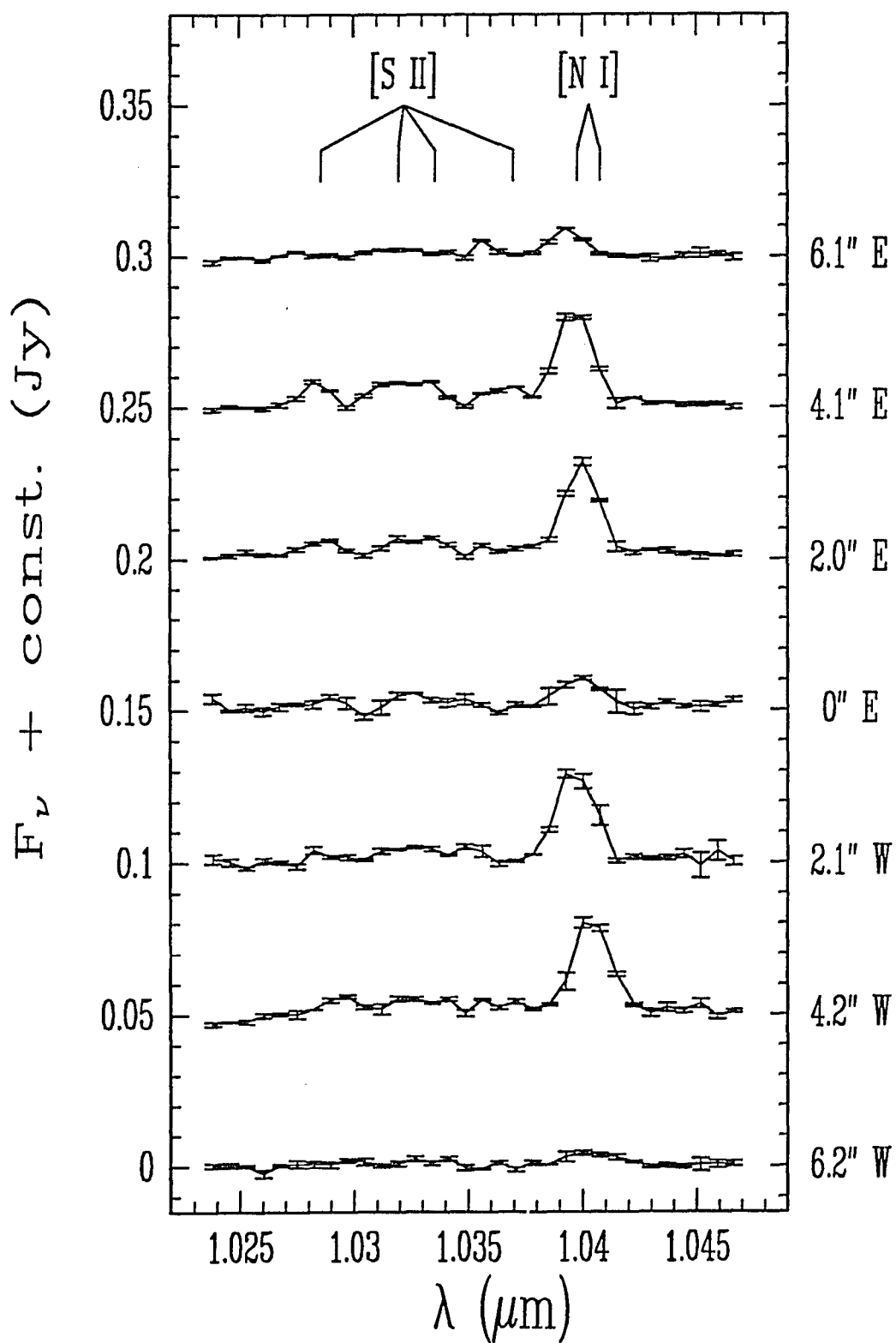
We collected new visible data of AFGL 618 at the 2.3 m telescope in 1991 March using the Boller and Chivens spectrometer with an 800 x 800 Texas Instruments CCD array. The slit was set at a width of 2".5, and it was oriented east-west along the polar axis of the source to provide coverage of both lobes. We used a 300 l/mm grating to give a dispersion of 0.00037 $\mu\text{m}/\text{pixel}$, and the grating angle was set to give spectral coverage from 0.4004 - 0.6865 μm . We employed standard IRAF reduction procedures, using BD +28°4211 for flux calibration (Massey et al. 1988).

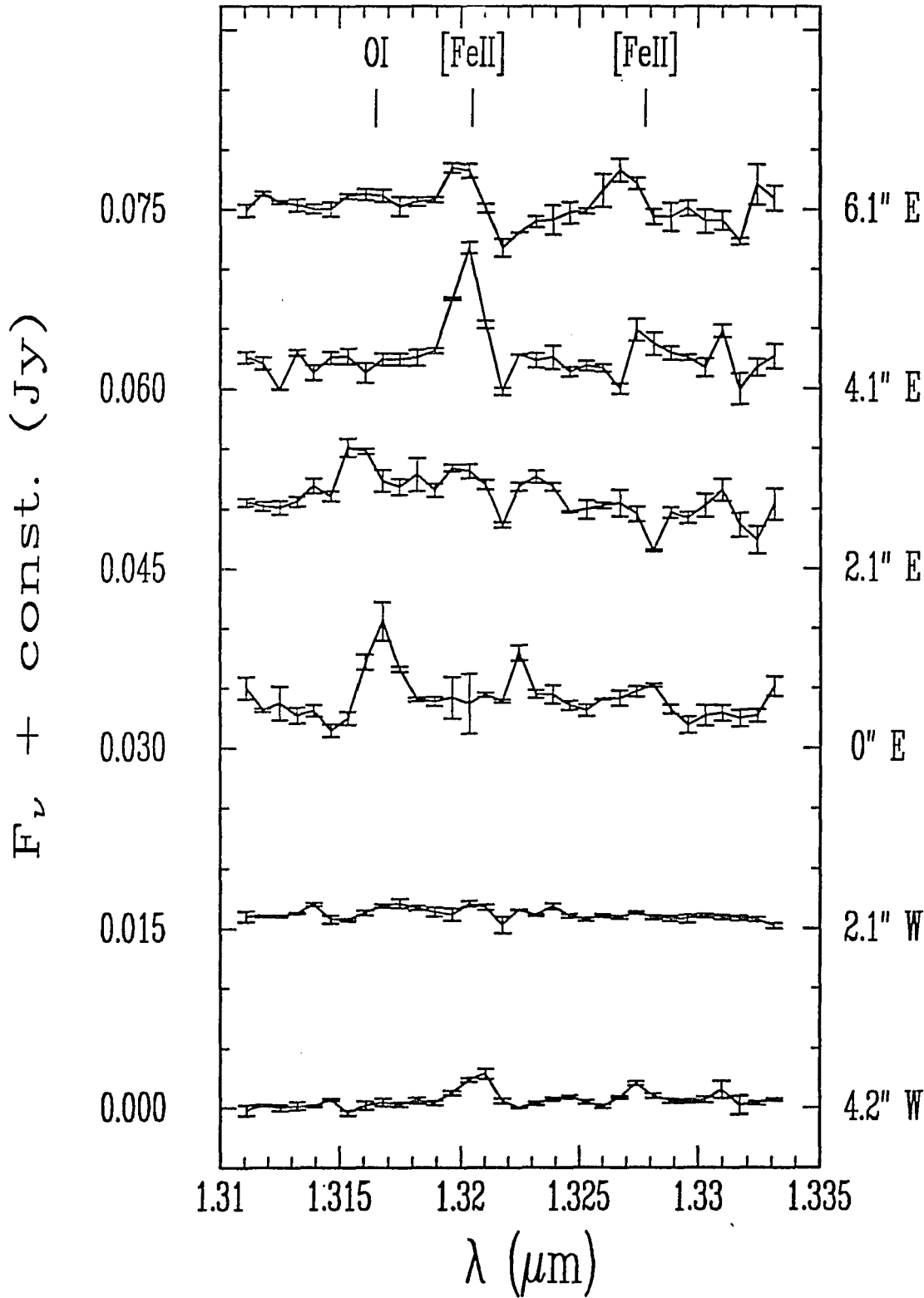
It was necessary to rescale our visible data because they were taken in non-photometric conditions. We did this by comparison with Westbrook et al. (1975). They had coverage from 0.35 - 1.05 μm with a single instrument. We used the lines they had in common with our infrared spectrum to rescale their data. We then used the lines they had in common with our visible spectrum to rescale our visible data. In addition to correcting for non-photometric conditions, this rescaling procedure also makes a rough beamsize correction and corrects for any variability between when our visible and infrared spectra were measured. The rescaled spectrum of the eastern lobe is shown in Figure 2.5.

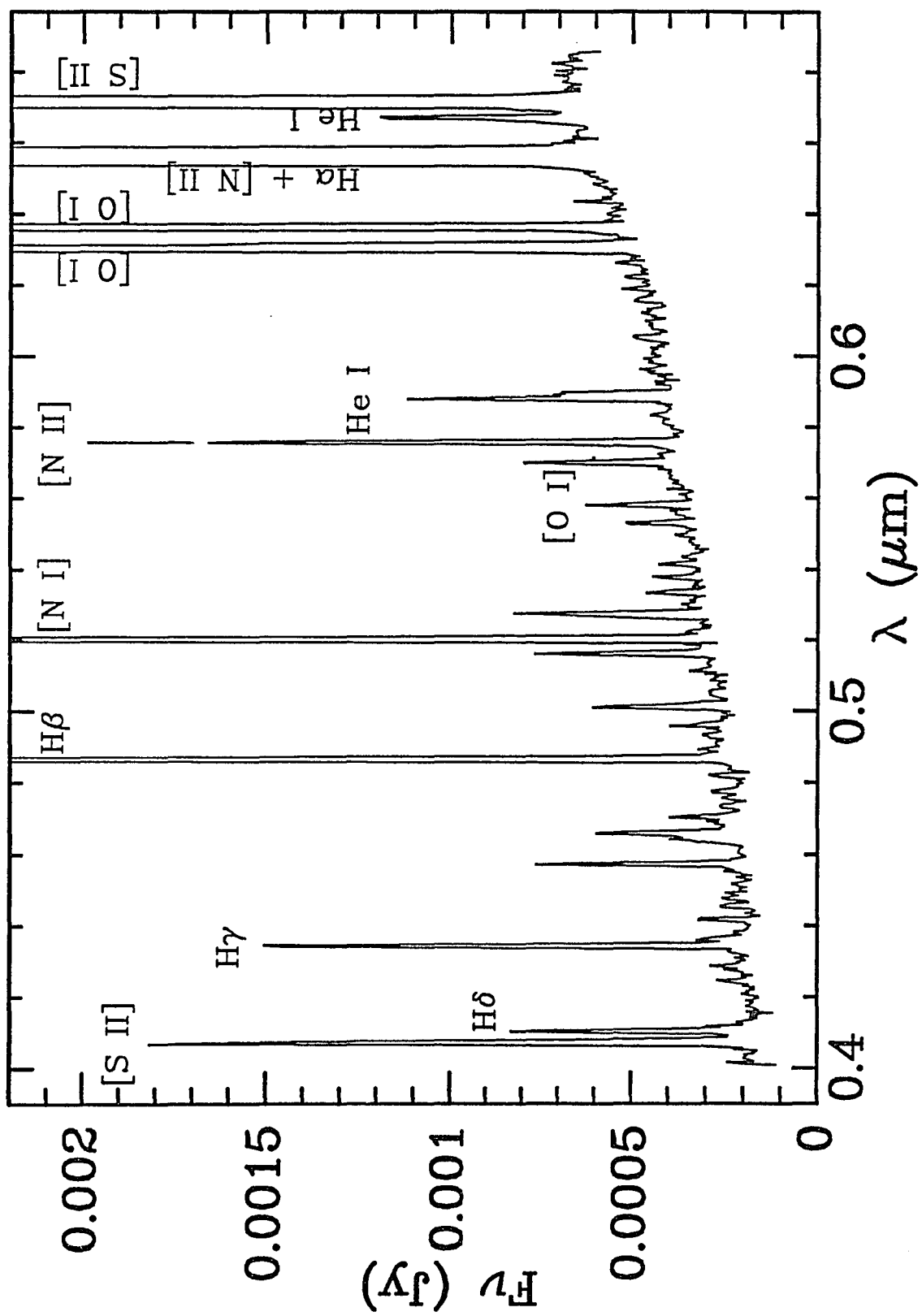
Figure 2.3: Sequence of infrared spectra of AFGL 618 acquired with the Multiple Mirror Telescope and Ge spectrometer. Observations were made with a 3" round aperture placed at various positions along the axis connecting the two visible lobes. Positions were measured relative to a point midway between the two lobes. Consecutive spectra have been offset by multiples of 0.05 Jy to prevent overlap. Line identifications are marked at the rest wavelengths of the transitions. There is some evidence for Doppler shifting of the [N I] line. The shifts correspond to an outflow velocity of $\sim 60 \text{ km s}^{-1}$, consistent with the measurements of Carsenty & Solf (1982).

Figure 2.4: Similar to Figure 2.3. Consecutive spectra are offset by multiples of 0.015 Jy to prevent overlap.

Figure 2.5: 0.4004 - 0.6865 μm spectrum of the eastern lobe of AFGL 618 acquired with the Steward Observatory 2.3 m telescope and a grating spectrometer with a 2"5 slit. The spectrum has been renormalized to match the infrared spectrum (see text). Prominent atomic features are identified. Line identifications and fluxes are listed in Table 2.1.







The extinction to the line-emitting regions is considerable, reported to be 3.5 magnitudes in the visible (Westbrook et al. 1975, Calvet & Cohen 1978, SC81, Latter et al. 1992). In the next section we calculate new values for the extinction to the eastern and western lobes. We correct for this attenuation using the standard interstellar extinction curve of Cardelli, Clayton, & Mathis (1989) with $A_V/E(B-V) = 3.1$. As discussed in Section 2.5.1, the standard interstellar curve might not provide accurate extinction estimates since part of the extinction is caused by grains within the carbon-rich circumstellar envelope.

The wavelength resolution of our infrared data is insufficient to make accurate linewidth measurements so we were unable to keep the linewidth a free parameter during line fitting. We used the strongest lines to determine widths of 0.0011 μm FWHM for the atomic lines and 0.0010 μm for the H_2 lines. We used these widths for all infrared line measurements.

Line identifications, fluxes, and extinction-corrected fluxes for both the visible and infrared data are listed in Table 2.1. The uncertainty in these line strengths due to fluxing errors is estimated to be 15%. For some lines, more than one transition might be contributing to the observed flux. Where we had insufficient resolution to resolve a blend, we list all transitions that might have made a

substantial contribution to the line flux. Laboratory wavelengths are listed in the first column of Table 2.1. All lines in the visible spectrum appeared within roughly $0.0002 \mu\text{m}$ of their laboratory wavelengths, and all lines in the infrared spectrum appeared within roughly $0.0005 \mu\text{m}$ of the laboratory wavelengths.

2.4 Atomic Spectrum

2.4.1 Background

AFGL 618 has a very rich spectrum. Over 150 transitions are listed in Table 2.1. We identified the lines by comparison with similar objects presented in the literature and by comparison with H_2 spectral models (Section 2.5.2; also Black & van Dishoeck 1987). Most of the lines in the visible spectrum were previously identified by SC81. There is still one unidentified feature in the visible spectrum and four in the near-infrared, including relatively bright lines at 0.934 and $1.209 \mu\text{m}$.

The spectrum of AFGL 618 contains lines produced by a variety of mechanisms. The dominant atomic features are the [C I], [N I], [N II], [O I], [S II], [S III], and [Fe II] forbidden lines and the H I and He I recombination lines. There are also strong H_2 lines in the infrared, produced partly by fluorescence but predominantly by thermal or shock excitation (Section 2.5.2). The H_2 features are so numerous

that in places the spectrum is confusion-limited.

This assortment of emission mechanisms is possible because of the complex geometry of AFGL 618. SC81 presented the following model, which includes three emission regions. The first region consists of the central star and surrounding H II region. Some of the light from these sources is scattered into the line of sight by dust in the lobes. These sources contribute the visible continuum light and most of the flux in the hydrogen and helium lines. The lack of scattered forbidden line emission implies an electron density in the H II region large enough to collisionally depopulate the forbidden transitions, or $n_e \geq 10^6 \text{ cm}^{-3}$. The other two emission regions are in the visible lobes. One is a hot, mostly ionized region exposed to direct illumination from the central star. It is heated to an electron temperature of $T_e \approx 18000 \text{ K}$ and has $n_e \approx 5 \times 10^4 \text{ cm}^{-3}$. This region is the source of the [S II], [S III], [N II], and [Fe II] emission and the remainder of the H I and He I flux. The other region is shielded from direct starlight. It has a temperature of $T_e \approx 10000 \text{ K}$, an electron density of $n_e \approx 10^3 \text{ cm}^{-3}$, and a hydrogen density of $n_H \approx 10^5 \text{ cm}^{-3}$. This region is the source of the [C I], [N I], and [O I] lines in the model of SC81.

2.4.2 The Diagnostic Lines

There are a number of diagnostic features that can be

used to determine temperatures, densities, and extinctions to line-emitting regions, some of the best of which involve our infrared data. All of our forbidden-line diagnostics except for [Fe II] can be explained using two Grotrian diagrams. S^+ and N^0 have the energy level structure shown in Figure 1.3, resulting in pairs of blue and red lines and four near-infrared lines. The ratio of the two red lines is a useful density indicator, although the temperature dependence is important as well. The ratio of the blue lines to the red lines also provides a locus of points in the density-temperature plane. It can be combined with the first ratio to find n_e and T_e . The ratio of the infrared lines to the red lines contains the same information as the blue to red ratio and has a slightly smaller extinction correction. The final useful diagnostic is the ratio of the blue lines to the infrared lines. This ratio is nearly independent of density and temperature and provides a large baseline for determining the extinction.

The other level structure is shown in Figure 1.2. It is applicable to C^0 , N^+ , O^0 , O^{++} , and S^{++} , except the order of the fine-structure sublevels is inverted in the ground term of O^0 . All but a few percent of the electrons excited to the 1S_0 state cascade back to the ground state via the 1D_2 state. As a result, the $^3P - ^1S_0$ lines are usually too faint to detect. The $^3P_0 - ^1D_2$ line is also usually well below

detection limits. The other $^3P - ^1D_2$ lines could be used to determine the extinction, but the differential extinction is too small to get an accurate result. That leaves the ratio of the $^1D_2 - ^1S_0$ line to the two $^3P - ^1D_2$ lines. This ratio has a very strong temperature dependence and only a modest to small density dependence. That makes it an excellent temperature diagnostic.

Using collision rates and transition probabilities from Mendoza (1983) and assuming five-level atoms (see Section 1.4), we solved rate equations to find predicted line ratios as functions of density, temperature, and visible extinction. We discuss our results in Section 2.4.4, where we compare them to the model of SC81. Below, we give details regarding the diagnostic line ratios and the conclusions to be drawn from them.

2.4.3 Individual Sets of Diagnostic Lines

2.4.3.1 [S II]

Full rate equations were written assuming collisional population of states, and line ratios were calculated. We started by determining the extinction to each lobe from the [S II] $(0.4069 + 0.4076)/(1.0286 + 1.0320 + 1.0336 + 1.0370)$ line ratio. We then found the densities and temperatures that were consistent with the [S II] $0.6716/0.6731$ and [S II] $(0.4069 + 0.4076)/(0.6716 + 0.6731)$ line ratios. The best

fit gave $T_e = 25000 \pm 3000$ K, $n_e = 7000 \pm 800$ cm⁻³, $A_v = 2.1 \pm 0.2$ mag for the eastern lobe, and $T_e = 25000 \pm 5000$ K, $n_e = 7700 \pm 700$ cm⁻³, $A_v = 2.9 \pm 0.3$ mag for the western lobe. These parameters fit all the line ratios within the errors. The errors reflect uncertainties in the infrared fluxes and in the scaling of the visible to the infrared flux.

2.4.3.2 [N I]

In the spectrum of N⁰, the blue lines are a close pair at $\lambda\lambda 0.3466, 0.3467$ μm , the red lines are a close pair at $\lambda\lambda 0.5198, 0.5200$ μm , and the infrared lines consist of pairs at both $\lambda 1.0398$ and $\lambda 1.0408$ μm . We used [S II] 0.6716/0.6731 as a density indicator. Here the close pairing makes it difficult to use [N I] 0.5198/0.5200 for the same purpose.

[N I] $(0.3466 + 0.3467)/(1.0398 + 1.0408)$ is useful for determining A_v , but our spectrum does not extend to 0.34 μm . That leaves [N I] $(0.5198 + 0.5200)/(1.0398 + 1.0408)$, which depends strongly on both T_e and n_e . We assumed that the [N I] emission is subject to the same extinction as the [S II]. We corrected for the extinction and found pairs of densities and temperatures to match the observed line ratio (see Table 2.2). The errors correspond to a 20% uncertainty in the line ratio.

2.4.3.3 [N II]

The [N II] lines are among the brightest in the visible spectrum. The [N II] 0.5755/(0.6548 + 0.6583) line ratio,

which depends heavily on both density and temperature, is nearly a factor of two larger in the eastern lobe than in the western lobe. The resolution of our data is large enough to avoid serious blending of these lines with $H\alpha$ at $\lambda 0.6563 \mu\text{m}$, so we do not believe that blending is the source of this difference, (see Section 2.4.4.3 for further discussion). The predicted densities and temperatures for each lobe are listed in Table 2.3. We assumed the same extinction as for [S II], and errors correspond to a 10% uncertainty in the line ratio.

2.4.3.4 [Fe II]

Table 2.1 includes 42 [Fe II] lines. These lines have great potential as temperature and density indicators. Unfortunately, [Fe II] is so complicated that few of these lines have been included in models. Recently, Hudgins, Herter, & Joyce (1990) solved for the populations of the 16 lowest levels of Fe^+ assuming collisional excitation by electrons. They plotted a ${}^6\text{D}$ -a ${}^4\text{D}$ line ratios versus n_e for $T_e = 13000 \text{ K}$. The a ${}^6\text{D}$ -a ${}^4\text{D}$ transitions include 7 of our 42 [Fe II] lines. Two useful line ratios come out of this, [Fe II] 1.2941/1.2567 and [Fe II] 1.3278/1.3205. Each has a small temperature dependence and can be used to determine the electron density. Comparing our eastern lobe data with the plot from Hudgins, et al. (1990), we found $n_e = 18000 \pm 8000 \text{ cm}^{-3}$ from the first ratio and $n_e = 23000 \pm 5000 \text{ cm}^{-3}$ from

the second. The errors correspond to uncertainties in the flux ratios of 20% and 10% respectively. There is less uncertainty in the second ratio because the lines are close enough to be observable at a single grating tilt. The errors might be underestimated if the [Fe II] emission comes from the same $T_e \approx 25000$ K region that the sulphur and nitrogen emission comes from. Also, Hudgins, et al. caution that some of the collision strengths used in their calculations might be off by as much as a factor of two. Despite the uncertainties, these two ratios illustrate the usefulness of [Fe II] lines as probes of physical conditions and show the need for more detailed modelling of [Fe II] emission, both to improve the accuracy of these diagnostics and to reveal others.

2.4.3.5 [O I]

The density dependence of the ratio [O I] ($0.6300 + 0.6364$)/ 0.5577 is weak and the temperature dependence is quite strong, so it works as a very accurate temperature indicator. Assuming a 10% uncertainty in the line ratio and the same extinction corrections as for [S II], we find $T_e = 9800 \pm 400$ K for the eastern lobe, and $T_e = 9300 \pm 400$ K for the western lobe.

2.4.3.6 [C I]

These are among the strongest near-infrared lines in

AFGL 618. The $[\text{C I}] \ 0.8727/(0.9824 + 0.9850)$ ratio increases significantly with both density and temperature and provides a locus of points in the density-temperature plane. We assumed the same extinction as for $[\text{S II}]$ and found the density-temperature pairs listed in Table 2.4. Errors correspond to a 20% uncertainty in the line ratio.

2.4.3.7 $[\text{S III}]$

The $\lambda\lambda 0.9069, 0.9532 \ \mu\text{m}$ lines of $[\text{S III}]$ can be among the brightest lines in the near-infrared. A determination of T_e can be made from $[\text{S III}] \ (0.9069 + 0.9532)/0.6312$. However, this object is too cool to produce much S^{++} , so we were unable to resolve $[\text{S III}] \ \lambda 0.6312 \ \mu\text{m}$ from the much brighter $[\text{O I}] \ \lambda 0.6300 \ \mu\text{m}$.

2.4.3.8 H I

SC81 found that the H I emission comes in part from a hot, central nebula with $n_e \geq 10^6 \text{ cm}^{-3}$, $T_e < 27000 \text{ K}$ and partly from the unshadowed portion of the lobe, where $T_e \approx 18000 \text{ K}$, $n_e \geq 2 \times 10^4 \text{ cm}^{-3}$. Extinction-free case B recombination line ratios can be derived from Osterbrock's Table 4.4 (1989). The line ratios change little with density and temperature but are very sensitive to the amount of dust reddening, the form of the extinction law, and the distribution of dust in the source. $\text{Pa}9$ is unusable due to a blend with $[\text{Fe II}]$, and $\text{Pa}10$ is too faint to measure accurately. The ratios of $\text{Pa}\gamma$, $\text{Pa}\delta$, and $\text{Pa}\epsilon$ to $\text{Pa}\beta$ give an average of $A_v = 5.6 \pm 1.4$

magnitudes. The ratios of the four Paschen lines to $H\beta$ give an average of $A_v = 3.3 \pm 0.2$. $H\delta/H\beta$ indicates $A_v = 1.4 \pm 0.2$, $H\gamma/H\beta$ gives 2.5 ± 0.3 , and $H\alpha/H\beta$ suggests $A_v = 4.5 \pm 0.2$. Some of the difference between these extinction estimates is due to the distribution of gas and dust in the lobes. There is also a difficult-to-quantify contribution due to scattered light from the central star. These topics will be addressed in more detail in Section 2.4.4.1.

2.4.3.9 He I

There are He I lines in both the visible and infrared spectra of AFGL 618. Since S^+ and He^0 have similar ionization potentials, the presence of [S III] in the infrared spectrum indicates that recombination must be important in producing the He I flux. The triplet He I lines are often enhanced in nebulae by collisional excitation from the metastable $2s^3S$ state (Clegg 1987). For the conditions proposed by SC81 for the central nebula, He I 1.0830/0.5876 should be enhanced by a factor of 7. A similar enhancement is expected for emission from the lobes. We assumed that the He I is subject to the same extinction as the [S II] and determined the dereddened line ratio for the eastern lobe. The reddening-corrected line ratio shows only a factor of 3 enhancement over the ratio predicted by case B recombination, although when a correction is added for scattering efficiencies, the factor of 7 is reproduced. Scattering is

discussed in more detail in Section 2.4.4.1.

2.4.3.10 O I

We detected infrared O I lines at 0.8446, 1.1287, and 1.3165 μm (see Figure 2.6). These lines can be used to test

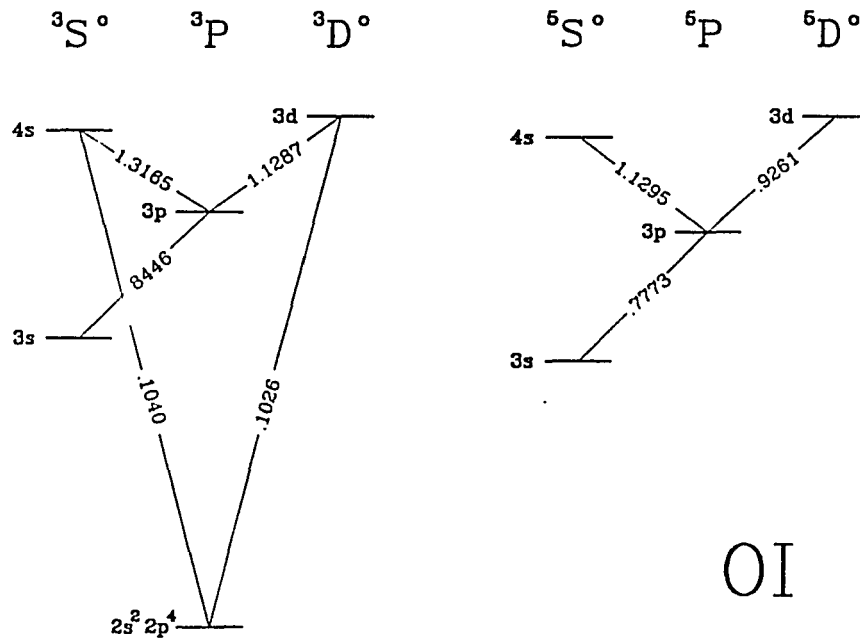


Figure 2.6: Grotrian Diagram for O I

for fluorescence. The $n \geq 4$ levels of O I can be populated by absorption of UV photons, a process known as starlight or UV continuum fluorescence, and cascades from these levels contribute to the emission in all three infrared O I lines.

Oxygen and hydrogen have similar ionization potentials so O I and H I lines are often closely paired in wavelength. H I $\text{Ly}\beta$ is coincident with the O I $2s^2 2p^4 \ ^3P - 3d \ ^3D^\circ$ transition at $\lambda 0.1026 \mu\text{m}$ so the $3d \ ^3D^\circ$ term can be excited by

absorption of Ly β photons. This resonance enhances the $\lambda 0.8446 \mu\text{m}$ and $\lambda 1.1287 \mu\text{m}$ lines, especially when the Ly β line is in emission (Rudy, Rossano, & Puetter 1989). Grandi (1975) investigated starlight and Ly β fluorescence of O I in the Orion nebula. In his model of an O7 V star surrounded by an H II region with $n_{\text{H}} = 4000 \text{ cm}^{-3}$ and Ly β in absorption, he found O I $0.8446/1.3165 = 3.2$ and O I $1.1287/1.3165 = 0.1$. If Ly β were not attenuated, these line ratios would be about 10 and 6 respectively. Our data suggest line ratios of 1.3 and 0.44 respectively, with an uncertainty of about 20%. These line ratios are strongly model dependent so not too much should be made of small differences between the models and our data. However, it is clear that the Ly β flux must be suppressed in AFGL 618 if fluorescence is responsible for the O I emission. We note that fluorescence is known to contribute to the H $_2$ emission (see Section 2.5.2), and the H $_2$ line intensities indicate that Ly β is in absorption.

An alternative source of the O I is recombination. Recombination of oxygen is usually tested for by comparing strengths of triplet and quintet lines (see Figure 2.6). When recombination is responsible for the emission, the triplet and quintet lines scale as their statistical weights. We compared $\lambda\lambda 1.1287, 1.3165 \mu\text{m}$ with their quintet counterparts $\lambda\lambda 0.9261, 1.1295 \mu\text{m}$. The triplet to quintet line ratios are larger than expected from recombination

theory. We conclude that recombination is not the primary mechanism producing the O I emission.

The spectra in Figure 2.4 reveal a peculiarity in the spatial distribution of O I. There are three prominent lines in these spectra, O I at $\lambda 1.3165 \mu\text{m}$ and [Fe II] at $\lambda\lambda 1.3205, 1.3278 \mu\text{m}$. The spatial distribution of the [Fe II] lines is typical of all of the lines in our longslit, visible spectrum and of the infrared [N I] and [S II] lines of Figure 2.3. It is peaked in the eastern and western lobes and low elsewhere. The O I line is different; it is weak in the lobes but strong towards the region between the lobes. We can assume that the O I is not coming directly from the recombination region because the H I recombination lines are weak between the visible lobes. Yet, the large inclination of AFGL 618 ($i \approx 45^\circ$) and the low dust density in the polar directions (see Latter et al. 1992) make it possible to see unscattered emission from gas fairly close to the central star. The O I emission probably comes from the inner edge of the eastern emission lobe, where the UV flux should be substantial. Hydrogen has an ionization potential very close to that for oxygen and should shield the oxygen from much of the UV flux, so most of the oxygen should be neutral and $\text{Ly}\beta$ should be in absorption. The H_2 fluorescence emission might come from the same region, but we need careful, spatially resolved spectra of the fluorescence-dominated H_2 lines to be

certain.

2.4.4 Discussion

2.4.4.1 Extinction

The results presented in Section 2.4.3 bring into question the true value of the visual extinction to the emitting regions. Westbrook et al. (1975) adopted $A_v = 3.5$ mag after estimating the extinction using three methods. In their first method, they used the same [S II] line ratio used in our study. That method gave $A_v = 3.7$ mag, although their data actually indicate a much smaller extinction since they did not correct for the [N I] $1.04 \mu\text{m}$ contribution. Their second approach was to use Balmer line ratios. That gave $A_v = 3.5 \pm 1$ mag, but that result is misleading due to geometrical effects that we discuss below. Their third method was to compare the slope of the continuum from 0.35 to $1.05 \mu\text{m}$ with a Rayleigh-Jeans law slope. The observed reddening corresponds to $A_v = 4.7 \pm 0.4$ mag. However, scattering efficiencies will also affect the shape of the spectrum. If Rayleigh scattering is dominant, the visual extinction could easily be underestimated by as much as 4 magnitudes. This results in an extinction much larger than our estimate, but as discussed by Latter et al. (1992), the light might be heavily attenuated in the region surrounding the central star. Calvet & Cohen (1978) used the hydrogen

line ratio and continuum shape methods and found results similar to those of Westbrook et al. In Section 2.5.1, we examine ratios of H_2 lines with common upper states and find $A_v = 3.4^{+4.0}_{-2.0}$ mag. The best fit to the H_2 spectral models of Section 2.5.2 is with $A_v = 3.0$ mag.

We investigated a simple model for the extinction to the [SII] emitting region. Our model consists of two regions: the first is a homogeneous region filled with gas and dust, and the second is a foreground screen of dust. This model should adequately represent the [S II] emission, with the mixed region representing the lobes and the foreground screen representing interstellar and circumstellar extinction. Our data show that the foreground component accounts for at least 0.6 and possibly all of the 2.1 magnitudes of visual extinction to the eastern lobe and at least 1.4 of the 2.9 magnitudes to the western lobe. The balance of the extinction is due to dust in the emitting region.

The H I emission is much more complicated than our simple, two component model. As discussed in SC81, a significant portion of the H I emission originates near the central star and is scattered in our direction by grains in the lobes. Without detailed knowledge of the scattering properties of the grains, the reflected component cannot be incorporated into our model accurately. However, we can determine the extinction to the lobes by examining the

unscattered component. We used data on the eastern lobe from Figure 1 in SC81 to determine the polarization and scattering fractions for each of the Balmer lines. We calculated new values for the extinction based on the unscattered component alone. The values are $A_v \approx 2.6$ mag from $H\delta/H\beta$ and $H\gamma/H\beta$, similar to the extinction we found to the lobes from [S II] line ratios, and $A_v \approx 4.7$ from $H\alpha/H\beta$. Scattering processes are inefficient in the infrared, so the Paschen lines are likely to come mostly from the lobes. Ratios of Paschen lines give $A_v \approx 5.6$. The larger extinctions determined from the $H\alpha$ and Paschen line ratios are consistent with probing deeper into the nebular material at longer wavelengths.

We investigated the scattered light component seen in the lobes by SC81. They used spectropolarimetry to conclude that scattering contributes $\approx 49\%$ of the permitted-line flux from the eastern lobe and $\approx 21\%$ of the permitted-line flux from the western lobe. The eastern lobe is tilted towards Earth and the western lobe away (see discussion in Latter et al. 1992), so the difference in the scattered light contribution from the two lobes suggests that the grains are preferentially forward-scattering. We investigated how this scattering would affect the relative extinction to the two lobes, $(A_v)_{\text{west}} - (A_v)_{\text{east}}$, determined by comparing line fluxes from the two lobes. We assumed that the continuum comes entirely from the central star, the forbidden lines come

entirely from the lobes, and the permitted lines come from both regions. For a scattering function that produces the scattering fractions mentioned above, the differential extinction determined from the permitted lines should be ≈ 0.5 magnitudes greater than the differential extinction determined from the forbidden lines. Our data show a difference of 0.6 ± 0.5 magnitudes. Similarly, the differential extinction found from the continuum fluxes should be ≈ 1.4 magnitudes greater than the differential extinction found from the forbidden lines. Our data show a difference of 0.8 magnitudes, consistent within the 1σ uncertainty in the scattering percentages from SC81.

In conclusion, the methods used to determine the extinction to the lobes must take into account scattering and radiative transfer effects. The [S II] lines should work well because they include no scattered component (SC81) and because the lines are unlikely to be optically thick. The [S II] lines indicate $A_v \approx 2.1$ to the eastern lobe and $A_v \approx 2.9$ to the western lobe. These low values for the extinction are confirmed by the unscattered components of the H I lines. There is some evidence that longer wavelength hydrogen lines probe further into the nebular material. There is also evidence that the dust grains in the lobes are preferentially forward-scattering.

2.4.4.2 Temperature Regimes

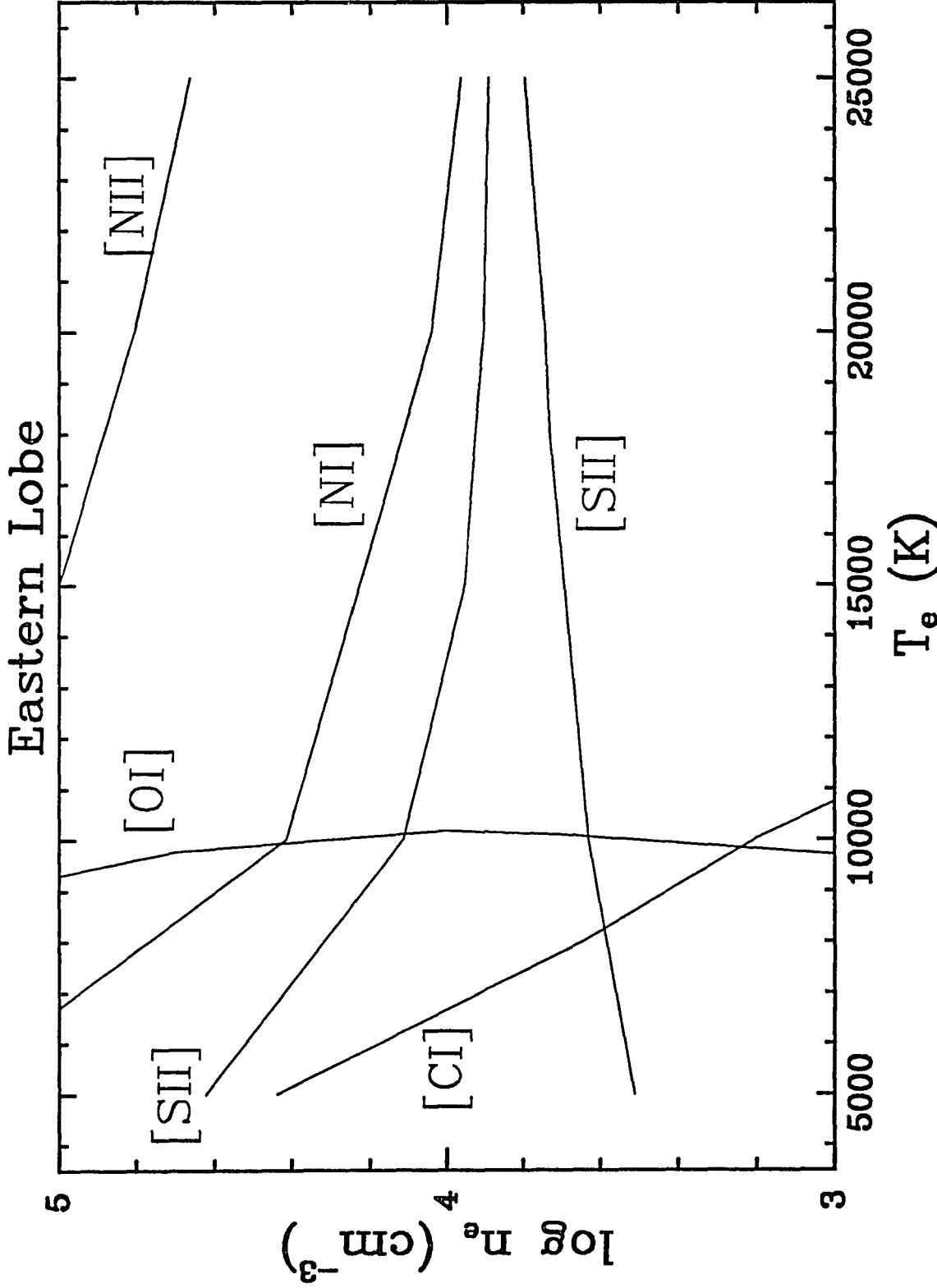
The atomic line ratios discussed in Section 2.4.3 support the two temperature model introduced by SC81 for emission from the lobes. Our density-temperature curves for the eastern and western lobes are shown in Figures 2.7.1 and 2.7.2 respectively. [O I] and [C I] line ratios indicate an electron temperature of $T_e \approx 10000$ K and an electron density of $n_e \approx 1600 \text{ cm}^{-3}$. [S II], [N II], and [N I] imply $T_e \approx 25000$ K and $n_e \approx 8000 \text{ cm}^{-3}$. The low temperature results are consistent with SC81. The high temperature results differ; we find a higher temperature and a much lower electron density. However, SC81's line ratios are negligibly different from ours, and the different results appear to be due to our use of the newer atomic constants summarized in Mendoza (1983). Another difference between our analysis and SC81's is for [N I]. They assumed the [N I] must come from the low temperature region because the $0.52 \text{ } \mu\text{m}$ lines are quite bright and have a critical density of $n_e \approx 2000 \text{ cm}^{-3}$. What SC81 did not anticipate is the prominence of the $1.04 \text{ } \mu\text{m}$ lines. The red/infrared line ratio is in fact small, consistent with a high density origin.

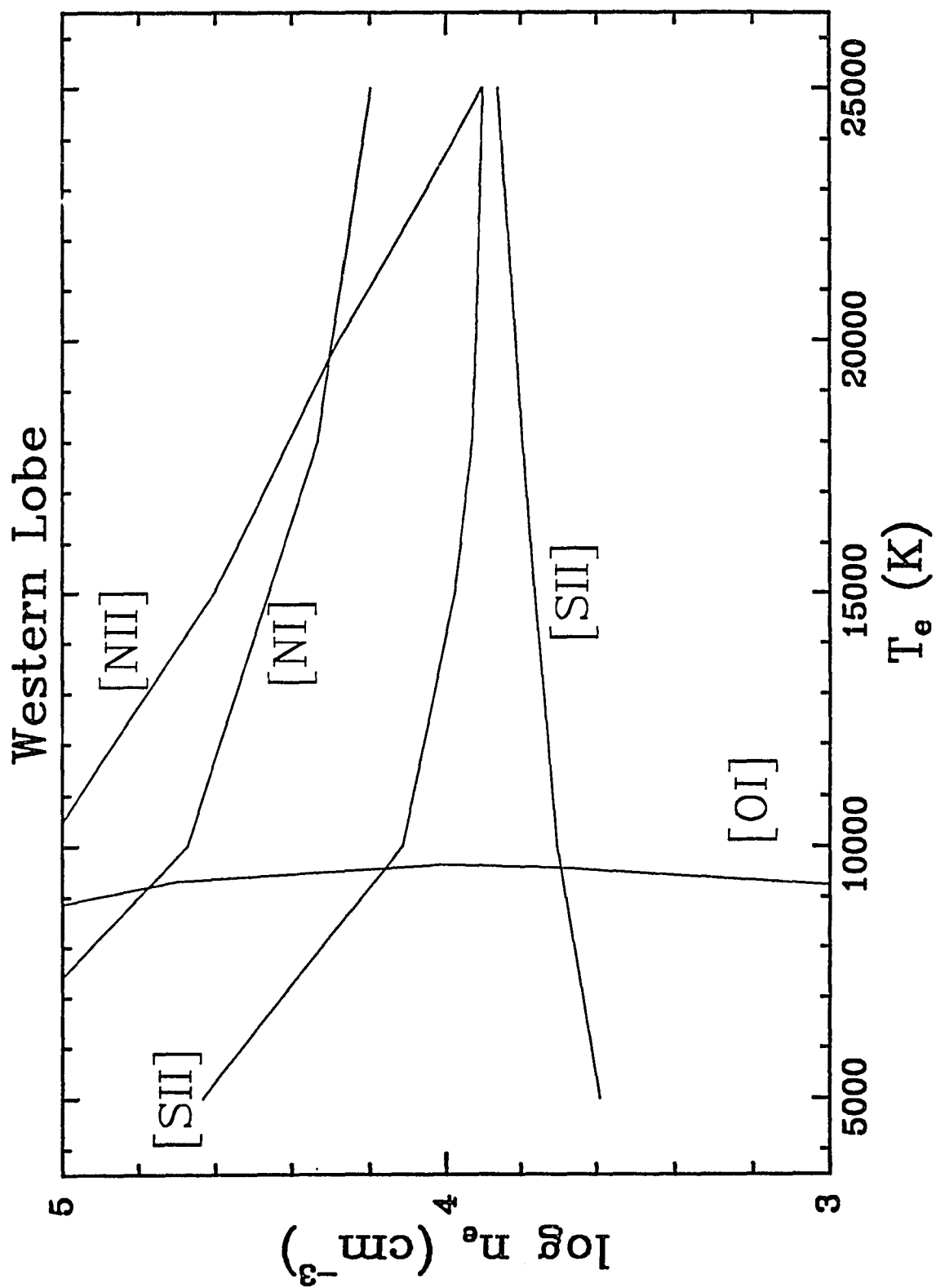
2.4.4.3 Shocks

The striking difference in the [N II] line ratio for the two lobes indicates a real, physical difference between the two. The eastern lobe appears to have a very hot, highly

Figure 2.7.1: Density-temperature plot for the eastern lobe of AFGL 618. Each of the curves shows the density-temperature values that match the reddening-corrected data for that diagnostic. Line ratios were dereddened assuming $A_v = 2.1$ mag (see text). The line ratios shown in the figure are [N II] $0.5755/(0.6548 + 0.6583)$, [O I] $(0.6300 + 0.6364)/0.5577$, [C I] $0.8727/(0.9824 + 0.9850)$, [S II] $(0.4069 + 0.4076)/(1.0286 + 1.0320 + 1.0336 + 1.0370)$ (upper [S II] curve), [S II] $0.6716/0.6731$ (lower [S II] curve), and [N I] $(0.5198 + 0.5200)/(1.0398 + 1.0408)$.

Figure 2.7.2: Density-temperature plot for the western lobe of AFGL 618. Each of the curves shows the density-temperature values that match the reddening-corrected data for that diagnostic. Line ratios were dereddened assuming $A_v = 2.9$ (see text). The line ratios are the same as in Figure 2.7.1.





ionized component not present in the western lobe. Eleven years earlier, both lobes had a line ratio similar to the one we found for the western lobe (SC81). It seems unlikely that the rapid change in the eastern lobe is due to brightening of the central star since that should affect both lobes equally. It seems more likely that the rapid heating and ionization is due to the passage of a shock.

The strongest evidence for shocks in AFGL 618 is the presence of 25000 K gas. Among planetary nebulae, such high electron temperatures are found only in objects with very hot central stars. Given that AFGL 618 has a central star temperature of only about 30000 K, shocks are needed to produce the extreme heating. There is other evidence that shocks are present in AFGL 618. First, the observed outflows have a wide range of velocities (Lo & Bechis 1976; Carsenty & Solf 1982; Burton & Geballe 1986; Gammie et al. 1989; Cernicharo et al. 1989). This supports the idea of interacting winds and consequently shocks. Second, there is the presence of [Fe II] emission, which is often seen in the shock-heated regions of supernovae and Herbig-Haro objects. Finally, as shown in Section 2.5.2, the H_2 line ratios indicate a contribution from shock excitation (see also Thronson 1981; Burton et al. 1989).

2.4.4.4 Filling Factors

SC81 investigated the filling factors of the neutral and

ionized gas in the lobes. We now have very different values for the electron density and temperature in the ionized region, so we calculated new filling factors. We used level populations from our atomic models, dereddened eastern lobe fluxes from Table 2.1, and a distance to AFGL 618 of 1.8 kpc (SC81) to calculate the number of S^+ , S^{++} , N^0 , N^+ , O^0 , and C^0 atoms in the emitting regions. By assuming that S^+ and S^{++} occupy equal volumes of gas and that a negligible amount of sulfur is in other ionization states, we were able to determine the total number of sulfur atoms in the emitting region. Similar assumptions were made to determine the number of nitrogen, oxygen, and carbon atoms. Assuming the hotter gas in the eastern lobe, taken to be the source of the sulfur and nitrogen emission, is totally ionized, then $n_H = n_{H^+} \approx n_e \approx 8000 \text{ cm}^{-3}$. To maintain pressure equilibrium, the cooler gas, taken to be the source of the oxygen and carbon emission, must have a total density of 40000 cm^{-3} . Since $n_{H^+} \approx n_e \approx 1600 \text{ cm}^{-3}$, the hydrogen density must be $n_H = n_{H^0} + n_{H^+} \approx 38000 \text{ cm}^{-3}$. We combined these hydrogen densities with mean elemental abundances for carbon-rich planetary nebulae from Aller and Czyzak (1983) to determine the number density of sulfur, nitrogen, oxygen, and carbon atoms in the lobe. Combined with the total number of atoms of each element and the assumption that each element has a homogeneous density distribution, this leads to the volume of each emitting

region. Oxygen has a volume that corresponds to a spherical source 1.91 in diameter, roughly the size of the visible lobe. Nitrogen and sulfur occupy a volume about one-half this large. If the carbon is all neutral, then the carbon-emitting region occupies only about one-twentieth the volume of the lobe. However, there is a hint of C II emission at $0.9903\ \mu\text{m}$, and we suspect that the carbon is mostly ionized. Oxygen appears to be predominantly neutral in spite of having only a slightly larger ionization potential than carbon. Hydrogen, which has an ionization potential very close to that for oxygen, probably shields the oxygen from ionizing photons.

We conclude that most of the lobes are filled with the cooler, $T_e \approx 10000\ \text{K}$ gas, whereas the hotter, $T_e \approx 25000\ \text{K}$ gas fills only 25 - 35% of the lobes. The many assumptions that went into these calculations are unlikely to change this basic result. These results support the claim by SC81 that the abnormally large strengths of the [O I] and [N I] lines in AFGL 618 are due, at least in part, to the low ionization state of AFGL 618 compared with fully-developed planetary nebulae.

2.4.5 Summary of Atomic Data

The $0.84 - 1.35\ \mu\text{m}$ spectrum of the eastern lobe of the proto-planetary nebula AFGL 618 has been measured through a

6" aperture using a germanium photodiode array. Our data show a weak continuum with strong forbidden and permitted emission lines. These infrared data have been combined with new visible spectra of both lobes to determine the extinction to the emitting regions and densities and temperatures in the emitting regions. We found visual extinctions of $A_v = 2.1$ mag to the eastern lobe and $A_v = 2.9$ mag to the western lobe.

We found evidence for several different emission regions. The permitted line radiation does not all come from the lobes; some of it originates in a central nebula and is scattered into the line-of-sight by dust in the lobes (SC81). The dust appears to be preferentially forward-scattering. The lobes themselves contain material at several different electron temperatures. There is a cool, predominantly neutral region with $T_e \approx 10000$ K, $n_e \approx 1600$ cm⁻³ and a hot, mostly ionized region with $T_e \approx 25000$ K, $n_e \approx 8000$ cm⁻³. The cool region, which is the source of the forbidden [O I] and [C I] emission, fills most of the visible lobes. The oxygen at the inner edge of the lobes is excited by UV fluorescence, so there is strong, permitted O I emission towards the region between the lobes. There is a third, hotter component in the eastern lobe that was not present eleven years ago. The rapid development of this component, the high electron temperature of the ionized gas, the presence of high-velocity winds, and evidence from H₂ and [Fe II] emission combine to

provide strong support for shock heating in AFGL 618.

The results of our atomic line analysis are basically consistent with the picture of AFGL 618 presented by SC81. Our greater wavelength coverage allowed us to refine the numbers for the dust reddening to the lobes, and the extra indicators available in the near-infrared allowed us to improve on the density estimates of SC81. The two-component model we found for the gas in the lobes is essentially the same model formulated by SC81. They suggested that clumps near the central star allow narrow filaments of ionizing radiation to penetrate the lobes and heat the gas. The bulk of the lobes is in the shadows of the clumps and remains cooler and neutral. We see no reason to alter their basic model, although we note that shocks must also contribute to the gas heating. Complex models are clearly needed to fully explain this and similar objects, and we are doing narrow-band H_2 imaging and near-IR polarization mapping to provide further constraints for such models.

2.5 Molecular Hydrogen Emission

In our spectrum of AFGL 618, many features can be identified with quadrupole vibration-rotation transitions in the ground electronic state of H_2 . Indeed, most of the structure seen longward of $1.1\ \mu\text{m}$ is caused by H_2 line emission, and in some regions the spectrum appears

confusion-limited in H_2 lines.

2.5.1 Extinction to the H_2 Emitting Region

Observations of millimeter-wave emission from a number of molecular species (e.g. Thronson & Mozurkewich 1983; Bachiller et al. 1988; Bujarrabal et al. 1988) demonstrate that a great deal of material surrounds AFGL 618, with an expansion velocity consistent with it being the remnant mass-loss shell (Knapp & Morris 1985; Bachiller et al. 1988). This material would have been ejected from AFGL 618 while it was on the AGB and prior to its evolution to a bipolar nebula. As a result, a large amount of attenuation due to dust in the extended circumnebular material is expected. However, a standard interstellar extinction law is probably inappropriate for an object like a PPN. Unfortunately, it is currently impossible to assess how much the true extinction law might differ from that determined for the general interstellar medium. There are indications that grains formed in carbon-rich circumstellar envelopes are both smaller and more amorphous than grains found in the general interstellar medium (Martin & Rogers 1987; Thronson et al. 1987; Rowan-Robinson & Harris 1983). However, as was discussed in Section 2.4.4.1, the grains in the lobes are preferentially forward-scattering, as would be expected for large grains.

Thronson (1981) used a standard interstellar extinction

law and four pairs of H_2 lines in the wavelength range 1.9 - 2.5 μm to determine a visual extinction of $A_v = 8 \pm 6$ magnitudes toward the H_2 -emitting lobes. By combining his data with the observations presented here, a longer spectral baseline is available over which to determine the amount of attenuation. In the spectral region covered by the GeSpec, there are eight $v = 2 \rightarrow 0$ lines which share the same upper states with the four $v = 2 \rightarrow 1$ lines present in Thronson's spectrum. Comparison of observed and predicted intensity ratios from such emission lines provides a measure of the attenuation. These eight $v = 2 \rightarrow 0$ lines and measured peak flux densities are listed in Table 2.5. Listed in Table 2.6 are the $v = 2 \rightarrow 0$ and $v = 2 \rightarrow 1$ lines that arise from the same upper state. For lines originating from the same upper state, a predicted line ratio is just the ratio of the products $\Delta E_{u1} A_{u1}$, where ΔE_{u1} is the energy of transition $u \rightarrow 1$ and A_{u1} is the spontaneous transition probability. Our best estimate using a standard interstellar extinction law (Rieke & Lebofsky 1985) is $A_v = 3.4^{+4.0}_{-2.0}$ magnitudes. The relatively large uncertainty is a result of scatter in the extinction as determined from single line pairs, uncertainty in individual line fluxes, uncertainty in relative flux calibration for the two data sets, and blending with atomic and H_2 fluorescence emission lines. This value for A_v is well within the errors on A_v as found by Thronson. There is

an uncertainty in A_v that cannot be estimated associated with the form of the extinction law. A differential extinction between 1.2 μm and 2.2 μm of $A_{\lambda 1.2} - A_{\lambda 2.2} = 0.62^{+0.73}_{-0.36}$ mag is determined from the observations. However, there is a small dependence on the chosen extinction law in this estimate of the differential extinction. We also note that a best fit A_v as determined by H_2 spectral models (see Section 2.5.1) is found to be $A_v \sim 3.0$ mag. The position angle of polarization in the forbidden lines is nearly parallel to the galactic plane (SC81); the bulk of the attenuation may in fact be interstellar, rather than intrinsic.

2.5.2 Origin of the H_2 Spectrum

As demonstrated by Black & van Dishoeck (1987), reflection nebulae are likely to be ideal sources of fluorescent H_2 emission. Thus, AFGL 618 should be an excellent object in which to search for such emission. In addition, the spectral window accessible to the spectrometer includes a large number of molecular hydrogen lines which will be pumped by fluorescence, making it possible to search for relatively low levels of fluorescent molecular hydrogen emission. Ultraviolet photons with $\lambda > 0.0912 \mu\text{m}$ can escape the ionized nebula and illuminate the lobes where they can be absorbed in the Lyman ($\text{B } ^1\Sigma_u^+ - \text{X } ^1\Sigma_g^+$) and Werner ($\text{C } ^1\Pi_u - \text{X } ^1\Sigma_g^+$) bands of molecular hydrogen. Approximately 10% of the

resulting downward transitions will be to the vibrational continuum of the ground electronic state, thus leading to dissociation of the molecule (this mechanism was first described by Solomon in 1965 and discussed by Field, Somerville, & Dressler 1966). The remaining transitions to bound vibration-rotation levels of the ground state result in UV line fluorescence and produce a distinctive infrared spectrum of slow electric quadrupole transitions. This process is described in detail by Black & Dalgarno (1976), van Dishoeck & Black (1986), Black & van Dishoeck (1987), and Sternberg & Dalgarno (1989).

Emission from low-lying H_2 vibration-rotation levels can be collisionally excited in regions with kinetic temperature $T_k \sim 1000$ K. From the relatively weak $v = 2 \rightarrow 1$ S lines near $2 \mu m$, Thronson (1981) has argued that much of the H_2 emission from AFGL 618 is collisionally excited in shocks (see also Beckwith et al. 1984). An alternative hypothesis has been suggested by Jura & Kroto (1990) to explain the H_2 emission from AFGL 2688 (the "Egg Nebula"). In their model, H_2 is collisionally excited in hot gas which is created by a rapid grain streaming velocity.

We have attempted to reproduce the observed H_2 emission from AFGL 618 using the modelling techniques described by van Dishoeck & Black (1986) and Black & van Dishoeck (1987). Using an H_2 modelling code kindly provided by J.H. Black,

both fluorescent emission spectral models and models assuming thermal equilibrium (TE) have been calculated. In the fluorescence models, H_2 is formed primarily on grain surfaces and destroyed by the process of spontaneous radiative dissociation as described above. The abundance of H_2 is assumed to be in steady state. The calculation solves the equation of transfer for 22,445 absorption lines simultaneously in a plane-parallel cloud illuminated on one side by an external ultraviolet radiation source. This type of simple geometry is not intended to reproduce the actual distribution of material in AFGL 618. It should, however, produce results which are good averages of the conditions actually present. Also, such models can aid in line identification and verify the presence of fluorescent emission in addition to providing an estimate of the level of excitation by UV photons. Statistical equilibrium equations are solved for the populations of 211 vibration-rotation levels in the $X^1\Sigma_g^+$ state, 629 levels in the $B^1\Sigma_u^+$ state, and 476 levels in the $C^1\Pi_u$ state. Multiple steps are taken through the cloud, at each of which the cascade of 2937 vibration-rotation transitions in the $X^1\Sigma_g^+$ state is calculated.

The intensity of the radiation field at the molecular boundary is parameterized by the factor I_{uv} , such that $\phi = 4.5 \times 10^{-8} I_{uv}$ photons $cm^{-2} s^{-1} Hz^{-1}$ at $\lambda = 0.1000 \mu m$. In regions

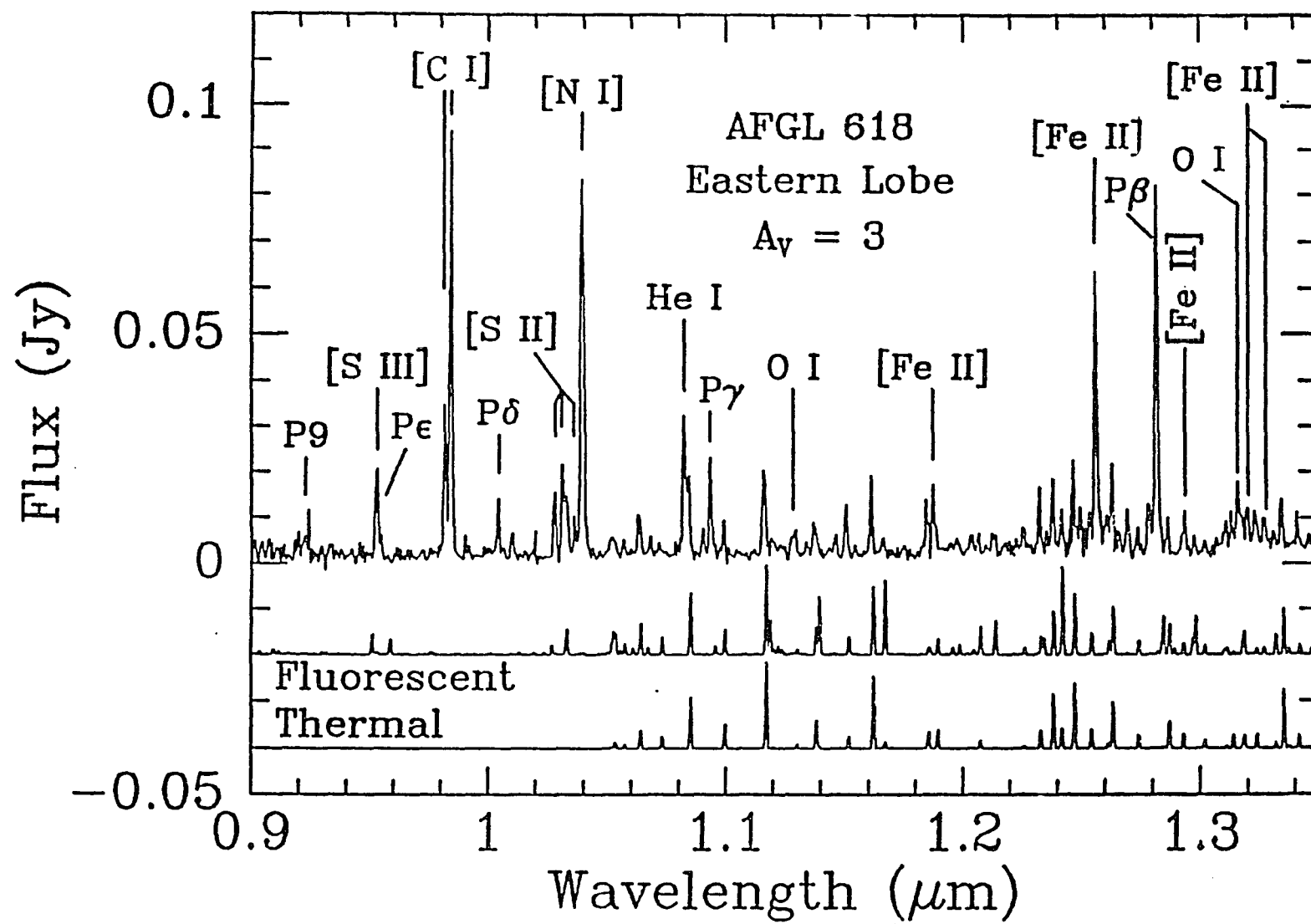
where the Ly α flux is large, enhanced H₂ excitation might occur due to accidental resonances with the B ¹ Σ_u^+ - X ¹ Σ_g^+ v = 1 - 2 P(5) and R(6) transitions, provided that v = 2 level in the X ¹ Σ_g^+ ground electronic state is already significantly populated. To explore this possibility in AFGL 618, we have examined the effect of a large Ly α flux on the IR fluorescence spectrum.

Thronson (1981) determined an H₂ vibration-rotation excitation temperature based on line fluxes in the 2 μ m region that were not corrected for extinction. To minimize error in the thermal model of H₂ emission, we have corrected the fluxes presented by Thronson for A_v = 3.0 mag and a standard extinction law. We have determined a new excitation temperature based on the corrected fluxes, even though the change was expected to be small. Assuming a Boltzmann distribution and including all 15 available lines in a least-squares fit to a plot of N_u/g_u versus T_u = E_u/k (see, e.g., Thronson 1981), we found that T_{ex} = 2250 K. However, as was also shown by Thronson, the four v = 2 \rightarrow 1 lines all appear to be systematically stronger than would be expected for TE, based on the v = 1 \rightarrow 0 lines. Since these are also the weakest lines in the spectrum, this might be a result of measurement error. In addition, scatter in the N_u/g_u versus T_u diagram is much larger in the v = 2 \rightarrow 1 lines. It therefore seems prudent to leave these lines out of the fit

(as was also done by Thronson) and determine a T_{ex} based only on the $v = 1 \rightarrow 0$ lines. For such a least-squares fit, it was found that $T_{\text{ex}} = 1942 \pm 200$ K. This can be compared to the value found by Thronson of $T_{\text{ex}} = 1950 \pm 200$ K. The difference between the two estimates is completely negligible.

Results of the modelling are presented in Figure 2.8. A thermal model appears on the bottom, and a fluorescent model is displayed directly below the data. Both models extend into the $2 \mu\text{m}$ region, and have been adjusted to give the same intensity in the $v = 1 \rightarrow 0$ S(1) line as that given by Thronson (1981). This results in an H_2 column density of $N_{\text{H}_2} = 5.2 \times 10^{18} \text{ cm}^{-2}$ for $T_k = 2000$ K. Characteristics of the spectrum are unchanged if $T_k = 1942$ K. The fluorescent model has been calculated for $I_{\text{UV}} = 200$, $n_{\text{H}} = 10^5$, and $T_k = 2000$ K. This value of I_{UV} is for a UV radiation field appropriate to a B0 (SC81) star embedded in an H II region, extinguished by about $A_v \sim 1.5 - 2.0$ mag, and diluted over a distance of $r \sim 10^{17}$ cm, which is comparable to the linear scale of the near-infrared lobes in AFGL 618. Both models include $A_v = 3.0$ mag along the observer's line-of-sight. (We are thus assuming that the derived extinction to the lobes derived in Section 2.5.1 is entirely interstellar.) It is important to note that these sources of attenuation are separate from the attenuation internal to the lobe, which is calculated using

Figure 2.8: Infrared spectrum of AFGL 618 compared with spectral models of thermal and fluorescent emission from H_2 . The data appear on top, the fluorescent model in the middle, and the thermal model on the bottom. Parameters for the models are: $T_{\text{ex}} = 2000$ K and $N_{H_2} = 5.2 \times 10^{18} \text{ cm}^{-2}$ (thermal), $I_{\text{UV}} = 200$, $n_H = 10^5$, and $T = 2000$ K (fluorescence; see text). The predicted fluxes have been corrected for $A_v = 3.0$ mag. The flux scale is referenced to the data.



a total gas column density to visual extinction of $N_{\text{tot}}/A_v = 6.36 \times 10^{20} \text{ cm}^{-2} \text{ mag}^{-1}$. This is consistent with the gas-to-dust ratio for carbon stars as found by Jura (1986).

A satisfactory fit to the strongest emission lines is produced by the thermal model alone, but a better fit is obtained when fluorescence is included. However, at least four features appear stronger in the data than predicted by either model. These lines include $v = 3 \rightarrow 1 \text{ S}(5)$ ($1.152 \mu\text{m}$), $3 \rightarrow 1 \text{ S}(3)$ ($1.185 \mu\text{m}$), $3 \rightarrow 1 \text{ S}(1)$ ($1.233 \mu\text{m}$), and $2 \rightarrow 0 \text{ Q}(3)$ ($1.247 \mu\text{m}$). The last two are in a region crowded by other lines. Several models were calculated in which the value of I_{UV} was varied over many orders of magnitude. A better fit than that presented was not obtained. It is possible that these lines are confused with unidentified atomic and molecular features. Also, the plane-parallel geometry used in the models might be an inadequate representation of AFGL 618.

In addition, it is important to note that at least three lines are predicted to be stronger by the fluorescence model than observed in the data. These are the $v = 3 \rightarrow 1 \text{ S}(6)$ ($1.139 \mu\text{m}$), $3 \rightarrow 1 \text{ S}(4)$ ($1.167 \mu\text{m}$), and $4 \rightarrow 2 \text{ S}(4)$ ($1.242 \mu\text{m}$) lines. Comparison with a model calculated for a large $\text{Ly}\alpha$ flux suggests that these lines can be enhanced by $\text{Ly}\alpha$ pumping. Therefore, it would appear that the $\text{Ly}\alpha$ flux used in the model shown is too large. The value chosen was based

on a simple estimate of the leakage of Ly α photons from the H II region and could easily be an overestimate for a region where dust competes effectively with resonant scattering. A full range in Ly α flux was not explored, however.

While the model fit might not be exact, it is important to note that everywhere a feature is predicted, one is seen. In some cases the detection is marginal, but no *anticoincidences* are found. If we assume that the discrepancies between the model results and the data are due to the complicated geometry actually present in AFGL 618, we can use them to infer details about the morphology within the bipolar lobes. Most importantly, it appears that I_{uv} is not uniform throughout the lobes. Possible variations in total density should also be taken into account.

2.5.3 Discussion

The H₂ ($v = 1 \rightarrow 0$) lines in the 2 μm region are rather intense and exhibit a rotational excitation temperature in the $v = 1$ levels of $T_{\text{ex}} \approx 2000$ K (Thronson 1981). This immediately suggests an important component of high-temperature thermal emission, perhaps even in lines of the $v = 2 \rightarrow 0$ band in the spectral region accessible to the Ge spectrometer ($\lambda \leq 1.6 \mu\text{m}$). If the excitation temperature were $T_{\text{ex}} \leq 2000$ K for all levels, however, little emission would be expected in transitions arising in $v' \geq 3$. The

presence of such highly excited lines would reveal a component of fluorescent emission. We have used model spectra to aid the identification of H_2 lines in the rich near-infrared spectrum. As discussed in Section 2.5.2, several $v = 3 \rightarrow 1$ lines seem to be present: although weak, their intensities are higher than expected from thermal emission alone.

Fluorescent emission is expected from bright reflection nebulae like AFGL 618, and its detection can provide information about the detailed morphology of this object. Since fluorescent emission is only weakly present in the spectrum of AFGL 618, the UV flux incident on the lobes must be highly extinguished in the region surrounding the central star. Alternatively, the dust distribution may prevent the observed region from having a direct view of the stellar photosphere. Also, fluorescent emission could be strong within the interior of the lobe, but extinguished by the large amount of circumnebular material to the intensity found in the spectrum presented here. The presence of reflected stellar continuum in the visible (SC81) and infrared (Latter et al. 1992) spectra demonstrates that some stellar light reaches the lobes. It is not possible with the current data to determine if the extinction to the fluorescent H_2 differs from that to the thermal component, or if the fluorescent and thermally excited H_2 are co-extensive. SC81 postulate the

presence of optically thick knots close to the central star that shadow much of the lobe material from direct exposure to the stellar radiation field. Evolved forms of these clumps might be visible as knots in images of PNe (e.g. Balick 1989). The analysis of Section 2.4 revealed that the unshielded material is ionized with an electron temperature of $T_e \approx 2.5 \times 10^4$ K and an electron density of $n_e \approx n_H \approx 8 \times 10^3$ cm⁻³. The shadowed component near the clumps is primarily neutral with $T_e \approx 10^4$ K, $n_e \approx 1.6 \times 10^3$ cm⁻³. Heating of the neutral component takes place through ionization of hydrogen by UV radiation reflected from the unshielded component. It is possible that UV-excited molecular hydrogen is present within the shadowed material, but farther out in the lobes where the gas is cool and molecules can easily survive. The fluorescence-producing UV photons are delivered into the shielded region by scattering off dust in the material that is directly exposed to starlight.

Models of collisionally excited H₂ emission were also compared to the data. These reproduce the observed spectrum adequately for a uniform excitation temperature of $T_{ex} \sim 2000$ K, but a significantly better fit results when a component of fluorescent emission is included. Thronson (1981) and Burton & Geballe (1986) have discussed in detail the origin of the thermal emission in AFGL 618. Thronson argued that the molecular hydrogen is excited by shocks with velocities

of $\sim 10 \text{ km s}^{-1}$. He found the total mass of shocked H_2 to be $M_{\text{H}_2} \sim 10^{-4} M_\odot$ if the object is at 1 kpc. Adopting the column density in our thermal models of $N_{\text{H}_2} = 5.2 \times 10^{18} \text{ cm}^{-2}$ and assuming the emission arises from a spherical region with $r = 5 \times 10^{16} (D/1.8 \text{ kpc}) \text{ cm}$, we find the total mass of H_2 to be $M_{\text{H}_2} \sim 5 \times 10^{-5} M_\odot$. This assumes that the emitting H_2 is uniformly distributed throughout the eastern lobe. If shocks are responsible, then the emission might be expected to arise from a relatively small region. It is not clear that this must be the case. Beckwith et al. (1984) have found the H_2 $v = 1 \rightarrow 0 \text{ S}(1)$ line emission to be extended. Spectra near $1.1 \mu\text{m}$ of higher signal-to-noise ratio acquired through a small aperture at various points on the bright eastern lobe could be revealing.

In a clumpy medium, cooling of the gas within the shadows might generate low velocity shocks of the type required to excite H_2 emission. Burton and Geballe (1986) suggest a similar model based on rapidly moving clumps. Shocks generated by the stellar mass-loss are probably also present. If there is a shock at the interface of the high velocity wind and the slower moving envelope material, it will likely be strongly dissociating, and therefore will not contribute significantly to the total H_2 emission. However, at least some of the H_2 emission must come from material accelerated by the fast wind, as evidenced by the very broad

velocity width ($\sim 250 \text{ km s}^{-1}$) of the $v = 1 \rightarrow 0 \text{ S}(1)$ line (Burton & Geballe 1986). It is possible that the high-velocity molecular material has reformed after being destroyed in a fast shock (e.g. Cernicharo et al. 1989). However, Cernicharo et al. also see high velocity emission from polyatomic species such as HCO^+ , HCN , and HC_3N . The rapid expansion of the material will make reformation of such species highly unlikely if the gas is directly exposed to the bright central star. Hartquist & Dyson (1987) have suggested a mechanism by which molecular material can be accelerated to high velocities without being dissociated in a fast shock. Also, Glassgold, Mamon, & Huggins (1991) have shown that molecule formation in a fast wind can be efficient. However, the UV brightness of their model star is much weaker than that present in AFGL 618. It is impossible to determine how much the high-velocity material contributes to the emission measured in our data. Also, while shock excitation is sufficient to explain the observed emission, it might not be necessary. There are neutral regions within AFGL 618 which are at high enough density and temperature (Section 2.4.4.2, SC81) to maintain H_2 nearly in LTE at $T_{\text{ex}} \sim T_{\text{K}} \sim 2000 \text{ K}$. The above-mentioned model of heating by rapid grain streaming suggested by Jura & Kroto (1990) could also be important.

Recently, Lequeux & Jourdain de Muizon (1990) presented a measurement of the $\text{H}_2 \text{ } v = 1 \rightarrow 0 \text{ O}(5)$ line ($3.234 \text{ }\mu\text{m}$) from

AFGL 618. A total flux in the line of $f = 8 \times 10^{-13} \text{ erg cm}^{-2} \text{ s}^{-1}$ was found in a $5''$ aperture. Contrary to a statement made in their paper, this value is significantly larger than predicted by thermal or fluorescent excitation when compared to the $v = 1 \rightarrow 0 \text{ S}(1)$ line of Thronson (1981). Comparison with our models at $T_k = 2000 \text{ K}$ suggests that $A_v \approx 23 \text{ mag}$ is required to reproduce the measured $v = 1 - 0 \text{ O}(5)$ line flux. Unless the true extinction law in AFGL 618 is extremely unusual, we must conclude that the discrepancy is due to differences in flux calibration.

In Section 2.4.4.1, we found an extinction of $A_v = 2.1 \text{ mag}$ to the eastern lobe. We also have determined that $A_v = 3.4^{+4.0}_{-2.0} \text{ mag}$ to the H_2 -emitting region (Section 2.5.1). Thus, the visible and infrared line radiation appear to be attenuated by approximately the same dust distribution. In contrast, Thronson (1981) found $A_v \geq 28 \text{ mag}$ to the region that emits $\text{H I Br}\gamma$ (see also Lequeux & Jourdain de Muizon 1990). As discussed by Thronson, the $\text{Br}\gamma$ emitting region is the compact H II region which lies behind a thick, dusty torus surrounding the central star, obscuring it from view at visible wavelengths. The intensity of fluorescent H_2 emission implies uneven, or extinguished ultraviolet illumination of the visible lobes. Also, it might be incorrect to assume a Case B recombination spectrum for the intrinsic Balmer decrement in a compact, very dense nebula

(cf. Thompson 1987 and references therein). The problem is compounded if a non-standard extinction law applies. The distributions of attenuating and emitting gas are complex and still not fully delineated.

2.5.4 Summary of Molecular Data

The H₂ data presented in this section reinforce the picture derived from earlier observations for the structure of AFGL 618.

A clumpy medium has been suggested by others (e.g. SC81; Burton & Geballe 1986) to explain the ionization and velocity structure. Our analysis of the molecular hydrogen fluorescent emission detected in our near-infrared spectrum is not inconsistent with this hypothesis. However, there is little new evidence in our data which strongly supports the idea of a clumpy medium. What is required, however, is that the observed molecular region be shielded from direct exposure to the UV flux of the central star. The H₂ emission in our spectrum is dominated by emission from collisionally excited molecules at an excitation temperature of $T_{\text{ex}} \sim 2000$ K, which is consistent with excitation in shocks (see also Jura & Kroto 1990). Such emission had previously been detected at $\lambda \sim 2 \mu\text{m}$ (e.g. Thronson 1981; Beckwith et al. 1984; Burton & Geballe 1986).

A complex distribution of gas and dust is vividly

displayed in both the spectrum and images of AFGL 618. Since this clearly is a rapidly evolving object at one of the most mysterious points in stellar evolution, continued monitoring of key features is important. As material flows away from the central star, its density will drop. Obscuration of UV starlight will decrease. Perhaps fluorescent emission from molecular hydrogen will increase. This type of emission has been observed from at least one other compact young planetary nebula; Hubble 12 (Section 5.3.3; Dinerstein et al. 1988). It is important to note that the wavelength range accessible to the Ge spectrometer is particularly useful for discriminating fluorescent from thermal H_2 emission. A survey for this type of emission in the nearest PPNe and young PNe is presently being carried out. The new data should provide additional insight into the evolution of these objects.

TABLE 2.1

LINE IDENTIFICATIONS AND FLUXES FOR AFGL 618

$(\lambda_{\text{air}})_{\text{lab}}$ (μm)	Flux ¹		Dereddened Flux ¹		Identification	
	east	west	east ²	west ³		
0.4069	2.96	0.78	48.2	36.7	[SII]	$3p^3 4S_{3/2}^o - 3p^3 2P_{3/2}^o$
0.4076	0.95	0.11	15.4	5.1	[SII]	$3p^3 4S_{3/2}^o - 3p^3 2P_{1/2}^o$
0.4102	1.32	0.13	21.0	6.0	HI	2-6
0.4244 ^a	0.14	-	2.0	-	[FeII]	$a^4F_{9/2} - a^4G_{11/2}$
0.4245 ^a					[FeII]	$a^4F_{7/2} - a^4G_{7/2}$
0.4277	0.07	-	1.0	-	[FeII]	$a^4F_{7/2} - a^4G_{9/2}$
0.4287	0.16	0.03	2.2	1.2	[FeII]	$a^6D_{9/2} - a^6S_{5/2}$
0.4340	2.20	0.30	29.8	11.0	HI	2-5
0.4358 ^a	0.22	-	2.9	-	[FeII]	$a^4F_{3/2} - a^4G_{5/2}$
0.4359 ^a					[FeII]	$a^6D_{7/2} - a^6S_{5/2}$
0.4414 ^a	0.21	0.04	2.7	1.5	[FeII]	$a^6D_{5/2} - a^6S_{5/2}$
0.4415 ^a					[FeII]	$a^6D_{7/2} - b^4F_{3/2}$
0.4416 ^a					[FeII]	$a^6D_{9/2} - b^4F_{9/2}$
0.4452 ^a	0.10	0.02	1.2	0.8	[FeII]	$a^6D_{3/2} - a^6S_{5/2}$
0.4458 ^a					[FeII]	$a^6D_{7/2} - b^4F_{7/2}$
0.4470 ^a	0.09	-	1.1	-	[FeII]	$a^6D_{5/2} - b^4F_{3/2}$
0.4472 ^a					HeI	$2p^3 P^o - 4d^3 D$
0.4571	0.78	0.18	9.0	5.3	MgI]	$3P_1^o - 1S_0$
0.4640	0.31	0.02	3.4	0.6	[FeII]	$a^6D_{3/2} - b^4P_{1/2}$
0.4657 ^a	0.71	0.05	7.7	1.3	FeII	$a^6S_{5/2} - z^4D_{5/2}^o$
0.4658 ^a					[FeIII]	$3d^6 5D_4 - 3d^6 3F_4$
0.4702	0.23	0.02	2.4	0.5	[FeIII]	$3d^6 5D_3 - 3d^6 3F_3$
0.4861	7.03	1.02	66.8	22.9	HI	2-4
0.4922 ^a	0.11	-	1.0	-	HeI	$2p^1 P_1^o - 4d^1 D_2$
0.4924 ^a					[FeII]	$a^6S_{5/2} - z^6P_{3/2}^o$
0.4959	0.15	0.04	1.3	0.8	[OIII]	$2p^3 P_1 - 2p^1 D_2$

0.5006 ^a	0.47	0.13	4.1	2.5	[FeII] a ⁴ F _{5/2} -b ⁴ F _{7/2}
0.5007 ^a					[OIII] 2p ³ P ₂ -2p ¹ D ₂
0.5007 ^a					[FeII] a ⁶ D _{3/2} -b ⁴ P _{5/2}
0.5016	0.14	-	1.2	-	HeI 2s ¹ S ₀ -3p ¹ P ₁ ^o
0.5112	0.07	0.02	0.6	0.3	[FeII] a ⁴ F _{9/2} -a ⁴ H _{11/2}
0.5159	0.60	0.16	4.8	2.9	[FeII] a ⁴ F _{9/2} -a ⁴ H _{13/2}
0.5198 ^a	6.82	1.95	53.9	33.8	[NI] 2p ⁴ S _{3/2} ^o -2p ² D _{3/2} ^o
0.5200 ^a					[NI] 2p ⁴ S _{3/2} ^o -2p ² D _{5/2} ^o
0.5261	0.25	0.05	1.9	0.9	[FeII] a ⁴ F _{7/2} -a ⁴ H _{11/2}
0.5270 ^a	0.58	0.09	4.4	1.5	[FeIII] 3d ⁶ ⁵ D ₃ -3d ⁶ ³ P ₂
0.5273 ^a					[FeII] a ⁴ F _{9/2} -b ⁴ P _{5/2}
0.5334	0.18	0.05	1.3	0.8	[FeII] a ⁴ F _{5/2} -a ⁴ H _{9/2}
0.5377	0.12	0.03	0.9	0.5	[FeII] a ⁴ F _{3/2} -a ⁴ H _{7/2}
0.5413 ^a	0.10	0.02	0.7	0.3	[FeII] a ⁴ F _{5/2} -a ² D _{3/2}
0.5413 ^a					[FeII] a ⁴ F _{9/2} -a ² H _{11/2}
0.5527	0.18	0.05	1.2	0.7	[FeII] a ⁴ F _{7/2} -a ² D _{5/2}
0.5551	0.04	-	0.3	-	[FeII] a ⁴ P _{5/2} -b ⁴ D _{7/2}
0.5577	0.29	0.07	1.9	1.0	[OI] 2p ⁴ 1D ₂ -2p ⁴ 1S ₀
0.5696	0.47	0.05	3.0	0.6	[FeI] 4s ² a ⁵ D-4s a ⁵ P
0.5755	1.49	0.22	9.3	2.8	[NII] 2p ¹ D ₂ -2p ¹ S ₀
0.5876	0.63	0.09	3.8	1.1	HeI 2p ³ P ^o -3d ³ D
0.5890	0.41	0.08	2.5	1.0	NaI 3s ² S _{1/2} -3p ² P _{3/2} ^o
0.6220	0.04	0.01	0.2	0.1	FeII 4sb ⁴ F _{5/2} -4pz ⁶ D _{3/2} ^o
0.6300	33.6	10.6	177.	105.	[OI] 2s ² 2p ⁴ ³ P ₂ -2p ⁴ ¹ D ₂
0.6364	11.3	3.86	58.3	37.2	[OI] 2s ² 2p ⁴ ³ P ₁ -2p ⁴ ¹ D ₂
0.6548	4.89	1.53	23.9	13.7	[NII] 2p ³ P ₁ -2p ¹ D ₂
0.6563	81.2	12.7	395.	113.	HI 2-3
0.6583	14.2	4.54	65.7	37.	[NII] 2p ³ P ₂ -2p ¹ D ₂
0.6665	0.10	0.04	0.5	0.3	?
0.6678	0.41	0.06	1.9	0.5	HeI 2p ¹ P ₁ ^o -3d ¹ D ₂
0.6716	9.12	3.20	42.4	26.7	[SII] 3p ³ ⁴ S _{3/2} ^o -3p ³ ² D _{5/2} ^o
0.6731	15.8	5.77	73.3	47.8	[SII] 3p ³ ⁴ S _{3/2} ^o -3p ³ ² D _{3/2} ^o
0.8446	2.0		5.7		OI 3s ³ S ^o -3p ³ P
0.8617	2.1		5.7		[FeII] a ⁴ F _{9/2} -a ⁴ P _{5/2}
0.8727	2.7		7.2		[CI] 2p ¹ S ₀ -2p ¹ D ₂

0.8975	0.3		0.8		?
0.9015	1.3		3.4		HI 3-10
0.9034	1.1		2.8		[FeII] $a^4F_{5/2}-a^4P_{1/2}$
0.9069	1.4		3.4		[SIII] $3p^2^3P_1-3p^2^1D_2$
0.9112	4.2		11.		Cl $2p3s^3P_2^o-3p^3P_1$
0.9218	0.8		2.1		MgII $4s^2S_{1/2}-4p^2P_{3/2}^o$
0.9227 ^a	1.8		4.3		[FeII] $a^4F_{5/2}-a^4P_{3/2}$
0.9229 ^a					HI 3-9
0.9244	4.0		9.8		MgII $4s^2S_{1/2}-4p^2P_{1/2}^o$
0.9268	0.7		1.6		[FeII] $a^4F_{3/2}-a^4P_{1/2}$
0.9335	1.4		3.2		?
0.9531	8.8		21.		[SIII] $3p^2^3P_2-3p^2^1D_2$
0.9546	1.9		4.5		HI 3-8
0.9824	13.		29.		[Cl] $2s^22p^2^3P_1-2p^1D_2$
0.9850	37.		83.		[Cl] $2s^22p^2^3P_2-2p^1D_2$
1.0031	0.3		0.7		HeI $3d^1D_2-7f^1F_3^o$
1.0049	4.2		9.1		HI 3-7
1.0109	1.7		3.7		NI $3p^4D^o-3d^4F$
1.0286	5.2	3.3	11.	9.3	[SII] $3p^3^2D_{3/2}^o-3p^3^2P_{3/2}^o$
1.0320	7.2	4.1	15.	11.	[SII] $3p^3^2D_{5/2}^o-3p^3^2P_{3/2}^o$
1.0336	5.3	2.8	11.	7.8	[SII] $3p^3^2D_{3/2}^o-3p^3^2P_{1/2}^o$
1.0370	2.4		5.1		[SII] $3p^3^2D_{5/2}^o-3p^3^2P_{1/2}^o$
1.0398	26.	(32.)	54.	(89.)	[NI] $2p^2D_{5/2}^o-2p^2P_{1/2,3/2}^o$
1.0408	18.	(32.)	37.	(89.)	[NI] $2p^2D_{3/2}^o-2p^2P_{1/2,3/2}^o$
1.0524	1.3		2.6		H ₂ (2,0) S(11)
1.0533	1.1		2.2		H ₂ (2,0) S(9)
1.0573	1.0		2.1		H ₂ (2,0) S(8)
1.0638	3.2		6.5		H ₂ (2,0) S(7)
1.0691	1.0		2.0		Cl $3s^3P_2^o-3p^3D_3$
1.0730 ^a	0.7		1.3		Cl $3s^3P_2^o-3p^3D_2$
1.0730 ^a					H ₂ (2,0) S(6)
1.0830	12.		24.		HeI $2s^3S-2p^3P^o$
1.0848	5.7		11.		H ₂ (2,0) S(5)
1.0913	1.4		2.7		HeI $3d^3D-6f^3F^o$
1.0938	6.2		12.		HI 3-6

1.0995	2.2	4.2	H ₂	(2,0) S(4)
1.1172	4.6	8.7	H ₂	(2,0) S(3)
1.1201	1.0	1.9	H ₂	(3,1) S(9)
1.1208	1.1	2.0	H ₂	(3,1) S(11)
1.1287	1.0	1.9	OI	3p ³ P-3d ³ D°
1.1301	1.1	2.1	H ₂	(3,1) S(7)
1.1379	2.1	4.0	H ₂	(2,0) S(2)
1.1394	0.9	1.6	H ₂	(3,1) S(6)
1.1450 ^a	0.4	0.7	[FeII]	b ⁴ F _{9/2} -b ⁴ D _{1/2}
1.1455 ^a			[FeII]	b ⁴ F _{9/2} -b ⁴ D _{3/2}
1.1468	1.3	2.4	[PII]	3p ³ P ₁ -3p ¹ D ₂
1.1516	2.8	5.3	H ₂	(3,1) S(5)
1.1553	0.5	0.9	?	
1.1619	4.0	7.4	H ₂	(2,0) S(1)
1.1668	0.8	1.5	H ₂	(3,1) S(4)
1.1755	0.4	0.7	Cl	3p ³ D-3d ³ F°
1.1828 ^a	0.4	0.8	[FeII]	b ⁴ F _{5/2} -b ⁴ D _{5/2}
1.1833 ^a			[FeII]	b ⁴ F _{3/2} -b ⁴ D _{7/2}
1.1854	2.9	5.2	H ₂	(3,1) S(3)
1.1882 ^a	3.7	6.7	[FeII]	a ⁴ D _{7/2} -a ² G _{7/2}
1.1883 ^a			[PII]	3p ³ P ₂ -3p ¹ D ₂
1.1892	1.4	2.6	H ₂	(2,0) S(0)
1.1955	0.4	0.6	H ₂	(4,2) S(9)
1.1984	0.6	1.0	H ₂	(4,2) S(8)
1.2044	0.8	1.4	H ₂	(4,2) S(7)
1.2073	0.8	1.4	H ₂	(3,1) S(2)
1.2090	1.3	2.3	?	
1.2260	1.1	2.0	H ₂	(4,2) S(5)
1.2327	2.6	4.6	H ₂	(3,1) S(1)
1.2380	3.5	6.1	H ₂	(2,0) Q(1)
1.2416 ^a	1.6	2.8	H ₂	(2,0) Q(2)
1.2418 ^a			H ₂	(4,2) S(4)
1.2470	3.4	6.0	H ₂	(2,0) Q(3)
1.2567	13.	23.	[FeII]	a ⁶ D _{9/2} -a ⁴ D _{7/2}
1.2632	3.4	5.7	H ₂	(2,0) Q(5)

1.2704	1.8	3.0	[FeII] a ${}^6D_{1/2}$ -a ${}^4D_{1/2}$
1.2741	0.8	1.3	H ₂ (2,0) Q(6)
1.2784 ^a	2.6	4.4	HeI 3d 3D -5f ${}^3F^o$
1.2788 ^a			[FeII] a ${}^6D_{3/2}$ -a ${}^4D_{3/2}$
1.2818	19.	32.	HI 3-5
1.2870	1.4	2.3	H ₂ (2,0) Q(7)
1.2929	0.7	1.1	H ₂ (2,0) O(2)
1.2943	1.9	3.2	[FeII] a ${}^6D_{5/2}$ -a ${}^4D_{5/2}$
1.2950	0.3	0.4	CI 3d ${}^1D^o$ -5p 1D
1.2978	0.7	1.2	[FeII] a ${}^6D_{1/2}$ -a ${}^4D_{3/2}$
1.3103	0.2	0.4	H ₂ (5,3) S(5)
1.3112	0.7	1.2	H ₂ (4,2) S(1)
1.3138	1.1	1.9	H ₂ (3,1) Q(1)
1.3165	2.6	4.3	OI 3p 3P -4s ${}^3S^o$
1.3177	1.3	2.1	H ₂ (3,1) Q(2)
1.3205	4.3	7.0	[FeII] a ${}^6D_{7/2}$ -a ${}^4D_{7/2}$
1.3237	1.0	1.6	H ₂ (3,1) Q(3)
1.3278	1.2	2.0	[FeII] a ${}^6D_{3/2}$ -a ${}^4D_{5/2}$
1.3316	0.4	0.7	H ₂ (3,1) Q(4)
1.3351	2.1	3.5	H ₂ (2,0) O(3)
1.3417	1.2	1.9	H ₂ (3,1) Q(5)
1.3468	0.3	0.5	H ₂ (5,3) S(3)

^a indicates flux comes from one of these lines or perhaps from a blend

¹ 10^{-14} erg/s/cm²

² Flux corrected for $A_v = 2.1$ mag.

³ Flux corrected for $A_v = 2.9$ mag.

TABLE 2.2

Electron density values that produce the reddening-corrected [NI] $(0.5198 + 0.5200)/(1.0398 + 1.0408)$ line ratio for given electron temperature. Errors correspond to a 20% uncertainty in the line ratio.

T_e	n_e (east, cm^{-3})	n_e (west, cm^{-3})
5000	$1.5 \pm 0.3 \times 10^5$	$2.1 \pm 0.4 \times 10^5$
10000	$2.6 \pm 0.6 \times 10^4$	$4.8 \pm 0.7 \times 10^4$
18000	$1.3 \pm 0.3 \times 10^4$	$2.2 \pm 0.6 \times 10^4$
20000	$1.1 \pm 0.3 \times 10^4$	$2.0 \pm 0.5 \times 10^4$
25000	$9.2 \pm 2.6 \times 10^3$	$1.7 \pm 0.3 \times 10^4$

TABLE 2.3

Electron density values that produce the reddening-corrected [NII] $0.5755/(0.6548 + 0.6583)$ line ratio for given electron temperature. Errors correspond to a 10% uncertainty in the line ratio.

T_e	n_e (east, cm^{-3})	n_e (west, cm^{-3})
5000	$> 10^6$	$> 10^6$
10000	$2.2 \pm 0.3 \times 10^5$	$1.1 \pm 0.2 \times 10^5$
15000	$1.0 \pm 0.2 \times 10^5$	$4.0 \pm 0.7 \times 10^4$
20000	$6.4 \pm 1.0 \times 10^4$	$1.9 \pm 0.5 \times 10^4$
25000	$4.6 \pm 0.9 \times 10^4$	$8 \pm 4 \times 10^3$

TABLE 2.4

Electron density values that produce the reddening-corrected [CI] 0.8727/(0.9824 + 0.9850) line ratio for given electron temperature. Errors correspond to a 20% uncertainty in the line ratio.

T_e	n_e (east, cm^{-3})
5000	27500 ± 7500
8000	4400 ± 1800
10000	1600 ± 1200
12000	450^{+950}_{-450}

TABLE 2.5
H₂ Line Flux Densities^a

$v = 2 \rightarrow 0$	λ (μm)	$F_v^{v=2 \rightarrow 0}$ (Jy)
S(0)	1.189	0.006 ± 0.001
S(1)	1.162	0.017 ± 0.002
S(2)	1.138	0.008 ± 0.001
S(3)	1.117	0.018 ± 0.001
Q(5)	1.263	0.017 ± 0.002
Q(4)	1.254	0.006 ± 0.005
Q(3)	1.247	0.017 ± 0.004
Q(2)	1.242	0.008 ± 0.001

^aUncertainties given are 1 σ statistical errors in data only. Systematic uncertainty in flux calibration is estimated to be $\sim \pm 15\%$.

TABLE 2.6

H_2 $v = 2 \rightarrow 0$ and $v = 2 \rightarrow 1$ Lines

Originating from the Same Upper State^a

$v = 2 \rightarrow 0$	λ (μm)		$v = 2 \rightarrow 1$	λ (μm)
S(0)	1.189	\leftrightarrow	S(0)	2.355
S(1)	1.162	\leftrightarrow	S(1)	2.247
S(2)	1.138	\leftrightarrow	S(2)	2.154
S(3)	1.117	\leftrightarrow	S(3)	2.073
Q(5)	1.263	\leftrightarrow	S(3)	2.073
Q(4)	1.254	\leftrightarrow	S(2)	2.154
Q(3)	1.247	\leftrightarrow	S(1)	2.247
Q(2)	1.242	\leftrightarrow	S(0)	2.355

^aData for H_2 $v = 2 \rightarrow 1$ line fluxes are taken from Thronson (1981; see text).

Chapter 3

THE TEMPERATURE SCALE FOR M DWARFS DERIVED USING SPECTRA FROM 0.6 TO 1.5 MICRONS

3.1 Introduction

In this chapter, we combine the red and infrared spectra of a sequence of M dwarfs. We then compare these spectra to recently developed theoretical models and derive a temperature sequence. This research was conducted in collaboration with J. Davy Kirkpatrick, George Rieke, France Allard, Rainer Wehrse, and Jim Liebert. My contributions to this project include observing and reducing the infrared data, identifying the atomic and molecular features in the infrared spectra, and constructing the H-R diagrams.

M dwarfs are the most common stars in the Galaxy, and they could be responsible in part for its missing mass. In spite of their importance, the physical properties of these objects are still poorly understood. Spectral data provide a wealth of information on such parameters as surface gravities, temperatures, and chemical compositions, but it has proven challenging to extract this information because

of the difficulty in relating existing data to theoretical models. Traditionally, spectra have been obtained in the visual, but for the coolest stars this has become an obstacle both because they are very faint and because the visual region lies on the Wien side of their blackbody emission, where modelling uncertainties can be very large. As a result, spectral atlases rarely contained data for stars later than M5. Recently, however, high quality spectra of M dwarfs have been obtained in the red and near-infrared, where these objects are emitting their peak fluxes. Spectral sequences are now available for the entire range of M dwarfs, and a comparison between observational and theoretical data can provide more insight into these objects.

Unfortunately, modelling the atmospheres of M dwarfs has proven to be a very complicated problem due to the large number of opacity sources present in their spectra, the uncertainty with which many molecular constants and oscillator strengths are known, and the inability of current models to describe adequately the transition from the radiative to the convective layers. (Convection itself, which is the main mode of energy transport in these stars, is fortunately not a major problem, and the high densities force the real temperature gradient to be very close to the adiabatic one.) The first attempt at modelling these atmospheres was the work of Mould (1976), who studied only the early M stars. Two recent PhD theses - Allard (1990) and

Ruan (1991) - have attempted to refine these models and to extend them to the temperatures of the coolest dwarfs. The energy distributions from both model grids are quite similar since the majority of subroutines employed was identical.

In this paper we present an M-dwarf spectral sequence against which to check the success of these new models. We have obtained spectra from 0.6 to 1.5 μm of well-studied, nearby stars with accurate trigonometric parallaxes. The observations and reductions are presented in Section 3.2. The method for combining the red and the infrared data is given in Section 3.3. Features which serve well as temperature discriminants are discussed in Section 3.4. Model spectra from Allard (1990) are fit to the empirical data and discussed in Section 3.5. The resulting temperature sequence and H-R Diagram for M dwarfs are given in Section 3.6, and the shortcomings of the present models are discussed in Section 3.7. The conclusions are highlighted in Section 3.8.

3.2 Observations and Data Reduction

The objects observed for this project are listed in Table 3.1. Spectral classifications are from Kirkpatrick, Henry, & McCarthy (1991, hereafter KHM). All of the red spectra were observed at the Multiple Mirror Telescope (MMT) and have a resolution of 0.0018 μm . Spectral coverage,

observation date, and integration time are given in columns (4) - (6). Observing setups and reduction procedures can be found in KHM. Since many of these observations were taken through spotty cloud cover, corrections for atmospheric absorption were considered unreliable and thus not attempted. Features such as the A- and B-band of telluric O₂ are still present.

The infrared spectra were taken at the Steward Observatory 2.3 m telescope using the GeSpec. The spectrometer was used with a pair of round, 6" apertures separated by 60". The 150 line/mm grating provides sampling every 0.0030 μm , and the observational linewidth is 0.0048 μm . Each grating setting covers about 0.1 μm , so many settings were needed to cover the spectral range. Each setting had a central wavelength displaced by 0.05 μm from the previous one to insure overlap between adjacent spectral pieces. Adjacent pieces were connected by renormalizing one of the two by the median flux ratio in the region of overlap. Dwarf stars of type F and G were observed for flatfielding and flux calibration. Telluric absorption was removed during the flatfielding procedure. However, Paschen absorption features in the spectra of the F and G dwarfs introduced small residual "emission lines" into the spectra of several of the program objects. For a more detailed discussion of the observing procedure and data reduction, see Section 1.3. Spectral coverage, observation date, and total integration

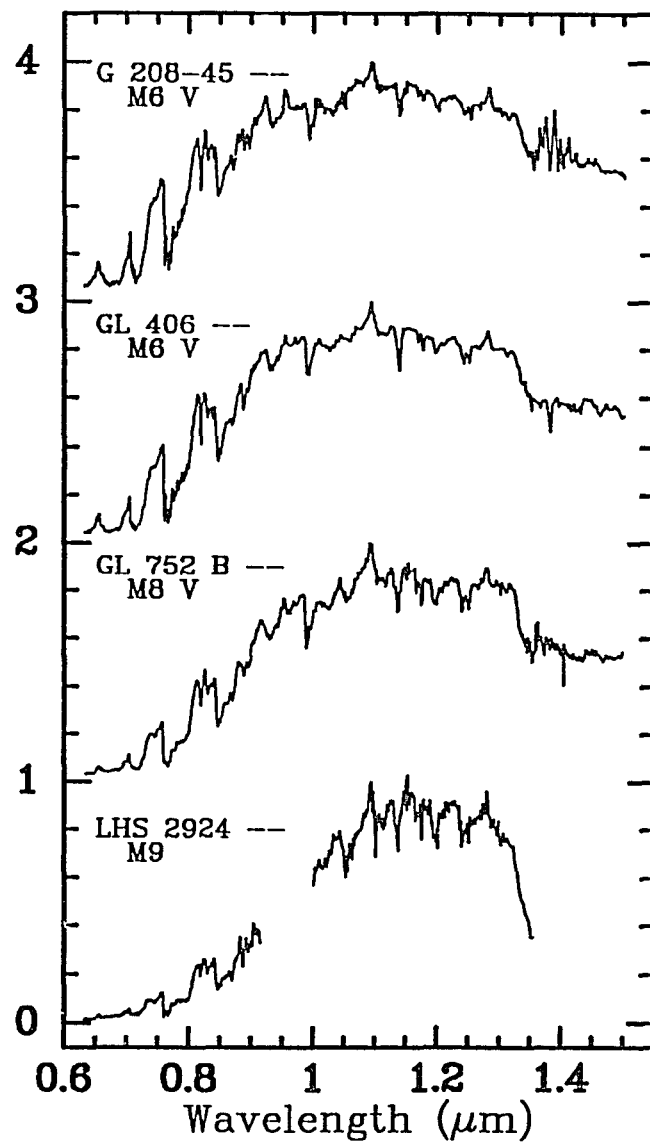
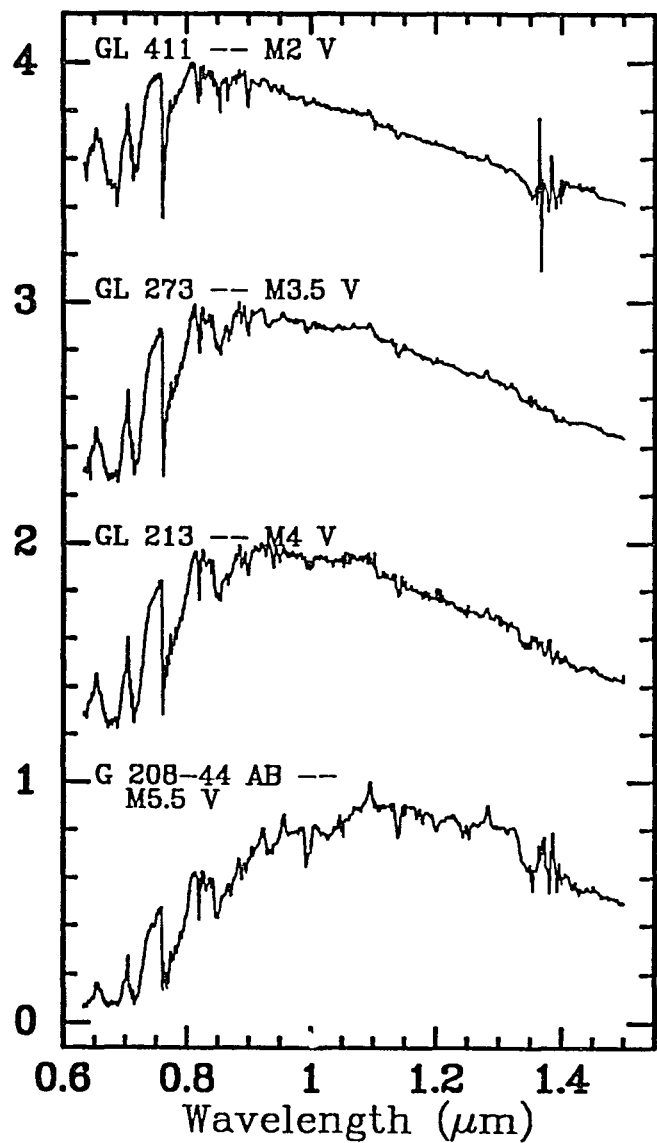
time for each object are given in columns (7) - (9) of Table 3.1.

3.3 Combining the Red and Infrared Spectra

To fit the two parts of the spectrum together, the infrared data for each object were renormalized relative to the red data by using a least-squares minimization technique (described in KHM) on the overlap region. This procedure takes the difference between the flux values of the two spectra at $0.0003 \mu\text{m}$ intervals in wavelength. The sum of the squares of these differences is computed over the overlap region. The infrared spectrum is then shifted vertically up or down relative to the red spectrum, and a new sum is calculated. In this way the shift giving the smallest residual is found. (Because absorption by unremoved telluric H_2O is present, the red spectra were truncated shortward of $0.905 \mu\text{m}$. For each object, the remaining amount of overlap between the red and infrared spectra can be determined from column (7) of Table 3.1.) Once the shift was found, the spectra were renormalized and then connected by averaging the flux values in the overlap region at intervals equivalent to the pixel size for the red data ($\sim 0.00035 \mu\text{m}$). The resulting spectra are shown in Figure 3.1. Each spectrum is normalized to one (in units of F_λ) at its peak flux. Since the two pieces of spectra for LHS 2924 do not overlap, their

Figure 3.1: Spectra of the eight objects listed in Table 3.1. The red portion ($0.63 - 0.92 \mu\text{m}$), of the spectra has a resolution of $0.0018 \mu\text{m}$, and the infrared portion ($0.92 - 1.50 \mu\text{m}$) has a resolution of $0.0048 \mu\text{m}$. Each spectrum is normalized to unity at its peak flux (which is in units of F_λ), and integral offsets have been added to separate the spectra vertically. Note that for early M dwarfs, the infrared region is relatively featureless compared to the red region. For late M dwarfs, many absorption features are seen in the infrared, the most striking of which is the water vapor band at $1.35 \mu\text{m}$.

Normalized Flux (F_λ) + Constant



relative normalizations relied solely upon the photometric data discussed below.

The fitted spectra include the regions investigated by broadband I and J filters, so it is possible to extract an I - J color for each spectrum to evaluate the effectiveness of our fitting technique. These extracted I - J colors were compared to values listed in Berriman & Reid (1987, hereafter BR) and Leggett & Hawkins (1988, hereafter LH). The I-band photometry from both sources is on the Kron-Cousins system. However, BR give J photometry on the AAO system, whereas LH give their J (and K) data on the CIT (or CTIO) system. The data sets can be placed on the same system by converting the J_{CIT} values into J_{AAO} values via the equation:

$$J_{\text{AAO}} = 1.115J_{\text{CIT}} - 0.115K_{\text{CIT}} + 0.004,$$

which can be derived from Elias et al. (1983). The resulting $I_{\text{KC}} - J_{\text{AAO}}$ colors for the program objects are listed in columns (2) and (3) of Table 3.2. Two of our objects - GL 411 and GL 406 - had photometry listed in both sources. Column (5) of Table 3.2 gives the difference between the LH and BR colors for these two stars. This comparison demonstrates that the colors agree to within ± 0.1 mag.

Photometry on the $I_{\text{KC}} - J_{\text{AAO}}$ system was extracted from the spectra of Figure 3.1. The values for $(F_{\lambda})_{I_{\text{KC}}}$ and $(F_{\lambda})_{J_{\text{AAO}}}$ were determined over a rectangular bandpass whose cut-on and cut-off wavelengths correspond to the wavelengths at half maximum

of the filter. Half power for the I_c ($\sim I_{KC}$) filter occurs at 0.725 and 0.875 μm (Bessell 1979), which gives a central wavelength for the rectangular bandpass of 0.80 μm . For J_{AAO} , half power occurs at 1.08 and 1.38 μm (Allen & Cragg 1983), giving a central wavelength of 1.23 μm . The colors measured from the spectra were therefore computed using the formula

$$\begin{aligned}
 I_{KC} - J_{AAO} &= 2.5 \log \left[\left(\frac{(F_\lambda)_{J_{AAO}}}{(F_\lambda)_{I_{KC}}} \right) \left(\frac{\lambda_{J_{AAO}}}{\lambda_{I_{KC}}} \right)^2 \left(\frac{(F_{v_0})_{I_{KC}}}{(F_{v_0})_{J_{AAO}}} \right) \right] \\
 &= 2.5 \log \left[\left(\frac{(F_\lambda)_{J_{AAO}}}{(F_\lambda)_{I_{KC}}} \right) \left(\frac{1.23 \mu m}{0.80 \mu m} \right)^2 \left(\frac{2550 Jy}{1640 Jy} \right) \right]
 \end{aligned}$$

The zero-magnitude fluxes are taken from BR and Allen & Cragg (1983). The derived colors are shown in column (4) of Table 3.2. Column (6) shows the differences between our photometry and that of LH. The average difference of 0.08 mag is similar to the disagreement found between the BR and LH color data and is small enough that we consider our technique of combining the spectra to be reliable.

Since the red and infrared spectra of LHS 2924 do not overlap, the photometry from LH was used to find the relative normalizations of the two pieces. Since the $I - J$ values derived from the spectra are systematically ~ 0.1 mag bluer than the LH values, a value of $I - J = 3.3$ was assumed for the normalization, and, of course, no independent measurement of the color was possible.

For M dwarfs, the purest temperature index of all the red/infrared colors (according to LH) is $I - J$. Table 3.2 shows that $I - J$ increases with increasing spectral type through the M stars, with the possible exception of the G 208-44/45 system. According to our photometry, G208-44 AB, whose red spectrum is classified as an M5.5 V, is 0.07 mag redder in $I - J$ than its sister star G 208-45, whose red spectrum is classified as an M6 V. Although this difference is within the errors determined above, the composite spectrum of G 208-44 AB may be too bright at J for its type due to the contribution from its very red, low-mass secondary, G 208-44 B. The same color effect is found in the photometry presented in McCarthy et al. (1988).

3.4 Spectral Features

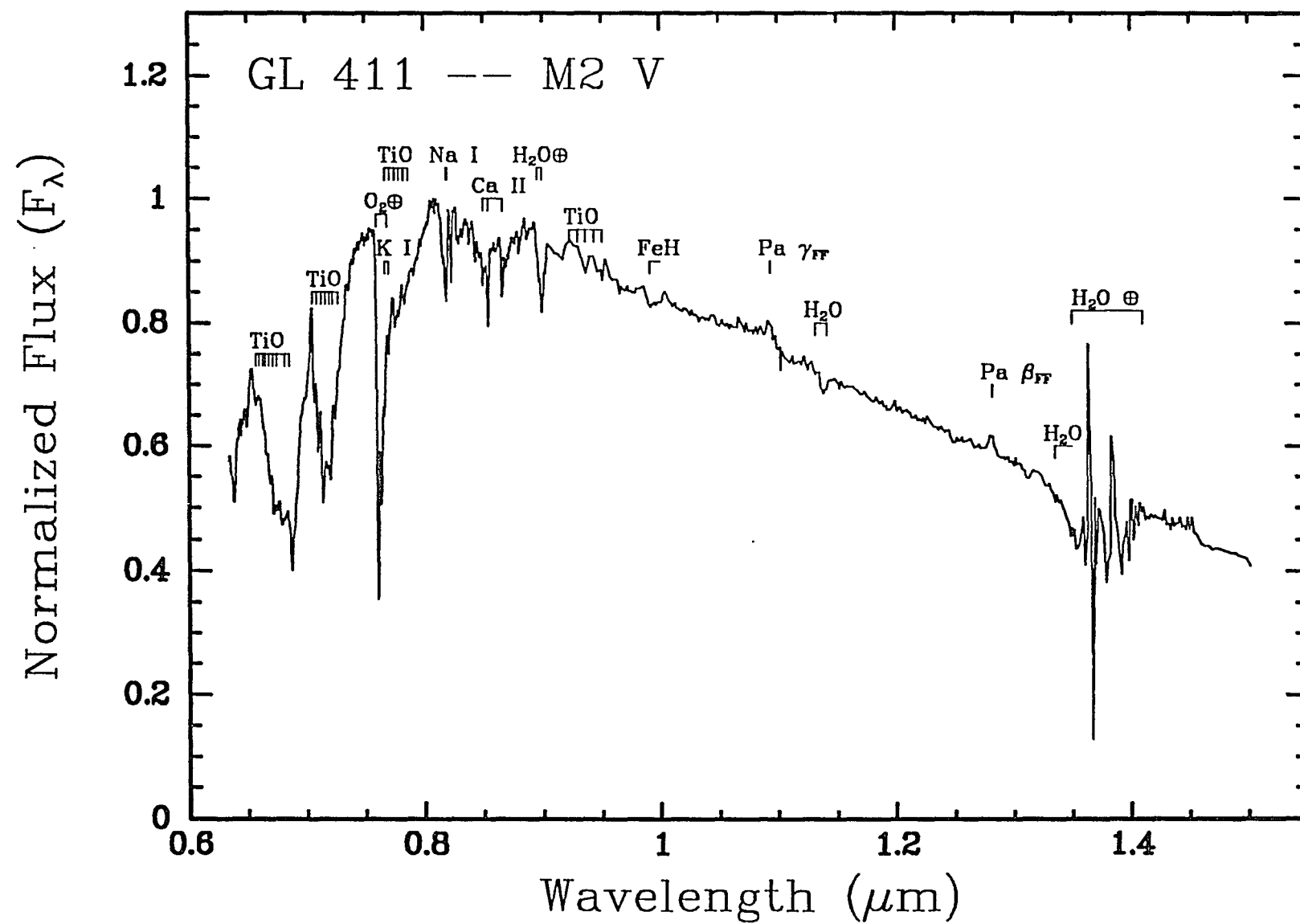
The spectra of Figure 3.1 show many changes in spectral shape and feature strengths along the sequence of M stars. The peak flux (in units of F_λ) for an M2 star occurs in the red portion of the spectrum, around 0.80 μm . By M8 and M9, the flux in the infrared portion around 1.1 to 1.2 μm greatly dominates. If these peaks corresponded to blackbody maxima, temperatures ranging from 3600 to 2400 K would be derived. Clearly, though, these spectra are far different from those of blackbodies, so a temperature determination based on model fitting and calibration of temperature-sensitive features

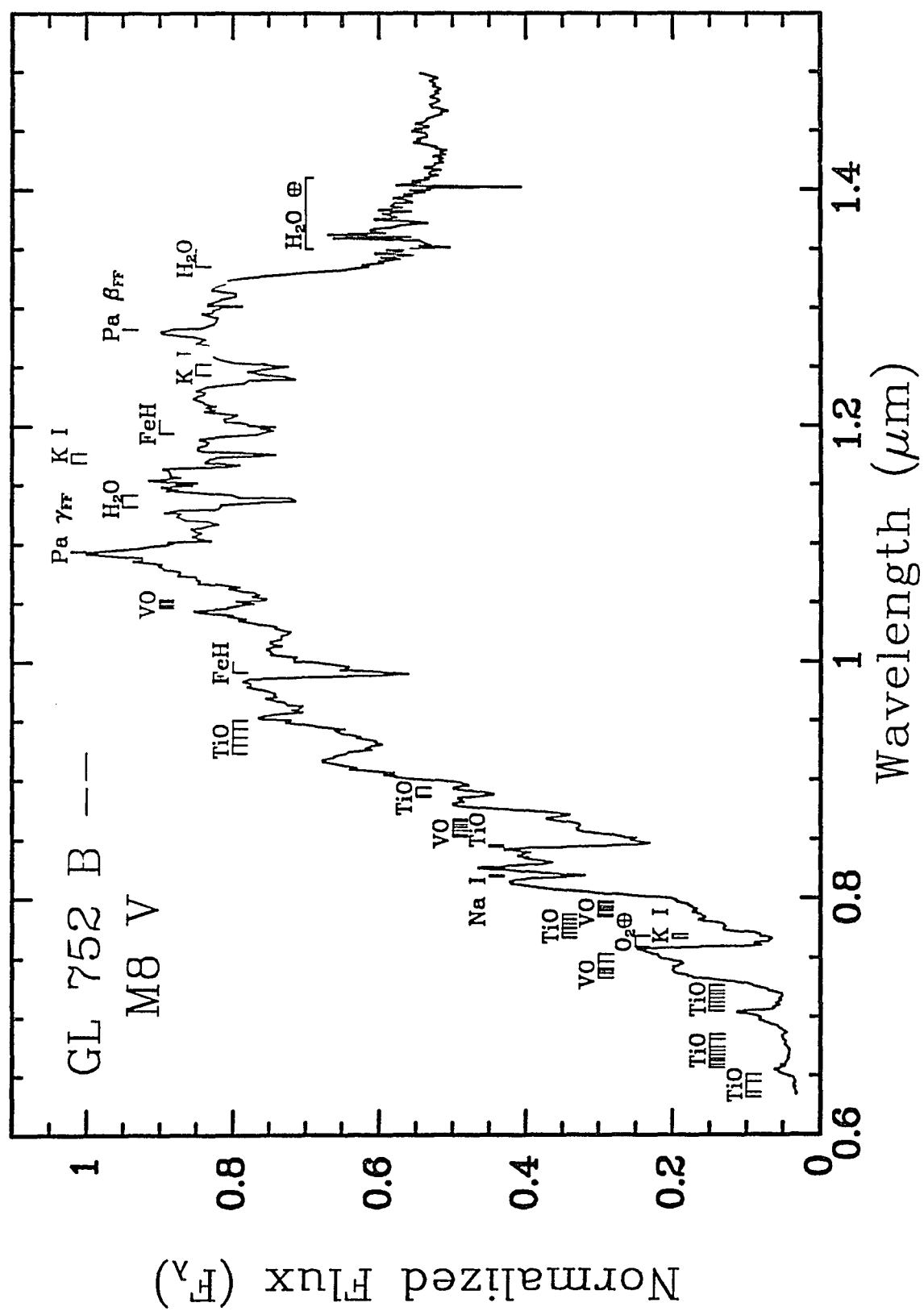
would be better.

There are several temperature-sensitive atomic lines and molecular bands that are easily visible in this spectral range. Figure 3.2.1 shows identifications for an M2 spectrum, and Figure 3.2.2 for an M8 spectrum. Most obvious perhaps are the red TiO bands, which gain prominence through the early- and mid-M stars, saturating beyond spectral type M6. At our resolution, VO absorption begins to appear after M6 and is a good indicator of temperature for the latest objects. The most obvious temperature-dependent features in the infrared are the H₂O absorption at 1.35 μm , which is the most striking feature in the entire spectrum of the M9 dwarf LHS 2924, and the FeH band at 0.99 μm , which begins to appear after M4 and increases with decreasing temperature throughout the sequence. Other prominent features in the infrared are H₂O at 1.14 μm , OH at 1.20 μm , and in our coolest objects, sharp absorption features at 1.169, 1.177, 1.243, and 1.252 μm . These last four lines coincide with the only K I features in the 1.1 - 1.5 μm solar spectrum of Livingston & Wallace (1991). The 1.177 μm line was first identified in the spectrum of R Leo by Spinrad & Wing (1969), who note that K I lines are favored at lower temperatures. A more detailed identification of features in the far red portion of the spectrum can be found in KHM.

Figure 3.2.1: Identifications of the most prominent features in the 0.63 - 1.50 μm spectrum of GL 411 - spectral type M2 V. Bands of VO, OH, FeH, and H₂O, are all effective as temperature indicators. The subscript "FF" refers to residual Paschen lines, an artifact of flatfielding with F and G stars.

Figure 3.2.2: Identifications of the most prominent features in the 0.63 - 1.50 μm spectrum of GL 752 B (VB 10) - spectral type M8 V. Bands of VO, OH, FeH, and H₂O are all effective as temperature indicators. The subscript "FF" refers to residual Paschen lines, an artifact of flatfielding with F and G stars.





3.5 Fits to Theoretical Spectra of M Dwarfs

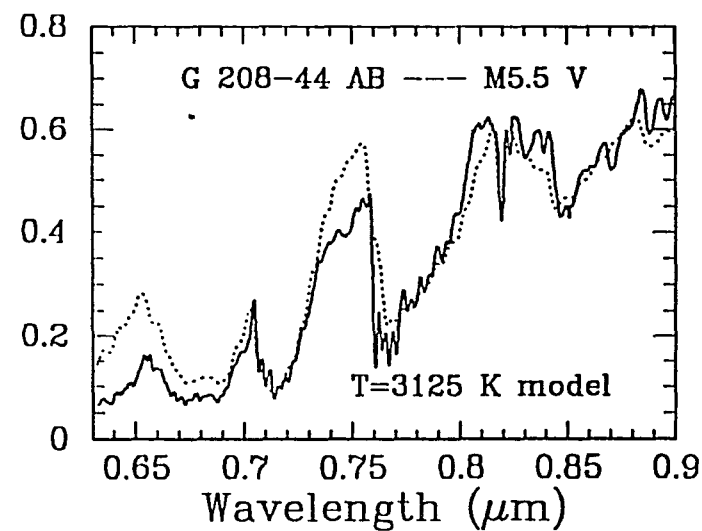
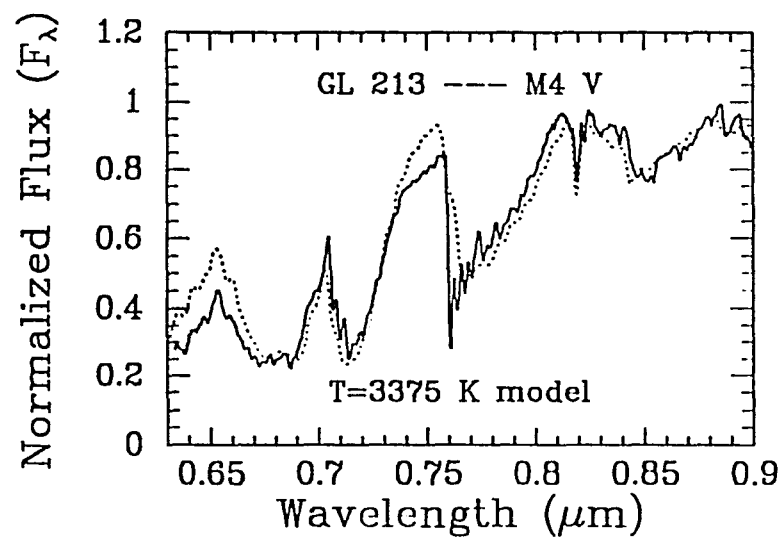
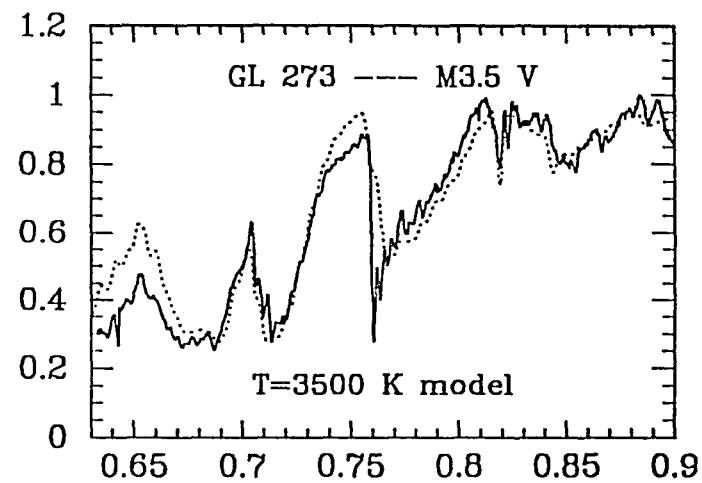
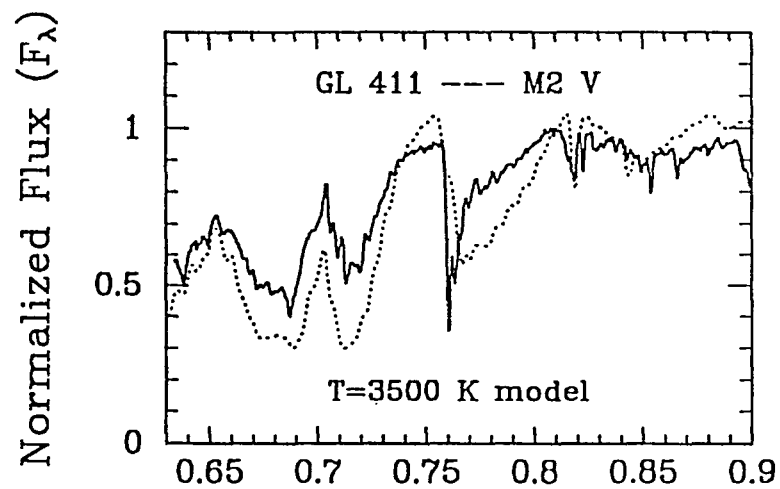
The spectra of Figure 3.1 can be compared to the theoretical models of Allard (1990). (Additional discussion of Allard's models can be found in Leinert et al. 1990.) Her models cover a grid of metallicities ($\log (M/H)/(M/H)_\odot = 0, -1, -2, -3, -4$), surface gravities ($\log g = 4, 5, 6$), and temperatures (3500, 3250, 3000, 2750, 2500, 2250, 2000 K). Surface gravities for some of the stars in this paper can be determined using radii derived in Lacy (1977) and masses derived from M_K values, and the M_K vs. mass relation, presented in Henry and McCarthy (1990). Independent determinations can be made using the radii and masses given in Caillault and Patterson (1990). The results, which are shown in Table 3.3, indicate that an integral value of $\log g = 5$ best describes the stars from type M2 to M6. (The surface gravities of GL 752 B and LHS 2924 are not known since masses have not been determined for either.) Therefore, only the models with $\log g = 5$ have been considered further. As for metallicity, the models with $[M/H] = -1$ have a very striking CaH absorption feature at $0.675 \mu\text{m}$, which is typical of extreme subdwarfs such as LHS 515 and LHS 2045 (Kirkpatrick 1992). Since none of the spectra presented here show this strong feature, only the models with $[M/H] = 0$ were used.

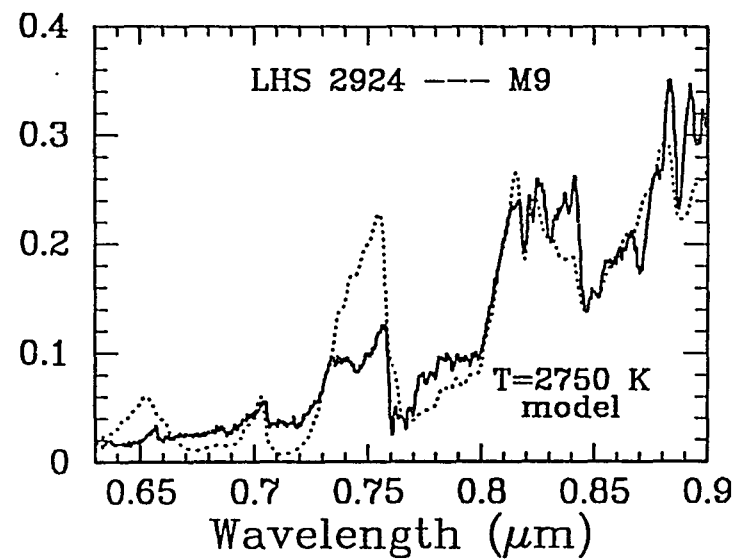
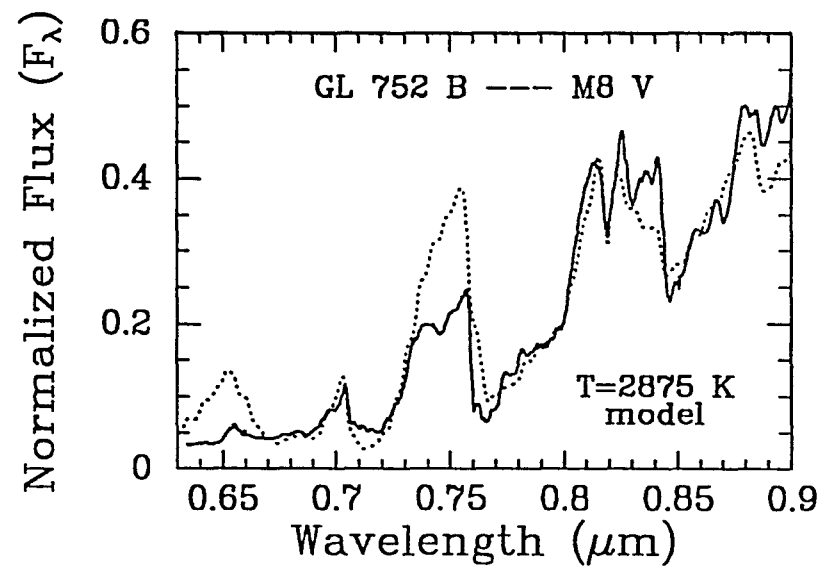
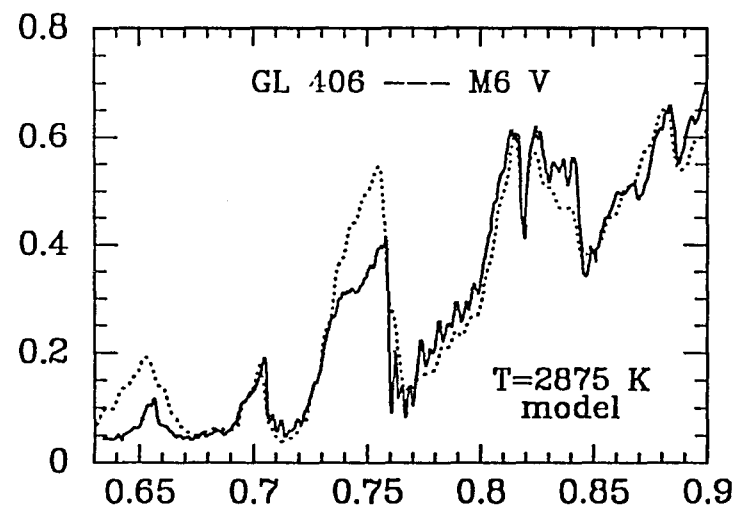
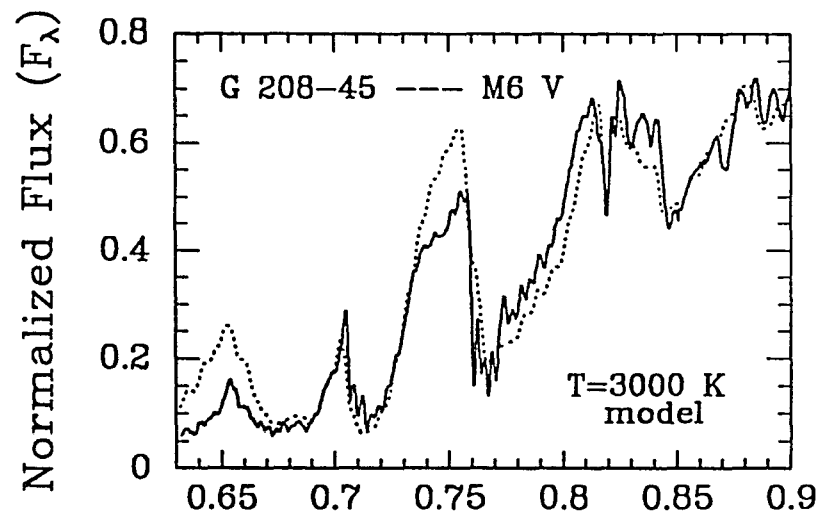
3.5.1 Fits in the Red Region

As with the observational data, each model spectrum was normalized to unity at its peak flux, in units of F_λ . By applying the least-squares minimization technique (see Section 3.3) on only the red portion (0.70 - 0.90 μm), each observed spectrum was compared to each of the model spectra, and the best match in temperature was found. In order to make a finer grid in temperature, a linear interpolation between Allard's spectra was used to produce models with $T = 3375, 3125, 2875, 2625, 2375$, and 2125 K, giving us a resolution of 125 K.

Figure 3.3 shows each of the red spectra overplotted with the model spectrum that provided the best match. In the case of GL 411, a model warmer than the one at 3500 K would clearly have provided a better match. Generally, the Na I feature at 0.82 μm is fit well by the models, as is the slope of the spectrum between 0.77 and 0.81 μm and the relative opacity minimum from 0.69 to 0.72 μm that lies between consecutive TiO bands. The similar minimum between 0.64 and 0.67 μm is not fit well, nor is the one between 0.73 and 0.76 μm . For the later spectra ($\geq M6$), the models predict less flux at 0.90 μm than is indicated in the observational data, and the overall appearance of the model spectra is in worse agreement with the true spectra. The temperatures of these fits in the red are given in column (2) of Table 3.4.

Figure 3.3: The best fits to the red spectra. The observational data are shown by the solid lines, and the model data by the dotted lines. The method for determining the best match is explained in the text. The spectrum of GL 411 could be better fit by a warmer model, but the Allard models do not go hotter than 3500 K. The agreement is generally very good, although the flux near 0.65 and 0.75 μm is always overestimated. For cooler objects the disagreement between the true spectra and the predicted ones is much more pronounced.



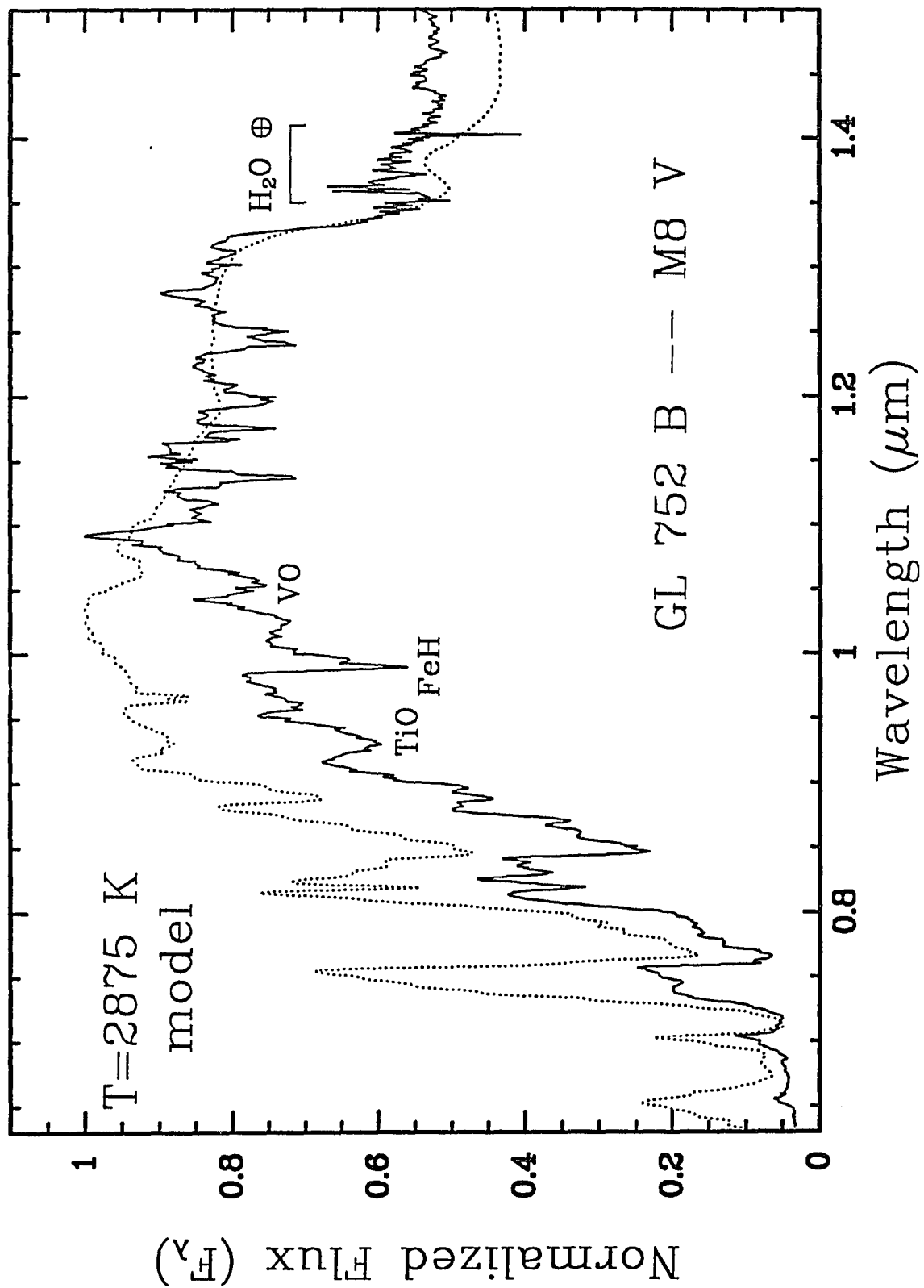


3.5.2 Fits in the Infrared Region

When the infrared portion of the spectrum is compared to the models, the discrepancy in the region around $1.00\ \mu\text{m}$ is immediately apparent (see Figure 3.4). A small part of this discrepancy arises because Allard (1990) does not include FeH at $0.99\ \mu\text{m}$ in her calculations. The models from Ruan (1991), which do include FeH, show substantial discrepancies in the $1.00\ \mu\text{m}$ region as well. For example, in both the Allard and Ruan models the VO absorption around $1.05\ \mu\text{m}$ is virtually absent. In general it appears that throughout this region there are important opacity sources not yet included in the models.

The general *shape* of the spectral "continuum," however, is traced out well from $\sim 1.08\ \mu\text{m}$ to the steam feature at $1.35\ \mu\text{m}$, even though the models do not include many of the sharp features such as the H₂O absorption at $1.14\ \mu\text{m}$ and OH absorption at $1.20\ \mu\text{m}$. To obtain a second set of temperature estimates, the least-square minimization technique was again applied, this time over 1.08 to $1.35\ \mu\text{m}$, to find the model providing the best match. Specifically, only the pseudo-continuum and the H₂O feature at $1.35\ \mu\text{m}$, both of which are temperature-dependent, were fit. Absorptions not reproduced in the models ($1.10 - 1.12\ \mu\text{m}$, $1.13 - 1.145\ \mu\text{m}$, $1.165 - 1.18\ \mu\text{m}$, $1.19 - 1.215\ \mu\text{m}$, and $1.235 - 1.28\ \mu\text{m}$) were excluded from the fit. For the latter half of the spectral sequence, at least as late as M8, the models give a fair match to both the

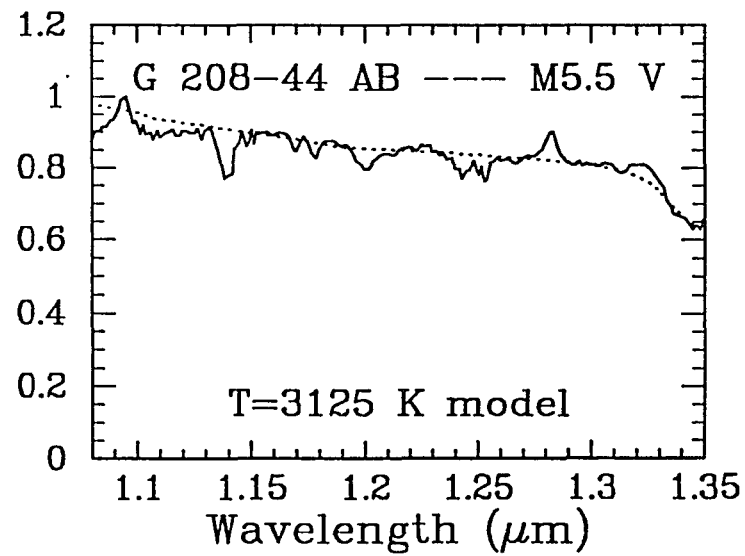
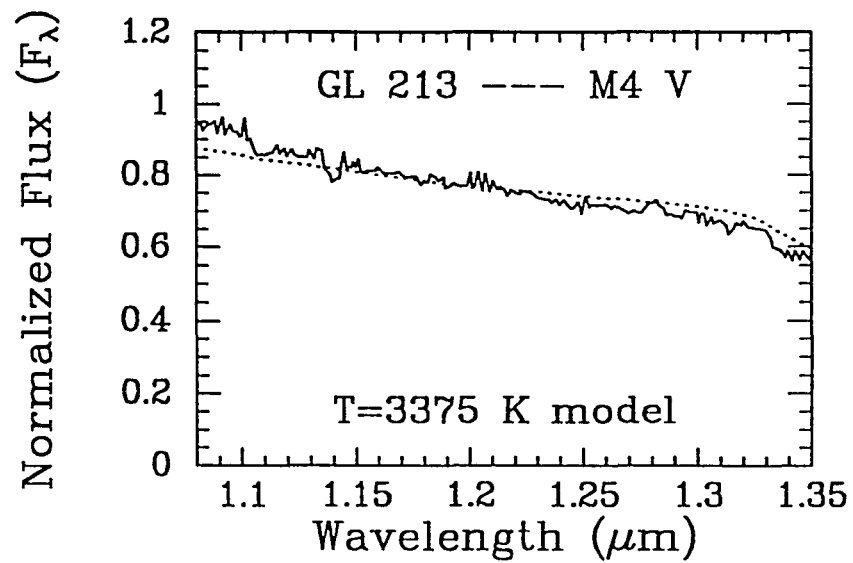
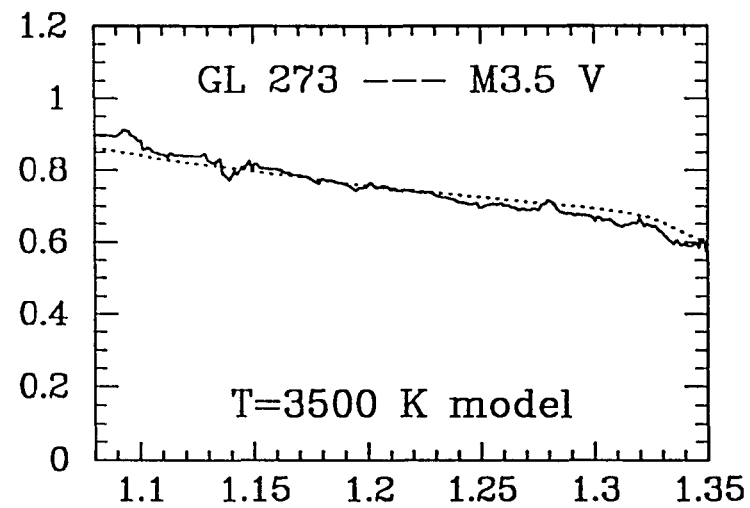
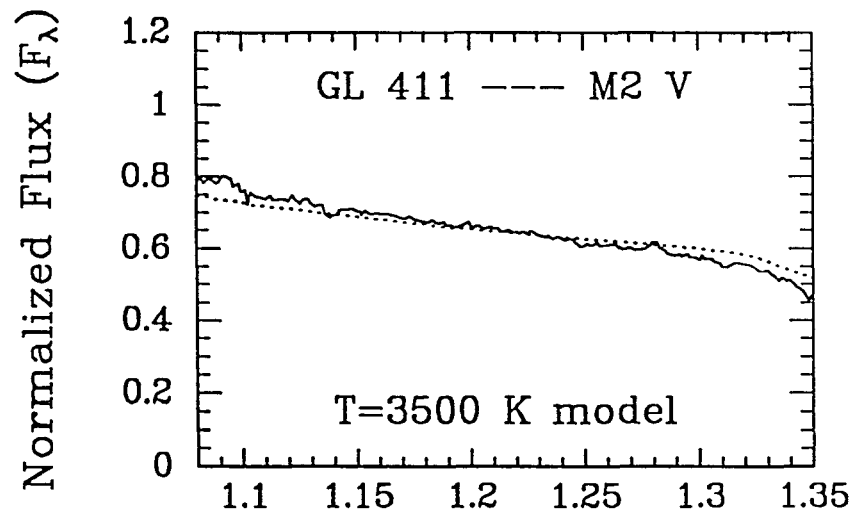
Figure 3.4: The spectrum of an M8 dwarf and the model that provides the best fit in the red. Unlike Figure 3.3, each spectrum here is normalized to unity at its peak flux. Note the failure of the model to predict the shape of the stellar "continuum" in the region from 0.9 - 1.1 μm . Notably absent from the models are FeH at 0.99 μm and VO at 1.3 μm . The strength of the TiO band at 0.93 μm is also underestimated. Coincidentally, the least-squares minimization technique finds the 1.08 - 1.35 μm fit plotted here to be the best, correctly normalized fit to the J region. This illustrates another point: although the fit at J looks adequate, the same model would have to be shifted downward in the 0.70 - 0.90 μm region to achieve a good fit. In other words, I - J colors for the observational and theoretical spectra do not agree. See text for more details.

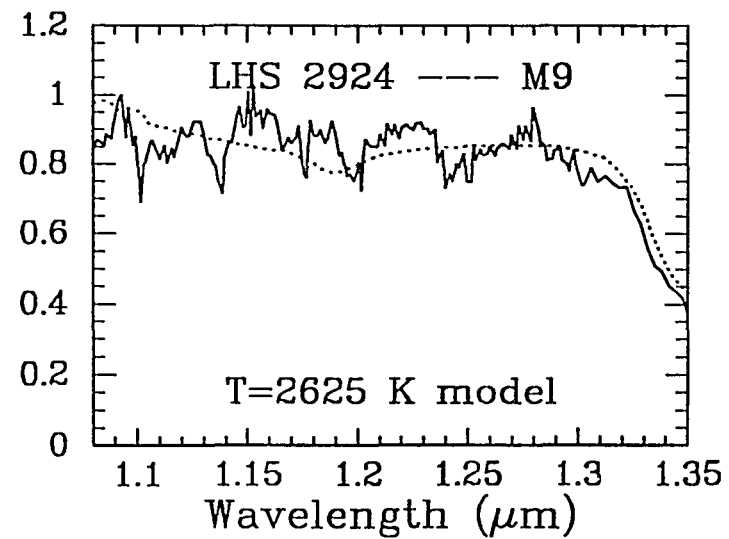
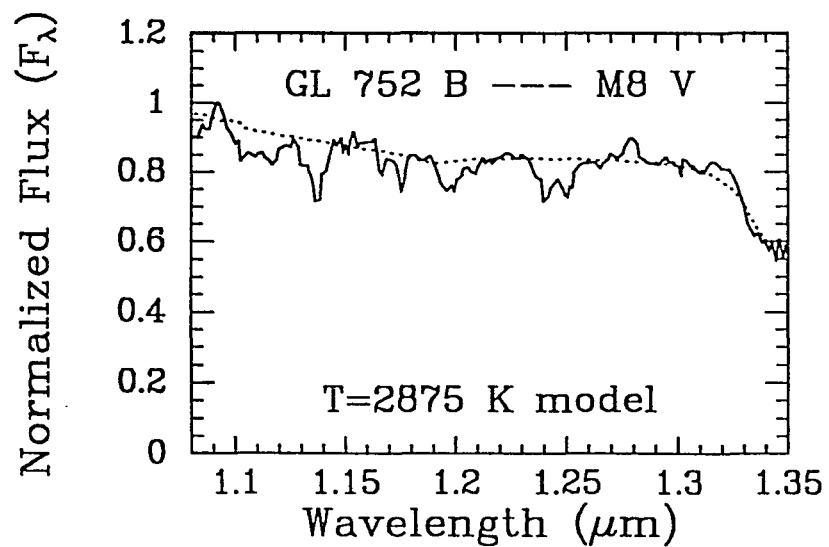
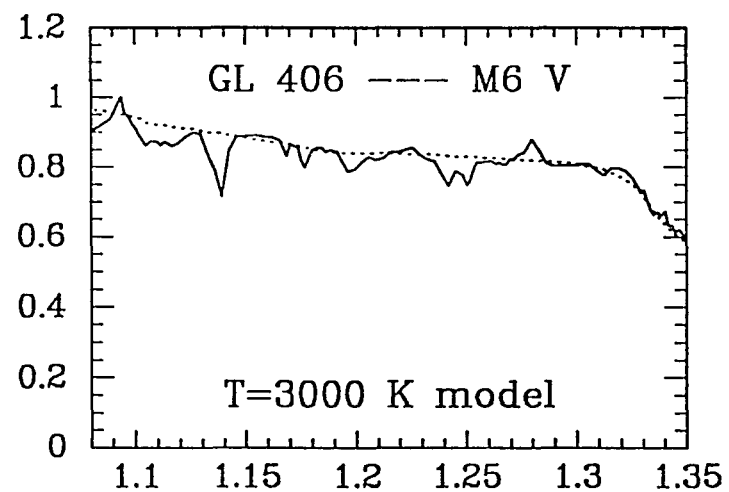
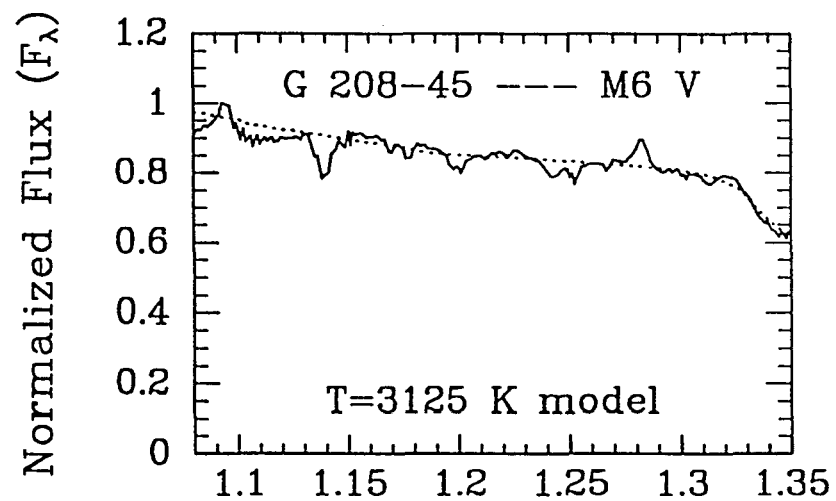


"continuum" and the $1.35\ \mu\text{m}$ steam feature. The best fits are illustrated in Figure 3.5, and the resulting temperatures are listed in column (3) of Table 3.4. This comparison of the infrared spectra with theoretical models suggests, even for the coolest stars, a modelled continuum which is approximately correct but which has a number of missing absorption species.

As demonstrated in Figure 3.4 (see Section 3.5.3), fits that simultaneously match the red and infrared data give poor results. Nonetheless, when taken *singly*, the red and infrared portions of the models provide, in many cases, reasonably good fits to the data. Specifically, good fits are obtained in the red region for stars earlier than about M6. However, the density of features in the spectra of cooler objects makes a continuum in the red difficult to identify, and the models are generally poor fits to the data. These later objects, on the other hand, are fit well by the infrared portions of the theoretical models, but these same models cannot be fit reliably to stars earlier than M6 because of the lack of strong temperature-sensitive features in the infrared. Therefore, the combination of red and infrared spectra promises to provide improved accuracy in relating the stars to a sequence of models of differing temperatures.

Figure 3.5: The best fits to the infrared spectra. The observational data are shown by the solid lines, and the model data by the dotted lines. The method for determining the best match is explained in the text. As in Figure 3.3, the spectrum of GL 411 could be better fit by a warmer model. In general, the steam feature at $1.35\ \mu\text{m}$ and the pseudo-continuum are fit well.





3.5.3 Synthetic Photometry

Figure 3.4 is plotted so that the best fit to the data in the 1.08 to $1.35\ \mu\text{m}$ region is shown. Notice that the red portion (0.70 to $0.90\ \mu\text{m}$) of the model should be shifted downward to achieve a better match. Although the least-squares minimization technique found that the same model yielded the best fits in both the red and infrared portions of the spectrum, the normalization of the model in each region was different. This shift cannot be accounted for on observational grounds because, as discussed in Section 3.3, the combined red/infrared spectra successfully reproduce the observational I - J colors. Clearly, the I - J color of the model and that of the true data are in disagreement. To explore this effect further, synthetic IJHK photometry was obtained from the best-fit models and was compared to observed colors. These values are listed in Table 3.5. The J - H and J - K colors were derived using central wavelengths and zero-magnitude fluxes of $1.64\ \mu\text{m}$ and $1030\ \text{Jy}$ for H_{AAO} , and $2.19\ \mu\text{m}$ and $650\ \text{Jy}$ for K_{AAO} (Allen & Cragg 1983). For each of the observed spectra, synthetic colors were derived from the model that fit best in the red for spectral types $< \text{M6}$ and from the model that fit best in the infrared for spectral types $\geq \text{M6}$.

For early M dwarfs, the disagreement between the observed and modelled I - J is around $0.05\ \text{mag}$, which is within the uncertainty noted before. However, for later

types, the disparity becomes increasingly large; for LHS 2924, the difference between the true $I - J$ and that of the model is 0.86 mag! Part of this discrepancy arises because the modelled I flux is too large due to an under-estimation in the opacity around $0.74 \mu\text{m}$. The true $J - H$ and $J - K$ colors increase for later spectral types, whereas the $J - H$ and $J - K$ colors from the models *decrease* for later spectral types. Despite this backward trend, the $J - H$ color of the models is still in general only ~ 0.1 mag different from the true color. For the early M dwarfs, the same difference is seen in the $J - K$ colors, but for later types the discrepancy is ~ 0.4 mag.

Allard (1990) derives her own synthetic photometry of the models and notes the same effect presented above, i.e., that $J - H$ and $J - K$ get bluer for the cooler models. This effect can be attributed to gross incompleteness in the opacities, or specifically to the strong influence of water blanketing in the models. Nonetheless, these models are certainly closer to the actual spectra of M dwarfs than are blackbodies and should be used in preference to blackbody curves. The colors of these objects are distinctly unlike those of a blackbody and are likewise not well predicted by the models, especially beyond M5. The best match to the true data is, therefore, achieved by fitting theoretical models to observed *spectra*.

3.5.4 Comparison to Ruan's Models

Ruan (1991) overplots her model spectra with those of Allard (1990). From 0.70 to 0.90 μm , these two sets of $\log g = 5$, $[\text{M}/\text{H}] = 0$ models are virtually identical, convincing us that a temperature scale derived from Ruan's models would give us the same results as Allard's for stars earlier than M6. Ruan's overplots in the infrared show nearly identical H_2O strengths and continuum slopes as well, reassuring us that the same temperature scale would also have been derived for objects of type M6 and later. The major difference between the Ruan and Allard models is the inclusion of 0.99 μm FeH in the Ruan set. A temperature sequence could be derived, potentially, based on this feature alone, as the Ruan models show its strengthening with later type in accordance with observations. Unfortunately, these models do not include either of the obvious absorption species just redward and just blueward of the FeH band, making an accurate fit to the feature impossible. Like Allard, Ruan also notes a blueward trend of $J - H$ and $J - K$ in the models, i.e., that these colors become bluer for later spectral types. Based on this information, we are confident that a temperature scale derived from Ruan (1991) would not differ from that presented here.

3.6 Temperature Scale

As discussed in Section 3.5.2, an accurate temperature sequence can be established for all M dwarfs by using temperatures from red fits for stars earlier than M6 and temperatures from infrared fits for objects of later spectral type. As Table 3.4 demonstrates, the temperatures of the best-fit models in the red and the best-fit models in the infrared are never different by more than 125 K. For objects earlier than type M6, the red and infrared fits assign identical temperatures. In fact, for five of the eight spectra, the same model provided the best fit in both regions. In light of such agreement, we are confident in adopting the temperature determined by the part of the spectrum giving the better fit. These assigned temperatures are listed in column (2) of Table 3.6, where the objects are presented in order of increasing M_V . Based on the agreement of the red and infrared fits to the data, we assign an uncertainty in our temperatures of ± 125 K.

The luminosities of these objects can be determined from their parallaxes and from photometry. The parallaxes are listed in column (3) of Table 3.6 and were used to calculate the absolute magnitudes M_V , M_I , and M_J in columns (4) - (6). A linear interpolation of Bessell's (1991) M_I vs. BC_I relationship gave the values of BC_I (column 7) used to determine the bolometric magnitude in column (8). Notice

that these assigned temperatures decrease monotonically with increasing M_V , M_I , M_J , and M_{bol} . Finally, luminosities were determined (column 9) assuming that the Sun has $M_{bol} = 4.75$.

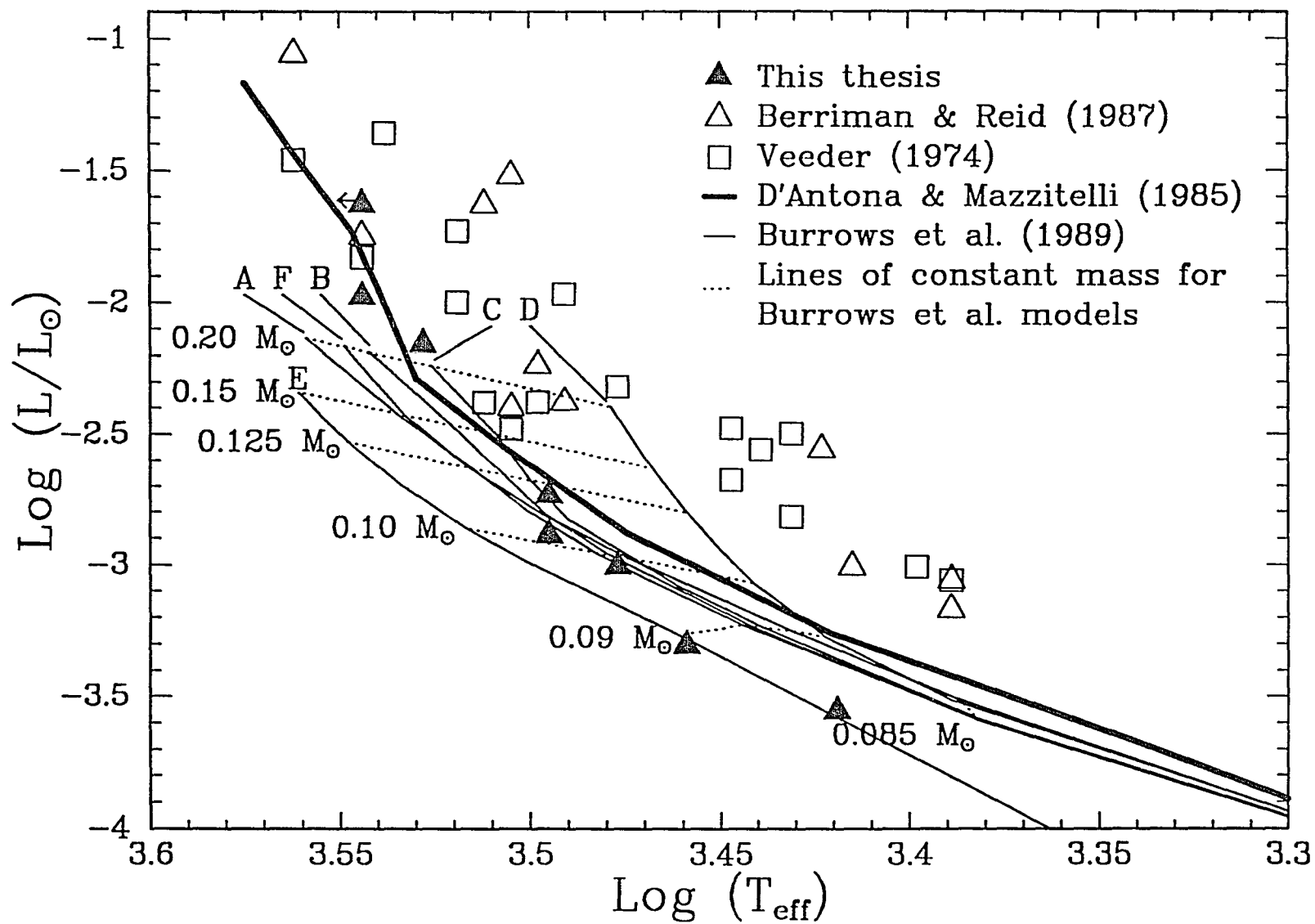
As a test of the accuracy of the bolometric corrections, we compared for GL 752 B the flux determined by integration of the 0.6 - 1.5 μm spectrum with the flux determined by trapezoidal integration under the broadband magnitudes. In spite of the strengths of the absorption features in the spectrum, the two techniques agreed to within roughly 5%. For earlier spectral types, the agreement should be much better. Compared to typical uncertainties in distances, the bolometric corrections given by Bessell seem to be fairly reliable. For later spectral types, however, it is clearly preferable to determine the bolometric flux from spectra rather than from broadband photometry.

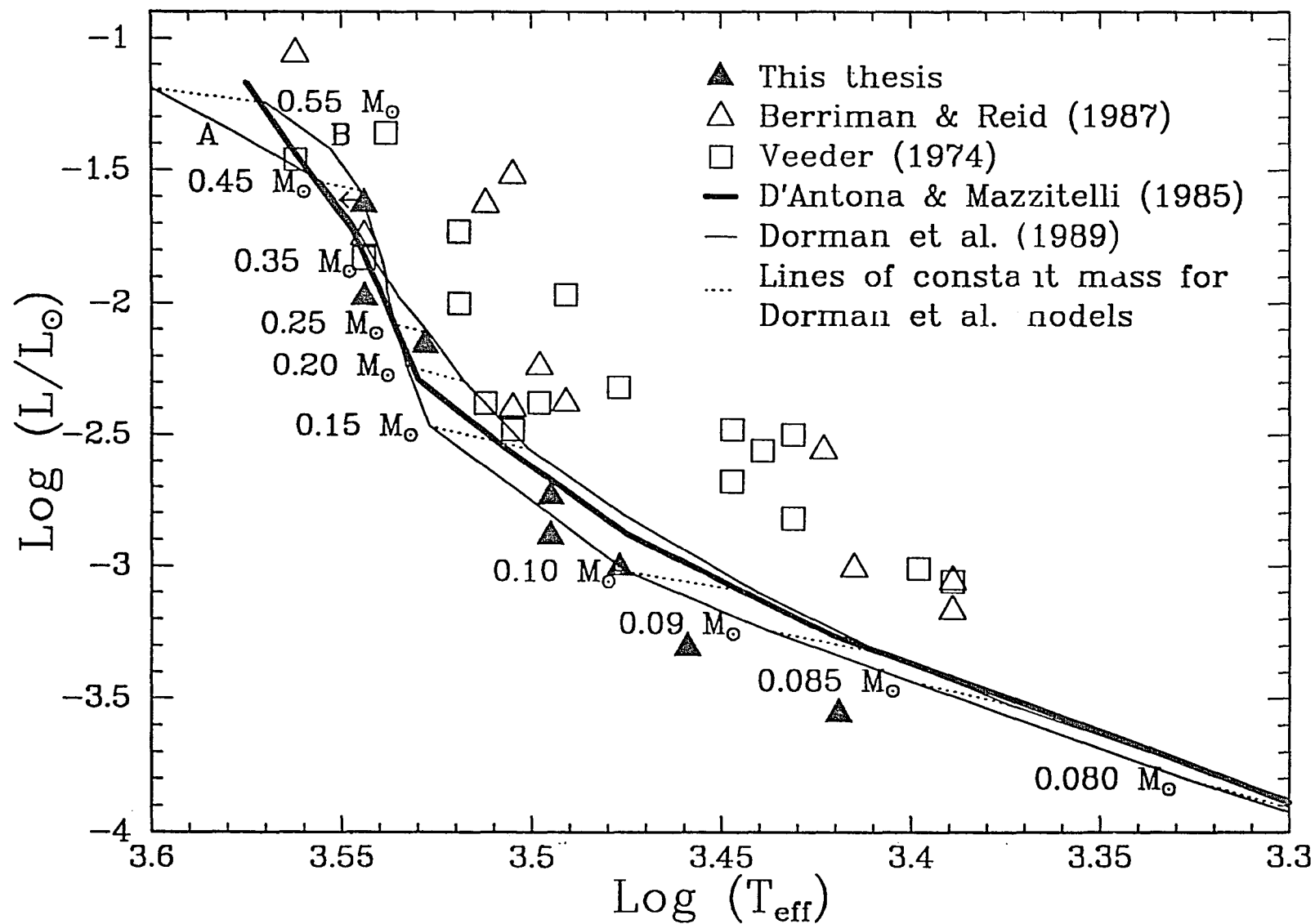
Also listed in Table 3.6 are the temperature sequences assigned by BR and by Veeder (1974). To assure a set of data on a standard system, the luminosities of their stars and ours were calculated using parallaxes, photometry, and bolometric corrections from the same sources. Neither the BR or Veeder sequences exhibit the monotonic behavior that ours does, but perhaps this is not too surprising considering the number of data points present in those two sequences, the errors inherent in assigning temperatures from photometric data, and the uncertainties in the parallax. The temperatures assigned by Veeder are determined by fitting a

blackbody (by eye) to the observed broad-band colors of each star. Short wavelengths are assumed to have a certain amount of blocking, but the total flux under the blackbody curve and the total flux observed from the star are required to be equal. BR assumed that no significant backwarming or blanketing occurs at $2.2\ \mu\text{m}$. The temperature for each star was determined from the blackbody curve having (1) flux equal to the observed flux at $2.2\ \mu\text{m}$ and (2) the same total flux observed from the star. BR quote an uncertainty in their temperatures (which do not differ significantly from the revised temperatures presented in Berriman, Reid, & Leggett (1992)) of $\pm 110\ \text{K}$, whereas Veeder (1974) quotes one of $\pm 150\ \text{K}$.

The temperatures and luminosities from all three sequences are presented in the H-R diagrams of Figure 3.6.1 and 3.6.2. The temperatures assigned in this paper are generally warmer at a given absolute magnitude than the temperatures assigned by either BR or Veeder, particularly for the lowest-luminosity objects. For $\log(L/L_{\odot}) \leq -3.0$, the difference between our temperatures and those of the other authors is $\sim 500\ \text{K}$. This is not surprising since the models show strong pressure and temperature dependences as well as radiative transfer effects. Figure 3.6.1 shows theoretical tracks of the lower main sequence by D'Antona & Mazzitelli (1985, hereafter DM) and by Burrows, Hubbard, & Lunine (1989, hereafter BHL). The DM curve is for the zero-age main

Figures 3.6.1 and 3.6.2: The H-R diagram for M dwarfs. Data from this paper are represented by filled triangles, data from Berriman & Reid (1987) by open triangles, and data from Veeder (1974) by open squares. (The data point for GL 411 is indicated with an arrow since our derived temperature is a lower limit.) (3.6.1) - The theoretical main sequence of D'Antona & Mazzitelli (1985 - heavy line) and the 10 Gyr tracks of models A,B,C,D,E, and F from Burrows, Hubbard, & Lunine (1989 - lighter lines) overplotted with the three temperature sequences. Lines of constant mass (dashes) are indicated on the Burrows et al. models. (3.6.2) - The theoretical main sequence tracks A and B of Dorman, Nelson, & Chau (1989 - lighter lines), with the track of D'Antona & Mazzitelli (1985 - heavy line) and the three temperature sequences shown again for comparison. Lines of constant mass (dashes) are also indicated on the Dorman et al. models. As both figures show, the temperature sequence presented here brings the observed M dwarf track into close agreement with theoretical tracks. Note that the Burrows et al. and the Dorman et al. models (and also the Burrows et al. models for an age of 1 Gyr) predict all of the objects presented here to lie within the locus of hydrogen-burning stars ($M \geq 0.08 M_{\odot}$).





sequence, and the BHL curves are for an age of 10 Gyr. (The BHL curves for an age of 1 Gyr are in very close agreement with those plotted here. Only at the low luminosity end do these tracks deviate noticeably from the 10 Gyr models. Specifically, these younger tracks bring the models closer to our plotted positions of GL 752 B and LHS 2924.) Figure 3.6.2 shows the theoretical tracks of Dorman, Nelson, & Chau (1989, hereafter DNC), with the DM curve plotted again for comparison. The DNC models are also calculated for the zero-age main sequence. Using our temperature scale, the positions of M dwarfs on the H-R Diagram fall closer than previous determinations to theoretical tracks of the lower main sequence.

3.7 Discussion

This first attempt to fit a sequence of M dwarf spectra with model energy distributions demonstrates clearly that the general slope of the distributions and many of the features can be well reproduced by present-day models. As a result, it is possible to construct an improved temperature scale that is quite consistent with interior models. Shortcomings of the atmospheric models are, however, obvious. For example, the fluxes for wavelengths between major absorption bands are often too high, indicating that additional opacity sources are important but have not yet been included in the

calculations (in most cases, due to the lack of laboratory data). It should also be noted that the electronic f -values for many bands are of very low accuracy (cf. Bessell & Scholz 1990).

These problems show up in the spectra more strongly when the gradient of the Planck function is steep, i.e., the uncertainties are highest for the coolest models (as can be seen in the comparison of observed and calculated spectra in Figure 3.5). In a given model, the uncertainties are strongest for the short wavelength, or Wien, portion of the spectrum. This latter point implies that an analysis based on fluxes at wavelengths shorter than that of the maximum flux is rather unreliable (cf. the analogous discussion for limb-darkening by Scholz & Takeda 1987). Therefore, in this paper we draw our main conclusions from the energy distributions in the region of the peak flux.

The differences between the observed and the calculated colors are also largely due to problems with the opacities. In particular, colors using the I filter are much redder in the data than in the models because of high fluxes in the 0.74- μm region of the models. Synthetic photometry obtained from combined red and infrared data agrees to within 0.1 mag with the observed colors (see Section 3.3), so uncertainties in the filter functions and color equations appear to have little effect on the colors. Changing the width of the J bandpass by $\pm 10\%$ only alters the I - J colors of the 2750

K model by ~ 0.02 mag. Since these differences are small compared to the differences noted between observed and theoretical photometry, it must be concluded that the biggest factor contributing to the color discrepancy is the absence or uncertain modelling of opacity sources in the models.

3.8 Summary

This chapter includes the first set of $0.6 - 1.5 \mu\text{m}$ spectra for a full sequence of M dwarfs. Strong, temperature-sensitive absorptions by H_2O , TiO , VO , OH , K I , and FeH are present. The observed spectra show many more features than are currently included in the models. Identifications have been made of the strongest of these missing absorption species, and follow-up observations are planned at higher resolution.

Using these spectra, a new temperature sequence has been determined for M dwarfs. Allard's (1990) models have been used for the temperature fits and yield the same results as Ruan's (1991) models. Dwarfs of type M6 and later have a significant steam feature at $1.35 \mu\text{m}$ that increases with later spectral type, and the shape of the infrared "continuum" is also temperature-dependent. As a result, temperatures were determined for these later dwarfs by fitting models to the infrared data. Temperatures for dwarfs earlier than type M6 were determined by fitting models to the

data in the region around the I bandpass.

The colors deduced from the models are in sharp contrast with observed colors determined from broad-band photometry. The models predict consistently bluer I - J colors than are observed. Also, the J - H and J - K colors from the models get bluer with later spectral type, in direct contrast to the observed trend. These trends illustrate that it is difficult to assign temperatures to M dwarfs based on colors. The preferred method is to fit models to temperature-sensitive features in the spectra.

The temperatures assigned here are warmer than those of Veeder (1974) and Berriman & Reid (1987), particularly at the lowest luminosities. When plotted on an H-R Diagram, our sequence is in better agreement with theoretical tracks of the lower main sequence.

TABLE 3.1
LOG OF M DWARF OBSERVATIONS

Gliese No.	Other Name	Spectral Type	Far Red			Infrared		
			Spectral Range (μ m)	Date Obs. (UT)	Int. (sec)	Spectral Range (μ m)	Date Obs. (UT)	Int. ^a (sec)
411	HD 95735	M2 V	0.63-0.92	1990 Jan 22	9	0.90-1.50	1990 Jun 12	238
273	BD +5° 1668	M3.5 V	0.63-0.92	1990 Jan 22	120	0.90-1.60	1990 Nov 06	904
213	Ross 47	M4 V	0.63-0.92	1990 Jan 22	130	0.90-1.60	1990 Nov 05	2515
—	G 208-44 AB	M5.5 V	0.63-0.92	1989 Jul 13	75	0.85-1.60	1989 Sept 20	1860
—	G 208-45	M6 V	0.63-0.92	1989 Jul 13	225	0.85-1.60	1989 Sept 20	1800
406	Wolf 359	M6 V	0.63-0.92	1990 Jan 20	80	0.85-1.51	1990 Apr 11	1135
752 B	VB 10	M8 V	0.63-0.92	1989 Jul 10	1800	0.85-1.55	1989 Sept 17/20	2700
—	LHS 2924	M9	0.63-0.92	1989 Jul 13	1980	1.00-1.35	1990 Apr 14	2190

a=Total integration time for all of the spectral segments

TABLE 3.2
COMPARISON OF I-J VALUES

Name	LH ^a	(I-J) BR ^b	us ^c	$\Delta I_{KC} - J_{\Lambda\Lambda O}$	
				LH-BR	LH-us
GL 411	1.13	1.23	1.04	-0.10	+0.09
GL 273	1.40	—	1.32	—	+0.08
GL 213	1.47	—	1.39	—	+0.08
G 208-44 AB ^d	—	—	2.11	—	—
G 208-45 ^e	—	—	2.04	—	—
GL 406	2.31	2.27	2.24	+0.04	+0.07
GL 752 B	2.74	—	2.65	—	+0.09
LHS 2924 ^f	3.38	—	—	—	—

^a Data from Leggett & Hawkins 1988

^b Data from Berriman & Reid 1987

^c Data from this paper

^d ($I_{KC} - J_{Steward}$) = 2.19 from McCarthy et al. 1988.

^e ($I_{KC} - J_{Steward}$) = 2.15 from McCarthy et al. 1988.

^f Because there is no overlap between the far red and the infrared data, Leggett & Hawkins 1988 photometry was used to scale the two spectral pieces. Thus, no independent measurement of I-J was possible.

TABLE 3.3

SURFACE GRAVITIES

Name	log g	
	(1) ^a	(2) ^b
GL 411	4.59	—
GL 273	4.71	5.00
GL 213	—	5.11
GL 406	5.08	5.49

^a Based on data from Lacy 1977 and Henry and McCarthy 1990

^b Based on data from Caillault & Patterson 1990

TABLE 3.4

TEMPERATURES DERIVED FROM THE BEST FIT TO
ALLARD'S MODEL SPECTRA WITH $[M/H]=0$, $\log g=5$

Name	Far-red Portion (0.70 - 0.90 μm)	IR Portion (1.08 - 1.35 μm)
GL 411	>3500 K	>3500 K
GL 273	3500 K	3500 K
GL 213	3375 K	3375 K
G 208-44 AB	3125 K	3125 K
G 208-45	3000 K	3125 K
GL 406	2875 K	3000 K
GL 752 B	2875 K	2875 K
LHS 2924	2750 K	2625 K

TABLE 3.5
OBSERVED VS. SYNTHETIC COLORS^a

Name	Observed Colors			Colors from Best-fit Model		
	I-J	J-H	J-K	I-J	J-H	J-K
GL411 ^b	1.13	0.54	0.75	—	—	—
GL 273	1.40	0.52	0.77	1.35	0.63	0.84
GL 213	1.47	0.53	0.78	1.42	0.62	0.84
G 208-44 AB ^c	2.19	0.52	0.89	1.64	0.59	0.82
G 208-45 ^c	2.15	0.50	0.89	1.64	0.59	0.82
GL 406	2.31	0.62	0.98	1.78	0.56	0.80
GL 752 B	2.74	0.67	1.11	1.99	0.54	0.78
LHS 2924	3.38	0.65	1.12	2.52	0.48	0.72

^a Photometry is I_{KC} , J_{MO} , H_{MO} , and K_{MO} from Leggett & Hawkins 1988, unless otherwise noted

^b None of the models is warm enough to fit this spectrum adequately

^c Observed colors are from McCarthy et al. 1988 and are not on a standard system

TABLE 3.6
COMPARISON OF TEMPERATURE SEQUENCES

Name	T(K)	$\pi(^{\circ})^a$	M_c^a	M_i^b	M_j^b	BC_i^c	M_{bol}	$\log(L/L_0)^d$
This paper								
GL 411	>3500	0.397	10.49	8.32	7.10	0.50	8.82	-1.63
GL 273	3500	0.270	11.98	9.33	7.83	0.36	9.69	-1.98
GL 213	3375	0.168	12.73	9.86	8.30	0.30	10.16	-2.16
G 208-44 AB	3125	0.211	15.03	11.59*	9.40*	0.00	11.59	-2.74
G 208-45	3125	0.211	15.61	12.10*	9.95*	-0.12	11.98	-2.89
GL 406	3000	0.426	16.68	12.63	10.21	-0.36	12.27	-3.01
GL 752 B	2875	0.173	18.57	13.98	11.11	-0.95	13.03	-3.31
LHS 2924	2625	0.0908 ^f	19.37 ^g	15.09	11.57	-1.45	13.64	-3.56
Beiraman & Reid (1987) ^h								
GL 884	3650	0.130	8.46	6.79	5.80	0.61	7.40	-1.06
GL 752 A	3200	0.173	10.31	7.99	6.69	0.55	8.54	-1.52
GL 411	3250	0.397	10.49	8.32	7.10	0.50	8.82	-1.63
GL 821	3500	0.093	10.5	8.67	7.50	0.45	9.12	-1.75
GL 643	3150	0.161	12.73	10.09	8.60	0.26	10.35	-2.24
GL 699	3100	0.552	13.25	10.50	9.04	0.19	10.69	-2.38
GL 447	3200	0.301	13.50	10.57	8.91	0.18	10.75	-2.40
GL 866 AB	2650	0.305	14.60	11.06	8.94	0.09	11.15	-2.56
GL 406	2600	0.426	16.68	12.62	10.21	-0.35	12.27	-3.01
GJ 1111	2450	0.278	17.03	12.86	10.46	-0.45	12.41	-3.06
GL 644 C	2450	0.161	17.69	13.32	10.80	-0.65	12.67	-3.17

TABLE 3.6, CONT.

Name	T(K)	$\pi(^{\circ})^a$	M_v^a	M_1^b	M_2^b	BC_1^c	M_{bol}	$\log(L/L_{\odot})^d$
Verder (1974)								
GL 278 C	3750	0.069	8.26	—	5.16	—	—	—
GL 820 B	3900	0.296	8.39	—	5.85	—	—	—
GL 717	4000	0.054	.4	—	—	—	—	—
GL 205	3600	0.170	9.17	—	—	—	—	—
GL 239	3650	0.104	9.71	7.85	6.71	0.56	8.41	-1.46
GL 48	3400	0.114	10.34	—	—	—	—	—
GL 644 AB	3450	0.161	10.80	7.59	6.31	0.56	8.15	-1.36
GL 661 A	3450	0.155	10.91	—	—	—	—	—
GL 725 A	3450	0.282	11.15	—	7.45	—	—	—
GL 745 A	3500	0.119	11.15	8.92	7.69	0.41	9.33	-1.83
GL 669 A	3300	0.095	11.25	8.63	7.18	0.45	9.08	-1.73
GL 829	3300	0.153	11.27	8.63	7.23	0.45	9.08	-1.73
GL 860 A	3350	0.253	11.87	—	—	—	—	—
GL 725 B	3300	0.282	11.94	9.37	7.97	0.38	9.75	-2.00
GL 285	3100	0.165	12.29	9.30	7.69	0.37	9.67	-1.97
GL 669 B	3100	0.095	12.81	—	—	—	—	—
GL 234 A	3050	0.252	13.08	—	—	—	—	—
GL 699	3250	0.552	13.25	10.50	9.04	0.19	10.69	-2.38
GL 15 B	3150	0.282	13.29	10.51	9.01	0.19	10.70	-2.38
GL 729	3000	0.345	13.3	10.34	8.89	0.22	10.56	-2.32
GL 299	3200	0.151	13.66	10.83	9.27	0.13	10.96	-2.48
GL 51	2950	0.107	13.81	—	—	—	—	—
GL 69-47	2700	0.079	14.30	10.86	8.97	0.13	10.99	-2.50
GL 866 AB	2750	0.305	14.60	11.06	8.94	0.09	11.15	-2.56
GL 905	2800	0.318	14.80	11.41	9.39	0.03	11.44	-2.68
GL 473 AB	2800	0.231	15.09	10.80	8.79	0.14	10.94	-2.48

Name	T(K)	$\pi(^{\circ})^a$	M_v^a	M_1^b	M_2^b	BC_1^c	M_{bol}	$\log(L/L_{\odot})^d$
Veeder (1974), cont.								
GL 65 A	2700	0.367	15.27	—	—	—	—	—
G 158-27	2700	0.214	15.39	11.84	9.96	-0.05	11.79	-2.82
GL 551	2700	0.761	15.45	—	—	—	—	—
GL 406	2500	0.426	16.68	12.63	10.21	-0.36	12.27	-3.01
G 51-15	2450	0.278	17.03	12.86	10.46	-0.45	12.41	-3.06

^a from Gliese 1969 or Gliese & Jahreiss 1979 unless otherwise noted

^b calculated using I_{Kc} and J_{CT10} values from Leggett & Hawkins 1988 unless otherwise noted

^c linearly interpolated from BC_1 vs. M_1 relation in Table 2 of Bessell 1991

^d assuming $(M_{bol})_{\odot} = 4.75$

^e on the Steward system of McCarthy et al. 1988

^f from Dahn, Probst, & Liebert (unpublished)

^g from Monet et al. 1992

^h temperatures do not differ significantly from the revised values presented in Berriman, Reid, and Leggett 1992

Chapter 4

Near-Infrared Spectroscopy of Young Stellar Objects

We present spectra between 0.9 and 1.35 μm for seven young stellar objects: MWC 349, LkH α 101, R Mon, V645 Cyg, GL 490, T Tau, and HH 1. The spectra are rich in emission lines, mostly from the Paschen series of hydrogen and from forbidden and permitted transitions of Fe⁺. We find evidence for many different emission regions. Several objects have bipolar outflows and possibly also circumstellar disks. Others have optically thick regions in which the O I emission is excited by UV and Ly β fluorescence. We discuss the physical implications of the observed lines and the role spectroscopy between 0.9 and 1.35 μm can play in future investigations of the evolution of young stars.

4.1 Introduction

The early phases of stellar evolution present a challenge for observational astronomy. Most stars form in large molecular clouds, where obscuration by dust makes visible observations difficult or impossible. As these young

stars evolve, they exchange mass, energy, and momentum with the circumstellar environment. These interactions are vitally important both to the appearance and to the evolution of the stars.

With the development of large infrared arrays, there has been a growing emphasis on mapping star formation regions in the near-infrared (e.g. Eiroa & Casali 1989; Lada et al. 1991a; Lada et al. 1991b). These searches show that most of the stars in giant molecular clouds are deeply embedded in the clouds, hidden from view in visible light. A number of the less embedded sources have been observed spectroscopically in the visible and red parts of the spectrum. In this chapter, we examine seven of these objects in the 0.9 - 1.35 μm region.

Features in the visible and red spectra of young stellar objects have been used to determine densities, temperatures, abundances, and reddening. In addition, they provide evidence for outflows, ionized winds, disks, and fluorescent emission. In the following sections, we show that much of the same information is available in the 0.9 - 1.35 μm spectra of young stellar objects. Similar information is not expected in the 2 μm region, where there are few bright atomic lines. The 0.9 - 1.35 μm region is therefore the best option for observing more heavily embedded sources. In this chapter, we present and discuss the 0.9 - 1.35 μm spectra of seven young stellar objects, all with $A_v \leq 14$.

4.2 Observations and Data Reduction

Near-infrared spectra were measured for seven young stellar objects using the GeSpec on the Steward Observatory 2.3 m telescope. The aperture size was 6", and observations were made with both the 150 l/mm and the 600 l/mm gratings. F and G dwarf stars were used for flatfielding and flux calibration. A summary of the infrared observations is given in Table 4.1.

The basic data reduction routine is discussed in Section 1.3. The wavelength coverage at a given grating tilt is 0.10 μm in the low and 0.022 μm in the high resolution mode. To facilitate piecing together the spectra, grating settings were selected to provide some overlap between adjacent spectral pieces. Neighboring pieces differed from each other by only a few percent in their absolute flux levels. The spectral pieces of HH 1 were not renormalized before piecing them together because there was insufficient signal-to-noise to determine the continuum level accurately. Fluxes of all objects were compared with photometry from the literature (see Table 4.1 for references), and corrections were applied when necessary.

We also measured visible spectra for five of the seven objects (see Table 4.2). These observations were made at the Steward Observatory 2.3 m telescope using a Boller and Chivens spectrometer with an 800x800 Texas Instruments CCD

array. The slit width was set at $2''.5$, and the position angle was aligned with the direction of atmospheric refraction. The observations were made in non-photometric conditions. The spectra were renormalized by comparison with photometry in the literature. For two of the objects, MWC 349 and LkH α 101, the visible and the infrared photometry both come from the same set of observations. The same is not true for the other objects, so caution is advised when comparing their infrared and visible line strengths.

The visible data were reduced using standard IRAF techniques, and both the visible and infrared line fluxes were determined using an IRAF line fitting routine. The visible data are presented in Figure 4.1. The infrared data are presented in Figures 4.2.1 - 4.2.7. Line identifications and fluxes are presented in Tables 4.3.1 - 4.3.4. More than one transition is listed per line when blends are present or when identifications are uncertain. We also present A_λ/A_v values derived from the extinction law of Cardelli, Clayton, & Mathis (1989) for $R_v = 3.1$. Many features remain unidentified in the visible and infrared spectra.

4.3 Analysis

Before analyzing line ratios and determining physical conditions in these objects, it is necessary to make corrections for interstellar and circumstellar reddening.

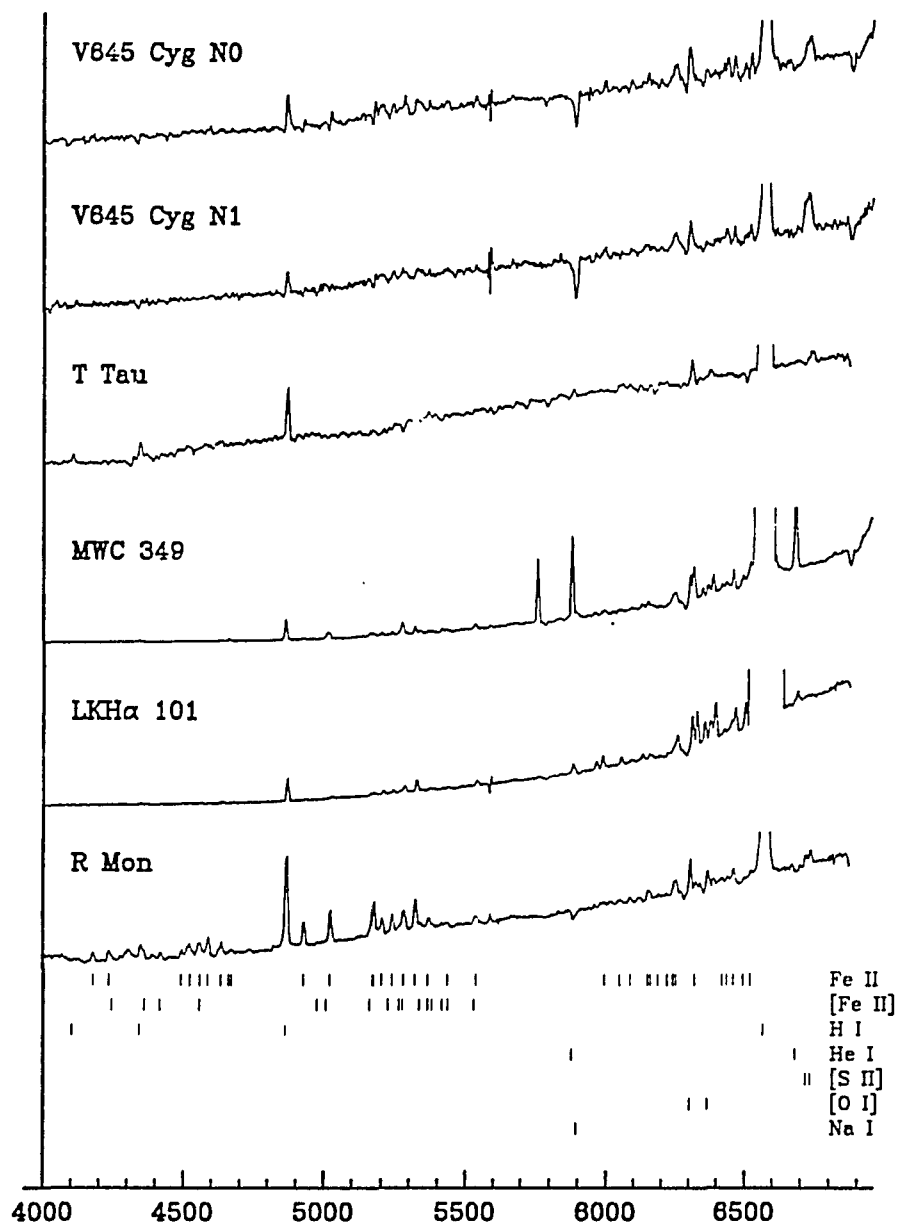


Figure 4.1: 0.40 - 0.69 μm spectra of V645 Cyg, T Tau, MWC 349, LkH α 101, and R Mon. Tickmarks show the positions of the most prominent features.

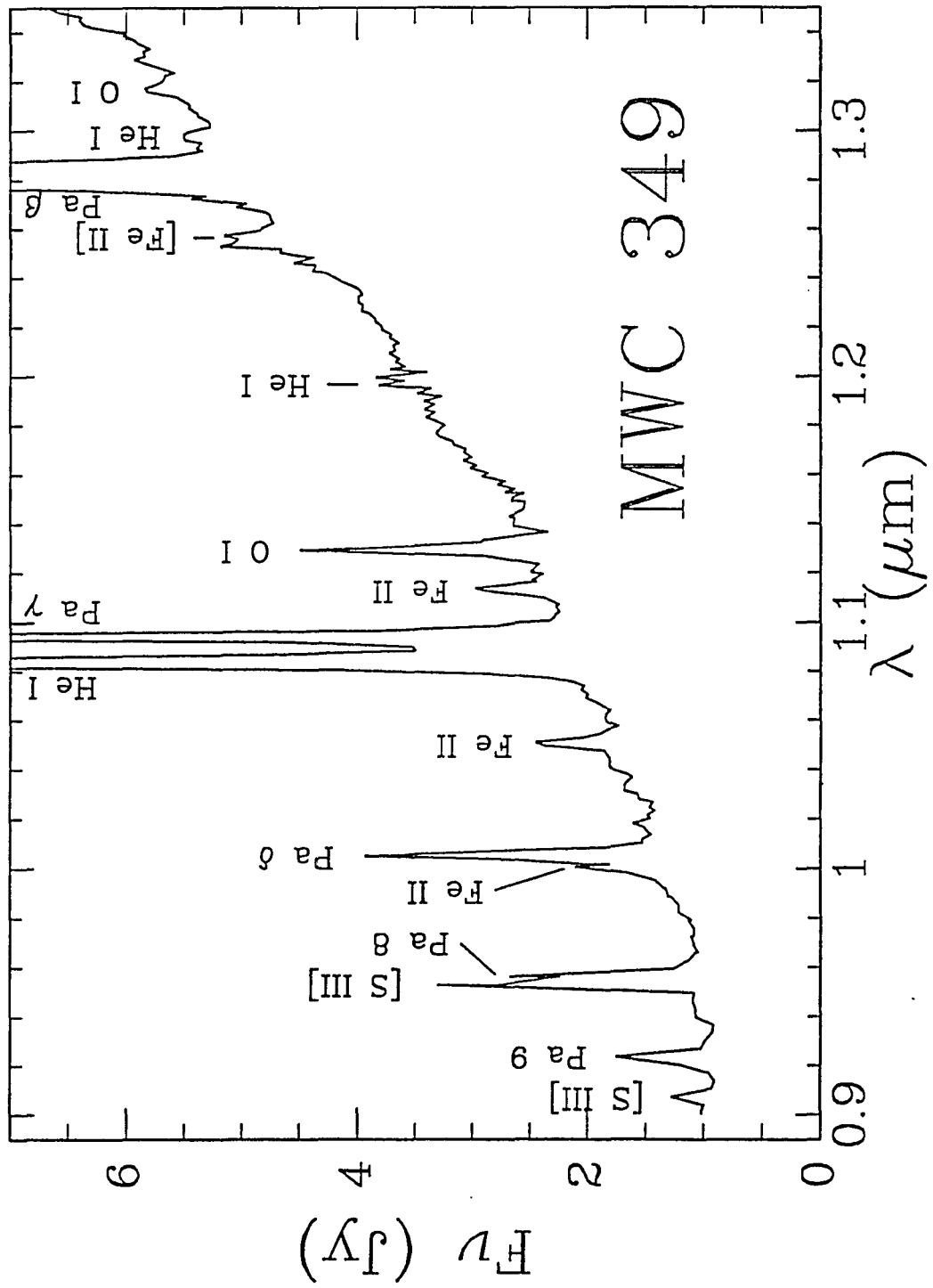


Figure 4.2.1: 0.90 - 1.35 μm spectrum of MWC 349

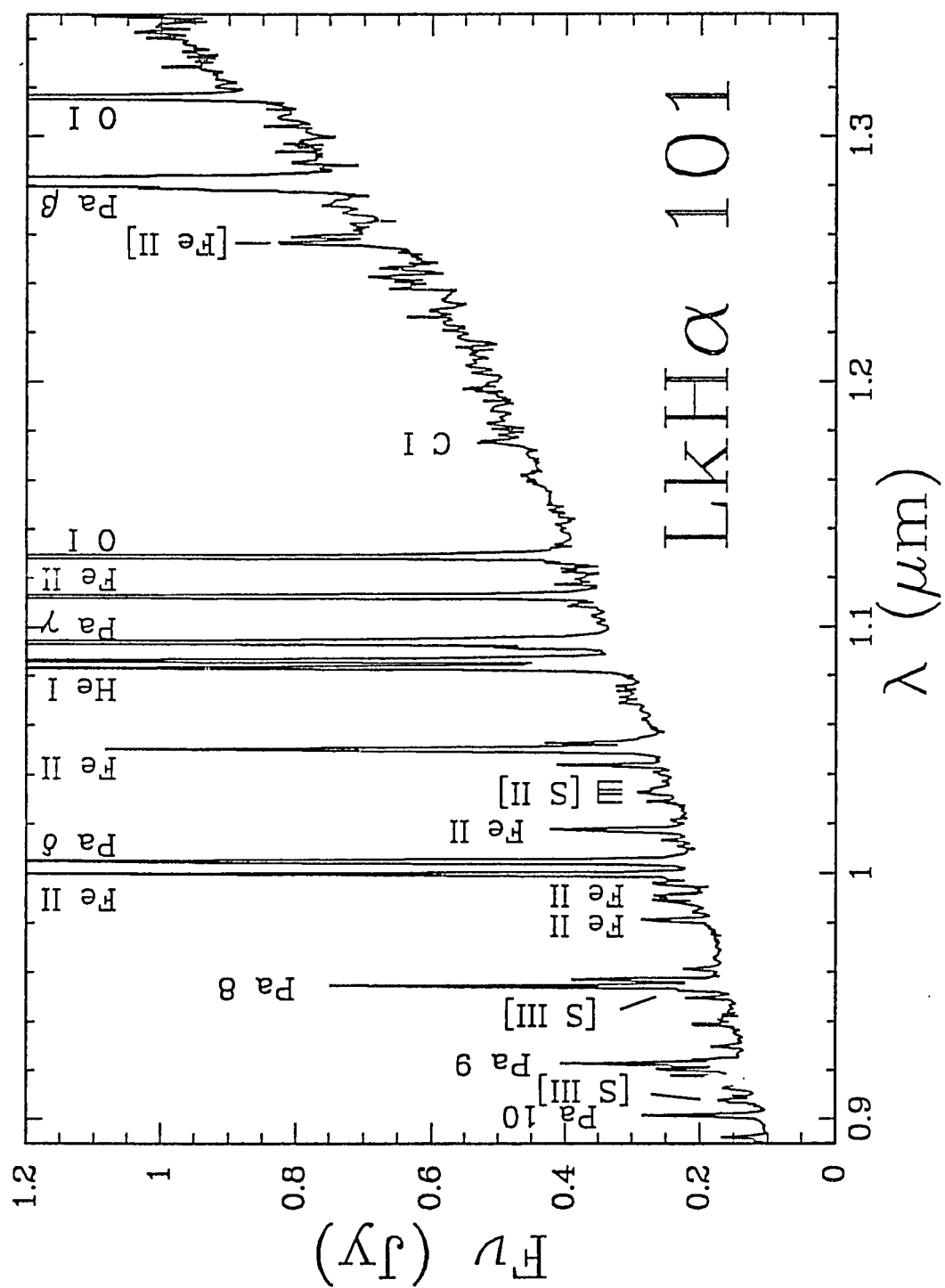


Figure 4.2.2: 0.90 - 1.35 μm spectrum of LkHα 101

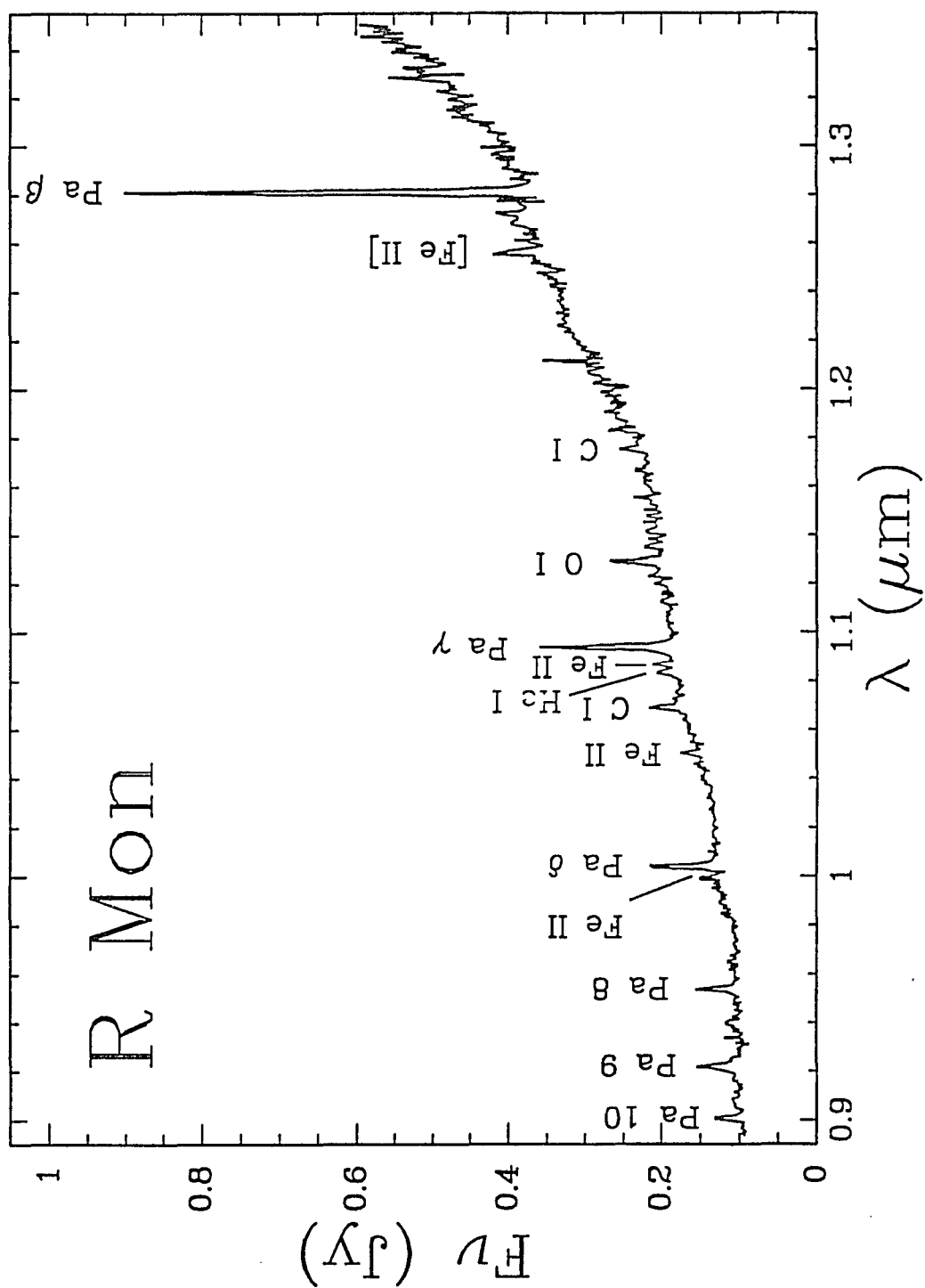


Figure 4.2.3: 0.90 - 1.35 μm spectrum of R Mon

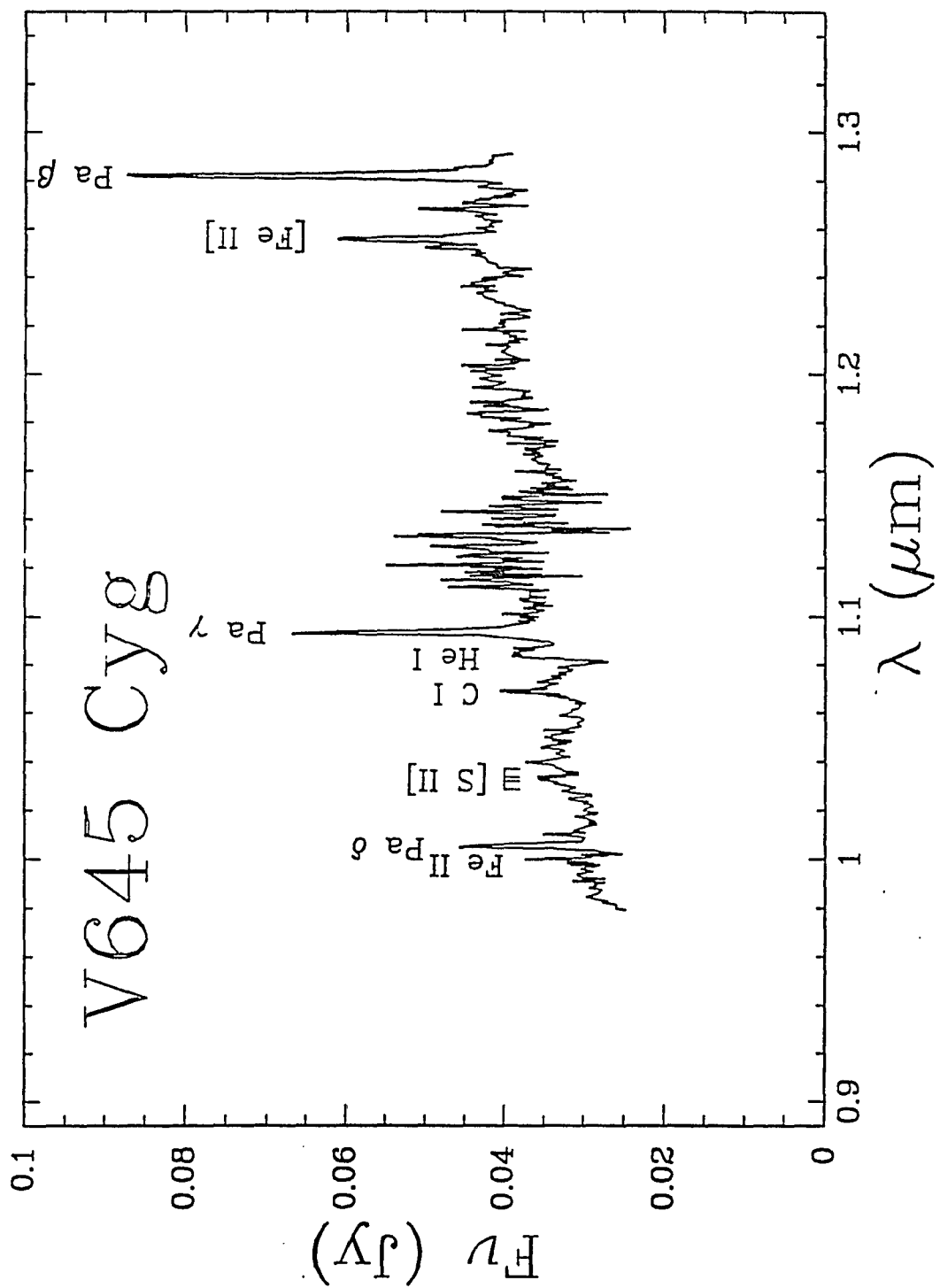


Figure 4.2.4: 0.90 - 1.35 μm spectrum of V645 Cyg. The beam covered N0, with some contribution from N1 and N2.

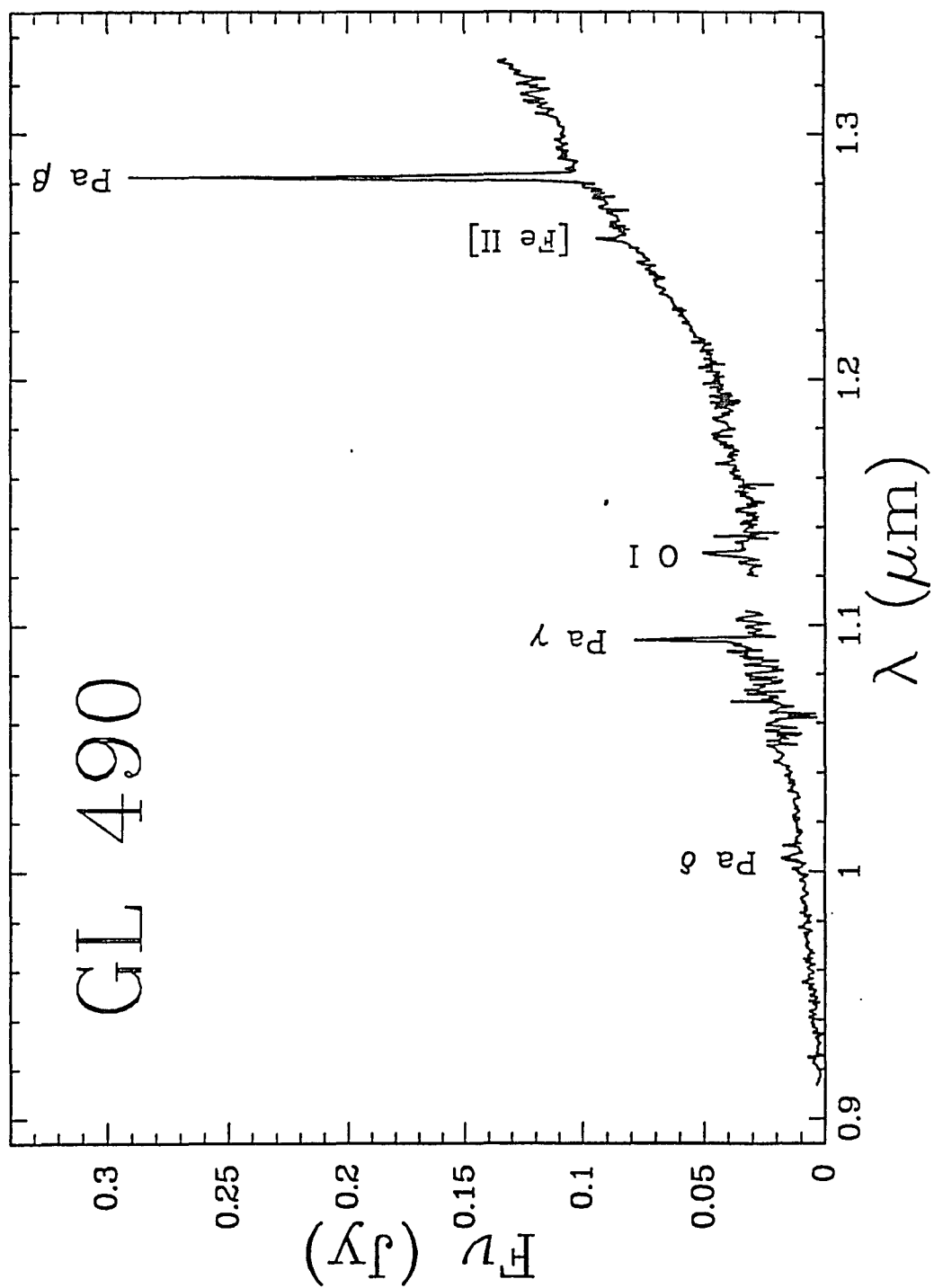


Figure 4.2.5: 0.90 - 1.35 μm spectrum of GL 490

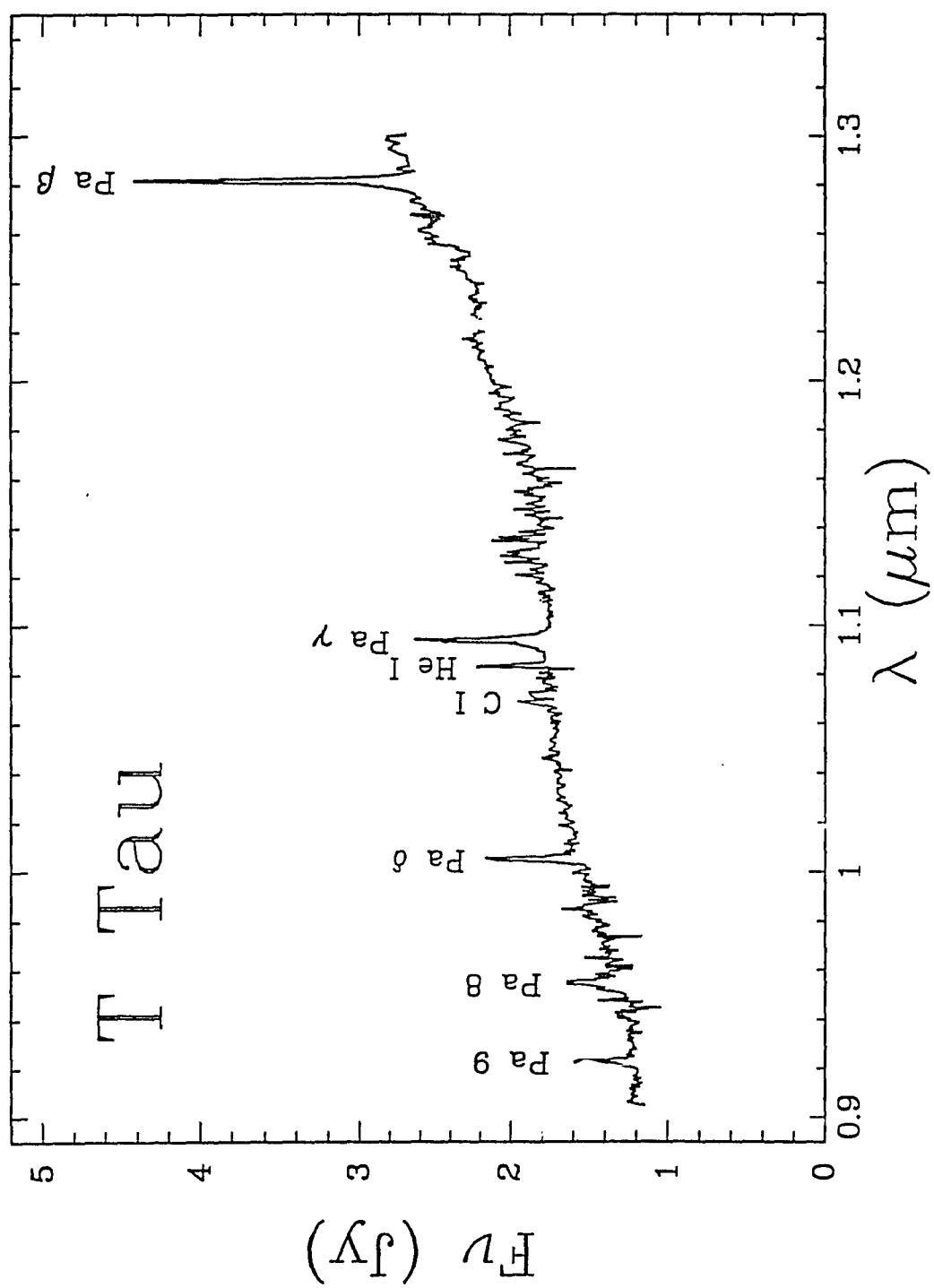


Figure 4.2.6: 0.90 - 1.35 μm spectrum of T Tau

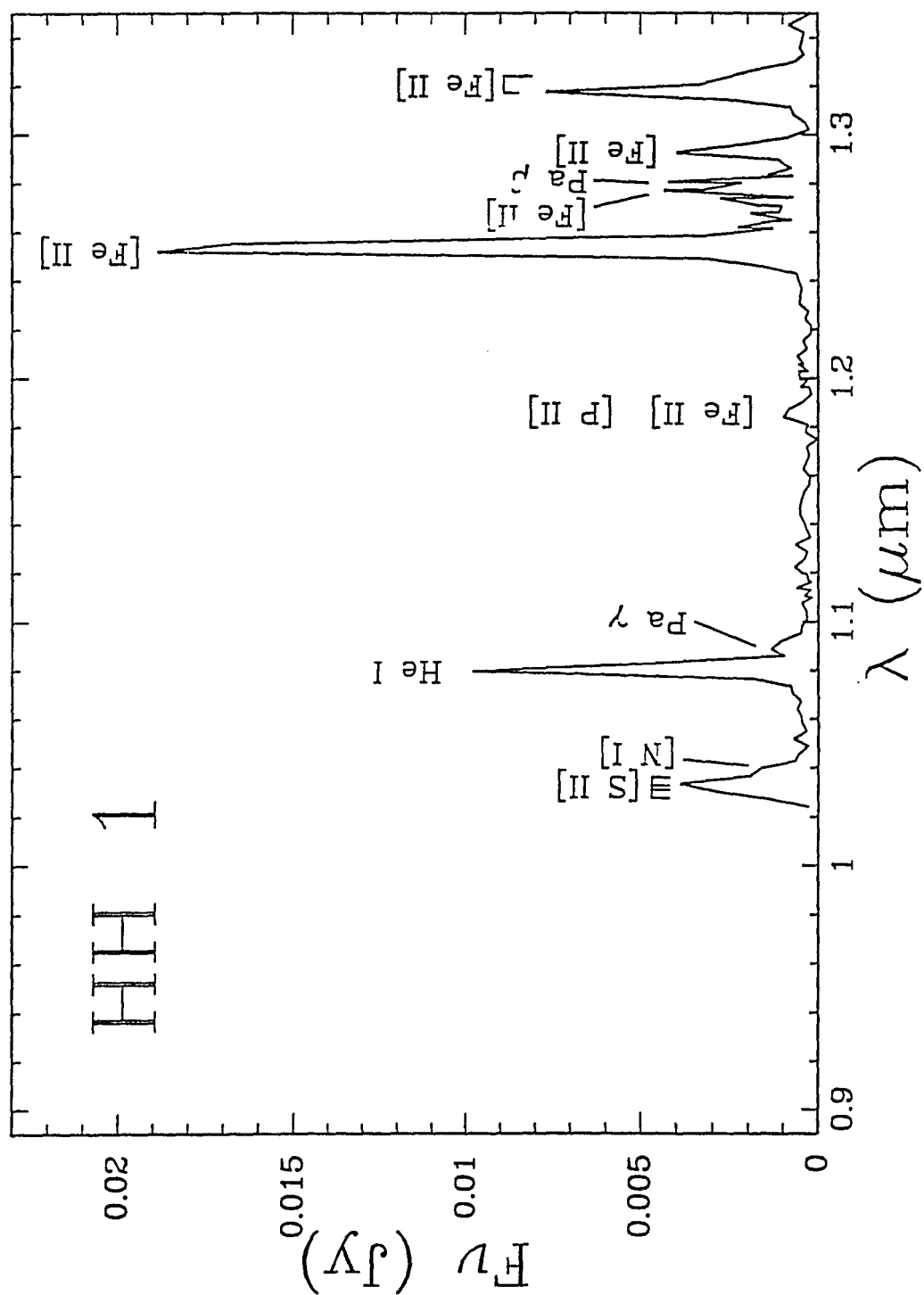


Figure 4.2.7: 0.90 - 1.35 μm spectrum of HH 1

The combination of visible and infrared spectra provides a large baseline for using reddening indicators. However, the spectra are so heavily reddened that it is difficult to measure the short wavelength lines. As a result, we were unable to use the [S II] 0.407/1.032 μm ratio to determine the reddening. Instead, we use ratios of Balmer and Paschen lines. Several factors besides reddening are expected to affect the hydrogen line ratios. First, there is strong evidence that the hydrogen lines are optically thick in most of these objects. Second, the longer wavelength lines might be due in part to thermal excitation rather than just to recombination (Krolik & Smith 1981). Third, several of the objects are highly polarized, showing that much of their emission is due to scattered light. Scattering will tend to enhance the bluer lines. Finally, in high density regions such as circumstellar shells, dust grains can grow to be larger than interstellar grains. Unlike interstellar grains, for which $R_V = 3.1$, large circumstellar grains are better represented by the Cardelli et al. (1989) extinction law for $R_V = 5$. For $\lambda \geq 0.55 \mu\text{m}$ ($A_\lambda/A_V \leq 1.0$), the reddening curves for $R_V = 3.1$ and $R_V = 5$ are nearly identical. For $\lambda < 0.55 \mu\text{m}$, the $R_V = 5$ curve gives smaller A_λ/A_V values.

Ignoring other complications for the moment, we consider optically thin HI emission produced by recombination in a region that lies behind a foreground screen of absorbing interstellar dust. In this simplified case, the extinction

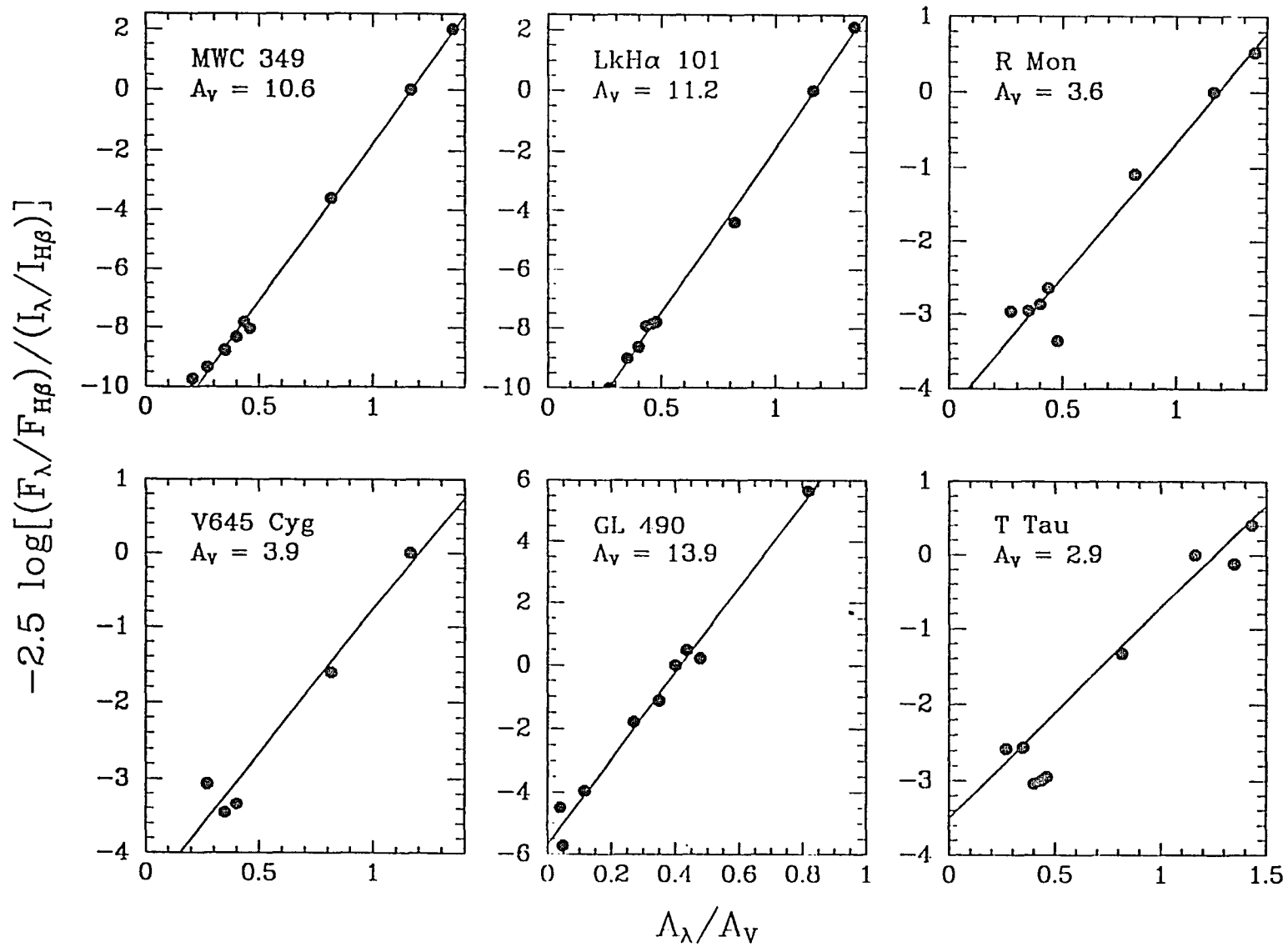
is given by:

$$A_{\lambda} - A_{H\beta} = -2.5 \log \frac{(I_{\lambda}/I_{H\beta})_{obs}}{(I_{\lambda}/I_{H\beta})_{no\ ext}}$$

Since our observations lack spatial information, we measure fluxes rather than intensities. In Figure 4.3 we plot $-2.5 \log[(F_{\lambda}/F_{H\beta})_{obs}/(I_{\lambda}/I_{H\beta})_{no\ ext.}]$ vs. A_{λ}/A_V . For GL 490, line ratios were calculated relative to Pa δ and include Brackett and Pfund line fluxes taken from Persson et al. (1984), Simon et al. (1983), and Thompson & Tokunaga (1979). The zero-extinction, Case B, line intensity ratios are from Hummer & Storey (1987). We take $T_e = 10^4$ K for all objects but T Tau, for which we adopt $T_e = 5 \times 10^3$ K (see Section 4.3). We assume $n_e = 10^4$ cm $^{-3}$ for R Mon, V645 Cyg, and HH 1, $n_e = 10^6$ cm $^{-3}$ for MWC 349 and LkH α 101, and $n_e = 10^{10}$ cm $^{-3}$ for T Tau. If the lines were produced by Case B recombination and the reddening were caused by interstellar dust, the points in Figure 4.3 would fall on a straight line with slope A_V and y-intercept $-A_{H\beta}$. As can be seen from Figure 4.3, most of the points fall close to the reddened Case B line. For R Mon and T Tau, slightly better fits are obtained using a reddening law with $R_V = 5$.

The good agreement of the hydrogen line ratios with the reddened Case B curves has several implications. First, it shows that, except in the cases of R Mon and T Tau, most of

Figure 4.3: Reddening curves for young stellar objects. The data points are determined from our hydrogen line data, theoretical line ratios from Hummer & Storey (1987), and the extinction curve of Cardelli, Clayton, & Mathis (1989). When Case B recombination applies, the data points are expected to fall on a straight line with slope equal to the visual extinction (see text).



the reddening is due to interstellar dust. Second, it shows that the observed line ratios are reasonably consistent with Case B recombination theory, a somewhat surprising result given that large $H\alpha$ optical depths are required in several of the sources to produce fluorescence-excited lines. It is possible that LTE conditions exist and that the resulting H I ratios mimic Case B recombination ratios.

For five of the six sources, we have measurements of Balmer and Paschen lines from a common upper level. When Case B recombination applies, the ratio of these lines is nearly independent of density and temperature. Scattering and optical depth effects will still be important. For MWC 349 and LkH α 101, the $H\gamma/\text{Pa}\beta$ ratio gives an extinction estimate very similar to that of Figure 4.3. For R Mon and T Tau, the $H\gamma/\text{Pa}\beta$ estimates are 15-30% smaller than the values given in Figure 4.3. Finally, for GL 490, the $\text{Pa}\delta/\text{Br}\gamma$ ratio is consistent with Figure 4.3.

4.3.1 MWC 349

MWC 349 is often included in young star studies even though there is considerable evidence that it is an evolved object (Olson 1975; Harvey, Thronson, & Gatley 1979; Hartmann, Jaffe & Huchra 1980; White & Becker 1985; Cohen et al. 1985;). MWC 349 consists of two stars separated by $2''.4$ (see Figure 4.4.1). MWC 349A, the brighter of the two, provides most of the radio and emission line flux and has

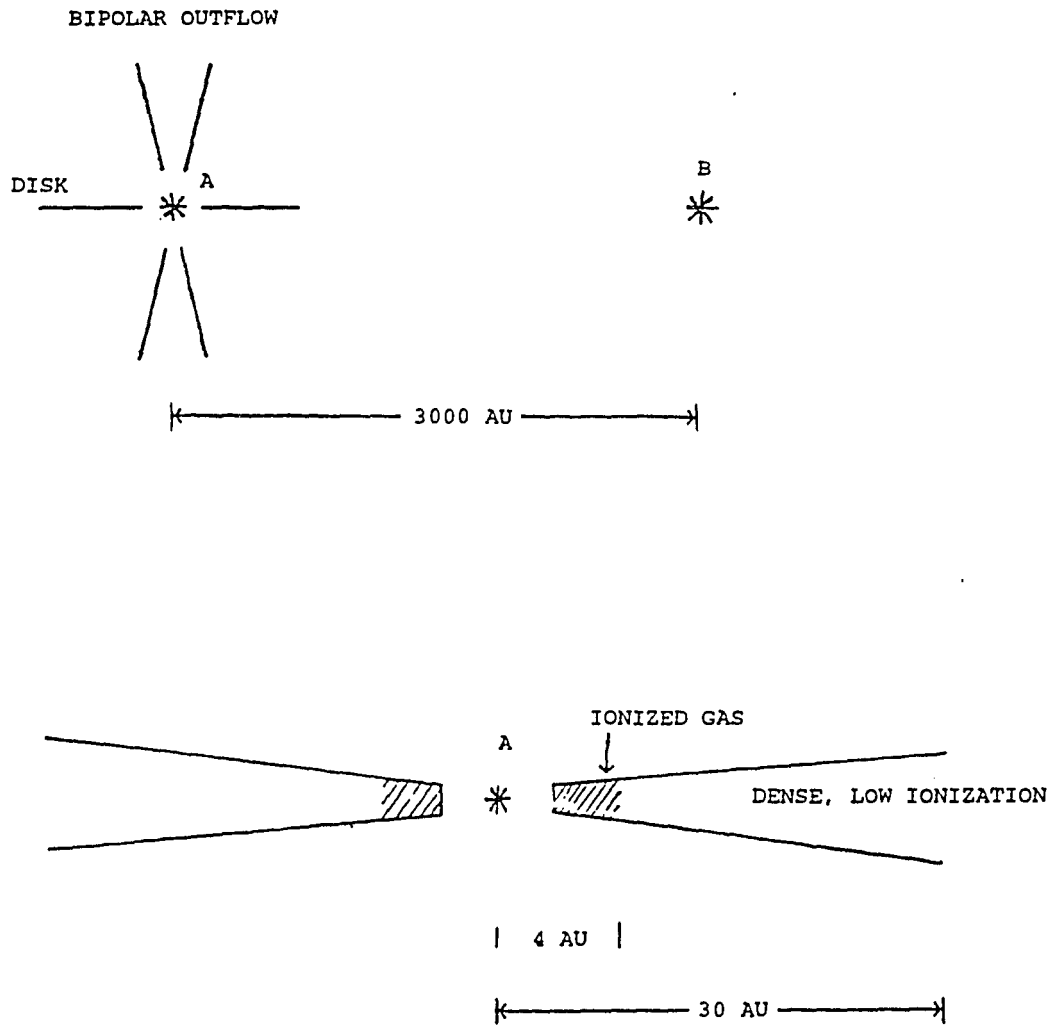


Figure 4.4.1: Schematic diagram of MWC 349

radio and emission line properties similar to those of the luminous young stellar objects LkH α 101 and R Mon (see discussion in Hamann & Simon 1988). The most promising model for MWC 349A was presented by Hamann & Simon (1986). In their model, MWC 349A is surrounded by a disk lying in the plane of the two stars. A slow (50 km s^{-1}), bipolar wind, possibly fed by evaporated disk material, emanates from the vicinity of MWC 349A. The expanding, ionized wind accounts for the observed radio emission. Double-peaked line profiles provide evidence for a circumstellar disk (Hamann & Simon 1986; 1988).

Emission in lines as diverse as K I and [S III] reveals that MWC 349 has a variety of physical regions. Hamann & Simon (1988) list five emitting regions, the first four of which are associated with the disk. First is a hot, modest density H^+ and He^+ zone that gives rise to H I and He I recombination emission. Second is a high density neutral region where collisions excite K I, Ca II, C I, N I, and Fe II lines. Third is a dense but warmer $\text{H}^0 - \text{H}^+$ transition region where Lyman line fluorescence excites O I, Mg II, and Fe II transitions. Fourth is a hot, low density region where collisions excite [S III] and [Ar III] emission. Fifth is a much cooler, low density region, probably associated with the outflow from the star, in which [Fe II] and [Cr II] lines are excited by collisions. These vastly different emitting regions arise naturally as temperatures and densities

decrease with distance from the central star and height above the plane. The widths of the lines indicate that most of the emission is produced within 30 AU of the central star. The higher ionization species appear to come from within about 4 AU of the central star. As we discuss below, we find evidence in our infrared spectrum for each of these emitting regions.

4.3.1.1 Extinction

Several papers have shown that the hydrogen line ratios in MWC 349A are roughly consistent with Case B recombination theory, a result confirmed by Figure 4.3. The good agreement with recombination theory shows that the H I emission must come from an optically thin recombination region rather than from the ionized wind. Since star B is a comparatively weak source of hydrogen line emission, the extinction estimate given by Figure 4.3 can be taken as the extinction to MWC 349A. We corrected all line ratios for $A_v = 10.8$ before completing the following analysis.

4.3.1.2 Physical Structure

The second region in the Hamann & Simon (1988) model is a high density neutral region. Among the evidence they found for this region was optically thick N I and C I emission. High densities and mostly neutral gas are required to maintain high populations in the lower levels of these transitions. The infrared spectrum of MWC 349 also shows

N I emission. The lines are heavily blended so we cannot tell if the emission is optically thick. The C I lines near $1.069\ \mu\text{m}$ also appear to be present in our spectrum, but they are too faint to extract without higher resolution data.

The fourth region in the Hamann & Simon (1988) model is a region hot enough to doubly ionize sulfur and argon, yet with low enough density to permit forbidden line emission. Several [S III] lines are present in our spectra. The observed [S III] $(0.9069 + 0.9531)/0.6312\ \mu\text{m}$ line ratio indicates a density $n_e > 3 \times 10^6\ \text{cm}^{-3}$ for $T_e = 2 \times 10^4\ \text{K}$. At lower electron temperatures, the infrared lines are excited less often so even higher electron densities are required to collisionally de-excite the $0.6312\ \mu\text{m}$ line and produce the observed line ratio. Since the [S III] lines are bright in MWC 349, it seems unlikely that the electron temperature is lower than $2 \times 10^4\ \text{K}$ in this region.

[N II] and [S II] lines appear in our spectrum but have no transitions in the wavelength intervals covered by Hamann & Simon (1986; 1988). Based on the ionization potentials of N^0 (14.5 eV) and S^0 (10.4 eV), we suspect that the [N II] lines are produced in the H I recombination zone and the [S II] lines in an adjacent region, perhaps the region producing the [Fe II] and [Cr II] lines. The [S II] $1.0320/1.0336\ \mu\text{m}$ ratio is primarily a function of the electron density, and the [N II] $(0.6548 + 0.6583)/0.5755\ \mu\text{m}$ ratio depends heavily on the electron temperature. If

physical conditions are similar in the [N II] and [S II] regions, then these two ratios imply $T_e \approx 6 \times 10^3$ K and $n_e \approx 1 \times 10^6$ cm⁻³.

The fifth region in the Hamann & Simon (1988) model is the source of the [Fe II] emission. From the [Fe II] 1.2941/1.2567 μ m ratio and the line ratio vs. density curves of Hudgins, Herter, & Joyce (1990), we find that the density in this region is $n_e \approx 10^5$ cm⁻³, slightly smaller than the density determined from the [N II] and [S II] lines. If the [S II] and [N II] lines arise in the bipolar outflow, they must be produced slightly closer to the central star than the [Fe II] emission.

[Fe II] and H₂ lines are often indicators of shocks. Hamann & Simon (1986) did not detect any H₂ lines in the 2 μ m spectrum of MWC 349. Nor do we detect any H₂ lines in the 1 μ m region. In addition, the [Fe II] lines from MWC 349 are quite weak. Apparently there is little or no shock heating in the low density regions of MWC 349.

4.3.1.3 Fluorescence

The third region discussed by Hamann & Simon (1988) is a warm, dense region where H α is optically thick and Lyman line fluorescence is an important excitation mechanism. As initially reported by Thompson et al. (1977), the O I 1.1287 μ m line is anomalously strong in MWC 349. In our spectrum, the O I 1.1287/1.3165 μ m ratio equals 17.65, much larger than

the ratio of 0.1 listed by Grandi (1975) for UV continuum fluorescence from an HII region with Ly β in absorption. The observed ratio is also considerably above the ratio of 6.2 expected if the Ly β flux were at the UV continuum level. The O I emission in MWC 349 must therefore be dominated by Ly β fluorescence. Since Ly β fluorescence is only possible if there is a large population in the $n = 3$ level of hydrogen, this result shows that H α is optically thick in this region. We see no evidence in the spectrum of MWC 349 for fluorescent excitation of molecular hydrogen.

4.3.2 LkH α 101

LkH α 101 is an extremely rich emission line source. Herbig (1971) detected 70 lines from 0.65 - 0.86 μ m. We find nearly 100 lines in the infrared and 50 lines in the visible spectra. The Fe II spectrum is particularly impressive, rivaling that of Eta Carinae.

At the heart of LkH α 101 is an O9.5 V star (Thompson et al. 1977). Radio observations show a compact ($< 1''$) source coincident with the visible position (Cohen, Bieging, & Schwartz 1982). The radio spectrum of the compact source is consistent with a r^{-2} density profile, indicating that the compact source might be an ionized wind. LkH α 101 is also surrounded by an extended, optically thin region, roughly $60''$ in diameter (Altenhoff et al. 1976).

The strengths of the radio emission and of the Paschen

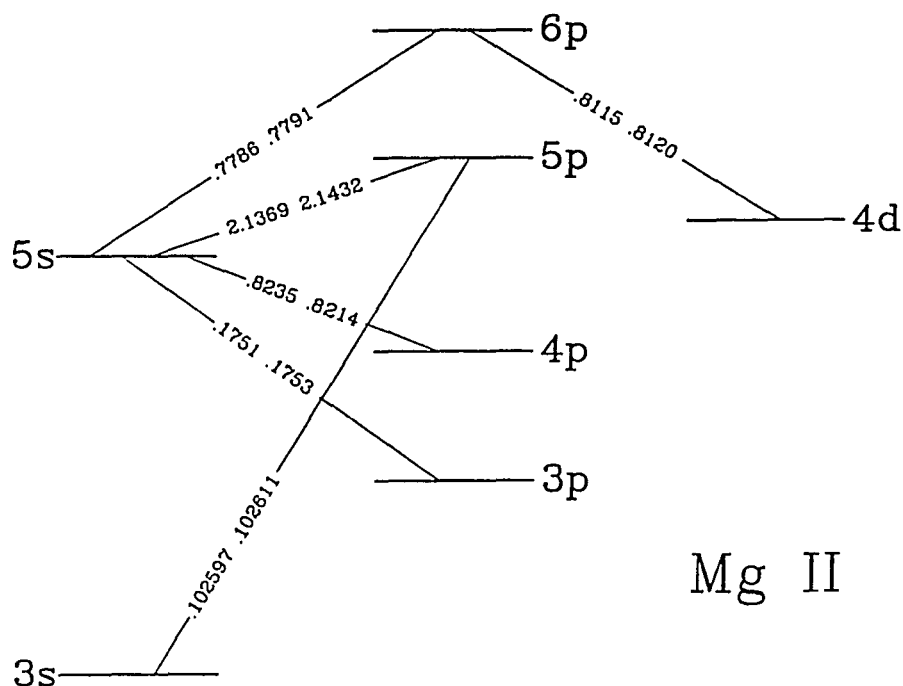
and Brackett lines are a factor of roughly 100 times greater than expected for an O9.5 V star (Simon & Cassar 1984). Simon & Cassar suggest that high optical depths in the hydrogen lines result in a large population of electrons in the $n = 2$ level, creating an environment in which Balmer continuum photons are capable of ionizing the gas. Balmer continuum photoionizations greatly enhance the number of free electrons and consequently the strength of the recombination lines. As with MWC 349, in spite of large optical depths in the hydrogen lines, the relative strengths of the infrared recombination lines are consistent with nebular Case B recombination theory (Simon & Cassar 1984).

4.3.2.1 Extinction

LkH α 101 is very highly reddened. Estimates range from $A_v = 9.7$ (McGregor, Persson, & Cohen 1984) to $A_v = 15.7$ (Rudy et al. 1991). The extinction needs to be known to within a few tenths of a magnitude for all of the visible and near-infrared line diagnostics to produce meaningful results. With our visible and infrared data, we can reduce the uncertainty in the reddening corrections. The H I lines point towards $A_v = 11.2$ (see Figure 4.3). Similarly, the H γ /Pa β ratio implies $A_v = 11.3$. We also compared the strengths of the He I $\lambda\lambda 0.6678, 1.1969, \text{ and } 1.2785 \mu\text{m}$ lines with the strength of the He I $0.5876 \mu\text{m}$ line. Theoretical He I recombination line ratios are listed in Robbins (1968).

Since the $\lambda 0.5876 \mu\text{m}$ line is quite sensitive to collisional excitation, we used the formalism of Clegg (1987) to correct for collisions. The resulting helium line ratios suggest $A_v = 10.8 \pm 0.6$. Rudy et al. (1991) used a fourth method to determine the reddening. They measured the O I 1.1287/0.8446 μm ratio, which has a fixed value in the case of pure Ly β fluorescence. They calculated an extinction of $A_v = 15.7$, which is several magnitudes larger than the extinction predicted by other techniques. As a test of this technique, we used the O I line ratio method on MWC 349, where Ly β fluorescence is clearly the dominant source of O I emission. The reddening estimate we derived is $A_v \approx 6.5$, much smaller than the extinction determined from hydrogen line ratios. We conclude that O I line ratios are unreliable for measuring the attenuation to a source. The exact line ratios in fluorescence-excited O I depend too heavily on factors other than the strength of the Ly β flux.

Although the O I line ratio method does not work well for MWC 349 and LkH α 101, it does suggest an alternative approach for determining the reddening that appears to work much better. This second approach is to balance the number of electrons in and out of the $5s^2S$ level of Mg II. There are only two paths out of and one main path into the $5s$ level of Mg $^+$ (see Figure 4.5), so this procedure is less complicated than balancing the number of electrons in and out of the $3p^3P$ level of O I. A potential stumbling block with



Mg II

Figure 4.5: Grotrian diagram for Mg II transitions

the Mg II method is the need for accurate fluxing. A 10% error in the relative fluxing of the visible and infrared data will cause an error of 0.23 mag in the extinction estimate.

We used the 0.8235 μm line flux from Hamann & Persson (1989b) in combination with branching ratios to determine the depopulation rate from the 5s level of Mg^+ . We combined the 0.812 μm lines from Hamann & Persson with branching ratios to determine the rate of population from the 6p level. The 2.14 μm lines (Simon & Cassar 1984) were used to determine the population rate from the 5p level. The extinction was adjusted until detailed balance was achieved. The resulting

value of $A_v = 10.5$ differs little from the value of $A_v = 10.3$ that results if transitions from the 6p level are ignored. It thus seems unlikely that cascades from higher levels contribute much to the population rate, especially if the Mg II emission is dominated by Ly β fluorescence. However, if densities exceed 10^{13} cm^{-3} (Hamann & Persson 1989b), then collisions will affect the level populations and make this technique for measuring the extinction ineffective.

In summary, the reddening to LkH α 101 is likely to be in the range 10.5 - 11.5. Collisions and radiative transfer effects make it difficult to be more precise. For the following discussion, we adopt a reddening estimate of 11.2.

4.3.2.2 Physical Structure

Few forbidden lines are present in the visible and infrared spectra of LkH α 101. Unlike in MWC 349, there is evidence for only one forbidden line region. The [S II] 1.0320/1.0336 ratio, which is sensitive to the electron density, suggests $n_e \approx 1 \times 10^6 \text{ cm}^{-3}$. The [Fe II] lines were compared with the predicted line ratios from Nussbaumer & Storey (1988). The [Fe II] 0.90519/1.2567 μm ratio indicates that $T_e = 1.0^{+0.5}_{-0.3} \times 10^4 \text{ K}$, $n_e \geq 10^6 \text{ cm}^{-3}$, where the temperature uncertainties correspond to a 30% error in the line ratio. Using the [Fe II] 1.533 μm line from Hamann & Persson (1989b), we find the [Fe II] 1.533/1.2567 μm ratio to be consistent with $n_e \geq 10^5 \text{ cm}^{-3}$. Together, the [Fe II] and [S

II] indicators point to a region with $T_e \approx 10^4$ K and $n_e \approx 10^6$ cm⁻³. The other forbidden lines in the spectrum of LkH α 101 were useful for establishing line identifications, but they provided little other physical information because of line blends, missing lines, and lines too faint to place useful constraints.

4.3.2.3 Fluorescence

In LkH α 101, the ratio O I 1.1287/1.3165 μ m = 6.5, far in excess of the ratio of 0.1 predicted by Grandi (1975) for starlight fluorescence from a nebula surrounding an O star with Ly β in absorption. However, in a starlight fluorescence model where Ly β is neither in emission nor in absorption, the predicted O I ratio is roughly 6.2. Comparison of our O I line fluxes with the λ 0.8446 μ m flux of Hamann & Persson (1989b) again shows that the O I emission is consistent with starlight fluorescence with at best a slight enhancement of the Ly β flux over the UV continuum level. The weakness of Ly β fluorescence in LkH α 101 further argues against the Rudy et al. (1991) reddening estimate and points out the danger of using the O I models of Grandi (1975) to argue for Ly β fluorescence without considering the sensitivity of the models to input parameters. As with MWC 349, we detect no H₂ lines in the 1 μ m spectrum of LkH α 101.

Other suggestions have been made for Ly β fluorescence in LkH α 101. Simon & Cassar (1984) and Hamann & Persson

(1989b) discuss Ly β fluorescence as a possible mechanism for exciting the Mg II lines and several of the Fe II lines. As pointed out by Hamann & Persson, the problem with explaining the Mg II emission by Ly β fluorescence is the strength of the $\lambda\lambda$ 0.8115, 0.8120 μm lines, which arise from the 6p level (see Figure 4.5). Since Ly β fluorescence populates the 5p level, one needs either a significant contribution from recombination or high enough densities ($n_e \approx 10^{13} - 10^{14} \text{ cm}^{-3}$) for collisions to build up a sizable population in the 6p level. The Mg II lines in the 0.9 - 1.35 μm region are blended with H I and He I lines, making it difficult to add any new insights.

4.3.2.4 Shocks

H₂ lines are not seen in the 2 μm spectrum of LkH α 101 (Simon & Cassar 1984). Since H₂ molecules are dissociated in strong shocks, the absence of H₂ lines is not too surprising. Quite a few [Fe II] lines are present in the spectrum of LkH α 101. Given that few other forbidden lines are present in the spectrum of LkH α , it is likely that the [Fe II] lines are produced in shocks.

4.3.3 R Mon

R Mon is a bright point source at the edge of the nebula NGC 2261 (see Figure 4.4.2). Both R Mon and NGC 2261 are

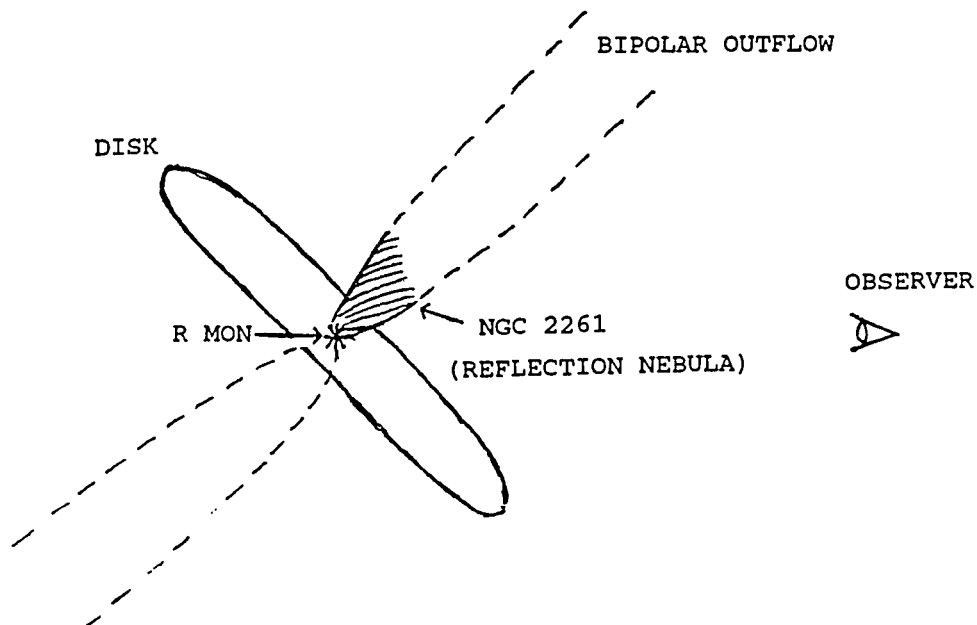


Figure 4.4.2: Schematic diagram of R Mon

highly polarized and have been the subject of several polarization studies (Jones & Dyck 1978; Aspin, McLean, & Coyne 1985; Aspin et al. 1988; Minchin et al. 1991). The polarization pattern of NGC 2261 is nearly centro-symmetric around R Mon, indicating that the nebular emission is primarily due to reflection. The centro-symmetric pattern breaks down close to R Mon (Aspin, McLean, & Coyne 1985). The polarization is ~50% to the north and south of R Mon and only ~5% to the east and west (Minchin et al. 1991). The low polarization to the east and west might be due to a circumstellar disk. A high density, disk environment would produce low polarization because of multiple scattering. The

similarity in the strengths of the Ca II triplet lines indicates that high density gas is present near R Mon (Bohm, Siegmund, & Schwartz 1976). From the appearance of the CO emission, it appears that NGC 2261 is one lobe of a bipolar outflow and that a circumstellar disk obscures the southern lobe (Canto et al. 1981).

4.3.3.1 Extinction

Bohm et al. (1976) compared the $H\alpha$, $H\beta$, and $H\gamma$ line strengths from R Mon. They found that the line ratios are consistent with Case B recombination and a reddening of $E(B-V) = 0.37$ ($A_V = 1.15$). We see very different hydrogen line ratios. Our Balmer and Paschen line data support $A_V = 3.6$ (see Figure 4.3), and the $H\gamma/Pa\beta$ ratio gives $A_V = 3.2$. Spectropolarimetry shows $H\alpha$ to be partially polarized so the extinction might be even larger. Our much larger extinction estimates are due to beamsize effects and to differences in the attenuation to R Mon and to NGC 2261. Bohm et al. measured a significantly higher $H\alpha/H\beta$ ratio with a $3''.6$ aperture than they did using a $9''.9$ aperture. Our visible spectrum of R Mon was measured using a $2''$ slit centered on R Mon and is unlikely to include much emission from NGC 2261. The Paschen lines were measured with a $6''$ beam. They are consistent with the higher extinction estimate, showing that the infrared hydrogen line emission is dominated by R Mon rather than by NGC 2261.

4.3.3.2 Physical Structure

The [S II] line strengths provide information on physical conditions in NGC 2261. The [S II] 0.6716/0.6731 μm ratio indicates a density of $n_e \approx 2 \times 10^3 \text{ cm}^{-3}$. The infrared [S II] lines are below our sensitivity limits, but the non-detection provides a lower limit for the [S II] $(0.6716 + 0.6731) / (1.0286 + 1.0320 + 1.0336 + 1.0370)$ μm ratio. This lower limit, when corrected for $A_v = 3.3$, implies $n_e < 5 \times 10^3 \text{ cm}^{-3}$ (assuming $T_e = 10^4 \text{ K}$).

The highest ionization lines in the spectrum of R Mon are the hydrogen recombination lines. The absence of [N II] and [Fe III] lines shows that either the central star is too cool to ionize N^0 and Fe^+ atoms or that forbidden lines are quenched in the hydrogen recombination region. The former explanation is hard to justify since the ionization potentials for N^0 and Fe^+ are only slightly larger than that for hydrogen. The latter explanation requires an electron density of at least 10^6 cm^{-3} in the hydrogen recombination zone.

Finally, there are two pieces of evidence for outflows in R Mon. First, the [O I] lines both have P Cygni profiles. Second, the NaD line is seen in absorption with a blueshift of about 300 km/s.

4.3.3.3 Fluorescence

The infrared spectrum of R Mon includes an O I line at

0.9266 μm . This line is the quintet counterpart to the O I 1.1287 μm line, and its presence shows that recombination produces some of the O I emission. However, if all the O I emission were produced by recombination, the quintet line would be the stronger of the two. In R Mon, the 1.1287 μm line is much stronger than the 0.9266 μm line. In addition, the O I 1.3165 μm line is not detected. The great strength of the 1.1287 μm line relative to the 1.3165 μm line is strong evidence that the 1.1287 μm line is enhanced by Ly β fluorescence. Finally, we note an absence of fluorescent H₂ emission in R Mon.

4.3.4 V645 Cyg

V645 Cyg has an unusual morphology (see Figure 4.4.3).

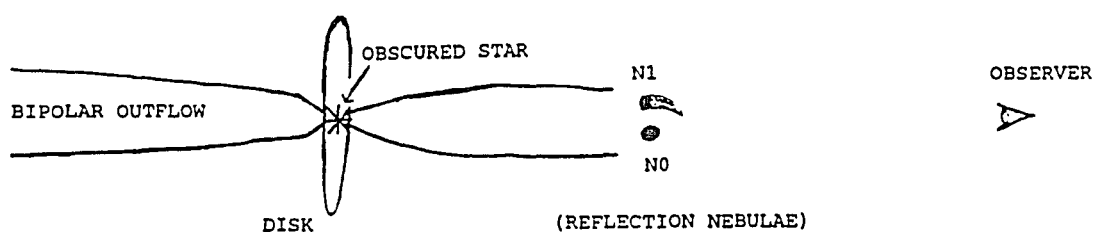


Figure 4.4.3: Schematic diagram of V645 Cyg

In visible light, it consists of a bright, point-like

condensation and a short arc of emission (Cohen 1977). The point source is referred to as N0, and the brightest condensation in the arc is called N1. These two visible sources have very similar spectra and polarization properties. In the infrared, a bright point source is seen slightly offset from N0. Cohen suggested that N0 and N1 are reflection nebulae illuminated by the heavily obscured infrared source. Further support for this model was provided by Lenzen (1987). His polarization image of GL 2789, the nebula surrounding V645 Cyg, is centric-symmetric with its center slightly offset to the northwest of N0.

Hamann & Persson (1989a) obtained high resolution spectra of N0 and N1 between 0.63 and 1.1 μm . Many of the lines exhibit P Cygni profiles, indicating mass loss. The mass is ejected in weakly-collimated bipolar outflows, probably oriented face-on to the line-of-sight (Schulz et al. 1989). Hamann & Persson also detected transitions of K I, Fe I, and Ca II. Since these lines are only expected in regions with densities $\geq 10^{10} \text{ cm}^{-3}$, Hamann & Persson suggest that these low-ionization lines might originate in a circumstellar disk. Additional evidence for a disk comes from the [S II] line profiles, which include blue-shifted but not red-shifted emission. Hamann & Persson point out that a disk could obscure the receding part of a bipolar outflow, leaving just blue-shifted emission.

4.3.4.1 Extinction

There has been considerable discussion about the distance and extinction to V645 Cyg. The distance, determined after correcting for deviations from standard Galactic rotation, is in the range 3.0 - 3.5 kpc (Goodrich 1986; Schulz et al. 1989). The visual extinction estimates cluster around $A_v = 4$ (Cohen 1977; Humphreys, Merrill, & Black 1980; McGregor, Persson, & Cohen 1984). Most of this attenuation is believed to be interstellar, but there might also be a circumstellar component. Our data support $A_v = 3.9$ (see Figure 4.3). In spite of the good agreement among the various extinction estimates, there is still uncertainty about the true amount of dust reddening. Existing extinction estimates are likely to have been influenced by deviations from Case B recombination, uncertainties about the nature of the central star, and wavelength dependences of scattering. For this study, we adopt $A_v = 3.9$.

4.3.4.2 Physical Structure

The 6" beam used to measure our infrared spectrum was centered on N0. The most interesting line in the spectrum is the He I 1.0830 μm line, which has a strong P Cygni profile with a 500 km/s separation between the components. Hamann & Persson (1989a) found a 510 km/s separation between the components of H α and smaller velocity separations for the other Balmer lines. They also found that the hydrogen lines

are optically thick and deduced that the $H\alpha$ line, which has the highest optical depth, reflects conditions furthest from the central star. We note that the He I 1.0830 μm line must have a large optical depth to produce a similarly large velocity separation.

The most puzzling aspect of the He I 1.0830 μm line is the relative strengths of its emission and absorption components. There is very little emission, and the blueshifted absorption is quite strong. When a He I 1.0830 μm photon is absorbed, it is usually reemitted as a 1.0830 μm photon. Even with many scatterings, it is extremely unlikely that collisions will remove enough He I 1.0830 μm photons for the line to appear in absorption (see further discussion of the 1.0830 μm line in Section 5.3.2).

The geometry of the outflow makes strong He I 1.0830 μm absorption possible. In a bipolar outflow, photons emerging from the side of the outflow will encounter slow moving gas and will not be reabsorbed. Photons emerging nearly perpendicular to the outflow will have a wavelength close to 1.0830 μm and will be reabsorbed. Thus some emission is expected at 1.0830 μm from the gas along the sides of the outflow. For an observer looking along the axis of a bipolar outflow, there would be absorption at wavelengths from just blueward of 1.0830 μm out to the velocity where the He I 1.0830 μm line becomes optically thin. There would also be some emission near 1.0830 μm . The 1.0830 μm line in V645 Cyg

has these characteristics. Thus, as suggested by Schulz et al. (1989), we believe that N0 lies nearly along the axis of the bipolar outflow from V645 Cyg.

The other lines in the infrared spectrum of V645 Cyg show extended emission on the red side of the line center and at least a hint of absorption on the blue side. Only one forbidden line was strong enough to detect in our infrared spectrum, the $\lambda 1.2567 \mu\text{m}$ line of [Fe II]. The visible spectrum includes lines of [S II] and [O I]. As has been noticed previously (Cohen 1977), the spectra of N0 and N1 are nearly identical except for the relative strengths of the forbidden lines. In comparison with the permitted lines, the [O I] lines are slightly brighter in N0 than in N1, and the [S II] lines are much brighter in N1 than in N0. The spectra of Hamann & Persson (1989a) show that the [Fe II] lines are comparatively brighter in N0 than in N1.

The data include several clues to the nature of the forbidden line emission. First, the [O I] lines have P Cygni profiles and the [S II] lines do not. It is not clear from our data whether the [Fe II] lines also have P Cygni profiles. Second, Cohen (1977) used the ratio [O I] $0.5577/(0.6300 + 0.6364) \mu\text{m}$ to find densities of $4 \times 10^5 \text{ cm}^{-3}$ for N0 and $1 \times 10^6 \text{ cm}^{-3}$ for N1. In our data, the [S II] $0.6716/0.6731 \mu\text{m}$ line ratio suggests $n_e \approx 2 \times 10^3 \text{ cm}^{-3}$ for N0 and $1.5 \times 10^3 \text{ cm}^{-3}$ for N1. The [Fe II] $0.8617/1.2567 \mu\text{m}$ ratio indicates $n_e < 10^4 \text{ cm}^{-3}$ and $T_e \approx 6000 \text{ K}$. These observations

of line profiles and density indicators show that the [Fe II] and [S II] lines might be related, but the [O I] and [S II] lines are not.

4.3.4.3 Shocks

It is likely that the [O I] lines are produced in the outflow and the [Fe II] and [S II] lines are excited by shocks. Goodrich (1986) investigated the nature of the [S II] emission and found evidence for a Herbig-Haro object about 10 arcseconds south of N1. He also detected [S II] emission throughout the region surrounding V645 Cyg. It is therefore unlikely that the [S II] emission is associated with the hidden infrared source. Spectropolarimetry would help explain the origin of the [S II] and [Fe II] lines.

4.3.5 GL 490

GL 490 is a source of great complexity. A schematic diagram of the GL 490 region is presented in Figure 4.4.4. Campbell, Persson, & McGregor (1986) show the relative positions of the optical, CO, and radio continuum emission. Their optical images of the region show three emission regions: the slightly elongated source known as GL 490; a large, diffuse cone of emission extending roughly 150 arcseconds, or 0.8 pc, to the SW of GL 490; and a bright bar of emission located at the near edge of the cone, oriented perpendicular to the axis of the cone. There are many

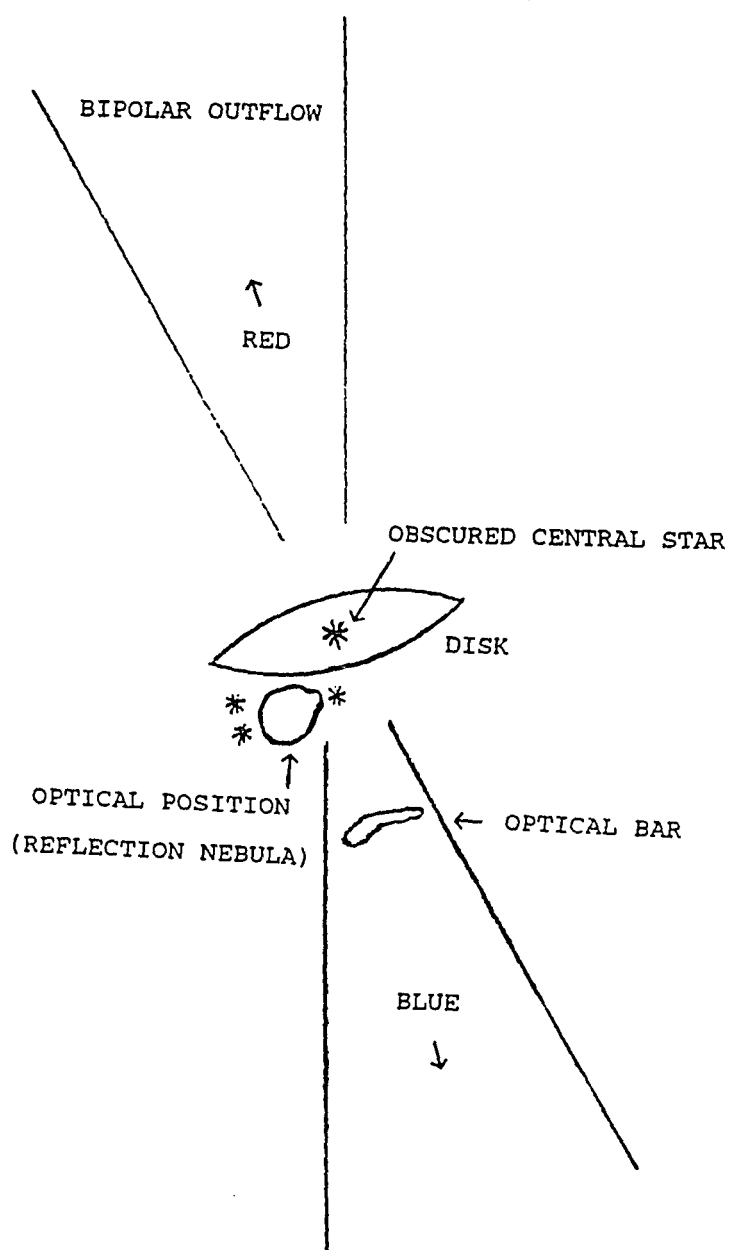


Figure 4.4.4: Schematic diagram of GL 490

neighboring stars, including three faint stars which lie directly adjacent to GL 490. The radio source associated with GL 490 is elongated and is centered 1.5 arcseconds to the NE of GL 490 (Campbell et al. 1986). The CO image of Snell et al. (1984) shows a bipolar outflow, oriented mostly along the line-of-sight but with a slight extension to the NE and SW. The CO emission is centered roughly 30 arcseconds to the SW of GL 490. The blueshifted CO emission coincides roughly with the diffuse cone of optical emission.

GL 490 is highly polarized in the near infrared (Hodapp 1984). The light at these wavelengths is probably scattered emission from an obscured star (Hodapp 1984; Campbell et al. 1986). There is a bar-shaped distribution of CS emission that is nearly coincident with the optical position of GL 490 and perpendicular to the axis of the bipolar CO outflow (Kawabe et al. 1984). The CS emission probably arises in a disk-like structure.

4.3.5.1 Extinction

GL 490 is highly reddened. McGregor et al. (1984) predicted $A_v = 11.2$ based on the shape of the continuum. The true extinction is likely to be larger still since the shape of the spectrum is influenced by scattering. Persson, McGregor, & Campbell (1988) compared H I line strengths and found visual extinctions ranging from 14 to 28 mag. The longer wavelength lines imply larger extinctions, indicating

that the obscured source is probably seen directly at these longer wavelengths. As can be seen in Figure 4.3, our data are in good agreement with Case B recombination theory and indicate $A_v = 13.9$.

4.3.5.2 Fluorescence

The O I 1.1287, 1.3165 μm lines are both present in the near infrared spectrum of GL 490. Combined with the O I 0.8446 μm line from Persson et al. (1988), we used the infrared O I lines to study the importance of UV and Ly β fluorescence in GL 490. The 1.1287/ 1.3165 μm ratio equals 7.1, well above the value of 0.1 from the starlight fluorescence model of Grandi (1975). The reddening-corrected ratio is also slightly above the ratio of 6.2 expected when the flux at Ly β is equal to that of the surrounding continuum. Similarly, the 0.8446/1.1287 μm ratio is a factor of four larger than the ratio expected for pure starlight fluorescence and is consistent with Ly β fluorescence. Since no triplet lines are seen, we can conclude that the O I emission from GL 490 is produced by UV fluorescence, with enhancement of the 0.8446 and 1.1287 μm lines by Ly β fluorescence.

4.3.6 T Tau

T Tau, with a luminosity of 26 L_\odot (Cohen 1973), is much less energetic than most of the other objects in this survey.

The absorption spectrum of T Tau implies a spectral type of K0 or K1 (Schwartz 1974). T Tau is associated with a monopolar, high-velocity CO outflow (Edwards & Snell 1982) and an optical jet (Buhrke, Brugel, & Mundt 1986). The slope of the power-law radio spectrum suggests an approximately spherically symmetric nebula with an electron density that falls off as $r^{-(2-2.5)}$ (Cohen, Bieging, & Schwartz 1982). In the visible, a nebula can be seen around T Tau that extends about 2" north and 8" south of the star (see Figure 4.4.5).

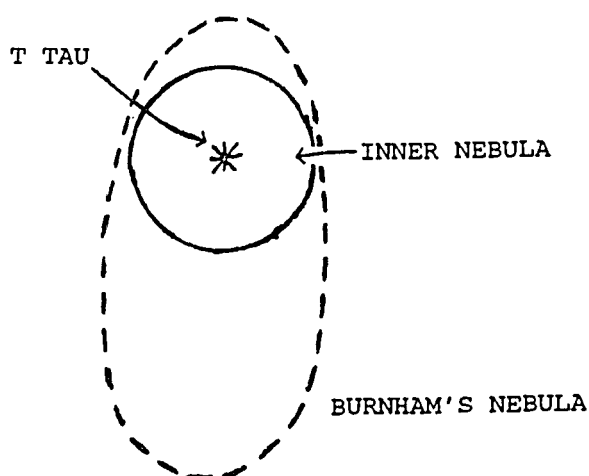


Figure 4.4.5: Schematic diagram of T Tau and Burnham's Nebula

Many of the lines from T Tau are non-gaussian and variable. $H\alpha$ has a broad profile, roughly 500 km/s wide at

the base, with a varying amount of absorption superposed on the blue side of line center (Hartmann 1982; Schneeberger, Worden, & Wilkerson 1979). The NaD lines are also variable, with both the emission and absorption features blueshifted. Hartmann (1982) suggested that the central star might obscure the redshifted part of the NaD emission.

4.3.6.1 Extinction

The complex line profiles in T Tau make it difficult to use hydrogen lines to determine the extinction. Schwartz (1974) observed the nebula surrounding T Tau (Burnham's Nebula), and he found $A_v = 0.9$ from the $H\delta/Pa\gamma$ ratio and from the ratio of the blue to infrared [S II] lines. He also compared the visual spectrum of T Tau to the spectrum of a K0 III with a similar luminosity, and he found that T Tau experiences 1.8 magnitudes of circumstellar extinction in addition to the 0.9 mag of interstellar extinction.

In our infrared spectrum, there is not much of a dropoff in flux from $Pa\beta$ to $Pa9$. This trend indicates high densities and low temperatures in the Paschen line region ($n_e \approx 10^{10} \text{ cm}^{-3}$, $T_e < 10^4 \text{ K}$). If all the reddening were interstellar, the hydrogen lines would give $A_v = 2.9$ (see Figure 4.3). However, as discussed by Schwartz (1974), $A_v/E(B-V)$ might be as large as 8 in the circumstellar environment so A_v may be several magnitudes larger. The $P\alpha\gamma/H\delta$ and $Pa\beta/H\gamma$ ratios give $A_v \approx 2.3 - 2.8$. For this study, we correct line strengths

for $A_v = 2.7$.

4.3.6.2 Physical Structure

Schwartz (1974) determined the physical conditions in the nebular regions around T Tau. In the chromosphere-like inner nebula, he found $10^4 \leq n_e \leq 4 \times 10^4 \text{ cm}^{-3}$ and $9000 \leq T_e \leq 13000 \text{ K}$. In the nebular region south of T Tau he found $3 \times 10^3 \leq n_e \leq 10^4 \text{ cm}^{-3}$ and $7000 \leq T_e \leq 9000 \text{ K}$. Using the [S II] 0.6716/0.6731 μm ratio, he found average densities of $n_e = 2.5 \times 10^4 \text{ cm}^{-3}$, $1.2 \times 10^4 \text{ cm}^{-3}$, and $6.5 \times 10^3 \text{ cm}^{-3}$ within 3", 5", and 7" apertures, respectively. Our signal-to-noise was insufficient to deconvolve either the 0.6716 μm and 0.6731 μm lines or the 1.0320 μm and 1.0336 μm lines. Nevertheless, we can still determine the [S II] $(0.6716 + 0.6731)/(1.0286 + 1.0320 + 1.0336 + 1.0370) \mu\text{m}$ ratio, which gives $n_e = 1.5 \times 10^4 \text{ cm}^{-3}$ for an assumed temperature of $T_e = 10^4 \text{ K}$. This estimate, which is for a 6" aperture, is in good agreement with the results of Schwartz (1974).

Ulrich & Wood (1981) measured line profiles for He I lines in T Tauri stars. They found that the He I 1.0830 μm line in T Tau has a P Cygni profile. Our data confirm this result and show a separation of 300 km/s between the emission and absorption components. The line profile is unlike that of the He I 1.0830 μm line in V645 Cyg. In T Tau, the absorption component is much weaker than the emission. The velocity in the inner part of the optical jet is 150 km/s

(Buhrke et al. 1986), consistent with the velocity of the He I absorption feature. If the He I emission is related to the jet outflow, then the redshifted emission probably comes from the receding part of the outflow.

4.3.6.3 Fluorescence

Hamann & Persson (1992) observed the 0.8446 μm line of O I and report a flux very similar to the flux we measure for the 1.1287 μm line. For UV fluorescence from a star with Ly β in absorption, the 0.8446 μm line is predicted to be about 30 times stronger than the 1.1287 μm line. If Ly β is weakly in emission, the two lines are expected to have similar strengths. It therefore appears that the O I emission from T Tau is partly excited by Ly β fluorescence. Our spectral coverage of T Tau stops just shy of the 1.3165 μm line so we cannot assess the importance of UV continuum fluorescence.

4.3.6.4 Shocks

The spectrum of Burnham's Nebula is very similar to the spectra of Herbig-Haro objects (Herbig 1951; Schwartz 1974; Solf, Bohm, & Raga 1988). Solf et al. note that Herbig-Haro activity is apparent in spectra within 4" of T Tau. Given that Herbig-Haro objects are the result of shocks, it is perhaps surprising that the shock excited lines of [Fe II] and H₂ are not brighter in our infrared spectrum of T Tau. Two factors lead to this result. First, we integrated on T Tau for only about 1 minute per grating setting, as compared

to the 15-20 minutes per grating setting on HH 1. Second, Fe seems to be depleted by about a factor of 3 relative to its abundance in HH 1 (Solf et al. 1988). Several [Fe II] lines are present in our infrared spectrum, but more careful observations are required if a study is to be made of Burnham's Nebula.

4.3.7 HH 1

HH 1 is the brightest of the Herbig-Haro objects. It is quite extended, with a diameter of roughly 10". The emission from Herbig-Haro objects is the result of radiative shocks created in the interaction of a supersonic stellar mass outflow with ambient gas (Schwartz 1975). Both HH 1 and HH 2 are excited by an obscured T Tauri star located midway between the two (Pravdo et al. 1985; Strom et al. 1985; Harvey et al. 1986). HH 1 has a tangential velocity of about 350 km/s in the direction opposite from HH 2.

4.3.7.1 Extinction

The extinction to HH 1 is small compared to the extinction to the other objects in this study. Bohm, Schwartz, & Siegmund (1974) compared blue and infrared [S II] line strengths to determine $A_v \approx 1.86$. Solf, Bohm, & Raga (1988; hereafter SBR) settled on $A_v \approx 1.33$ after considering [S II] and H I line ratios. If one assumes $n_e = 10^4 \text{ cm}^{-3}$ and $T_e = 1.5 \times 10^4 \text{ K}$, the Balmer line data of SBR indicate $A_v \approx$

1.6. We found $A_v \approx 1.7$ by comparing our $\text{Pa}\beta$ and $\text{Pa}\gamma$ line strengths with the $\text{H}\gamma$ and $\text{H}\delta$ data from SBR. Finally, we compared our infrared $[\text{S II}]$ lines with the blue $[\text{S II}]$ lines of SBR and found $A_v \approx 1.6$. For the following analysis of HH 1, we adopt $A_v = 1.6$.

4.3.7.2 Physical Structure

The spectrum of HH 1 is dominated by bright emission lines. The He I 1.0830 μm line is one of the more prominent features in the infrared spectrum. The lower level of the transition is the ground level of the He I triplet terms. It is a metastable state, and it lies only 4.79 eV below the ionization continuum. As a result, all triplet lines are prone to enhancement by collisional excitation. The degree of enhancement of the triplet lines is highly dependent on the density and temperature in the He I emitting region and on the energy required to excite a given transition. The He I singlet lines are weakly affected by collisions, so comparisons of singlet and triplet line strengths show the effects of collisional enhancements and provide information on the density and temperature in the He I emitting region. Using data from SBR and the collisional corrections of Clegg (1987), we compared the singlet and triplet He I line strengths in HH 1 for an assumed density of $n_e = 10^4 \text{ cm}^{-3}$. We find that the strong density and temperature dependences of the helium triplet lines bias the line ratios toward

conditions at the high density, high temperature shock front. The helium line ratios in HH 1 are consistent with $T_e = 1.4 \times 10^4$ K, close to the peak temperature found by SBR.

4.3.7.3 Fluorescence

The 1.1287 and 1.3165 μm lines of oxygen are not detected in our infrared spectrum of HH 1. SBR detected the O I 0.8446 μm line with a dereddened flux of 0.004 relative to He I 1.0830 μm . Our non-detection of the 1.1287 μm line argues weakly against Ly β fluorescence, but nothing further can be said about O I excitation mechanisms based on our spectrum.

We detected two H₂ lines in the J-band spectrum of HH 1, and Elias (1980) detected four H₂ lines in the 2 μm spectrum. We compared these H₂ line strengths with the H₂ models of Black & van Dishoeck (1987). The 1 μm H₂ lines are clearly too weak for any of the fluorescence models. The full set of H₂ line strengths are in reasonably good agreement with the shock model S2 of Black and van Dishoeck (which is for $T = 2000$ K) but not with their model S1 (for $T = 1000$ K).

4.3.7.4 Shocks

Elias (1980) compared the 2 μm H₂ lines with the shock models of Shull & Hollenbach (1978), computed for $T = 1000$ K. The line intensities are very dependent on the preshock density, and the line ratios are highly dependent on the shock velocity. The H₂ lines in the 2 μm spectrum of HH 1

indicate a preshock density of 10^4 cm^{-3} and a shock velocity of 15 km/s. The strength of the (2,0) Q(1) line in our spectrum shows that the shock velocity is probably closer to 12 km/s. With these shock conditions, we should be able to see the (2,0) S(1) and (2,0) S(2) lines near $1.15 \mu\text{m}$ in high resolution data. Line blending in our low resolution spectra prevents definite detections.

If shocks are responsible for producing the [O III] and [Ne III] lines in the visible spectrum of HH 1, then post-shock temperatures must be at least 50000 K. Such temperatures require shock velocities of $\geq 60 \text{ km s}^{-1}$. Based on the high-ionization lines found in the spectrum of HH 1, the shock velocity has been estimated to be between 70 and 100 km s^{-1} (Ortolani & D'Odorico 1980; Schwartz 1978). Most of the other lines present in the spectrum of HH 1, including lines of [C I], [N I], and [O I], can be produced in cooling regions behind shocks. These low-ionization lines are often quite bright in shocked regions (see Chapter 2). H_2 lines probably result from the propagation of shocks into dense molecular regions (Schwartz 1981).

The [Fe II] lines are very prominent in the infrared spectrum of HH 1. We used a number of the [Fe II] lines in our infrared spectrum and in the spectrum of SBR to determine the temperature and density in the Fe^+ region. From the line ratio vs. density curves of Hudgins et al. (1990), assuming $T_e = 1.3 \times 10^4 \text{ K}$, we determined densities of $n_e = (1-2) \times 10^4$

cm^{-3} from the ratios [Fe II] 1.3278/1.3205, 1.2703/1.2567, and 1.2941/1.2567 μm . The 1.3278/1.3205 μm ratio, measured with a single grating setting in high resolution mode, is likely to be the most accurate indicator. It gives a density of $1.0 \times 10^4 \text{ cm}^{-3}$. Nussbaumer & Storey (1988) provide further line ratio vs. density curves for a variety of electron temperatures and [Fe II] line pairs. Using [Fe II] 0.8617 and 0.9268 μm line strengths from SBR, we examined the [Fe II] 0.8617/0.9268 and 0.8617/1.2567 line ratios. The former gives $n_e = 1.0 \times 10^4 \text{ cm}^{-3}$ for $T_e = 3000 \text{ K}$ and $n_e = 3.5 \times 10^4 \text{ cm}^{-3}$ for $T_e = 15000 \text{ K}$. The latter ratio gives $n_e = 4 \times 10^4 \text{ cm}^{-3}$ for $T_e = 5000 \text{ K}$ and $n_e = 9 \times 10^3 \text{ cm}^{-3}$ for $T_e = 7000 \text{ K}$. An electron temperature as high as 10^4 K is only permitted if the 0.8617/1.2567 μm line ratio is underestimated by at least 15%. The electron temperature in the Fe^+ region thus seems to be near 7000 K, and the electron density is $\approx 1.0 \times 10^4 \text{ cm}^{-3}$.

The electron density and electron temperature are not uniform across the surface of HH 1. Electron temperatures range from $(5-20) \times 10^3 \text{ K}$, and electron densities range from $(2-10) \times 10^3 \text{ cm}^{-3}$ (SBR). The [Fe II] lines in HH 1 have a spatial distribution similar to that of the high-ionization lines (SBR). The [Fe II] lines in this work were measured through a 6" beam. It is clear from the line ratios and by comparison with the densities and temperatures presented in SBR that the [Fe II] lines do not depend just on conditions

at the shock front. Instead, the good agreement with other forbidden line indicators shows that the [Fe II] lines provide an average temperature over the shock front and the cooling regions. Hence, large beam [Fe II] measurements cannot be used to make a direct determination of shock temperature and shock velocities.

4.4 Conclusions

4.4.1 Extinction

The primary advantage of the infrared over shorter wavelengths is the diminished effect of dust obscuration. The attenuation at $1.2\ \mu\text{m}$ is only 30% as large as the attenuation at $0.55\ \mu\text{m}$. This advantage is particularly beneficial for star formation studies, where sources are often attenuated by ten or more magnitudes of visual attenuation. From our observations of MWC 349 and LkH α 101, it appears that similar objects could be observed through at least 3 more magnitudes of infrared attenuation, or to a total depth of $A_v \sim 20$. The $0.9 - 1.35\ \mu\text{m}$ region thus should be of great importance in future star formation studies.

We also note that the reddening curves of Figure 4.3 are all in reasonable agreement with the predictions of Case B recombination plus a foreground screen of absorbers. Apparently, deviations from Case B recombination do not

severely alter the line ratios in these objects. Furthermore, for several of the objects, reliable fits could be made based on the infrared data alone. In heavily obscured objects, ratios of Paschen and Balmer lines should provide reliable extinction estimates.

4.4.2 Physical Structure

One of the most important results from this chapter is that 0.9 - 1.35 μm spectra provide evidence for all of the physical regions seen in visible and red data. This result is quite important since it is likely that infrared spectroscopy will be used to study sources too reddened for visual observation.

Lines of He I, [S II], [S III], and [Fe II] can be used to determine physical conditions in the emitting regions. The He I lines are difficult to use because the triplet lines are strongly affected by collisions. The [S III] lines provide an estimate of the electron temperature, but only when combined with the 0.6312 μm line. Electron densities can be determined using just the infrared [S II] and [Fe II] lines.

Finally, the He I 1.0830 μm line is usually optically thick, and it exhibits a P Cygni profile in several young stellar object spectra. The 1.0830 μm line is thus useful for detecting outflows and for determining outflow velocities. Furthermore, the He I 1.0830 μm line is

consistently one of the strongest lines in the spectra of young stellar objects. Narrow-band imaging of star formation regions using a 1.0830 μm filter would probably reveal the locations of a large number of embedded stars.

4.4.3 Fluorescence

Most of the young stellar objects exhibit O I fluorescence. By comparing the strengths of the 1.1287 and 1.3165 μm lines, we were able to determine whether Ly β fluorescence contributes to the O I emission. None of the sources shows fluorescent H₂ emission even though each has the key ingredients - an abundant supply of molecular material and a strong source of UV radiation. Either our measurements are not sensitive enough to detect weak H₂ fluorescence lines in these objects, or perhaps the UV radiation field is attenuated by circumstellar gas and dust, preventing fluorescent emission. In either case, it is clear that H₂ fluorescence is much less common than O I fluorescence.

4.4.4 Shocks

[Fe II] and H₂ lines are often excited by shocks in young stellar objects. [Fe II] line ratios can be used to determine densities in the shocked regions. Comparison of our large beam [Fe II] measurements with the longslit measurements of SBR shows that large beam measurements

provide an average electron density over the beam. It is thus necessary to use longslit spectroscopy if one wants to determine the velocity of a shock and the density at the shock front. In sources excited purely by shocks, an estimate can be made of the shock velocity based on the temperature required to excite the highest ionization lines in the spectrum.

TABLE 4.1

LOG OF INFRARED OBSERVATIONS OF YOUNG STELLAR OBJECTS

Object	Dates	Resolution*	Wavelength Coverage (μm)	Reference Star	Spectral Type	On-source Integration Time (min)	Photometry Reference ^b
MWC 349	11/10/89	low	0.90 - 1.60	HR 7887	F0 V	29	MPC
	11/2/90	high	0.94 - 0.96 1.025 - 1.045 1.275 - 1.295	HR 7887	F0 V	27	MPC
LkH α 101	11/10/89	high	0.99 - 1.35	HR 1489	G0 V	96	MPC
	11/2/90	high	0.89 - 0.99	HR 1489	G0 V	52	MPC
V645 Cyg	11/12,13/89	high	0.98 - 1.29	HR 8170	F8 V	168	MPC
T Tau	11/11/89	high	0.94 - 1.30	HR 1331	F0 V	73	Low
	10/27/90	high	0.905 - 0.945 1.025 - 1.045 1.275 - 1.295	HR 1391	F7 V	71	Low
R Mon	11/10,12/89	high	0.98 - 1.00 1.025 - 1.35	HR 2208	G2 V	73	JD
	11/2/90	high	0.895 - 1.03	HR 2208	G1 V	53	JD
HH 1	11/12/89	low	1.02 - 1.35 1.44 - 1.54	HR 1967	F3 V	93	Elias
	11/12/89	high	1.23 - 1.25 1.31 - 1.33	HR 1967	F3 V	56	Elias
GL 490	11/10/89	high	0.985 - 1.005 1.12 - 1.14 1.19 - 1.33	HR 937	G0 V	109	MPC
	11/11/89	high	0.915 - 1.225	HR 1071	F7 V	203	MPC

*High resolution indicates use of the 600 l/mm grating, $R \approx 1000$ at J. Low resolution indicates use of the 150 l/mm grating, $R \approx 250$ at J.

^bMPC = McGregor, Persson, & Cohen (1984); Low = Low et al. (1970); JD = Jones & Dyck (1978); Elias = Elias (1980).

TABLE 4.2

LOG OF VISIBLE OBSERVATIONS OF YOUNG STELLAR OBJECTS

Object	Date	Wavelength Coverage (Å)	Integration Time (min)	Photometry Reference ^a
MWC 349	6/11/91	4002 - 6947	20	MPC
LkHα 101	3/5/91	4004 - 6865	30	MPC
V645 Cyg N0	6/11/91	4002 - 6947	5	-
V645 Cyg N1	6/11/91	4002 - 6947	8	-
T Tau	3/5/91	4004 - 6865	7	HK
R Mon	3/5/91	4004 - 6865	10	-

^aMPC = McGregor, Persson, & Cohen (1984); HK = Herbst & Koret (1988).

TABLE 4.3.1
LINE IDENTIFICATIONS AND FLUXES IN THE 0.41 - 0.68 μm
SPECTRA OF MWC 349, LkH α 101, AND R Mon

λ (μm)		IDENTIFICATION	$\Lambda_\lambda/\Lambda_\nu$	MWC 349	LkH α 101	R Mon
0.41734	Fe II	$b^4P_{5/2} - z^4D_{5/2}^o$	1.4067			8.91(-14)
0.41789	Fe II	$b^4P_{5/2} - z^4F_{7/2}^o$	1.4047			
0.42332	Fe II	$b^4P_{5/2} - z^4D_{7/2}^o$	1.3854			8.37(-14)
0.42440	[Fe II]	$a^4F_{9/2} - a^4G_{11/2}$	1.3814			3.35(-14)
0.4282			1.3678			5.74(-14)
0.4300			1.3612			1.60(-13)
0.43405	H I	2-5	1.3466	2.11(-14)	1.44(-15)	1.85(-13)
0.43584	[Fe II]	$a^4F_{3/2} - a^4G_{5/2}$	1.3398		1.40(-15)	
0.43593	[Fe II]	$a^6D_{7/2} - a^6S_{5/2}$	1.3395			
0.4385			1.3300			3.28(-14)
0.44138	[Fe II]	$a^6D_{5/2} - a^6S_{5/2}$	1.3194		5.50(-16)	3.91(-14)
0.44145	[Fe II]	$a^6D_{7/2} - b^4F_{3/2}$	1.3192			
0.44163	[Fe II]	$a^6D_{9/2} - b^4F_{9/2}$	1.3185			
0.44892	Fe II	$b^4F_{7/2} - z^4F_{5/2}^o$	1.2918		7.52(-16)	4.61(-14)
0.45202	Fe II	$b^4F_{9/2} - z^4F_{7/2}^o$	1.2806		7.94(-16)	1.28(-13)
0.45226	Fe II	$b^4F_{5/2} - z^4D_{3/2}^o$	1.2797			
0.45550	[Fe II]	$a^6D_{3/2} - b^4F_{7/2}$	1.2680		1.33(-15)	1.20(-13)
0.45559	Fe II	$b^4F_{7/2} - z^4F_{7/2}^o$	1.2677			
0.45828	Fe II	$b^4F_{5/2} - z^4F_{7/2}^o$	1.2581		1.41(-15)	1.31(-13)
0.45838	Fe II	$b^4F_{9/2} - z^4D_{7/2}^o$	1.2577			
0.45840	Fe II	$b^4P_{3/2} - z^6P_{3/2}^o$	1.2577			

0.4621			1.2446			1.20(-14)
0.46293	Fe II	$b^4F_{9/2} - z^4F_{9/2}^o$	1.2416		1.83(-15)	7.75(-14)
0.4657	Fe II	$a^6S_{5/2} - z^4D_{5/2}^o$	1.2320	2.86(-14)		
0.46581	[Fe III]	$3d^6^5D_4 - 3d^6^3F_4$	1.2316			
0.46668	Fe II	$b^4F_{7/2} - z^4F_{9/2}^o$	1.2286			3.66(-14)
0.4697			1.2182	1.15(-14)		
0.47015	[Fe III]	$3d^6^5I_3 - 3d^6^3F_3$	1.2168	4.89(-15)		
0.4730			1.2070			2.74(-14)
0.48613	H I	2-4	1.1643	2.82(-13)	2.14(-14)	6.40(-13)
0.49239	Fe II	$a^6S_{5/2} - z^6P_{3/2}^o$	1.1448	2.04(-14)	1.20(-15)	1.38(-13)
0.49734	[Fe II]	$a^4F_{5/2} - b^4F_{5/2}$	1.1300		4.91(-16)	
0.5006	[Fe II]	$a^4F_{5/2} - b^4F_{7/2}$	1.1205	6.58(-14)		
0.50068	[O III]	$2p^3P_2 - 2p^1D_2$	1.1203			
0.5007	[Fe II]	$a^6D_{3/2} - b^4P_{5/2}$	1.1202			
0.50184	Fe II	$a^6S_{5/2} - z^6P_{5/2}^o$	1.1169	7.06(-14)	2.05(-15)	1.79(-13)
0.51588	[Fe II]	$a^4F_{9/2} - a^4H_{13/2}$	1.0785	3.62(-14)	1.95(-15)	
0.51690	Fe II	$a^6S_{5/2} - z^6P_{7/2}^o$	1.0759	3.24(-14)	2.40(-15)	2.38(-13)
0.51976	Fe II	$a^4G_{5/2} - z^4F_{3/2}^o$	1.0686	2.88(-14)	2.53(-15)	1.14(-13)
0.52201	[Fe II]	$a^4F_{7/2} - a^4H_{9/2}$	1.0629		7.42(-16)	
0.52346	Fe II	$a^4G_{7/2} - z^4F_{5/2}^o$	1.0593	2.82(-14)	3.07(-15)	1.20(-13)
0.52616	[Fe II]	$a^4F_{7/2} - a^4H_{11/2}$	1.0525	2.28(-14)	2.21(-15)	5.58(-14)
0.52734	[Fe II]	$a^4F_{9/2} - b^4P_{5/2}$	1.0499	1.65(-13)		

0.52760	Fe II	$a^4G_{9/2} - z^4F_{7/2}^o$	1.0491		6.12(-15)	1.57(-13)
0.53166	Fe II	$a^4G_{11/2} - z^4F_{9/2}^o$	1.0395	7.32(-14)	9.58(-15)	1.96(-13)
0.53337	[Fe II]	$a^4F_{5/2} - a^4H_{9/2}$	1.0354	2.36(-14)		3.82(-14)
0.53621	[Fe II]	$a^4F_{9/2} - a^2D_{5/2}$	1.0289	1.50(-14)	1.46(-15)	8.96(-14)
0.53629	Fe II	$a^4G_{9/2} - z^4D_{7/2}^o$	1.0288			
0.53765	[Fe II]	$a^4F_{3/2} - a^4I_{7/2}$	1.0258	1.47(-14)	6.86(-16)	
0.54127	[Fe II]	$a^4F_{5/2} - a^2D_{3/2}$	1.0175	3.02(-14)	6.53(-16)	
0.54133	[Fe II]	$a^4F_{9/2} - a^2H_{11/2}$	1.0175			
0.5427			1.0145	2.61(-14)		
0.54330	Fe II	$b^2H_{9/2} - z^4F_{7/2}^o$	1.0131		1.58(-15)	
0.54332	[Fe II]	$a^4F_{7/2} - b^4P_{5/2}$	1.0131			
0.5437			1.0123	6.30(-15)		
0.55273	[Fe II]	$a^4F_{7/2} - a^2D_{5/2}$	0.9933	5.69(-14)		
0.55349	Fe II	$b^2I_{11/2} - z^4F_{9/2}^o$	0.9916		5.20(-15)	5.08(-14)
0.5583			0.9819	2.78(-14)		2.48(-14)
0.57548	[N II]	$2p^1D_2 - 2p^1S_0$	0.9492	5.59(-13)		
0.58757	He I	$2p^3P^o - 3d^3D$	0.9278	7.95(-13)	7.48(-15)	
0.58760	He I	$2p^3P^o - 3d^3D$	0.9277			
0.58900	Na I	$3s^2S_{1/2} - 3p^2P_{3/2}^o$	0.9253	5.81(-14)		5.00(-14)
0.58959	Na I	$3s^2S_{1/2} - 3p^2P_{1/2}^o$	0.9243			
0.59576	Si II	$4^2P_{1/2}^o - 5^2S_{1/2}$	0.9138	2.73(-14)	4.76(-15)	9.51(-15)
0.59790	Si II	$4^2P_{3/2}^o - 5^2S_{1/2}$	0.9102	2.22(-14)	7.20(-15)	1.42(-14)

0.59914	Fe II	$n^4G_{11/2} - z^6F_{9/2}^o$	0.9081	4.03(-14)		1.89(-14)
0.6014			0.9044			2.07(-14)
0.60455	Fe II	$4s^4F_{3/2} - 4p^4F_{3/2}^o$	0.8992	2.40(-14)	4.12(-15)	2.06(-14)
0.60841	Fe II	$n^4G_{9/2} - z^6F_{7/2}^o$	0.8929			2.27(-14)
0.6114			0.8881			2.20(-14)
0.6125			0.8863	3.50(-14)	2.84(-15)	1.14(-14)
0.61477	Fe II	$4s^4D_{3/2} - 4p^4P_{1/2}^o$	0.8826	5.06(-14)	2.36(-15)	5.43(-14)
0.61493	Fe II	$4s^4D_{1/2} - 4p^4P_{1/2}^o$	0.8824			
0.61580	Fe II	$4s^4F_{5/2} - 4p^4F_{7/2}^o$	0.8810	2.12(-14)	1.65(-15)	
0.61853	Fe II	$n^4G_{9/2} - z^6F_{11/2}^o$	0.8766		1.56(-15)	1.74(-14)
0.62180	Fe II	$4s^4F_{3/2} - 4p^6D_{1/2}^o$	0.8713		2.78(-15)	1.22(-14)
0.62196	Fe II	$4s^4F_{5/2} - 4p^6D_{3/2}^o$	0.8712			
0.62384	Fe II	$4s^4D_{3/2} - 4p^4P_{3/2}^o$	0.8682	6.55(-14)	6.05(-15)	
0.62394	Fe II	$4s^4F_{9/2} - 4p^6D_{7/2}^o$	0.8681			
0.62400	Fe II	$4s^4D_{1/2} - 4p^4P_{3/2}^o$	0.8680			
0.62489	Fe II	$4p^4D_{7/2}^o - 4s^2^4D_{5/2}$	0.8666	8.70(-14)	1.43(-14)	9.75(-14)
0.6277			0.8621			2.98(-14)
0.63002	[O I]	$2s^22p^4^3P_2 - 2p^4^1D_2$	0.8585	1.95(-13)	1.95(-14)	1.06(-13)
0.63102	[S III]	$^1S_0 - ^1D_2$	0.8567	2.70(-13)		
0.63174	Fe II	$4s^4F_{7/2} - 4p^4F_{9/2}^o$	0.8558		1.70(-14)	2.27(-14)
0.63180	Fe II	$4p^4D_{7/2}^o - 4s^2^4D_{7/2}$	0.8557			
0.6335			0.8531			1.18(-14)

0.63471	Si II	$4^2S_{1/2} - 4^2P_{3/2}^o$	0.8512	7.40(-14)	1.08(-14)	1.92(-14)
0.63639	[O I]	$2s^22p^4^3P_1 - 2p^4^1D_2$	0.8485	9.20(-14)	1.25(-14)	5.87(-14)
0.6384			0.8454	1.28(-13)	2.23(-14)	2.26(-14)
0.6404			0.8423			8.75(-15)
0.64169	Fe II	$4s^4D_{5/2} - 4p^4P_{5/2}^o$	0.8403	2.56(-14)	4.44(-15)	1.66(-14)
0.64327	Fe II	$a^6S_{5/2} - z^6D_{5/2}^o$	0.8379	3.05(-14)		1.76(-14)
0.6445			0.8360		6.64(-15)	
0.64564	Fe II	$4s^4D_{7/2} - 4p^4P_{5/2}^o$	0.8342	9.15(-14)	1.48(-14)	4.37(-14)
0.64912	Fe II	$4p^4D_{3/2}^o - 4s^2^4D_{5/2}$	0.8288		1.48(-14)	
0.64930	Fe II	$4p^4D_{3/2}^o - 4s^2^4D_{3/2}$	0.8286			
0.65161	Fe II	$4s^2^6S_{5/2} - 4p^6D_{7/2}^o$	0.8250		2.35(-14)	
0.65481	[N II]	$2p^3P_1 - 2p^1D_2$	0.8201	9.15(-12)	4.33(-13)	
0.65628	H I	2-3	0.8177	2.16(-11)	3.43(-12)	5.01(-12)
0.65830	[N II]	$2p^3P_2 - 2p^1D_2$	0.8147	1.03(-11)	2.88(-14)	
0.66682	[Ni II]	$a^2D_{5/2} - a^2F_{5/2}$	0.8016			2.10(-14)
0.66781	He I	$2p^1P_1^o - 3d^1D_2$	0.8000	6.34(-13)	5.73(-15)	
0.67164	[S II]	$3p^3^4S_{3/2} - 3p^3^2D_{5/2}^o$	0.7940			3.84(-14)
0.67308	[S II]	$3p^3^4S_{3/2} - 3p^3^2D_{3/2}^o$	0.7918			5.50(-14)

TABLE 4.3.2

LINE IDENTIFICATIONS AND FLUXES IN THE 0.41 - 0.68 μm
SPECTRA OF V645 Cyg AND T Tau

λ (μm)		IDENTIFICATION	A_λ/Λ_v	V645 Cyg N0	V645 Cyg N1	T Tau
0.41017	H I	2-6	1.4313			9.36(-13)
0.43405	H I	2-5	1.3466			2.62(-12)
0.48613	H I	2-4	1.1643	-5.25(-15)		
0.48613	H I	2-4	1.1643	5.50(-14)	1.78(-14)	4.76(-12)
0.49239	Fe II	$a^6S_{5/2} - z^6P_{3/2}^o$	1.1448	-5.28(-15)	-2.88(-15)	
0.49239	Fe II	$a^6S_{5/2} - z^6P_{3/2}^o$	1.1448	6.86(-15)	4.58(-16)	
0.50184	Fe II	$a^6S_{5/2} - z^6P_{5/2}^o$	1.1169	-6.08(-15)		
0.50184	Fe II	$a^6S_{5/2} - z^6P_{5/2}^o$	1.1169	1.28(-14)		
0.51690	Fe II	$a^6S_{5/2} - z^6P_{7/2}^o$	1.0759	-7.63(-15)	-4.39(-15)	
0.51690	Fe II	$a^6S_{5/2} - z^6P_{7/2}^o$	1.0759	1.05(-14)	3.01(-15)	
0.5186			1.0715	9.75(-15)	-3.01(-15)	
0.51976	Fe II	$a^4G_{5/2} - z^4F_{3/2}^o$	1.0686	1.05(-14)	3.15(-15)	
0.52346	Fe II	$a^4G_{7/2} - z^4F_{5/2}^o$	1.0593	-4.33(-15)	-1.66(-15)	
0.52346	Fe II	$a^4G_{7/2} - z^4F_{5/2}^o$	1.0593	1.03(-14)	4.10(-15)	
0.52760	Fe II	$a^4G_{9/2} - z^4F_{7/2}^o$	1.0491	1.26(-14)		
0.53166	Fe II	$a^4G_{11/2} - z^4F_{9/2}^o$	1.0395	1.47(-14)		
0.58900	Na I	$3s^2S_{1/2} - 3p^2P_{3/2}^o$	0.9253	-4.68(-14)	-3.01(-14)	
0.58959	Na I	$3s^2S_{1/2} - 3p^2P_{1/2}^o$	0.9243			
0.59914	Fe II	$a^4G_{11/2} - z^6F_{9/2}^o$	0.9081	9.96(-15)	3.30(-15)	

0.6136			0.8845		2.43(-15)	
0.61477	Fe II	$4s^4D_{3/2} - 4p^4P_{1/2}^o$	0.8826	1.07(-14)	2.36(-15)	
0.61493	Fe II	$4s^4D_{1/2} - 4p^4P_{1/2}^o$	0.8824			
0.6229			0.8697	4.91(-15)	2.59(-15)	
0.62384	Fe II	$4s^4D_{3/2} - 4p^4P_{3/2}^o$	0.8682	1.39(-14)	9.34(-15)	
0.62394	Fe II	$4s^4F_{9/2} - 4p^6D_{7/2}^o$	0.8681			
0.62400	Fe II	$4s^4D_{1/2} - 4p^4P_{3/2}^o$	0.8680			
0.62489	Fe II	$4p^4D_{7/2}^o - 4s^2^4D_{5/2}$	0.8666	1.35(-14)	2.74(-15)	
0.63002	[O I]	$2s^22p^4^3P_2 - 2p^4^1D_2$	0.8585	-1.02(-14)	-3.44(-15)	
0.63002	[O I]	$2s^22p^4^3P_2 - 2p^4^1D_2$	0.8585	3.32(-14)	1.08(-14)	1.36(-12)
0.63639	[O I]	$2s^22p^4^3P_1 - 2p^4^1D_2$	0.8485	-4.35(-15)	-3.04(-15)	
0.63639	[O I]	$2s^22p^4^3P_1 - 2p^4^1D_2$	0.8485	6.24(-15)	1.20(-15)	4.82(-13)
0.64169	Fe II	$4s^4D_{5/2} - 4p^4P_{5/2}^o$	0.8403	6.50(-15)		
0.64327	Fe II	$a^6S_{5/2} - z^6D_{5/2}^o$	0.8379	1.23(-14)	6.04(-15)	
0.64564	Fe II	$4s^4D_{7/2} - 4p^4P_{5/2}^o$	0.8342	1.19(-14)	2.93(-15)	
0.6499			0.8276			-4.00(-13)
0.65161	Fe II	$4s^2^6S_{5/2} - 4p^6D_{7/2}^o$	0.8250	8.35(-15)	4.76(-15)	
0.65628	H I	2-3	0.8177	6.58(-13)	2.60(-13)	4.39(-11)
0.67164	[S II]	$3p^3^4S_{3/2} - 3p^3^2D_{5/2}^o$	0.7940	1.46(-14)	1.58(-14)	1.91(-13)
0.67308	[S II]	$3p^3^4S_{3/2} - 3p^3^2D_{3/2}^o$	0.7918	2.11(-14)	2.08(-14)	5.33(-13)
0.6878			0.7691	-1.90(-14)	-9.75(-15)	

TABLE 4.3.3

LINE IDENTIFICATIONS AND FLUXES IN THE 0.89 - 1.35 μm
SPECTRA OF MWC 349, LkH α 101, AND R Mon

λ (μm)		IDENTIFICATION	Λ_x/Λ_y	MWC 349	LkH α 101	R Mon
0.88919	[Fe II]	$a^4F_{7/2} - a^4P_{3/2}$	0.4886		1.56(-14)	
0.89124	Fe II	$z^6D_{5/2} - c^4F_{3/2}$	0.4867		4.28(-14)	
0.89265	Fe II	$5s^4D_{7/2} - 5p^4D_{5/2}^o$	0.4854		1.80(-13)	
0.90149	H I	3-10	0.4775		5.40(-13)	2.61(-13)
0.90519	[Fe II]	$a^4F_{7/2} - a^4P_{5/2}$	0.4744		4.86(-14)	
0.90615	C I	$3s^3P_1^o - 3p^3P_2$	0.4737			6.23(-14)
0.90625	C I	$3s^3P_0^o - 3p^3P_1$	0.4736			
0.90690	[C III]	$^3P_1 - ^1D_2$	0.4731	5.75(-12)	1.67(-13)	
0.90755	Fe II	$5s^4D_{5/2} - 5p^4P_{5/2}^o$	0.4725			
0.90774	Fe II	$5s^4D_{5/2} - 5p^4P_{3/2}^o$	0.4724			
0.90783	C I	$3s^3P_1^o - 3p^3P_1$	0.4723			
0.90886	C I	$3s^3P_1^o - 3p^3P_0$	0.4715		8.87(-14)	7.78(-14)
0.90949	C I	$3s^3P_2^o - 3p^3P_2$	0.4707			
0.91228	Fe II	$5s^4D_{7/2} - 5p^4D_{7/2}^o$	0.4684		9.43(-14)	5.12(-14)
0.91325	Fe II	$5s^4D_{7/2} - 5p^4F_{9/2}^o$	0.4676		1.07(-13)	
0.91759	Fe II	$5s^4D_{5/2} - 5p^4F_{7/2}^o$	0.4640		3.66(-13)	8.90(-14)
0.91780	Fe II	$5s^4D_{3/2} - 5p^4F_{5/2}^o$				
0.9189			0.4629	2.16(-12)		
0.91977	Fe II	$5s^4D_{3/2} - 5p^4D_{3/2}^o$	0.4622		4.00(-13)	7.17(-14)
0.92035	Fe II	$5s^4D_{1/2} - 5p^4F_{3/2}^o$	0.4618			

0.92182	Mg II	$4s^2S_{1/2} - 4p^2P_{3/2}^o$	0.4606		2.89(-13)	
0.92266	[Fe II]	$a^4F_{5/2} - a^4P_{3/2}$	0.4599	1.20(-11)	7.68(-13)	4.85(-13)
0.92290	H I	3-9	0.4597			
0.92443	Mg II	$4s^2S_{1/2} - 4p^2P_{1/2}^o$	0.4585		2.04(-13)	
0.92660	O I	$3p^5P_3 - 3d^5D_{4,3}^o$	0.4568		3.62(-14)	7.69(-14)
0.92676	[Fe II]	$a^4F_{3/2} - a^4P_{1/2}$	0.4566			
0.9286			0.4552	6.49(-13)		
0.92970	Fe II	$5s^4D_{5/2} - 5p^4D_{5/2}^o$	0.4543		1.56(-13)	
0.9352			0.4500		4.95(-14)	
0.9373			0.4484		3.02(-14)	
0.93868	N I	$3s^2P_{1/2} - 3p^2D_{3/2}^o$	0.4473	1.81(-12)	1.86(-13)	
0.93928	N I	$3s^2P_{3/2} - 3p^2D_{5/2}^o$	0.4469			
0.94058	C I	$3s^1P_1^o - 3p^1D_2$	0.4459		1.04(-13)	1.17(-13)
0.94607	N I	$3s^2P_{3/2} - 3p^2D_{3/2}^o$	0.4417	6.62(-13)		
0.94978	Fe II	$4p^4P_{5/2}^o - 4s^2^4P_{3/2}$	0.4389	5.07(-13)	1.49(-13)	
0.95311	[S III]	$^3P_2 - ^1D_2$	0.4364	2.30(-11)	1.89(-13)	
0.95459	H I	3-8	0.4354	1.39(-11)	1.17(-12)	2.67(-13)
0.95726	Fe II	$4p^4P_{5/2}^o - 4s^2^4P_{5/2}$	0.4334	2.77(-12)	6.42(-13)	
0.96132			0.4305		1.33(-13)	
0.96585	C I	$3s^3P_2^o - 3p^3S_1$	0.4272			4.55(-14)
0.9684			0.4254			1.90(-14)
0.98121	Fe II	$4p^4P_{3/2}^o - 4s^2^4P_{1/2}$	0.4165		3.05(-13)	

0.9837			0.4148			3.20(-14)
0.9846			0.4142		3.75(-14)	3.26(-14)
0.9877			0.4121		8.55(-14)	
0.98948	Fe II	$4p^4P_{3/2}^o - 4s^2^4P_{3/2}$	0.4109		2.26(-13)	6.04(-14)
0.9910	C II	$4f^2F^o - 5g^2G$	0.4099		2.22(-13)	
0.9950			0.4073			9.34(-14)
0.99563	Fe II	$4p^4F_{9/2}^o - 4s^2^4G_{9/2}$	0.4069		2.40(-13)	
0.99760	Fe II	$4p^4P_{3/2}^o - 4s^2^4P_{5/2}$	0.4056		1.16(-13)	
0.99976	Fe II	$4p^4F_{9/2}^o - 4s^2^4G_{11/2}$	0.4042	5.34(-12)	1.94(-12)	1.45(-13)
1.00494	Fe II	$4p^4P_{1/2}^o - 4s^2^4P_{1/2}$	0.4011	3.33(-11)	3.36(-12)	4.96(-13)
1.00451	H I	3-7	0.4008			
1.01318	Fe II	$4p^4P_{1/2}^o - 4s^2^4P_{3/2}$	0.3956		1.04(-13)	
1.01735	Fe II	$4p^4D_{7/2}^o - 4s^2^4G_{9/2}$	0.3930	1.72(-12)	6.45(-13)	
1.0212			0.3906		7.58(-14)	
1.02867	[S II]	$^2D_{3/2}^o - ^2P_{3/2}^o$	0.3861	9.09(-13)	9.02(-14)	2.74(-14)
1.03205	[S II]	$^2D_{5/2}^o - ^2P_{3/2}^o$	0.3840	2.15(-12)	1.76(-13)	
1.03364	[S II]	$^2D_{3/2}^o - ^2P_{1/2}^o$	0.3831	1.24(-12)	1.05(-13)	
1.03705	[S II]	$^2D_{5/2}^o - ^2P_{1/2}^o$	0.3810	6.00(-13)	4.41(-14)	
1.0398	[N I]	$^2D_{5/2}^o - ^2P_{1/2,3/2}^o$	0.3794	2.52(-12)	7.90(-14)	
1.04028	Fe II	$5s^6D_{9/2} - 4p^6F_{9/2}^o$	0.3791			
1.0408	[N I]	$^2D_{3/2}^o - ^2P_{1/2,3/2}^o$	0.3788			

1.04311	[Fe II]	$a^2G_{9/2} - a^4G_{11/2}$	0.3775	1.94(-12)	3.55(-13)	
1.04326	[Fe II]	$a^2H_{9/2} - b^2G_{9/2}$	0.3774			
1.04598	[Ni II]	$a^2F_{7/2} - b^2D_{5/2}$	0.3758			3.76(-14)
1.04909	Fe II	$4p^4F_{7/2}^o - 4s^2^4G_{7/2}$	0.3740	2.98(-12)	4.43(-13)	
1.05015	Fe II	$4p^4F_{7/2}^o - 4s^2^4G_{9/2}$	0.3734	1.57(-12)	1.99(-12)	1.08(-13)
1.05251	Fe II	$4p^4D_{5/2}^o - 4s^2^4G_{7/2}$	0.3721	1.67(-12)	3.96(-13)	
1.05464	Fe II	$5s^6D_{9/2} - 4p^6F_{11/2}^o$	0.3708		6.06(-14)	
1.06832	C I	$3s^3P_1^o - 3p^3D_2$	0.3632		1.02(-13)	2.50(-13)
1.06854	C I	$3s^3P_0^o - 3p^3D_1$	0.3631			
1.06913	C I	$3s^3P_2^o - 3p^3D_3$	0.3628			
1.07111	Fe II	$5s^6D_{3/2} - 4p^6D_{5/2}^o$	0.3617		8.48(-14)	
1.07296	C I	$3s^3P_2^o - 3p^3D_2$	0.3607		4.73(-14)	
1.07498	Fe II	$5s^6D_{7/2} - 4p^6F_{7/2}^o$	0.3596		9.23(-14)	
1.08302	He I	$2s^3S - 2p^3P^o$	0.3553	1.47(-10)	2.64(-12)	1.69(-13)
1.08626	Fe II	$4p^4F_{5/2}^o - 4s^2^4G_{7/2}$	0.3536		2.66(-12)	1.63(-13)
1.08716	Fe II	$4p^4F_{5/2}^o - 4s^2^4G_{5/2}$	0.3531		4.15(-13)	
1.09129	He I	$3^3D - 6^3F_0^o$	0.3510		4.18(-13)	
1.09142	Mg II	$3d^2D_{5/2} - 4p^2P_{3/2}^o$	0.3509			
1.09153	Mg II	$3d^2D_{3/2} - 4p^2P_{3/2}^o$	0.3509			
1.09170	He I	$3^1D - 6^1F^o$	0.3508			
1.09381	H I	3-6	0.3496	8.02(-11)	7.69(-12)	8.79(-13)
1.10131	He I	$3s^1S - 5p^1P^o$	0.3459		3.36(-14)	
1.10450	He I	$3p^1P^o - 6d^1D$	0.3443		6.09(-14)	

1.1087			0.3422		1.39(-13)	
1.11256	Fe II	$4p^4F_{3/2}^\circ - 4s^2^4G_{5/2}$	0.3403	5.04(-12)	3.24(-12)	9.38(-14)
1.1172			0.3380		9.94(-14)	
1.1223			0.3355		9.93(-14)	
1.1237			0.3348		8.85(-14)	
1.1261			0.3337		1.96(-13)	
1.1287	O I	$3p^3P - 3d^3D^\circ$	0.3325	2.05(-11)	5.14(-12)	2.81(-13)
1.1349			0.3295			8.26(-14)
1.1382			0.3280			2.71(-14)
1.1412			0.3266	2.62(-12)		8.14(-14)
1.1450	[Fe II]	$a^4P_{1/2} - b^4F_{9/2}$	0.3249		3.44(-14)	
1.1450	[Fe II]	$b^4F_{9/2} - b^4D_{1/2}$	0.3249			
1.1455	[Fe II]	$b^4F_{9/2} - b^4D_{3/2}$	0.3246			
1.1475			0.3237			4.33(-14)
1.1500			0.3226			2.64(-14)
1.1528			0.3213			3.31(-14)
1.1552			0.3203			7.86(-14)
1.16193	C I	$3p^3D_1 - 3d^3D_1^\circ$	0.3173		4.84(-14)	
1.16671	C I	$3p^3D_3 - 3d^3D_3^\circ$	0.3152			6.78(-14)
1.16671	C I	$3p^3S_1 - 3d^3P_2^\circ$	0.3152			

1.17475	C I	$3p^3D_1 - 3d^3F_2^o$	0.3117		1.33(-13)	1.36(-13)
1.17540	C I	$3p^3D_2 - 3d^3F_3^o$	0.3114			
1.17540	C I	$3p^3D_3 - 3d^3F_4^o$	0.3114			
1.1783			0.3102		6.24(-14)	4.98(-14)
1.18282	Mg I	$3p^1P_1^o - 4s^1S^o$	0.3083		9.66(-14)	1.37(-13)
1.1829	[Fe II]	$b^4F_{5/2} - b^4D_{5/2}$	0.3083			
1.1833	[Fe II]	$b^4F_{3/2} - b^4D_{7/2}$	0.3081			
1.18493	C I	$3p^3D_2 - 4s^3P_2^o$	0.3074		4.73(-14)	
1.18804	C I	$3p^3D_1 - 4s^3P_0^o$	0.3061		8.46(-14)	
1.18949	C I	$3p^3D_3 - 4s^3P_2^o$	0.3055		4.43(-14)	
1.18949	C I	$3p^3D_2 - 4s^3P_1^o$	0.3055			
1.19691	He I	$3p^3P^o - 5d^3D$	0.3025	4.86(-12)	6.18(-14)	
1.1990			0.3016		4.93(-14)	
1.2035			0.2998		8.54(-14)	
1.2062			0.2987		1.09(-13)	
1.20836	Mg I	<i>multiplet 26</i>	0.2979		6.52(-14)	
1.2120			0.2964			1.86(-13)
1.2380			0.2865		2.30(-13)	
1.2400			0.2857		9.80(-14)	
1.2427			0.2847		4.00(-13)	3.34(-13)
1.2465			0.2833		2.32(-13)	2.56(-14)
1.2480			0.2828			5.05(-14)

1.2537			0.2807	6.75(-12)		
1.25670	[Fe II]	$a^6D_{9/2} - a^4D_{7/2}$	0.2797		5.53(-13)	1.48(-13)
1.2580			0.2792			8.44(-14)
1.2595			0.2787		4.61(-13)	
1.2627			0.2775		2.43(-13)	
1.2643			0.2770		1.19(-13)	
1.2691			0.2753		1.38(-13)	1.33(-13)
1.2720			0.2743		2.50(-13)	
1.2727			0.2740			1.56(-13)
1.27848	He I	$3d^3D - 5f^3F^o$	0.2720	1.39(-11)	5.02(-13)	1.44(-13)
1.2805			0.2713		1.94(-12)	
1.28180	H I	3-5	0.2709	2.42(-10)	3.42(-11)	1.59(-12)
1.2899			0.2682	5.96(-13)		
1.29427	[Fe II]	$a^6D_{5/2} - a^4D_{5/2}$	0.2667	5.16(-13)		
1.29684	He I	$3p^1P^o - 5d^1D$	0.2658	7.21(-13)		
1.29777	[Fe II]	$a^6D_{1/2} - a^4D_{3/2}$	0.2656	1.04(-12)		
1.2985	He I	$3d^3D - 5p^3P^o$	0.2653			
1.31650	O I	$3^3P - 4^3S$	0.2595	2.40(-12)	1.68(-12)	
1.3208			0.2581		1.10(-13)	
1.3290			0.2556		1.66(-13)	
1.3434			0.2512		1.84(-13)	

1.3496			0.2493		2.02(-13)	
--------	--	--	--------	--	-----------	--

TABLE 4.3.4

LINE IDENTIFICATIONS AND FLUXES IN THE 0.89 - 1.35 μm
SPECTRA OF V645 Cyg, GL 490, T Tau, AND HH 1

λ (μm)		IDENTIFICATION	A_λ/A_v	V645 Cyg	GL 490	T Tau	HH1
0.9212			0.4611			4.08(-13)	
0.92290	H I	3-9	0.4597		1.62(-14)	1.73(-12)	
0.95459	H I	3-8	0.4354		1.46(-14)	3.04(-12)	
0.9816			0.4163			2.72(-13)	
0.9848			0.4141			6.00(-13)	
0.99976	Fe II	$4p\ ^4F_{9/2} - 4s^2\ ^4G_{11/2}$	0.4042	1.73(-14)	2.69(-14)	3.99(-13)	
1.00494	H I	3-7	0.4008	8.75(-14)	3.43(-14)	3.92(-12)	
1.0075			0.3992			5.73(-13)	
1.0104			0.3973		1.52(-14)		
1.0275			0.3867			1.08(-13)	
1.02867	[S II]	$^2D_{3/2}^\circ - ^2P_{3/2}^\circ$	0.3861			2.48(-13)	1.27(-14)
1.03205	[S II]	$^2D_{5/2}^\circ - ^2P_{3/2}^\circ$	0.3840			2.36(-13)	2.16(-14)
1.03364	[S II]	$^2D_{3/2}^\circ - ^2P_{1/2}^\circ$	0.3831			2.12(-13)	2.37(-14)
1.0359			0.3817			9.15(-14)	
1.03705	[S II]	$^2D_{5/2}^\circ - ^2P_{1/2}^\circ$	0.3810			1.16(-13)	2.18(-14)
1.0398	[N I]	$^2D_{5/2}^\circ - ^2P_{1/2,3/2}^\circ$	0.3794			9.59(-14)	[1.45(-14)]
1.0408	[N I]	$^2D_{3/2}^\circ - ^2P_{1/2,3/2}^\circ$	0.3788			7.23(-14)	[1.45(-14)]

1.0455			0.3761			2.85(-13)	
1.05015	Fe II	$4p^4F_{7/2}^o - 4s^2^4G_{9/2}$	0.3734		2.28(-14)		
1.06913	C I	$3s^3P_2^o - 3p^3D_3$	0.3628	2.74(-14)	4.40(-14)	9.27(-13)	
1.07074	C I	$3s^3P_1^o - 3p^3D_1$	0.3619			5.24(-13)	
1.07296	C I	$3s^3P_2^o - 3p^3D_2$	0.3607			5.64(-13)	
1.08302	He I	$2s^3S - 2p^3P^o$	0.3553	-5.12(-14)		-3.85(-13)	
1.08302	He I	$2s^3S - 2p^3P^o$	0.3553	2.52(-14)		1.51(-12)	1.18(-13)
1.0918			0.3507			5.75(-13)	
1.09381	H I	3-6	0.3496	1.57(-13)	1.57(-13)	3.41(-12)	1.26(-14)
1.0955			0.3488			4.33(-13)	
1.1134			0.3398			3.31(-13)	
1.116			0.3386				1.62(-15)
1.1206			0.3363			4.55(-13)	
1.125			0.3342				4.95(-15)
1.1287	O I	$3p^3P - 3d^3D^o$	0.3325		6.98(-14)	7.04(-13)	
1.1301			0.3318			4.90(-13)	
1.134			0.3300				3.61(-15)
1.141			0.3267				1.02(-15)
1.147			0.3240				3.76(-15)
1.151			0.3221				2.10(-15)
1.155			0.3204				2.07(-15)

1.1657			0.3156		1.50(-14)		
1.1838			0.3079		2.54(-14)		
1.18820	[Fe II]	$a^4D_{7/2} - a^2G_{7/2}$	0.3061				1.01(-14)
1.1883	[P II]	$^3P_2 - ^1D_2$	0.3060				
1.23266	H ₂	3-1 S(1)	0.2885				8.43(-16)
1.23800	H ₂	2-0 Q(1)	0.2865				2.08(-15)
1.2472			0.2831		1.28(-14)		
1.24760	[Fe II]	$a^6D_{5/2} - a^4D_{3/2}$	0.2829				3.73(-15)
1.25670	[Fe II]	$a^6D_{9/2} - a^4D_{7/2}$	0.2797	8.75(-14)	2.21(-14)		2.47(-13)
1.274			0.2736				1.54(-14)
1.27878	[Fe II]	$a^6D_{3/2} - a^4D_{3/2}$	0.2719				[4.56(-14)]
1.28180	H I	3-5	0.2709	2.01(-13)	5.16(-13)	7.67(-12)	[4.56(-14)]
1.2941	[Fe II]	$a^6D_{5/2} - a^4D_{5/2}$	0.2668				3.92(-14)
1.31650	O I	$3^3P - 4^3S$	0.2595		2.51(-14)		
1.3205	[Fe II]	$a^6D_{7/2} - a^4D_{7/2}$	0.2582				6.26(-14)
1.3278	[Fe II]	$a^6D_{3/2} - a^4D_{5/2}$	0.2559				1.59(-14)

Chapter 5

High-Excitation Objects

5.1 Introduction

In earlier chapters, I examined the spectra of a variety of emission line sources, all with central stars cooler than 35000 K. In this chapter, I will examine the spectra of objects with much harder radiation fields. Among the objects to be discussed are the planetary nebulae NGC 7027 and Hubble 12, the Wolf-Rayet star WR 110, the Seyfert 1 galaxy NGC 4151, the Seyfert 2 galaxy NGC 1068, and the Orion nebula.

NGC 7027 was included in this study because it is one of the richest emission line sources known. Hubble 12 was included for two reasons. First, it is much cooler than NGC 7027 so it has very different excitation conditions. Second, since fluorescent H_2 emission is seen in the 2 μm spectrum of Hubble 12, it is likely that fluorescent lines will also be present in the 1.1 - 1.5 μm region. WR 110, a WN6 star, was selected primarily on the basis of its brightness in the infrared. NGC 4151 and NGC 1068 were included because they are considered the prototypical Seyfert 1 and Seyfert 2

galaxies. Finally, the Orion nebula is an example of an object excited by early main sequence stars. It was included primarily as a comparison object.

5.2 Observations and Data Reduction

All six objects were observed with the GeSpec on the Steward Observatory 2.3m telescope. Observations of the Orion nebula were made by pointing at a bright condensation and making sure that the reference sky beams were pointing at comparatively dim parts of the nebula. The "object" position was not identical for all pieces of the spectrum. Each of the planetary nebula and Seyfert galaxy observations was made centered on the central source. A summary of the observations is given in Table 5.1. The observing and data reduction procedures are discussed in Section 1.3.

The individual spectral pieces were renormalized and combined. The resulting spectra are shown in Figures 5.1 - 5.6. Line fluxes were measured using IRAF, and line identifications and fluxes are given in Tables 5.2 and 5.3. More than one transition is listed when blends are present or when line identifications are uncertain. Most observations were made with little overlap between adjacent pieces. As a result, renormalization factors are fairly uncertain, and line fluxes are primarily given to show the relative strengths of the lines.

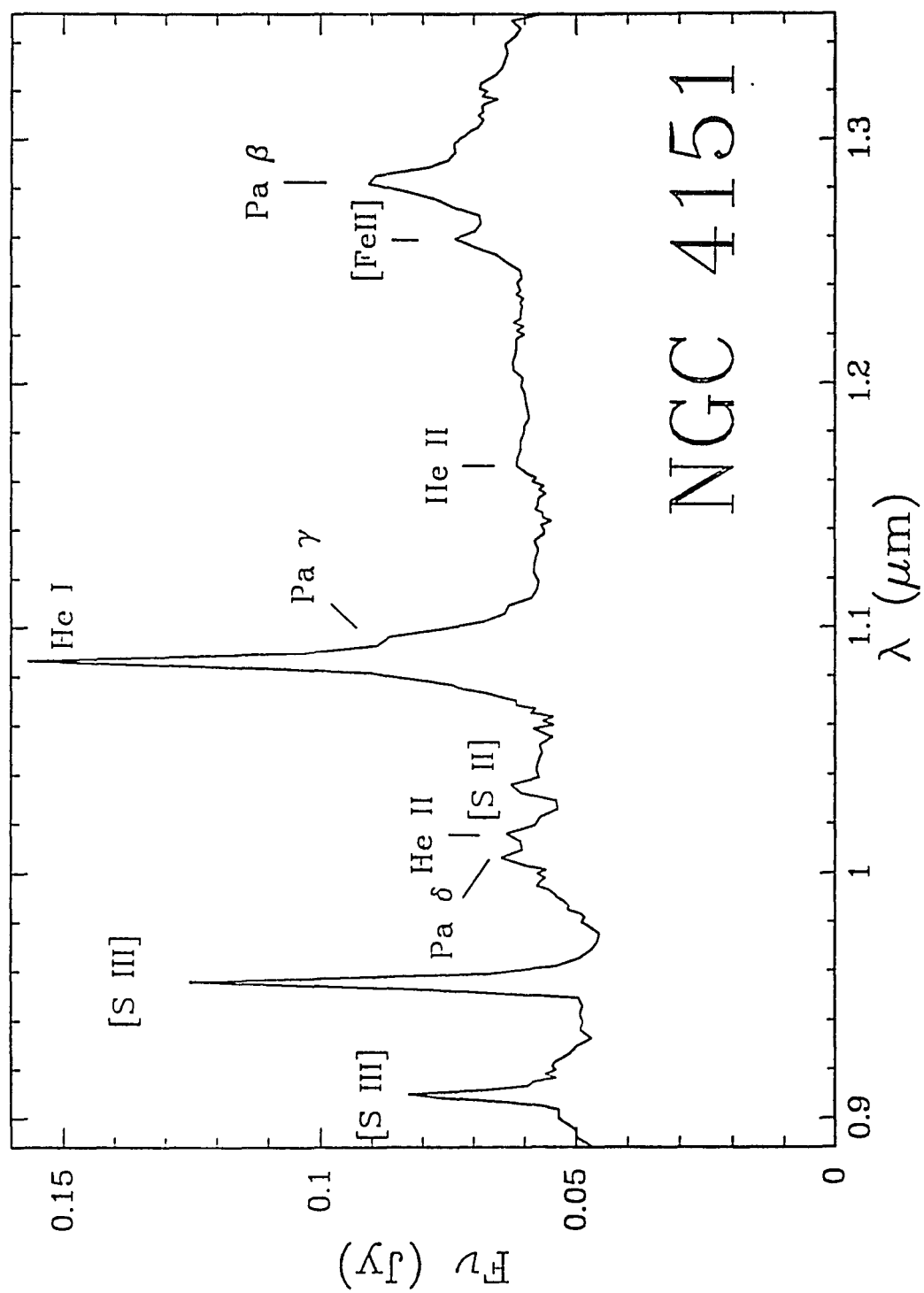


Figure 5.1: 0.89 - 1.35 μm spectrum of NGC 4151

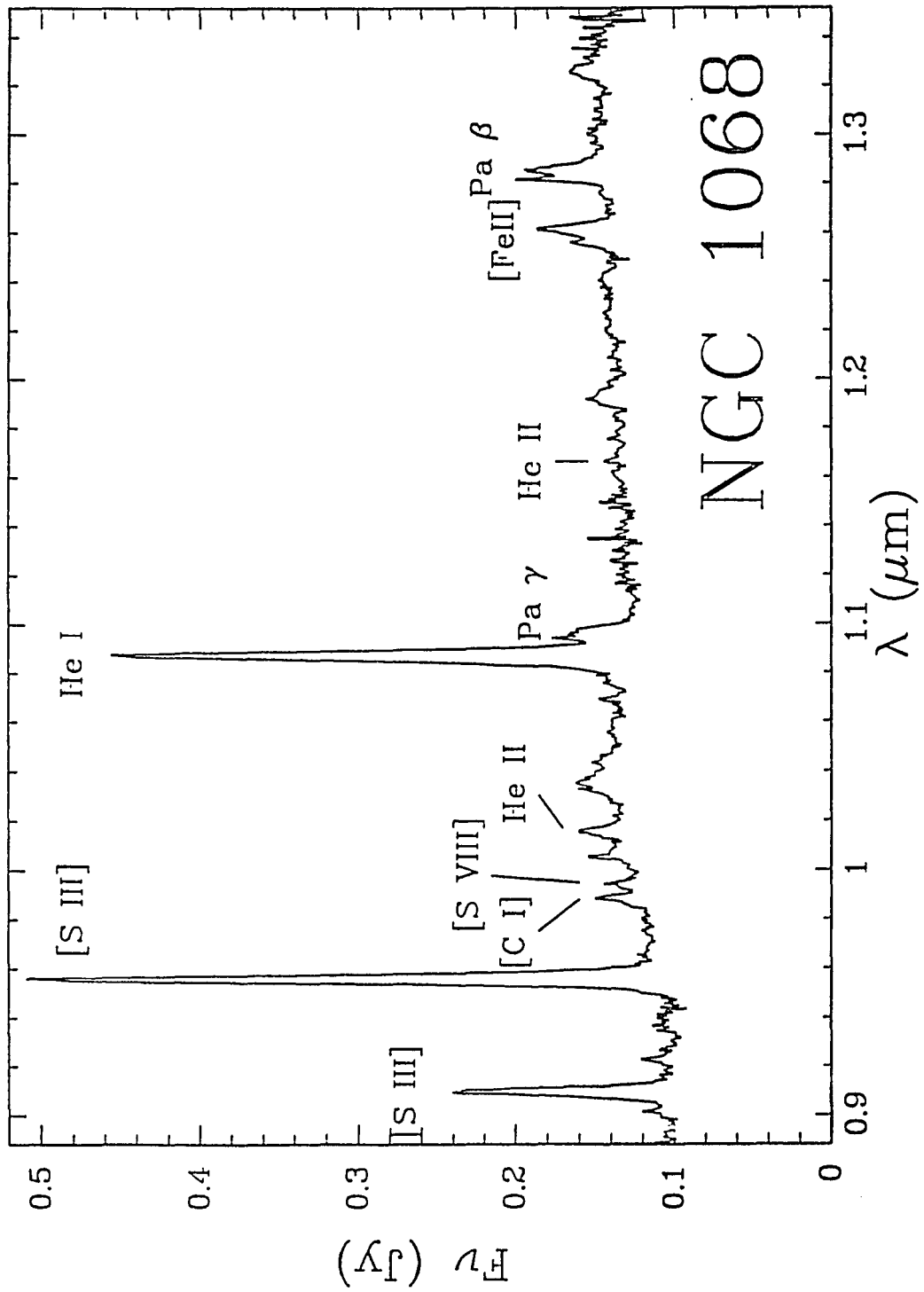


Figure 5.2: 0.89 - 1.35 μm spectrum of NGC 1068

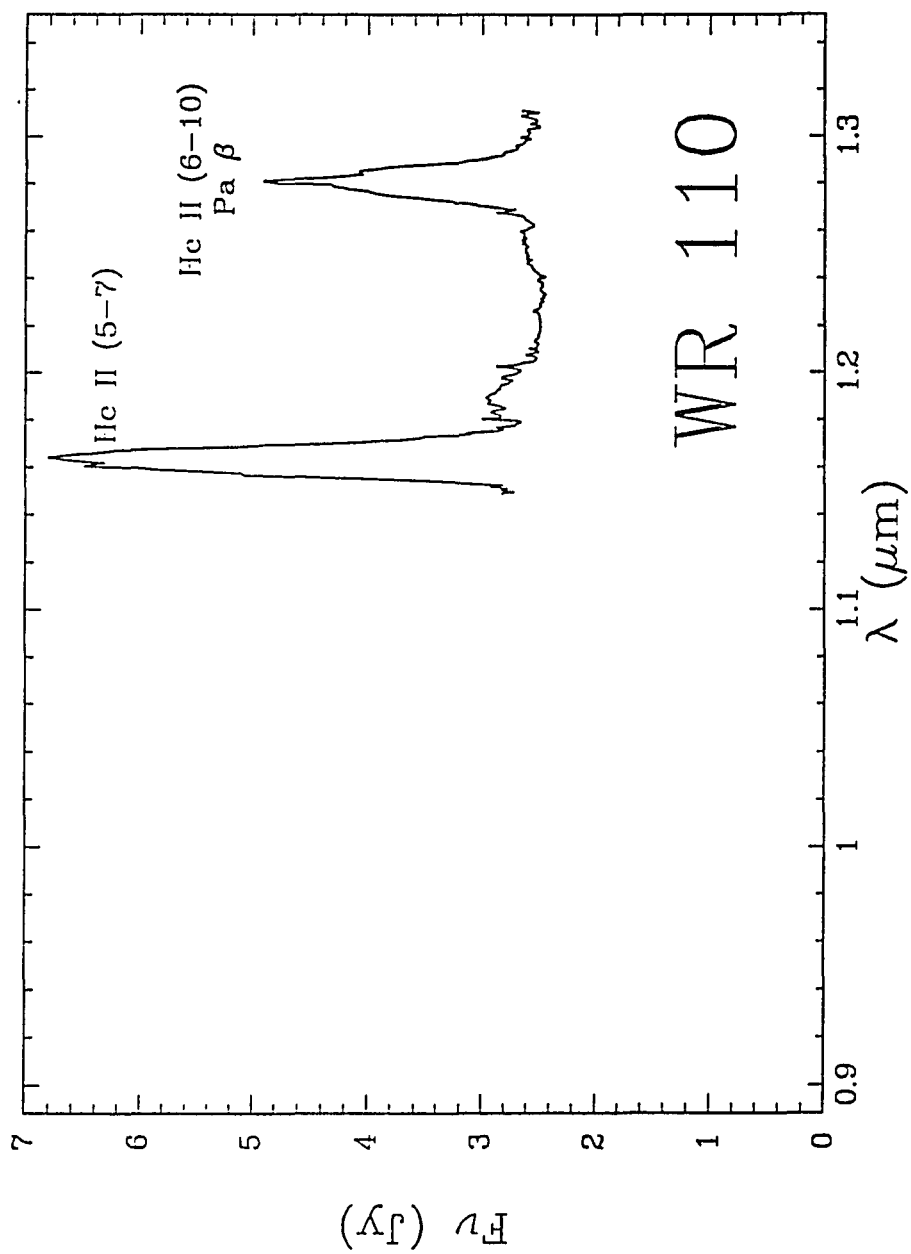


Figure 5.3: 1.14 - 1.31 μm spectrum of WR 110, plotted to the same wavelength scale as the other high-excitation objects. The He II (6-10) transition dominates the blend with Pa β .

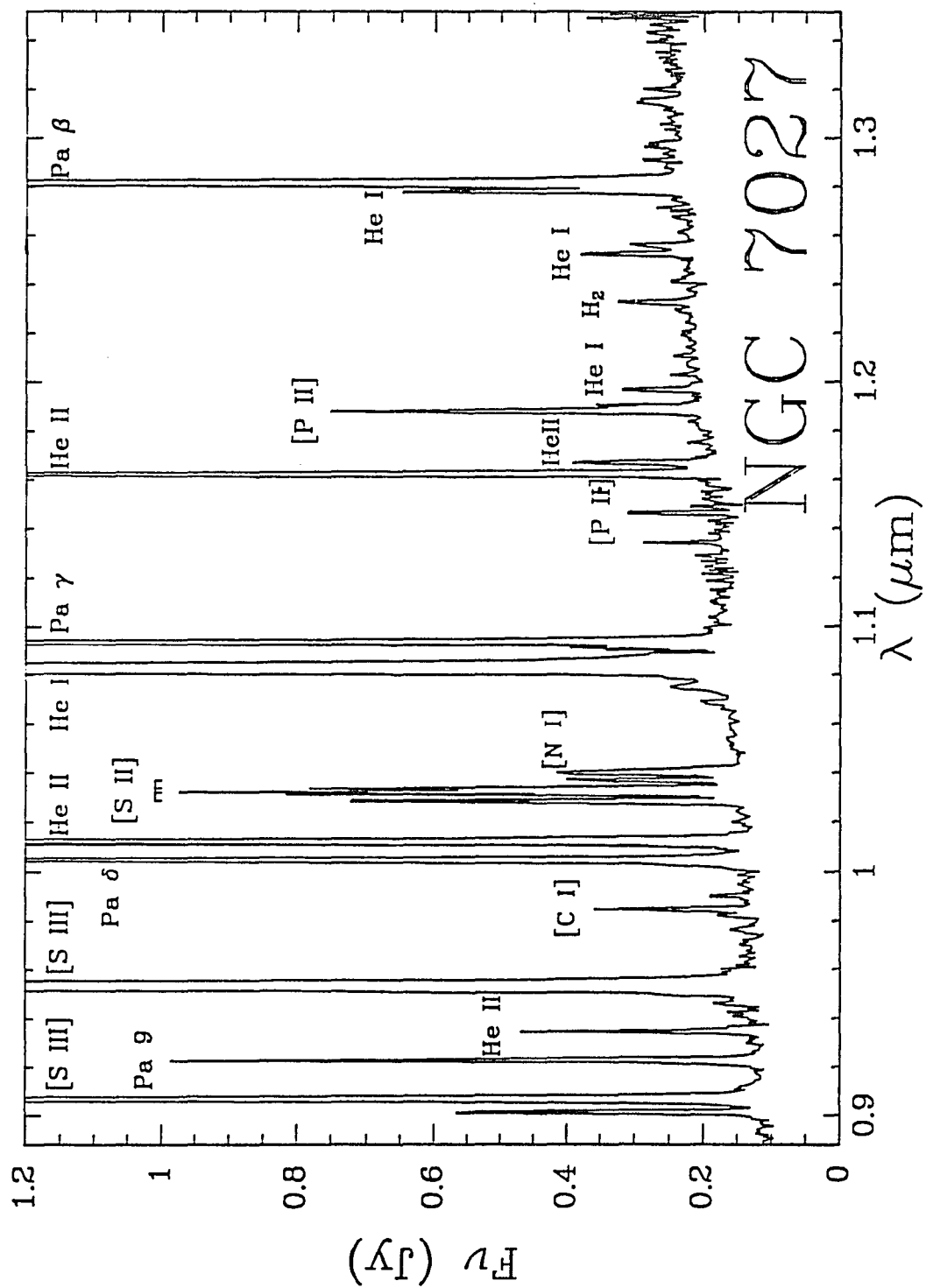


Figure 5.4: 0.89 - 1.35 μm spectrum of NGC 7027

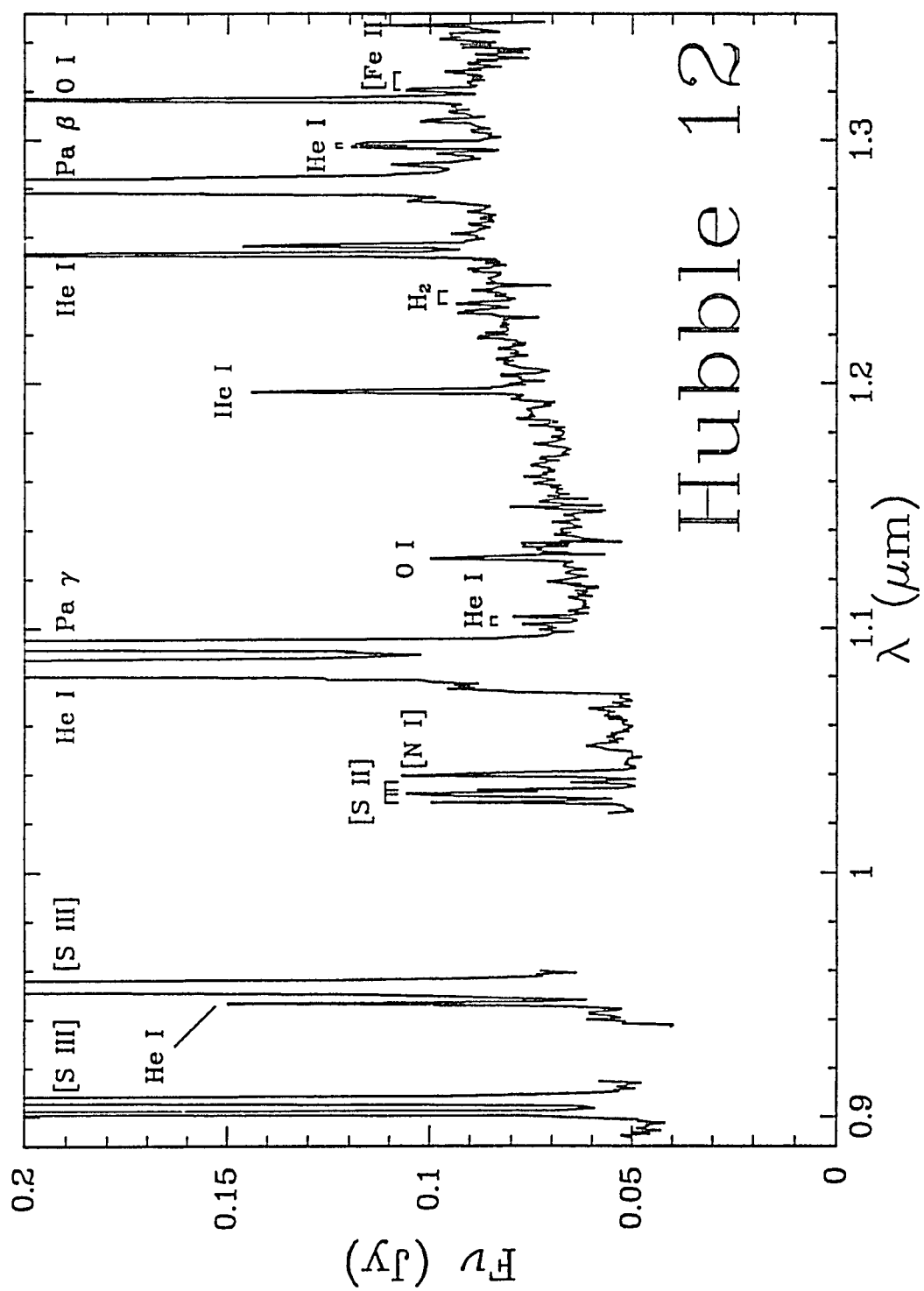


Figure 5.5: 0.89 - 1.35 μm spectrum of Hubble 12

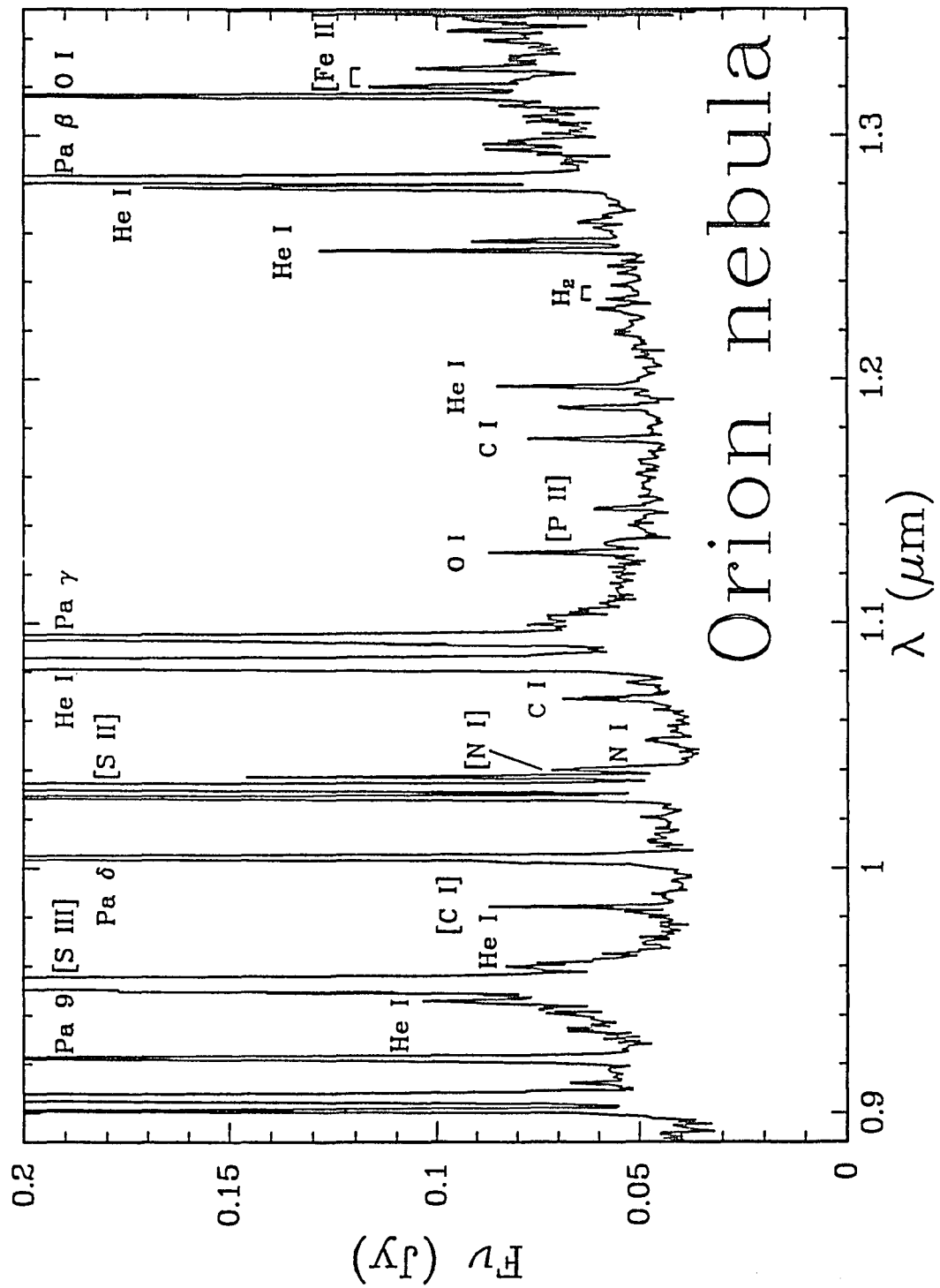


Figure 5.6: 0.89 - 1.35 μm spectrum of a bright knot in the Orion nebula.

5.3 Analysis

5.3.1 High-Excitation Lines

The primary property that distinguishes the objects in this chapter from those in earlier chapters is the hardness of the radiation field. Most of the young stellar objects are hot enough to ionize hydrogen, but only MWC 349 is hot enough to produce a significant flux in the [S III] lines. In contrast, the [S III] $0.9531\ \mu\text{m}$ line is one of the brightest lines in the spectra of the high excitation objects, and most of the objects in this chapter also produce emission in higher excitation lines.

A distinctive signature of very hot objects is emission in the He II recombination lines. He^+ has an ionization potential of 54.4 eV, well in excess of the 23.3 eV required to ionize S^+ and the 13.6 eV required to ionize hydrogen. He II lines are not seen in the spectra of Hubble 12 and the Orion nebula, neither of which is particularly hot. The 4-5, 5-7, and 5-8 lines are very strong in NGC 7027. The spectrum of NGC 1068 contains many faint He II lines, and the 4-5 and 5-7 lines are bright. In NGC 4151, only the 5-7 line stands out. Several other potentially bright lines are dwarfed by H I emission, which is produced by all of the objects in this study. Since H I and He II are in the same isoelectronic sequence, the $3 - n$ H I lines and $6 - 2n$ He II lines are nearly coincident in wavelength. The relative contributions

from H I and He II can be determined by comparison with the 6-9, 6-11, and 6-13 He II lines. Alternatively, one can use the strength of the He II 4-5 line and theoretical He II line ratios from Hummer & Storey (1987) to predict the strengths of the other He II lines. In Orion and the planetary nebulae, the H I lines are strong and dominate the blends. In WR 110, the H I lines are overwhelmed by very strong He II emission. The H I lines are fairly bright in the two Seyfert galaxies, and the spectrum of NGC 4151 includes a significant amount of broad line emission. Finally, in WR 110 the He II lines dominate the spectrum.

The He II 5-7 line profile in WR 110 is distinctly non-gaussian. The line has a small absorption dip on the blue side of line center, similar to the H I and He I line profiles seen in some T Tauri stars. This profile, which is a variation on the classical P Cygni profile, is a sign of outflow with self-absorption by the blueshifted gas.

He II line ratios are only weakly dependent on the electron density and electron temperature. As a result, the observed and predicted line ratios can be compared to determine the extinction to the He II emitting region. We compared the strengths of the 4-5, 5-7, and 5-8 lines in NGC 7027. The 4-5/5-7 ratio gives $A_v = 4.4$ mag. In comparison, the Paschen lines of H I imply $A_v = 2.5 \pm 0.3$ mag. Line ratios involving the He II 5-8 line are unreliable because there are several strong, sharp atmospheric absorption lines

between 0.9342 and 0.9346 μm that are difficult to divide out in low resolution data. The He II 5-8 line should be useful in high resolution studies and for studying extragalactic objects.

Both NGC 4151 and NGC 1068 have several coronal lines in their visible spectra. Korista & Ferland (1989) show that these high-ionization lines can be produced by exposing a typical galactic interstellar medium ($n_e \sim 1 \text{ cm}^{-3}$) to radiation from a "bare" Seyfert nucleus. Coronal lines are also present in the 0.9 - 1.35 μm spectra of the Seyfert galaxies. Ionization potentials relevant to this discussion are listed in Table 5.4. High resolution ($R \approx 1500$) 0.7 - 1.1 μm spectra of NGC 4151 by Osterbrock, Shaw, & Veilleux (1990) reveal the lines [Fe XI] 0.7892 μm and [S VIII] 0.9912 μm . The [S VIII] line is not apparent in our low resolution spectrum of NGC 4151. A 0.33 - 1.11 μm spectrum of NGC 1068 by Shields & Oke (1975) reveals an [Fe X] line at 0.6374 μm , but neither Shields & Oke nor Osterbrock, Tran, & Veilleux (1992) detected the [Fe XI] and [S VIII] lines. At wavelengths longer than about 0.9 μm , the GeSpec provides better sensitivity than CCDs, and the [S VIII] 0.9912 μm line appears clearly in our spectrum of NGC 1068. Given that [S VIII] and [Fe X] lines are present in the spectrum of NGC 1068, it is somewhat surprising that the [Fe XI] 0.7892 μm line was not detected. Its absence is apparently not due to a lack of high energy photons. Several other high excitation

lines appear in the infrared spectra of NGC 4151 and NGC 1068. A feature at $\sim 1.252 \mu\text{m}$ is present in high resolution GeSpec data on NGC 4151 taken by Nat Carleton (personal communication) and in our spectrum of NGC 1068. This feature is either [S IX] $1.2520 \mu\text{m}$ or He I $1.2528 \mu\text{m}$. In NGC 7027, Hubble 12, and the Orion nebula, the line is roughly twice as strong as the adjacent [Fe II] $1.2567 \mu\text{m}$ line, and it is produced by He I. In NGC 4151 and NGC 1068, the feature is only about half as strong as the [Fe II] line. The other He I lines that would let us predict the strength of the He I $1.2528 \mu\text{m}$ line are all either in blends, in noisy parts of the spectrum, or coincident with absorption features in the host galaxy. As a result, the identity of the $1.252 \mu\text{m}$ line remains uncertain.

Another possible high excitation feature in the infrared spectrum of NGC 1068 is the [Fe XIII] $1.0798 \mu\text{m}$ line. An emission line is clearly present at $\sim 1.079 \mu\text{m}$, in the wing of the He I $1.0830 \mu\text{m}$ line, but a second [Fe XIII] line at $1.0747 \mu\text{m}$ is not detected. A line is seen near $1.079 \mu\text{m}$ in NGC 7027 and the Orion nebula that is probably due to Si I. No other Si I lines are seen in the spectrum of NGC 1068. Hence, the identity of the $1.079 \mu\text{m}$ feature in NGC 1068 remains uncertain.

Finally, there is evidence for [Ni VIII] lines at $0.9106 \mu\text{m}$ and $0.9977 \mu\text{m}$ in NGC 1068. The latter line could alternatively be [Mn X] $0.9978 \mu\text{m}$. There are no features at

these wavelengths in the spectra of Orion and the planetary nebulae.

In conclusion, the excitation level of a source can be estimated from strong lines in the 0.9 - 1.35 μm region alone. This is potentially important for heavily obscured sources. As the excitation increases, we first see a rapid growth in the strength of the [S III] lines at 0.9069 and 0.9531 μm . As the excitation increases beyond the level that can be supplied by main sequence stars, He II lines appear; the brightest in this spectral interval are He II 4-5 at 1.0124 μm and He II 5-7 at 1.1626 μm . Finally, non-stellar hard UV sources such as active galactic nuclei can produce lines of extremely high excitation. However, few strong examples lie in this spectral region. We find the [S VIII] line at 0.9912 μm to be the best indicator of an AGN-like underlying UV continuum.

5.3.2 Lines in Common to all Objects

In addition to the hydrogen lines, there are several other lines that appear to be common to all high excitation objects. These include He I, [N I], [S II], [S III], and [Fe II] lines. Each is discussed in greater detail below.

The He I spectrum is produced both by recombination and by collisional excitation. The ionization potential for He^0 is 24.6 eV so any source with [S III] emission is expected to also produce He I recombination emission. Of the

recombining electrons, 75% are expected to enter into triplet states, and most of these end up in the 2^3S triplet ground state. Since the 2^3S state is metastable, a large population develops, and lines with a 2^3S lower level are usually optically thick. The 2^3S level is less than 5 eV below the ionization continuum so any of the higher He^0 levels can be collisionally excited from this level. The most likely transition is to the 2^3P term. Electrons in the 2^3P term have nearly unity probability of emitting a $1.0830\ \mu\text{m}$ photon and returning to the 2^3S state. As a result, multiple scatterings have little effect on the strength of the $1.0830\ \mu\text{m}$ line. Electrons excited to higher triplet levels also usually return to the 2^3S state, sometimes cascading through the 2^3P term. Thus, collisions from the 2^3S state greatly increase the strength of the $1.0830\ \mu\text{m}$ line, and the $1.0830\ \mu\text{m}$ line is consistently one of the brightest lines in the spectra of high-excitation objects.

The spectra of NGC 7027, Hubble 12, Orion, and NGC 1068 all include a large number of He I lines. In NGC 7027 and the Orion nebula, the bright lines are at 1.0913 , 1.1969 , 1.2527 , and $1.2785\ \mu\text{m}$. Hubble 12 includes these He I lines as well as bright lines at 0.9464 , 1.0668 , 1.1013 , 1.1045 , 1.2968 , and $1.2985\ \mu\text{m}$. In NGC 1068, the He I lines that stand out are at 1.0031 , 1.0668 , 1.1226 , 1.5084 (not shown in Figure 5.2), and perhaps $1.2528\ \mu\text{m}$. The only obvious He I line in NGC 4151 is the $1.0830\ \mu\text{m}$ line, but more lines are

likely in higher resolution data.

The brightest He I lines in NGC 7027 and Orion are all triplet lines, indicating the importance of collisional excitation in these objects. Hubble 12 includes several singlet lines. For each of the singlet lines, the triplet counterpart is about three times as strong, as expected for recombination emission. In NGC 1068, both singlet and triplet lines are seen, again indicating that the He I emission is mostly due to recombination.

There is significant emission in the [S II] 1.0286, 1.0320, 1.0336, and 1.0370 μm lines from both of the Seyfert galaxies and from both planetary nebulae. The [S II] to H I ratio is quite a bit smaller in Hubble 12 than it is in the other objects. The density in the [S II] emitting region can be determined from either the [S II] 1.0320/1.0336 μm or the [S II] 1.0286/1.0370 μm ratio. The former pair of lines, though often blended together, have the advantage that they are the brightest of the four lines. In NGC 7027 and Orion, the [S II] lines indicate $n_e \lesssim 10^5 \text{ cm}^{-3}$. In Hubble 12, the lines indicate $n_e \gtrsim 10^6 \text{ cm}^{-3}$, similar to the critical density of $1 \times 10^6 \text{ cm}^{-3}$. It thus appears that the infrared [S II] lines in Hubble 12 are weakened by collisions. The [S III] 0.9069, 0.9531 μm lines have a critical density of about $2 \times 10^5 \text{ cm}^{-3}$, and they are also weak compared to the H I lines in Hubble 12. All four [S II] lines are blended together in the Seyfert galaxy spectra so they cannot be used to

determine the density.

[N I] lines are present at 1.0398 and 1.0408 μm in both of the Seyfert galaxies and in both planetary nebulae. The [N I] lines are blended together in all of these objects, and they are quite a bit fainter than the adjacent [S II] lines. In Hubble 12, the [N I] lines are comparable in strength to the [S II] 1.0320 μm line, implying that the [S II] and [N I] lines are not similarly diminished. The density in Hubble 12 is probably less than $7 \times 10^6 \text{ cm}^{-3}$, the critical density for the nitrogen lines. The ionization energy of nitrogen is slightly greater than that of hydrogen so these lines arise from a region similar in size to the H I recombination zone.

[Fe II] emission is often associated with shocks. [Fe II] lines are very bright in supernova remnants, and the [Fe II] emission from galaxies appears to be dominated by supernova remnants (Moorwood & Oliva 1988; Greenhouse et al. 1991). It is not clear whether the [Fe II] emission from the Seyfert galaxies and planetary nebulae in this study is excited by shocks or by collisions. The 1.2567 μm line is the brightest [Fe II] line in the 0.9 - 1.5 μm spectrum. The other lines are at best 10 - 30% as bright, regardless of physical conditions in the [Fe II] emitting region. We used theoretical line ratios to confirm [Fe II] line identifications. The relative strengths of lines that share the same upper level is fixed by their transition

probabilities. The relative strengths of [Fe II] lines from different upper levels depends mainly on the electron density in the [Fe II] emitting region but have a weak dependence on the electron temperature (Hudgins, Herter, & Joyce 1990). In NGC 1068, [Fe II] 1.2703/1.2567 \approx 0.12, consistent with $n_e \approx 10^5 \text{ cm}^{-3}$. In NGC 4151, the [Fe II] 1.2703/1.2567 μm ratio is consistent with $n_e \approx 7 \times 10^4 \text{ cm}^{-3}$. The [Fe II] 1.2567 μm line is not seen in WR 110, probably due to a lack of iron in the ionized wind. In NGC 7027, the [Fe II] lines are faint and cannot be used reliably to determine the density. In Hubble 12, the [Fe II] lines are more prominent. The [Fe II] 1.2941/1.2567 μm , 1.2703/1.2567 μm , and 1.3278/1.3205 μm ratios in Hubble 12 are consistent with $n_e \approx 6 \times 10^4 \text{ cm}^{-3}$. Ratios 20% larger would be consistent with $n_e \geq 10^6 \text{ cm}^{-3}$.

In summary, a number of lines are observed in all six high excitation sources and therefore must be common in this type of source. These objects contain many He I lines which can be used to identify whether the He I emission arises through collisional excitation or through recombination. The well-studied He I line at 1.0830 μm is the brightest of these lines. The 1.0830 μm line is useful for observation of very faint sources, but it is subject to amplification processes that make quantitative interpretation of its strength difficult. The [S II] and [S III] lines are subject to collisional de-excitation and can be used in combination with

other lines to determine if the density in the emitting region is $\geq 10^6 \text{ cm}^{-3}$. A more detailed characterization of the density is available from the [Fe II] lines, although their weakness and blending with other features may result in difficulties in measurement.

5.3.3 Other Lines

There are quite a few lines present in the spectra of high excitation objects that are likely to have been produced in photoionized gas. These include [P II] forbidden lines, as well as recombination lines of C I and Si I. Phosphorus, carbon, and silicon can all be ionized by photons with less than 13.6 eV so these lines will be produced in a region that extends beyond the H I recombination zone. N I recombination lines, with an ionization potential of 14.5 eV, will not extend as far from the ionizing source. C⁺ has an ionization potential of 24.4 eV so C II recombination emission is likely to be produced close to the ionizing source.

[P II] emission is clearly seen in the infrared spectra of NGC 7027 and the Orion nebula. The 1.1468 and 1.1883 μm lines have a common upper level so their intrinsic ratio is fixed at 0.384 (Czyzak & Krueger 1963). In NGC 7027, the [P II] 1.1468/1.1883 μm ratio is only 0.30. As mentioned by Rudy et al. (1992), there seems to be a problem with the atomic data on [P II]. In our spectrum of the Orion nebula, the [P II] 1.1468/1.1883 μm ratio is 0.49. However, the

1.1883 μm line flux is highly uncertain and might be greatly underestimated. Neither of the [P II] lines was detected in our spectrum of Hubble 12. The 1.1468 μm line is in a noisy part of the spectrum, and the 1.1883 μm line, which is in a blend of lines, is very weak if present. The absence of

[P II] emission in Hubble 12 might be a result of high densities. The collision strengths of Krueger & Czyzak (1970) imply a critical density of $n_c \approx 2 \times 10^5 \text{ cm}^{-3}$ for the infrared [P II] lines, much lower than the electron density implied by the [S II] lines. In NGC 1068, it is not clear whether the 1.1468 μm line is present because of interference by terrestrial water vapor. The 1.1883 μm line is also not obvious because it is in a blend of at least two emission features and it is adjacent to several CO absorption features from the host galaxy. There is inadequate evidence for [P II] emission in our low resolution spectrum of NGC 4151.

No C I features are seen in the spectra of the two Seyfert galaxies or in the spectrum of WR 110. Faint C I emission is seen from Orion and from the two planetary nebulae. The brightest lines are at 1.0685, 1.0754, and 1.1755. The C I lines are significantly stronger in Orion, probably because the Orion nebula contains a significant amount of embedded, neutral material. Neutral filaments are clearly seen in narrow-band O I images of the Orion nebula (Münch & Taylor 1974; Cosmovici et al. 1979).

There are several likely Si I lines in the spectra of

WR 110, Orion, and the planetary nebulae. The most prominent lines are at 1.0749, 1.0787, 1.1984, 1.2032, and 1.2271 μm . Not all of these lines are detected in all four objects.

There is evidence for several N I lines in the spectra of NGC 1068, Hubble 12, and Orion. Each object has a broad line at 1.051 μm that might be due a blend of N I lines. The peak of the line is at 1.0518 μm . There is evidence for a weak N I line at 1.011 μm in NGC 1068 and Orion. The 1.011 μm line is not included in the spectral coverage of Hubble 12. A line at about 1.246 μm in Hubble 12 and Orion is either from N I or from H_2 . If the line at 1.238 μm is due to H_2 (2,0) Q(1), the 1.246 μm line has the right strength to be H_2 (2,0) Q(3). The 1.246 μm line is not apparent in the spectrum of NGC 1068, possibly due to an underlying galaxy absorption feature. No N I lines are expected or seen in our spectrum of WR 110. The absence of N I emission from NGC 7027 is a bit mysterious given that NGC 7027 is a source of [N I], [N II], N II, and N III emission. Either the three lines discussed above are not N I lines, or perhaps most of the nitrogen in NGC 1068 is at least doubly ionized.

There is only one strong C II line in the spectra of the high-excitation objects. The C II 0.99035 μm line appears in the spectra of NGC 7027, Orion, and possibly NGC 1068. Spectra were not taken of WR 110 and Hubble 12 at this wavelength, and the resolution of the NGC 4151 data is

inadequate to see if the C II line is present. A second C II line is possible at 1.0504 μm in Hubble 12 and Orion, but the emission might be from N I.

Several other species produce lines in the high excitation objects of this study. [C I] emission probably comes from thermally excited gas far from the ionizing source. H_2 emission is likely to come either from molecular material far from the ionizing source or from dense clouds at smaller radii. O I is produced partly by recombination and partly by UV fluorescence. The O I recombination zone coincides almost exactly with the region of ionized hydrogen, and the UV fluorescent emission is likely to come from neutral oxygen in the H I - H II transition region.

The two brightest lines of [C I] are at 0.9850 and 0.9824 μm . They have the same upper level, and their ratio is expected to be 2.97. The observed ratios in NGC 1068, NGC 7027, and Orion range from 3.0 - 3.5, with a fair amount of observational uncertainty. These lines were not included in the spectral coverage of WR 110 and Hubble 12, and they are blended with H I and He II features in NGC 4151. Condal et al. (1981) find [C I] $0.8727/(0.9824 + 0.9850) = 0.53$ in NGC 7027, which for $T_e = 10^4$ K implies $n_e \approx 4 \times 10^4 \text{ cm}^{-3}$. Osterbrock et al. (1990) find [C I] $0.9850/[\text{S III}] 0.9069 = 0.038$ in NGC 4151. A ratio of 0.18 is found in both our spectrum of NGC 1068 and in Shields & Oke (1975). These ratios can be compared to those in active galactic nuclei

models, such as Contini & Viegas (1992), to determine properties of the radiation field.

H₂ lines are present in the spectra of Hubble 12, Orion, and perhaps NGC 7027. The brightest lines are the (3,1) S(1) line at 1.2327 μm and the (2,0) Q(1) line at 1.2380 μm . Since these lines arise from different vibrational levels, their ratio depends heavily on whether the emission is excited thermally or by fluorescence. In the 2000 K thermal model of Black & van Dishoeck (1987), the (3,1) S(1) line is predicted to be 3.5 times fainter than the (2,0) Q(1) line. In their fluorescence models, the (3,1) S(1) line is 15 - 50% stronger than the (2,0) Q(1) line. In our spectra of Hubble 12 and Orion, the (3,1) S(1) line is 10% - 40% brighter than the (2,0) Q(1) line. In our spectrum of NGC 7027, however, the 1.2327 μm line is ten times as bright as the (2,0) Q(1) line and must come primarily from an unidentified transition.

According to the shock-excitation models of Shull & Hollenbach (1978), the (2,0) Q(3) line at 1.2470 μm should be slightly stronger than the (2,0) Q(1) line. The (2,0) Q(3) line is present in Hubble 12 and Orion but not in NGC 7027. Also, the (2,0) S(3) line at 1.1172 μm should be several times brighter than the (2,0) Q(1) line, but it is clearly absent from the spectra of NGC 7027 and Orion. Thus, the identity of the 1.2380 μm line is still uncertain.

Several other H₂ lines appear in the spectra of Hubble 12 and Orion. The (3,1) S(0) line at 1.2617 μm and the (2,0)

Q(3) line at 1.2470 are both prominent lines. The (2,0) S(0) line at 1.1892 μm , though blended with the [P II] 1.1883 μm line, also appears to be present in both objects. Hubble 12 additionally shows evidence for emission in the (2,0) S(4), (3,1) S(4), (3,1) S(3), (3,1) S(2), (4,2) S(3), (4,2) S(1), (3,1) Q(1), (3,1) Q(4), and (4,2) S(0) transitions. The presence of lines from high vibrational levels indicates that fluorescence contributes to the H_2 flux in Hubble 12 and perhaps Orion. Dinerstein et al. (1988) compared the 2 μm spectrum of Hubble 12 with the H_2 models of Black & van Dishoeck (1987) and also found evidence for fluorescent emission. Collisions are likely to affect the H_2 line ratios in Hubble 12, which is why the spectrum resembles a thermal spectrum even though the primary excitation mechanism is fluorescence (Sternberg & Dalgarno 1989).

UV fluorescence can also be important for exciting the O I 0.8446, 1.1287, 1.3165 μm lines. The 0.8446 μm line is not seen in NGC 1068 (Shields & Oke 1975) or in NGC 4151 (Osterbrock et al. 1990). We do not see the 1.1287 μm line in the spectrum of either object. The 1.3165 μm line appears to be present but faint in NGC 1068. The line near 1.32 μm in NGC 4151 might be either the O I line or [Fe II] 1.3205 μm .

The spectrum of NGC 7027 shows the 0.8446 and 1.3165 μm O I lines but not the 1.1287 μm line (Condal et al. 1981; Keyes, Aller, & Feibelman 1990; Rudy et al. 1992). For UV

continuum fluorescence, Grandi (1975) predicted $O\ I\ 1.1287/1.3165\ \mu\text{m} \approx 0.1$ and $O\ I\ 0.8446/1.3165\ \mu\text{m} \approx 3$. Rudy et al. report an $O\ I\ 0.8446/1.3165\ \mu\text{m}$ ratio that is consistent with UV fluorescence excitation. The expected $1.1287\ \mu\text{m}$ line flux is below the detection limit of our data.

The $O\ I\ 1.1287/1.3165\ \mu\text{m}$ ratio is 0.30 in our spectrum of Hubble 12. This ratio is slightly larger than the value expected for continuum fluorescence, indicating a possible contribution from $Ly\beta$ fluorescence. The absence of $O\ I$ triplet lines argues against recombination. Similar results are found for the Orion nebula - the $O\ I\ 1.1287/1.3165\ \mu\text{m}$ ratio equals 0.27, and Osterbrock et al. (1992) see many $O\ I$ singlet lines but no triplet lines. The detection of fluorescent $O\ I$ emission from Hubble 12 and Orion supports the idea that the H_2 emission from these objects is partly excited by UV fluorescence.

In summary, many lines appear in the spectra of some but not all of the high-excitation objects. A number of these lines are generated in low excitation regions that must be shielded from the exciting source; with adequate data, these lines could be used to deduce the conditions in the low excitation regions, much as discussed for the sources in Chapter 4. Two species of particular interest are H_2 and $O\ I$. This spectral region is ideal for detecting molecular hydrogen excited by fluorescence. We find fluorescent H_2 emission in Hubble 12 and possibly in Orion. We also find

O I lines in both of these objects that are excited fluorescently.

5.3.4 Line Widths in the Spectrum of NGC 1068

Line widths have been measured for several infrared lines in the spectrum of NGC 1068. The [Fe II] 1.644 μm line has a width of 800 km s^{-1} , the [Si VI] 1.962 μm line has a width of 1100 km s^{-1} , Br γ has a width of 900 km s^{-1} , Br α has a width of 800 km s^{-1} , and the $v = 1 \rightarrow 0$ S lines of H $_2$ have widths of about 300 km s^{-1} (Oliva & Moorwood 1990). The H $_2$ and [Fe II] lines have similar spatial distributions so they probably come from the same physical region. The narrow widths of the H $_2$ lines is probably a consequence of collisional dissociation in high velocity clouds (Oliva & Moorwood 1990).

Kawara, Nishida, & Phillips (1989) report widths of 1000 km s^{-1} for Br γ and 1700 km s^{-1} for Br α , and Kawara, Nishida, & Taniguchi (1988) report asymmetric Br γ and [Fe II] 1.644 μm line profiles. Kawara et al. (1988) comment that these observations indicate a complex geometry with significant optical depth or dust absorption effects, and they propose a detailed model to explain the observations. The quality of the Kawara et al. data is generally poor: the signal-to-noise is low, and there is little sampling of the continuum. Using higher resolution data and better wavelength coverage, Oliva & Moorwood (1990) measure widths of 800 km s^{-1} for both

Brackett lines, and they show that the asymmetries in the Br γ and [Fe II] line profiles are probably due to absorption features in the underlying galaxy spectrum. With these new results, the complex source geometry described by Kawara et al. (1988) is totally unnecessary.

Most of the lines in our spectrum of NGC 1068 are quite a bit broader than the instrumental line width of the GeSpec. We determined line widths for the seven brightest lines in the 0.89 - 1.54 μm spectrum. The [S III] 0.9069, 0.9531 μm lines have widths of 1100 km s $^{-1}$. The [C I] 0.9850 μm and [Fe II] 1.2567 μm lines have widths of about 800 km s $^{-1}$. Pa β has a width of 850 km s $^{-1}$, He I 1.0830 μm a width of 1150 km s $^{-1}$, and He II 1.0124 μm has a width of 900 km s $^{-1}$. These widths are in good agreement with previous measurements. The [S III], He I, and [Si VI] lines are wider than the hydrogen lines and the lower ionization forbidden lines. Moorwood & Oliva (1990) suggest that the high critical density of the [Si VI] line would let it survive in high density, high velocity gas and might account for the large width of the line. However, the [S III] lines have a critical density of only $2 \times 10^5 \text{ cm}^{-3}$, and they are equally broad. It is interesting that, with the exception of the hydrogen lines, all of the lines that tend to be bright in H II regions have a width of about 1100 km s $^{-1}$.

5.4 Summary

The high-excitation objects have many features in common with each other and with the lower excitation objects studied in earlier chapters. The high-excitation objects all have very strong [S III] emission, and some also produce emission in He II and higher ionization lines. The Seyfert 1 and Seyfert 2 galaxies have very similar spectra except for differences in their line widths. The planetary nebula spectra have a lot of differences. NGC 7027 produces strong He II and [P II] lines. In Hubble 12, high densities quench several of the forbidden lines, and the central star is not hot enough to excite He II emission. The [Fe II] lines are bright, pointing to the possible importance of shocks. Hubble 12 also shows evidence for H₂ and O I fluorescence, similar to the proto-planetary nebula AFGL 618. The spectrum of the WN6 star WR 110 is completely dominated by He II emission. Finally, the spectrum of Orion is very similar to the spectra of several lower excitation objects from early chapters. The main difference is in the strength of the [S III] lines.

TABLE 5.1

LOG OF OBSERVATIONS OF HIGH-EXCITATION OBJECTS

Object	Dates	Resolution*	Wavelength Coverage (μm)	Reference Star	Spectral Type	On-source Integration Time (min)
NGC 7027	11/14/89	high	0.89 - 1.35	HR 8170	F8 V	97
Hubble 12	10/27,28/89 11/3,4,5/89	high	0.89 - 0.91, 0.94 - 0.96, 1.02 - 1.35, 1.40 - 1.56	HR 8853	F7 V	245
WR 110	6/10/90	high	1.15 - 1.31	HR 6836	G0 V	52
NGC 4151	4/8/90	low	0.82 - 1.40	HR 4845	G0 V	93
NGC 1068	11/2,3,4,5/90	high	0.89 - 1.54	HR 783	F3 V	288
Orion	11/14,15,16/89 10/28/90 11/3/90	high	0.89 - 1.57	HR 2007	G4 V	486

*High resolution indicates use of the 600 l/mm grating, $R \approx 1000$ at J. Low resolution indicates use of the 150 l/mm grating, $R \approx 250$ at J.

TABLE 5.2

LINE IDENTIFICATIONS AND FLUXES IN THE INFRARED
SPECTRA OF NGC 4151, NGC 1068, AND WR 110

λ (μm)		IDENTIFICATION	NGC 4151	NGC 1068	WR 110
0.899				5.9 (-14)	
0.90690	[S III]	$^3P_1 - ^1D_2$	5.4 (-13)	1.7 (-12)	
0.919				1.2 (-13)	
0.92290	H I	3-9		1.2 (-13)	
0.947				1.9 (-13)	
0.95311	[S III]	$^3P_2 - ^1D_2$	1.4 (-12)	5.2 (-12)	
0.982				8.5 (-14)	
0.984				6.3 (-14)	
0.98502	[C I]	$2s^2 2p^2 ^3P_2 - 2p^1 D_2$		1.8 (-13)	
0.9885				7.8 (-14)	
0.9912	[S VIII]	$2s^2 2p_{3/2} - 2p^5 2p_{1/2}$		1.2 (-13)	
1.001				1.1 (-13)	
1.0035				3.0 (-14)	
1.00494	H I	3-7	8.4 (-13) (blend)		
1.01236	He II	4-5		3.0 (-13)	
1.02867	[S II]	$^2D_{3/2}^\circ - ^2P_{3/2}^\circ$	7.0 (-14)	1.5 (-13)	
1.03205	[S II]	$^2D_{5/2}^\circ - ^2P_{3/2}^\circ$	8.4 (-14)	2.3 (-13)	
1.03364	[S II]	$^2D_{3/2}^\circ - ^2P_{1/2}^\circ$	5.9 (-14)	8.4 (-14)	
1.03705	[S II]	$^2D_{5/2}^\circ - ^2P_{1/2}^\circ$	3.8 (-14)	1.3 (-13)	
1.0398	[N I]	$^2D_{5/2}^\circ - ^2P_{1/2, 3/2}^\circ$		4.4 (-14)	
1.0408	[N I]	$^2D_{3/2}^\circ - ^2P_{1/2, 3/2}^\circ$		9.2 (-14)	
1.043				4.9 (-14)	
1.053				1.5 (-14)	

1.065				4.7 (-14)	
1.0795				6.8 (-13)	
1.08302	He I	$2s^3S - 2p^3P^o$	3.3 (-12)	3.5 (-12)	
1.08302	He I	$2s^3S - 2p^3P^o$	(HeI+Pay)		
1.0895				4.2 (-13)	
1.09381	H I	3-6		3.1 (-13)	
1.0940	He II	6-12			
1.1468	[P II]	$^3P_1 - ^1D_2$		1.1 (-14)	
1.155				1.9 (-14)	
1.157				3.2 (-14)	
1.16264	He II	5-7	1.5 (-14)	3.9 (-14)	1.1 (-10)
1.16902	K I			-2.5 (-14)	
1.17696	K I			-3.0 (-14)	
1.17728	K I				
1.1828	Mg I			-3.1 (-14)	
1.185				1.4 (-14)	
1.187				5.9 (-14)	
1.1883	[P II]	$^3P_2 - ^1D_2$	1.2 (-13)		
1.1895				4.1 (-14)	
1.1964	CO	(5-1)		-3.1 (-14)	
1.198					4.3 (-13)
1.202					5.6 (-13)
1.2030			2.8 (-14)		
1.204					2.4 (-13)
1.210					1.4 (-13)
1.214					1.1 (-13)
1.226					1.5 (-13)

1.2418	Mg I			-2.8 (-14)	
1.2423	Mg I				
1.2434	Mg I				
1.251				1.7 (-13)	
1.2520	[S IX]		5.6 (-14)		
1.25275	He I	$3s^3S - 4p^3P^o$			
1.255				1.2 (-13)	
1.25670	[Fe II]	$a^6D_{9/2} - a^4D_{7/2}$	2.2 (-13)	2.7 (-13)	
1.267					3.1 (-13)
1.27848	He I	$3d^3D - 5f^3F^o$	1.1 (-13)	1.1 (-13)	
1.27878	[Fe II]	$a^6D_{3/2} - a^4D_{3/2}$	(ff abs. ?)		
1.28180	H I	3-5	2.5 (-13)	3.6 (-13)	2.3 (-12) (n)
1.2820	He II	6-10			4.5 (-11) (b)
1.29427	[Fe II]	$a^6D_{5/2} - a^4D_{5/2}$	1.2 (-13)		
1.302				-1.0 (-14)	
1.3205	[Fe II]	$a^6D_{7/2} - a^4D_{7/2}$		4.6 (-14)	
1.322				6.9 (-14)	
1.324				5.8 (-14)	
1.3278	[Fe II]	$a^6D_{3/2} - a^4D_{3/2}$		2.9 (-14)	

TABLE 5.3

LINE IDENTIFICATIONS AND FLUXES IN THE INFRARED
SPECTRA OF NGC 7027, HUBBLE 12, AND THE ORION NEBULA

λ (μm)		IDENTIFICATION	NGC 7027	HUBBLE 12	ORION NEBULA
0.89970	He I	$3^3D - 10^3F^\circ$		1.0 (-13)	
0.89998	He I	$3^1D - 10^1F^\circ$			
0.90149	H I	3-10	2.7 (-12)	1.3 (-12)	4.1 (-13)
0.90690	[S III]	$^3P_1 - ^1D_2$	3.8 (-11)	1.0 (-11)	6.9 (-12)
0.9132					2.2 (-14)
0.9184					1.4 (-14)
0.92290	H I	3-9	4.1 (-12)		6.8 (-13)
0.93449	He II	5-8	1.3 (-12)		
0.9362			2.0 (-13)		
0.94636	He I	$3^3S - 5^3P^\circ$	2.8 (-13)	3.0 (-13)	9.3 (-14)
0.9516				1.9 (-12)	
0.95311	[S III]	$^3P_2 - ^1D_2$	1.3 (-10)	4.2 (-11)	3.8 (-11)
0.95459	H I	3-8		3.1 (-12)	
0.96035	He I	$3^1S_0 - 6^1P_1^\circ$			1.6 (-13)
0.97027	He I	$3^3P^\circ - 7^3S$			4.3 (-14)
0.97558	[Fe II]	$a^2D_{5/2} - b^2G_{7/2}$	8.6 (-14)		
0.9770			1.5 (-13)		
0.98241	[C I]	$2s^2 2p^2 ^3P_1 - 2p^1D_2$	2.6 (-13)		3.5 (-14)
0.98502	[C I]	$2s^2 2p^2 ^3P_2 - 2p^1D_2$	9.1 (-13)		1.1 (-13)
0.99035	C II	$4f^2F^\circ - 5g^2G$	2.9 (-13)		3.1 (-14)
1.0014					3.3 (-14)
1.00312	He I	$3d^1D_2 - 7f^1F_3$			1.5 (-13)
1.00494	H I	3-7	9.4 (-12)		2.1 (-12)

1.01089	N I	$3p^4D_{3/2}^{\circ} - 3d^4F_{5/2}$			1.7 (-14)
1.01125	N I	$3p^4D_{5/2}^{\circ} - 3d^4F_{7/2}$			
1.01147	N I	$3p^4D_{7/2}^{\circ} - 3d^4F_{9/2}$			
1.01236	He II	4-5	2.2 (-11)		
1.01385	He I	$3^1P^{\circ} - 7^1D$			1.9 (-14)
1.0208					1.5 (-14)
1.02867	[S II]	$2D_{3/2}^{\circ} - 2P_{3/2}^{\circ}$	2.0 (-12)	1.6 (-13)	5.5 (-13)
1.03113	He I	$3^3P^{\circ} - 6^3D$		7.8 (-14)	
1.03205	[S II]	$2D_{5/2}^{\circ} - 2P_{3/2}^{\circ}$	2.9 (-12)	2.2 (-13)	7.8 (-13)
1.03364	[S II]	$2D_{3/2}^{\circ} - 2P_{1/2}^{\circ}$	2.2 (-12)	1.4 (-13)	6.2 (-13)
1.03705	[S II]	$2D_{5/2}^{\circ} - 2P_{1/2}^{\circ}$	1.0 (-12)	5.1 (-14)	3.0 (-13)
1.0398	[N I]	$2D_{5/2}^{\circ} - 2P_{1/2, 3/2}^{\circ}$	8.2 (-13)	1.6 (-13)	9.2 (-14)
1.0408	[N I]	$2D_{3/2}^{\circ} - 2P_{1/2, 3/2}^{\circ}$	6.6 (-13)	1.0 (-13)	4.1 (-14)
1.0420	He II	6-13	4.2 (-13)		
1.0505				2.3 (-14)	
1.0519				5.0 (-14)	3.8 (-14)
1.0651				1.8 (-14)	
1.06676	He I	$3^3P^{\circ} - 6^3S$		3.7 (-14)	1.6 (-14)
1.06831	C I	$3s^3P_1^{\circ} - 3p^3D_2$	1.8 (-13)		7.4 (-14)
1.06854	C I	$3s^3P_0^{\circ} - 3p^3D_1$			
1.0750				4.3 (-13)	
1.07541	C I	$3s^3P_2^{\circ} - 3p^3D_1$	4.5 (-13)		2.8 (-14)
1.08302	He I	$2s^3S - 2p^3P^{\circ}$	2.4 (-10)	9.7 (-11)	2.9 (-11)
1.09129	He I	$3^3D - 6^3F_0^{\circ}$	8.4 (-13)	7.0 (-13)	6.2 (-14)
1.09170	He I	$3^1D - 6^1F^{\circ}$			
1.09381	H I	3-6	1.7 (-11)	6.4 (-12)	2.9 (-12)
1.0997				1.8 (-14)	
1.10131	He I	$3s^1S - 5p^1P^{\circ}$		2.9 (-14)	
1.10450	He I	$3p^1P^{\circ} - 6d^1D$		3.6 (-14)	

1.1067	[Fe II]	$a^4P_{1/2} - b^4F_{5/2}$		9.0 (-15)	
1.1102			1.1 (-13)		
1.1189				2.2 (-14)	
1.1287	O I	$3p^3P - 3d^3D^o$		1.3 (-13)	6.5 (-14)
1.13303	C I	$3p^1P - 3d^1D^o$			5.4 (-14)
1.1344			2.4 (-13)		
1.1468	[P II]	$^3P_1 - ^1D_2$	5.1 (-13)		3.6 (-14)
1.1590				2.0 (-14)	
1.1610					1.7 (-14)
1.16190	H ₂	(2,0) S(1)		2.2 (-14)	
1.16264	He II	5-7	5.9 (-12)		
1.1659					1.5 (-14)
1.16597	C I	$3p^3D_3 - 3d^3D_3^o$		2.4 (-14)	
1.16696	C I	$3p^3S_1 - 3d^3P_2^o$			
1.1673	He II	6-11	8.2 (-13)		
1.1694				1.8 (-14)	
1.17482	C I	$3p^3D_1 - 3d^3F_2^o$	7.7 (-14)	2.2 (-14)	8.9 (-14)
1.17533	C I	$3p^3D_3 - 3d^3F_4^o$			
1.17548	C I	$3p^3D_2 - 3d^3F_3^o$			
1.1829	[Fe II]	$b^4F_{5/2} - b^4D_{5/2}$		2.4 (-14)	
1.1833	[Fe II]	$b^4F_{3/2} - b^4D_{7/2}$			
1.18537	H ₂	(3,1) S(3)		3.1 (-14)	
1.18820	[Fe II]	$a^4D_{7/2} - a^2G_{7/2}$	1.7 (-12)	2.4 (-14)	7.3 (-14)
1.18828	[P II]	$^3P_2 - ^1D_2$			
1.18925	H ₂	(2,0) S(0)		2.6 (-14)	
1.18929	C I	$3p^3D_2 - 4s^3P_1^o$	4.2 (-13)		
1.18958	C I	$3p^3D_3 - 4s^3P_2^o$			
1.1936				3.9 (-14)	1.9 (-14)
1.19691	He I	$3p^3P^o - 5d^3D$	3.9 (-13)	2.5 (-13)	9.1 (-14)

1.1990	C III	$4s^3S - 4p^3P^o$	2.6 (-14)		
1.20315	Si I	$4s^3P_2^o - 4p^3D_3$	9.2 (-14)		
1.2074			8.6 (-14)		
1.2108			7.5 (-14)		
1.2127					8.3 (-15)
1.2184					1.6 (-14)
1.2192				1.4 (-14)	
1.2206				4.4 (-15)	1.4 (-14)
1.2232					6.8 (-15)
1.22707	Si I	$4s^3P_2^o - 4p^3D_2$			8.5 (-15)
1.2292			8.0 (-14)	4.2 (-14)	2.5 (-14)
1.23266	H ₂	(3,1) S(1)	3.8 (-13)	3.2 (-14)	1.7 (-14)
1.2368					3.3 (-15)
1.23800	H ₂	(2,0) Q(1)	3.9 (-14)	2.9 (-14)	1.2 (-14)
1.24159	H ₂	(2,0) Q(2)	1.1 (-13)		
1.2426				1.4 (-14)	
1.2436					1.0 (-14)
1.24612	N I	$3p^2D_{3/2}^o - 3d^2F_{5/2}$		2.1 (-14)	1.3 (-14)
1.24696	N I	$3p^2D_{5/2}^o - 3d^2F_{7/2}$			
1.25275	He I	$3s^3S - 4p^3P^o$	5.0 (-13)	4.7 (-13)	1.3 (-13)
1.25495	C I	$3p^3P_0 - 3d^3P_1^o$	1.1 (-13)		
1.25670	[Fe II]	$a^6D_{9/2} - a^4D_{7/2}$	2.4 (-13)	1.7 (-13)	8.9 (-14)
1.26141	C I	$3p^3P_2 - 3d^3P_2^o$	3.7 (-14)		
1.26173	H ₂	(3,1) S(0)			2.2 (-14)
1.2648					2.9 (-14)
1.2672	[Fe II]	$a^4D_{7/2} - a^2G_{9/2}$	5.8 (-14)		1.7 (-14)
1.2703	[Fe II]	$a^6D_{1/2} - a^4D_{1/2}$		1.5 (-14)	
1.2720	He II	7-20	7.3 (-14)		

1.2749			5.3 (-14)	5.0 (-14)	4.5 (-15)
1.27848	He I	$3d^3D - 5f^3F^o$	1.2 (-12)	9.8 (-13)	1.9 (-13)
1.28180	H I	3-5	3.6 (-11)	1.8 (-11)	6.3 (-12)
1.2888					7.3 (-15)
1.2897				4.8 (-14)	
1.2914	He II	7-19	1.7 (-13)		
1.29427	[Fe II]	$a^6D_{5/2} - a^4D_{5/2}$	8.0 (-14)	3.9 (-14)	3.0 (-14)
1.29684	He I	$3p^1P^o - 5d^1D$	1.2 (-13)	6.7 (-14)	2.8 (-14)
1.2985	He I	$3d^3D - 5p^3P^o$	1.0 (-13)	8.4 (-14)	2.3 (-14)
1.3061					9.1 (-15)
1.3077				3.6 (-14)	1.2 (-14)
1.31124	H ₂	(4,2) S(1)		1.5 (-14)	
1.3121			5.1 (-14)		
1.3125					1.2 (-14)
1.31376	H ₂	(3,1) Q(1)	5.7 (-14)	2.3 (-14)	
1.3150	He II	7-18	1.3 (-13)		
1.31650	O I	$3^3P - 4^3S$	1.1 (-13)	4.4 (-13)	2.4 (-13)
1.3205	[Fe II]	$a^6D_{7/2} - a^4D_{7/2}$	9.8 (-14)	6.5 (-14)	5.7 (-14)
1.32368	H ₂	(3,1) Q(1)		1.1 (-14)	
1.3278	[Fe II]	$a^6D_{3/2} - a^4D_{5/2}$	4.0 (-14)	2.2 (-14)	4.0 (-14)
1.34167	H ₂	(3,1) Q(4)		3.1 (-14)	
1.3434				2.7 (-14)	2.6 (-14)
1.3440	He II	7-17	1.0 (-13)		
1.3472			6.2 (-14)	4.3 (-14)	
1.4139					1.8 (-14)
1.4275					1.5 (-14)
1.4307					2.1 (-14)

1.44290	C I	$3p^3P_1 - 3d^3D_1^o$			2.5 (-14)
1.44422	C I	$3p^3P_2 - 3d^3D_2^o$			
1.4490					3.5 (-14)
1.4588				2.6 (-14)	
1.4639				6.5 (-14)	3.1 (-14)
1.4658				7.1 (-14)	2.9 (-14)
1.49116	H I	4-27		2.7 (-14)	
1.49379	H I	4-26		4.5 (-14)	2.5 (-14)
1.49675	H I	4-25		6.1 (-14)	2.2 (-14)
1.4985					2.0 (-14)
1.50010	H I	4-24		5.8 (-14)	2.8 (-14)
1.50250	C I	$3d^3D^o - 5p^3D$			1.7 (-14)
1.50392	H I	4-23		8.3 (-14)	2.5 (-14)
1.5069					1.1 (-14)
1.50800	H I	4-22		1.1 (-13)	3.9 (-14)
1.50837	He I	$3s^1S - 4p^1P^o$			
1.51300	H I	4-21		9.1 (-14)	2.7 (-14)
1.51918	H I	4-20		9.7 (-14)	6.5 (-14)
1.52606	H I	4-19		1.1 (-13)	5.7 (-14)
1.5296					2.8 (-14)
1.53418	H I	4-18		1.1 (-13)	5.1 (-14)
1.5425					9.8 (-15)
1.54389	H I	4-17		9.4 (-14)	1.7 (-14)
1.5497	Si I	$3d^3P_1^o - 5p^3D_2$		2.9 (-13)	1.8 (-13)
1.55565	H I	4-16		1.1 (-13)	4.1 (-14)
1.57007	H I	4-15			4.0 (-14)

TABLE 5.4

IONIZATION POTENTIALS FOR IONS OF S, Ni, Fe, AND Mn

ion	χ (eV)	ion	χ (eV)	ion	χ (eV)
S ⁶⁺	281	Fe ⁹⁺	262	Mn ⁸⁺	222
S ⁷⁺	329	Fe ¹⁰⁺	290	Mn ⁹⁺	248
S ⁸⁺	379	Fe ¹¹⁺	330		
Ni ⁷⁺		Fe ¹²⁺	361		

Chapter 6

Conclusions

In this thesis, I presented 0.9 - 1.35 μm spectra from a wide variety of objects. Most of the objects have quite rich spectra, and I was able to extract a great deal of information from these data. In this chapter, I will review the most important features of the 0.9 - 1.35 μm wavelength region.

One important result from this thesis is that, in objects with regions covering a wide range of physical conditions, the lines between 0.9 and 1.35 μm can be used to study all of the same regions covered by visible spectroscopy. A similar sort of analysis is not possible with longer wavelength spectra. The 0.9 - 1.35 μm region thus becomes quite important for studying obscured sources.

A second significant aspect of the 0.9 - 1.35 μm region is its importance for studying shocks. [Fe II] lines can be very bright in regions with high velocity shocks. [Fe II] lines are useful for observing supernova remnants, and they might also prove quite useful in studies of star formation regions. As was shown in earlier chapters, the 1 μm [Fe II]

lines can be used to determine physical conditions in shocked regions. Until further modelling is done, the same cannot be said about [Fe II] lines at other wavelengths.

Low velocity shocks often excite the lower vibrational levels of molecular hydrogen. The strongest lines in shock-heated regions are the $\Delta v = 1$ lines, which are found in the 2 - 3 μm region. The $\Delta v = 2$ lines, between 1.0 and 1.4 μm , are not nearly as bright but can also be used to study shocks. The extinction to the H_2 emitting region can be determined by comparison of 1 μm and 2 μm lines with a common upper level.

The 1 μm region is very important for studying fluorescence processes. The $\Delta v = 2$ H_2 lines are much more sensitive to fluorescence than the $\Delta v = 1$ lines, and they can be used to detect fluorescent emission even in the presence of strong thermal emission. H_2 fluorescence lines can be useful indicators of conditions in the H_2 emitting region. Their intensity depends mainly on the cloud density and on the strength of the incident ultraviolet radiation (Black & van Dishoeck 1987; Sternberg 1988). The intensity also depends, to a lesser extent, on the temperature of the gas, the total thickness of the cloud, and the optical properties of the grains. The relative line intensities are rather insensitive to these parameters so the physical properties of the emitting region can be studied even if there is only one well resolved fluorescent line.

The 0.9 - 1.35 μm region is also ideal for detecting fluorescent emission from O I. The 1.1287 and 1.3165 μm lines are both excited by UV continuum fluorescence, and the 1.1287 μm line can be further enhanced by Ly β fluorescence. The relative contributions of the two fluorescence mechanisms can be determined by comparing the strengths of the two infrared O I lines. A large H α optical depth is required for the Ly β fluorescence mechanism to be effective so strong 1.1287 μm emission is also an indicator of optically thick Balmer line emission.

Oxygen has very efficient charge exchange reactions with hydrogen, and the two elements have very similar ionization potentials. As a result, the volumes of the H I and O I recombination regions are nearly identical, and the less abundant oxygen produces much fainter lines. However, the upper level of the 1.3165 μm line lies only 11.9 eV above the ground state, and that level and a number of higher levels can be excited by absorption of UV photons. By this fluorescence mechanism, bright O I emission can be produced in gas clouds surrounding strong UV sources. As a result, the 1.3165 μm line might be useful for finding stars in star formation regions. The 1.1287 μm line might be even more useful since it can be very strong in clouds excited by Ly β fluorescence.

As a final point, I would like to emphasize the importance of the line lists presented in this thesis. These

lists cover a wide variety of objects and show the features that one can expect to see in their infrared spectra. With this information in hand, it becomes much easier to plan more extensive observing programs. These line lists are also an obvious starting point when identifying features in new spectra. Finally, as was done in Chapter 5, a new spectrum can be compared to the spectra in this thesis to see what features are new or unusual. It is likely that these comparisons will produce some of the most interesting results.

References

- Allard, F. 1990, Ph.D. thesis, University of Heidelberg
- Allen, D.A., & Cragg, T.A. 1983, MNRAS, 203, 777
- Aller, L.H., & Czyzak, S.J. 1983, ApJS, 51, 211
- Altenhoff, W.J., Braes, L.L.E., Olton, F.M., & Wendker, J.H. 1976, AA, 46, 11
- Aspin, C., McLean, I.S., & Coyne, G.V. 1985, A&A, 149, 158
- Aspin, C., McLean, I.S., Rayner, J.T., & McCaughrean, M.J. 1988, A&A, 197, 242
- Bachiller, R., Gómez-González, J., Bujarrabal, V., & Martín-Pintado, J. 1988, A&A 196, L5
- Balick, B. 1989, in IAU Symposium 131, Planetary Nebulae, ed. S. Torres-Peimbert (Dordrecht: Kluwer), p. 83
- Bashkin, S., & Stoner, J.O. 1975, Atomic Energy Levels and Grotrian Diagrams, North-Holland Publishing Company, Amsterdam
- Beckwith, S., Beck, S.C., & Gatley, I. 1984, ApJ, 280, 648
- Berriman, G., & Reid, N. 1987, MNRAS, 227, 315 (BR)
- Berriman, G., Reid, N., & Leggett, S.K. 1992, ApJL, submitted
- Bessell, M.S. 1979, PASP, 91, 589
- Bessell, M.S. 1991, AJ, 101, 662
- Bessell, M.S., & Scholz, M. 1990 in *Accuracy of Element Abundances from Stellar Atmospheres* (Lecture Notes in Physics 356), ed. R. Wehrse (Springer-Verlag: New York), p. 85
- Black, J.H., & Dalgarno, A. 1976, ApJ, 203, 132
- Black, J.H., & van Dishoeck, E.F. 1987, ApJ, 322, 412
- Bohm, K.H., Schwartz, R.D., & Siegmund, W.A. 1974, ApJ, 193, 353

- Bohm, K.H., Siegmund, W.A., & Schwartz, R.D. 1976, A&A, 50, 361
- Bond, H.E., & Livio, M. 1990, ApJ, 355, 568
- Buhrke, T., Brugel, E.W., & Mundt, R. 1986, A&A, 163, 83
- Bujarrabal, V., Gómez-González, J., Bachiller, R., & Martín-Pintado, J. 1988, A&A, 204, 242
- Burrows, A., Hubbard, W.B., & Lunine, J.I. 1989, ApJ, 345, 939 (BHL)
- Burton, M.G., Brand, P.W.J.L., Geballe, T.R. & Webster, A.S. 1989, MNRAS, 236, 409
- Burton, M.G., & Geballe, T.R. 1986, MNRAS, 223, 13P
- Caillault, J.-P., & Patterson, J. 1990, AJ, 100, 825
- Calvet, N., & Cohen, M. 1978, MNRAS, 182, 687
- Calvet, N., & Peimbert, M. 1983, Rev. Mexicana Astr. Ap., 5, 319
- Campbell, B., Persson, S.E., & McGregor, P.J. 1986, ApJ, 305, 336
- Campins, H., Rieke, G.H., & Lebofsky, M.J. 1985, AJ, 90, 896
- Canto, J., Rodriguez, L.F., Barral, J.F., & Carral, P. 1981, ApJ, 244, 102
- Cardelli, J.A., Clayton, G.C., & Mathis, J.S. 1989, ApJ, 345, 245
- Carsenty, U., & Solf, J. 1982, A&A, 106, 307
- Cernicharo, J., Guelin, M., Martin-Pintado, J., Penalver, J., & Mauersberger, R. 1989, A&A, 222, L1
- Clegg, R.E.S. 1987, MNRAS, 229, 31P
- Cohen, M. 1973, MNRAS, 164, 395
- Cohen, M. 1977, ApJ, 215, 533
- Cohen, M., Bieging, J.H., Dreher, J.W., & Welch, W.J. 1985, ApJ, 292, 249

- Cohen, M., Bieging, J.H., & Schwartz, P.R. 1982, ApJ, 253, 707
- Condal, A., Fahlman, G.G. Walker, G.A.H., & Glaspey, J.W. 1981, PASP, 93, 191
- Contini, M., & Viegas, S.M. 1992, preprint
- Cosmovici, C.B., Olthof, H., Strafella, F., Barbieri, C., Canton, G., & D'Anna, E. 1979, A&A, 72, 241
- Czyzak, S.J., & Krueger, T.K. 1963, MNRAS, 126, 177
- D'Antona, F., & Mazzitelli, I. 1985, ApJ, 296, 502 (DM)
- De Robertis, M.M., Dufour, R.J., & Hunt, R.W. 1987, J.Roy.Ast.Soc.Can, 81, 195
- Deutsch, L.K. 1990, Ph.D. Thesis, Harvard University
- Dinerstein, H.L., Lester, D.F., Carr, J.S., & Harvey, P.M. 1988, ApJ, 327, L27
- Dorman, B., Nelson, L.A., & Chau, W.Y. 1989, ApJ, 342, 1003 (DNC)
- Edwards, S., & Snell, R.L. 1982, ApJ, 261, 151
- Eiroa, C., & Casali, M. 1989, in IAU Coll. 120, G. Tenorio-Tagle, M. Moles, J. Melnick (eds.), p.227
- Elias, J.H. 1980, ApJ, 241, 728
- Elias, J.H., Frogel, J.A., Hyland, A.R., & Jones, T.J. 1983, AJ, 88, 1027
- Field, G.B., Somerville, W.B., & Dressler, K. 1966, ARA&A, 4, 207
- Gammie, C.F., Knapp, G.R., Young, K., Phillips, T.G., and Falgarone, E. 1989, ApJ, 345, L87
- Glassgold, A.E., Mamon, G.A., & Huggins, P.J. 1991, ApJ, in press
- Gliese, W. 1969, Veroff.Astr.Rechen-Inst.Heidelberg, No. 22
- Gliese, W., & Jahreiss, H. 1979, A&AS, 38, 423
- Goodrich, R.W. 1986, ApJ, 311, 882

- Gottlieb, E.W., & Liller, W. 1976, *ApJ*, 207, L135
- Grandi, S.A. 1975, *ApJ*, 196, 465
- Greenhouse, M.A., Woodward, C.E., Thronson, H.A., Rudy, R.J.,
Rossano, G.S., Erwin, P., & Puetter, R.C. 1991, *ApJ*,
383, 164
- Hamann, F., & Persson, S.E. 1989a, *ApJ*, 339, 1078
- Hamann, F., & Persson, S.E. 1989b, *ApJS*, 71, 931
- Hamann, F. & Simon, M. 1986, *ApJ*, 311, 909
- Hamann, F. & Simon, M. 1988, *ApJ*, 327, 876
- Hartmann, L. 1982, *ApJS*, 48, 109
- Hartmann, L., Jaffe, D., & Huchra, J.P. 1980, *ApJ*, 239, 905
- Hartquist, T.W., & Dyson, J.E. 1987, *MNRAS*, 228, 957
- Harvey, P.M., Joy, M., Lester, D.F., & Wilking, B.A. 1986,
ApJ, 301, 346
- Harvey, P.M., Thronson, H.A., & Gatley, I. 1979, *ApJ*, 231,
115
- Henry, T.J., & McCarthy, D.W., Jr. 1990, *ApJ*, 350, 334
- Herbig, G.H. 1971, *ApJ*, 169, 537
- Hodapp, K.-W. 1984, *A.A.* 141, 255
- Hoffleit, D., & Jaschek, C. 1982, *Bright Star Catalog* (New
Haven: Yale Univ. Obs.)
- Hudgins, D., Herter, T., & Joyce, R.J. 1990, *ApJ*, 354, L57
- Hummer, D.G., & Storey, P.J. 1987, *MNRAS*, 224, 801
- Humphreys, R.M., Merrill, K.M., & Black, J.H. 1980, *ApJ*,
237, L17
- Jones, T.J., & Dyck, H.M. 1978, *ApJ*, 220, 159
- Jura, M. 1986, *ApJ*, 303, 327
- Jura, M., & Kroto, H. 1990, *ApJ*, 351, 222
- Kawabe, R., Ogawa, H., Fukui, Y., Takano, T., Takaba, H.,

- Fujimoto, Y., Sugitani, K., & Fujimoto, M. 1984, *ApJ*, 282, L73
- Kawara, K., Nishida, M., & Phillips, M.M. 1989, *ApJ*, 337, 230
- Kawara, K., Nishida, M., & Taniguchi, Y. 1988, *ApJ*, 328, L41
- Keyes, C.D., Aller, L.H., & Feibelman, W.A. 1990, *PASP*, 102, 59
- Kirkpatrick, J.D. 1992, Ph.D. thesis, University of Arizona, in preparation
- Kirkpatrick, J.D., Henry, T.J., & McCarthy, D.W., Jr. 1991, *ApJS*, 77, 417 (KHM)
- Kleinmann, S.G., Sargent, D.G., Moseley, H., Harper, D.A., Loewenstein, R.F., Telesco, C.M., & Thronson, H.A. 1978, *A&A*, 65, 139
- Knapp, G.R., Gammie, C.F., Young, K., & Phillips, T.G. 1990, in *Submillimetre Astronomy*, ed. G.D. Watt & A. Webster (Dordrecht: Kluwer), p. 33
- Knapp, G.R., & Morris, M. 1985, *ApJ*, 292, 640
- Korista, K.T., & Ferland, G.J. 1989, *ApJ*, 343, 678
- Krueger, T.K., & Czyzak, S.J. 1970, *Proc.Roy.Soc.Lon.A*, 318, 531
- Kwok, S., & Bignell, R.C. 1984, *ApJ*, 276, 544
- Kwok, S., & Feldman, P.A. 1981, *ApJ*, 267, L67
- Lacy, C.H. 1977, *ApJS*, 34, 479
- Lada, E.A., DePoy, D.L., Evans, N.J., & Gatley, I. 1991b, *ApJ*, 371, 171
- Lada, C.J., DePoy, D.L., Merrill, K.M., & Gatley, I. 1991a, *ApJ*, 374, 533
- Latter, W.B., Maloney, P.R., Kelly, D.M., Black, J.H., Rieke, G.H., & Rieke, M.J. 1992, *ApJ*, 389, 347
- Leggett, S.K., & Hawkins, M.R.S. 1988, *MNRAS*, 234, 1065 (LH)
- Leinert, Ch., Haas, M., Allard, F., Wehrse, R., McCarthy, D.W., Jr., Jahreiss, H., & Perrier, Ch. 1990, *A&A*, 236, 399

- Lenzen, R. 1987, *A&A*, 173, 124
- Lequeux, J., & Jourdain de Muizon, M. 1990, *A&A*, 240, L19
- Livingston, W., & Wallace, L. 1991, *An Atlas of the Solar Spectrum in the Infrared from 1850 to 9000 cm⁻¹ (1.1 to 5.4 μ m)* (NSO and NOAO: Tucson)
- Livio, M., Salzman, J., & Shaviv, G. 1979, *MNRAS*, 188, 1
- Lo, K.Y., & Bechis, K.P. 1976, *ApJ*, 205, L21
- Low, F.J. 1984, *Applied Optics*, 23, 1308
- Martin, P.G., & Rogers, C. 1987, *ApJ*, 322, 374
- Martín-Pintado, J., Bujarrabal, V., Bachiller, R.,
Gómez-González, J., & Planesas, P. 1988, *A&A*, 197, L15
- Massey, P., Strobels, K., Barnes, J.V., & Anderson, E. 1988, *ApJ*, 328, 315
- McCarthy, D.W., Jr., Henry, T.J., Fleming, T.A., Saffer, R.A., Liebert, J., & Christou, J.C. 1988, *ApJ*, 333, 943
- McGregor, P.J., Persson, S.E., & Cohen, J.G. 1984, *ApJ*, 286, 609
- Mendoza, C. 1983, in *IAU Symposium 103, Planetary Nebulae*, ed. D.R. Flower, (Dordrecht: D. Reidel), 143
- Minchin, N.R., Hough, J.H., McCall, A., Aspin, C., Yamashita, T., & Burton, M.G. 1991, *MNRAS*, 249, 707
- Monet, D.G., Dahn, C.C., Vrba, F.J., Harris, H.C., Pier, J.R., Luginbuhl, C.B., & Ables, H.D. 1992, *AJ*, 103, 638
- Moorwood, A.F.M., & Oliva, E. 1988, *A&A*, 203, 278.
- Münch, G., & Taylor, K. 1974, *ApJ*, 192, L93
- Morris, M. 1981, *ApJ*, 249, 572
- Morris, M. 1987, *PASP*, 99, 1115
- Mould, J.R. 1976, *A&A*, 48, 443
- Neri, S., Garcia-Burillo, S., Guélin, M., Cernicharo, J., Guilloteau, S., & Lucas, R. 1992, *A&A*, 262, 544
- Nussbaumer, H., & Storey, P.J. 1988, *A&A*, 193, 327

- Oliva, E., & Moorwood, A.F.M. 1990, *ApJ*, 348, L5
- Olnon, F.M. 1975, *A&A*, 39, 217
- Ortolani, S., & D'Odorico, S. 1980, *A&A*, 83, L8
- Osterbrock, D.E. 1989, *Astrophysics of Gaseous Nebulae and Active Galactic Nuclei* (Mill Valley: University Science Books)
- Osterbrock, D.E., Shaw, R.A., & Veilleux, S. 1990, *ApJ*, 352, 561
- Osterbrock, D.E., Tran, H.D., & Veilleux, S. 1992, *ApJ*, 389, 196
- Persson, S.E., Geballe, T.R., McGregor, P.J., Edwards, S., & Lonsdale, C.J. 1984, *ApJ*, 286, 289
- Persson, S.E., McGregor, P.J., & Campbell, B. 1988, *ApJ*, 326, 339
- Pravdo, S.H., Rodriguez, L.F., Curiel, S., Canto, J., Torrelles, J.M., Becker, R.H., & Sellgren, K. (1985), *ApJ*, 293, L35
- Rieke, G.H., & Lebofsky, M.J. 1985, *ApJ*, 288, 618
- Rieke, M.J. 1990, *NICMOS Instrument Selection Report*, unpublished
- Rix, H.-W., Carleton, N.P., Rieke, G., & Rieke, M. 1990, *ApJ*, 363, 480
- Robbins, R.R. 1968, *ApJ*, 151, 497
- Rowan-Robinson, M., & Harris, S. 1983, *MNRAS*, 202, 797
- Ruan, K. 1991, Ph.D. thesis, Australian National University
- Rudy, R.J., Erwin, P., Rossano, G.S., & Puetter, R.C. 1991, *ApJ*, 383, 344
- Rudy, R.J., Erwin, P., Rossano, G.S., & Puetter, R.C. 1992, *ApJ*, 384, 536
- Rudy, R.J., Rossano, G.S., & Puetter, R.C. 1989, *ApJ*, 346, 799
- Russell, R.W., Soifer, B.T., & Willner, S.P. 1978, *ApJ*, 220, 568

- Schmidt, G.D., & Cohen, M. 1981, ApJ, 246, 444 (SC81)
- Schneeberger, T.J., Worden, S.P., & Wilkerson, M.S. 1979, ApJS, 41, 369
- Scholz, M., & Takeda, Y. 1987, A&A, 186, 200
- Schulz, A., Black, J.H., Lada, C.J., Ulich, B.L., Martin, R.N., Snell, R.L., & Erickson, N.J. 1989, ApJ, 341, 288
- Schwartz, R.D. 1974, ApJ, 191, 419
- Schwartz, R.D. 1978, ApJ, 223, 884
- Schwartz, R.D. 1981, ApJ, 243, 197
- Shields, G.A., & Oke, J.B. 1975, ApJ, 197, 5
- Shull, J.M., & Hollenbach, D.J. 1978, ApJ, 220, 525
- Simon, M., & Cassar, L. 1984, ApJ, 283, 179
- Simon, M., Felli, M., Cassar, L., Fischer, J., & Massi, M. 1983, ApJ, 266, 623
- Snell, R.L., Scoville, N.Z., Sanders, D.B., & Erickson, N.R. 1984, ApJ, 284, 176
- Solf, J., Bohm, K.H., & Raga, A. 1988, ApJ, 334, 229 (SBR)
- Spinrad, H., & Wing, R.F. 1969, ARA&A, 7, 249
- Sternberg, A. 1988, ApJ, 332, 400
- Sternberg, A., & Dalgarno, A. 1989, ApJ, 338, 197
- Strom, S.E., Strom, K.M., Grasdalen, G.L., Sellgren, K., Wolff, S., Morgan, J., Stocke, J., & Mundt, R. 1985, AJ, 90, 2281
- Thompson, R.I. 1987, ApJ, 312, 784
- Thompson, R.I., Strittmatter, P.A., Erickson, E.F., Witteborn, F.C., & Strecker, D.W. 1977, ApJ, 218, 170
- Thompson, R.I., & Tokunaga, A.T. 1979, ApJ, 231, 736
- Thronson, H.A. 1981, ApJ, 248, 984
- Thronson, H.A., Latter, W.B., Black, J.H., Bally, J., & Hacking, P. 1987, ApJ, 322, 770

- Thronson, H.A., & Mozurkewich, D. 1983, ApJ, 271, 611
- Ulrich, R.K., & Wood, B.C. 1981, ApJ, 244, 147
- van Dishoeck, E.F., & Black, J.H. 1986, ApJS, 62, 109
- Veeder, G.J. 1974, AJ, 79, 1056
- Volk, K.M., & Kwok, S. 1989, ApJ, 342, 345
- Westbrook, W.E., Becklin, E.E., Merrill, K.M., Neugebauer,
G., Schmidt, M., Willner, S.P., & Wynn-Williams, C.G.
1975, ApJ, 202, 407
- White, R.L., & Becker, R.H. 1985, ApJ, 297, 677
- Zuckerman, B. & Gatley, I. 1988, ApJ, 324, 501